Robust quantum logic for trapped ion quantum computers

Anna Elizabeth Webb

Submitted for the degree of Doctor of Philosophy

University of Sussex, Brighton, United Kingdom. September 2018

Declaration

I hereby declare that this thesis has not been and will not be submitted in whole or in part to another University for the award of any other degree.

Signature:

Anna Elizabeth Webb

UNIVERSITY OF SUSSEX

Anna Elizabeth Webb, Doctor of Philosophy

Robust quantum logic for trapped ion quantum computers

This thesis describes experimental work on implementing single and two qubit gates in $^{171}Yb^{+}$ ions using methods suitable for a large scale quantum computer. By combining a magnetic field gradient with microwave and radiofrequency radiation, the spin and motional states of the ions are coupled which allows multi-qubit operations to be performed, as well as providing individual addressing of ions in frequency space. A dressed state qubit is used which exhibits an increase of over two orders of magnitude in the coherence time for a qubit that it is sensitive to the magnetic field gradient. Using this system, single qubit gates are characterised using the technique of randomised benchmarking, resulting in a measured average error per gate of $9(3) \times 10^{-4}$.

A new type of two qubit gate is experimentally demonstrated, which in comparison to a standard two qubit gate shows significantly increased resilience to two major sources of gate infidelity: heating of the motional mode of the ions during gate operations, and incorrectly set gate field frequencies. These types of errors are expected to become increasingly important with the move towards quantum processors with large numbers of qubits. Using this same technique, a two qubit gate is also demonstrated at a higher initial temperature with a significantly improved fidelity compared to standard methods.

These gate techniques are used to demonstrate work towards implementing position-dependent quantum logic, a method which could remove the correlation between the number of ions and the number of gate fields required in a large scale quantum computing architecture. A method to move the dressed state qubit through a magnetic field gradient while preserving quantum information is demonstrated, as well as a method to optimise the phase of a two qubit gate of unknown phase in order to implement a CNOT logic gate. This provides a path forwards to demonstrating a CNOT gate using position-dependent quantum logic.

Acknowledgements

Thank you first to my supervisor Prof. Winfried Hensinger, for giving me the opportunity to carry out this research in such a dynamic group. Thank you also to Dr. Sebastian Weidt for initially encouraging me to start this PhD and providing me with guidance and useful discussions along the way, as well as for all your help with this thesis.

A special thank you must go to Dr. Simon Webster for all of your hard work in reading and providing feedback on this thesis, as well as your support in the lab and helping me understand the physics of what we do. Thank you also to Dr. Joe Randall for handing on his expertise on the experiment at the beginning of my PhD and teaching me the ropes of working in the lab. Thank you to Dr. Tomas Navickas for so much support and help in the lab. Thank you all and Dr. David Murgia too for providing plenty of fun along the way. Thank you to all the members of IQT who I have worked with past and present, too many people to list here, who have been without exception willing to offer help and advice. It's been a pleasure to work with you all and you've made days in the lab (and Friday evenings in Falmer bar) a lot more fun.

Finally thank you to my family, and especially to my Mum and Dad, who instilled in me the curiosity and confidence to pursue this PhD, and have encouraged and supported me over many years of education.

Chapter contributions

The work in this PhD has been collaborative in nature, and here I summarise the major contributions of others. All other work is my own.

- Chapter 3: The main structure of the experiment was developed prior to my work by Dr. Robin Sterling, Dr. Altaf Nizamani, Dr. Sebastian Weidt, Dr. James Siverns, Dr. James McLoughlin, Dr. Kim Lake, and Dr. Joe Randall. Adam Lawrence programmed the AWG, and Dr. Tomas Navickas implemented the locking system. The experimental control program was written by Dr. Simon Webster, and improvements were made by David Bretaud.

- Chapter 4: The theory and experimental implementation of dressed states was developed prior to this PhD by Dr. Joe Randall, Dr. Simon Webster, and Dr. Sebastian Weidt, and further developed by myself.

- Chapter 5: Dr. Simon Webster provided useful discussions in analysing sources of error. The theory of depolarising of the dressed states was developed by Dr. Joe Randall.

- Chapter 6: The initial two qubit gate was developed and experimentally implemented by Dr. Sebastian Weidt, Dr. Joe Randall, Dr. Kim Lake, Dr. Simon Webster, and myself, and was presented along with a discussion of error sources in the thesis of Dr. Joe Randall. The theory of multi-tone Mølmer-Sørensen gates was extended to include symmetric detuning errors by Sam Collingbourne, Dr. Fahrang Haddadfarshi and Dr. Florian Mintert. The maximum likelihood method for analysis was developed by Adam Lawrence.

- Chapter 7: The proposal for a scalable architecture using global radiation fields was developed primarily by Dr. Sebastian Weidt and Dr. Bjoern Lekitsch. The theory and demonstration of mapping between the clock states and dressed states in one position was developed by Dr. Joe Randall and Adam Lawrence.

Publications

Ground-state cooling of a trapped ion using long-wavelength radiation

S. Weidt, J. Randall, S. C. Webster, E. D. Standing, A. Rodriguez, A. E. Webb, B. Lekitsch, and W. K. Hensinger

Phys. Rev. Lett. 115, 013002 (2015)

Trapped-ion quantum logic with global radiation fields

S. Weidt, J. Randall, S. C. Webster, K. Lake, A. E. Webb, I. Cohen, T. Navickas, B. Lekitsch, A. Retzker, and W. K. Hensinger

Phys. Rev. Lett. 117, 220501 (2016)

Resilient entangling gates for trapped ions

A. E. Webb, S. C. Webster, S. Collingbourne, D. Bretaud, A. M. Lawrence, S. Weidt, F. Mintert, and W. K. Hensinger

Phys. Rev. Lett. 121, 180501 (2018)

Contents

List of Tables

List of Figures

Chapter 1

Introduction

1.1 Quantum computing

The development of fast electronic computing over the past 50 years has had a profound influence on the modern world, and the development of quantum computing could make a similar impact. The beginning of the history of quantum simulation and computing is often attributed to a talk given by Richard Feynman in 1982, during which he noted in his inimitable style [1]

> ... nature isn't classical, dammit, and if you want to make a simulation of nature, you'd better make it quantum mechanical, and by golly it's a wonderful problem, because it doesn't look so easy.

The need for a controllable quantum system in order to accurately simulate a quantum mechanical world can be understood by considering a system of n spins. If these spins behaved classically, while there are 2^n possible states, only one state is occupied at any time so an n bit register would be large enough to store information about this system. However, since these n spins behave quantum mechanically, the phenomenon of superposition means the system can occupy all 2^n states simultaneously, so 2^n complex numbers are needed to describe it. By adding one further element to the system, the amount of information necessary in order to describe it doubles. This exponential increase in required information storage often makes it necessary to make approximations when simulating large quantum systems with classical computers.

The idea of a quantum simulator designed to emulate a specific quantum system was extended by Deutsch to a universal quantum computer that could simulate any physical, realisable system by programming an arbitrary unitary evolution [2]. Quantum algorithms were then developed with direct applications, such as Shor's algorithm for factorising large

numbers [3] and Grover's algorithm for searching large unsorted data sets [4]. This range of possibilities, including both simulations and other applications, make the construction of a universal computer of immense interest to not only the scientific community, but to the wider field of technology and industry.

The basic component of a universal quantum computer capable of running these types of algorithms is the quantum bit, or 'qubit'. This is analogous to the bit in a classical computer, which can be in state 0 or 1. However, the qubit can instead occupy a superposition of both states simultaneously, with a state expressed as

$$|\psi\rangle = \alpha\,|0\rangle + \beta\,|1\rangle \tag{1.1}$$

where α and β are complex coefficients with $|\alpha|^2 + |\beta|^2 = 1$. This ability to occupy both states simultaneously, as well as the possibility for entangling multiple qubits, is key to the speed up achievable in a quantum computer.

Quantum algorithms can be performed on a set of qubits by performing a sequence of quantum gates. It has been shown that all operations can be decomposed into a set of universal quantum gates which includes multiple gates acting on a single qubit, and one acting on two qubits. Gates can be expressed as unitary operators. For example, a typical single qubit gate is the Pauli-X gate, which is is described by the operator $\sigma_x = |0\rangle\langle 1| + |1\rangle\langle 0|$. The two qubit gate that forms a part of this set must be capable of producing an entangled state. A commonly used two qubit gate is the CNOT gate, with unitary operator

$$U_{\mathrm{CNOT}} = |00\rangle\langle 00| + |01\rangle\langle 01| + |10\rangle\langle 11| + |11\rangle\langle 10|\,. \tag{1.2}$$

The effect of this gate is to swap the state of the second ('target') qubit state if the first ('control') qubit state is 1. By applying the CNOT gate to two qubits with initial states $(|0\rangle + |1\rangle)/\sqrt{2}$ for the control qubit and $|0\rangle$ for the target qubit, a maximally entangled Bell state is produced of the form $(|00\rangle + |11\rangle)/\sqrt{2}$. In this thesis, a two qubit geometric phase gate is used, where ions state-selectively pick up phases, allowing for production of an entangled state. This can be transformed into the CNOT gate using single qubit rotations.

With a universal set of gates, it is possible to perform any quantum algorithm. For all physical implementations of these gates, however, error will be incurred at some level during a gate operation due to noise and decoherence. Quantum error correction codes can

be used overcome this problem, which use additional resources to compensate for these errors. In order for this error correction to be possible, gates must be performed with errors below the 'fault-tolerant' threshold. Some proposals, such as the 'surface code' [5], have thresholds as high as a 1% error per gate. However, the additional resources required are strongly dependent on the error per gate magnitude, so to perform useful computations, errors well below this 1% threshold are needed.

1.2 Trapped ions for quantum computing

In 2000, DiVincenzo identified a set of conditions for building a physical quantum computer. These are known as the DiVincenzo criteria [6] and can be summarised as

1. A scalable physical system with well-characterized qubits.
2. The ability to initialise the state of the qubits to a simple fiducial state, such as $|00...\rangle$.
3. Long relevant decoherence times, much longer than the gate operation time.
4. A 'universal' set of quantum gates.
5. A qubit-specific measurement capability.

Although they may not all ultimately be required, these criteria act as a guideline for assessing which physical systems could feasibly be used for constructing a quantum computer.

Research is ongoing into multiple candidate systems for implementing a scalable quantum computer, such as neutral atoms [7], superconducting circuits [8], and trapped atomic ions [9]. Trapped ions are a mature field of research and amongst the most promising platforms for constructing a quantum computer. One key advantage of using ions is the fundamentally unchanging nature of an atomic species, so that ions are identical wherever and whenever they are trapped. Laser cooling allows ions to form crystals due to their mutual Coulomb repulsion, and the internal states of a single ion can be used as a qubit. Qubit states can be initialised and measured using optical pumping and state-selective fluorescence, fulfilling criteria 2 and 5, which will be described in chapter 2. Ions are trapped in high vacuum environments, which means the ions are extremely well isolated from the environment and very long coherence times have been demonstrated [10], meeting criteria 3.

In order to perform a universal set of quantum gates (criteria 4), a qubit stored in the internal states of a single ion can be manipulated using electromagnetic radiation, either

laser or radiofrequency (RF) / microwave. Different single qubit gates can be performed by applying radiation with a specified frequency, phase and amplitude for the correct period of time. For quantum gates involving more than one ion, a coupling between the internal states of separate ions is required. This can be achieved using the collective motional mode that multiple ions exhibit when confined in a single harmonic trap. The first theoretical proposal for a trapped ion two qubit entangling gate was by Cirac and Zoller [9], and this method was first experimentally demonstrated on two ions some years later [11] alongside another two qubit entangling gate [12]. This gate, however, required cooling the ions to the ground state of motion, which, although achievable [13], is a large experimental overhead. This requirement was relaxed by the theoretical development of geometric phase gates by Mølmer and Sørensen [14, 15] and Milburn [16] which work independently of the initial motional mode of the ions. Both single and two qubit gates have now been demonstrated to high fidelity, with errors below fault-tolerant thresholds [17, 18, 19]. Trapped ions have therefore been shown to meet the criteria to be used as the building blocks for a quantum computer. However, the largest remaining challenge is to find a method to move from proof of principle experiments on small numbers of ions, to a large scale quantum computer.

1.3 Long-wavelength radiation quantum logic

There are two types of qubits used with trapped ions: optical qubits, or ground state qubits. Optical qubits are those with electronic transitions between states, typically with transition wavelengths in the visible or near visible regime, which in an alkali-like ion is normally an $S \leftrightarrow D$ transition. These present two main problems. The first is the typically short lifetime of the excited state, which places a limit on achievable gate fidelities. The second is the stringent requirement for the linewidth of the laser, which can limit the coherence time. Ground state qubits instead make use of two states from the electronic ground state as the qubit, for example two states from the electronic hyperfine ground state in an odd isotope with non-zero nuclear spin. These types of qubits have transitions in the GHz regime, with effectively infinite lifetimes. This makes ground state qubits more suitable for storing quantum information and performing quantum operations. A hyperfine qubit in the ground state of the ion $^{171}Yb^{+}$ is used in this work.

In order to perform multi-qubit operations, the shared motional mode of multiple ions is used as the intermediary mode, called the 'bus' mode. A coupling is then required between the internal spin states of each ion and the shared motional state, in order to

perform operations on the internal state of one ion which are dependent on the internal state of a different ion. This coupling is traditionally achieved using the photon momentum of the radiation used to perform the gate. The strength of this coupling is characterised by the Lamb-Dicke parameter, which is given by $\eta = z_0|\vec{k}|\cos\theta$ where z_0 is the position spread of the ground state wavefunction of the ion, given by $z_0 = \sqrt{\hbar/2m\nu_z}$, ν_z is the trap frequency, m is the mass of the ion, $\vec{k}$ is the wavevector of the incoming radiation, and θ is the angle between the wavevector and the motional mode being considered. For optical wavelengths, this Lamb-Dicke parameter is typically around 0.1. However, since the wavevector $\vec{k}$ depends inversely on the wavelength of the radiation, this parameter becomes very small for microwave radiation, with typical values of around 10^{-6}. In order to circumvent this problem, Raman transitions have typically been used for multi-qubit operations. A third state is employed to act as an intermediary in coupling the qubit states, with transitions in the optical regime. This allows for a sufficient Lamb-Dicke parameter to make multi-qubit operations possible. Ions can be individually addressed by deflecting tightly focussed laser beams onto single ions [20]. Various laser-driven methods have been used to demonstrate high fidelity two qubit entanglement [18] and entanglement of 14 ions [21].

However, despite the successes of laser driven quantum logic, it presents challenges in the context of a large scale quantum computer. The experimental control required is high, with the need for many lasers with highly stable beam pointing and amplitude, careful alignment, and tightly focussed beams. Furthermore, there is a fundamental limit to the fidelity of operations due to inelastic Raman scattering, which involves off-resonant scattering from the third state [22].

The use of microwaves instead for driving quantum logic presents many advantages for a trapped ion architecture suitable for scaling up to large numbers of ions. Low noise microwave sources are commercially available, with easily controllable phase, frequency and amplitude. They also overcome the limit to high fidelity of Raman scattering, since no third state is required during coherent manipulation. Since hyperfine qubits exhibit transition frequencies in the GHz regime, single qubit gates can be driven straightforwardly with resonant long-wavelength radiation. There are two challenges, however, which must be overcome in order to use microwaves for quantum logic. The first is the ability to overcome the small Lamb-Dicke parameters resulting from the use of microwaves in order to couple spin and motion to perform multi-qubit gates. The second is the need for a method to individually address ions to be able to perform quantum gates selectively.

In 2001, Mintert and Wunderlich proposed a scheme which uses static magnetic field gradients to overcome both of these problems [23]. This scheme takes away the dependence of the Lamb-Dicke parameter on the wavelength of the driving radiation, and instead the effective Lamb-Dicke parameter is dependent on the magnitude of the magnetic field gradient. This therefore allows a universal set of quantum gates to be performed solely with long-wavelength radiation and a magnetic field gradient, removing the need for lasers during coherent manipulation. The position dependent Zeeman splitting of the hyperfine qubits also allows ions to be individually addressed in frequency, rather than spatially as in the case of lasers. Microwaves can then be broadcast to large areas, without the need for any alignment to individual ions. This method for spin-motion coupling and individual addressing was first demonstrated by Johanning *et al.* [24], and a two qubit gate was first demonstrated in 2012 [25]. This method involving static magnetic field gradients and long-wavelength radiation is the basis for the work in this thesis.

There are, however, challenges involved in using this scheme. One of these is the necessity for using hyperfine states with different magnetic moments, which have an energy splitting which is dependent on the magnetic field. This means that the qubit is susceptible to decoherence resulting from magnetic field noise, which significantly reduces the coherence time. This can be mitigated to a certain extent by shielding from magnetic field noise [26]. The method employed in this thesis, though, is a scheme proposed by Timoney *et al.* [27], where by dressing the magnetic field sensitive states with radiation, states can be produced which retain the sensitivity to magnetic fields which allows for coupling of the spin and motional states, but exhibit longer coherence times. Using these dressed states, our laboratory has demonstrated a two qubit entangling gate with a fidelity of 0.985(12) using long-wavelength radiation [28]. Remaining challenges include the experimental task of generating high magnetic field gradients and microwave powers to perform faster gates, which is non-trivial.

An alternative scheme was proposed by Ospelkaus *et al.* [29], which uses near-field long-wavelength radiation, and relies on the resultant near field oscillating magnetic field gradient to couple the internal and motional states of the ions. This scheme has been used to demonstrate quantum logic to high fidelity [30], and benefits from some of the same advantages as the static gradient scheme over the use of lasers. However, this scheme also presents some challenges. The gradient produced by oscillating near-field radiation scales as around d^{-2} [31], which means that ions should be closer to the trap surface in order to produce higher effective Lamb-Dicke parameters. However, since heating rate scales as

approximately d^{-4} [32], this produces a higher heating rate, which induces error on multi-qubit operations. This method also does not incorporate natural individual addressability, but requires more complex methods in order to prevent cross talk between neighbouring ions [33, 34]. Finally, in order to perform gates on multiple ions in parallel, microwave voltages must be applied to many electrodes simultaneously.

1.4 Scalable architecture

In a large scale architecture capable of performing useful algorithms, like Shor's or Grover's algorithm, thousands or even more ions will be required, with quantum operations being performed on each ion. Quantum error correction involves encoding one logical qubit on to many physical qubits, with the number of physical qubits required highly dependent on the gate error. For example, using Shor's algorithm with surface code error correction to factorise a 2000 bit number, and assuming an error per gate of 0.1%, 4000 logical qubits are required which correlates to 220×10^6 physical qubits [5].

Many proof of principle experiments, including the work in this thesis, have been performed in macroscopic ion traps, with multiple ions trapped in a single harmonic potential. However, there is a limit to the number of ions which can successfully be manipulated in a single ion trap. This is largely due to spectral crowding. As the number of ions grows, the frequency spacing of the motional modes decreases. This means that off-resonant coupling to undesired modes can occur when performing multi-qubit operations, which induces decoherence and gate error. This error can be reduced by driving gate operations at a lower power, but this comes at a cost in terms of gate speed. For laser based quantum computing, there is the additional challenge of reduced spacing between ions when multiple ions are trapped in a single confining potential, making individual addressing with beams more challenging.

To overcome this problem, the 'quantum charge-coupled device' was proposed by Kielpinski *et al.* [35]. In this approach, ions are trapped in several separate confinement regions on the surface of a microfabricated ion trap. Different regions correspond to different operations, such as ion storage for memory, ion manipulation for quantum gates, and state detection. To perform algorithms, ions are shuttled between these separate regions. This allows the number of ions in any trapping region to be kept low, while maintaining the ability to perform quantum operations on many ions.

One of the major challenges of this approach in the context of high numbers of ions is the correlation between the number of ions and the number of radiation fields required,

whether using lasers or long-wavelength radiation. For thousands of ions, similar numbers of radiation fields would be required. Weidt *et al.* [28] recently proposed a scheme to overcome this problem using long-wavelength radiation and static gradients, replacing gate radiation fields for each individual ion with a smaller number of global radiation fields applied to all ions. Ions are shuttled between different regions, and only interact with the radiation fields that correspond to the operation for that region. This is possible using locally generated static magnetic field gradients in each region, and a qubit with a transition frequency that is dependent on the magnetic field. In a field gradient, this transition frequency is position dependent, so it is possible to ensure that ions only interact with specific fields by controlling the position of the ion. This method of position-dependent quantum logic crucially removes the dependence of the number of radiation fields on the number of ions in the architecture.

These approaches can be incorporated into a modular approach for constructing a quantum computer, in which individual stand-alone modules can be connected to reach the desired size. In order for modules to operate together, we require a method for connecting them. One such method is photonic interconnects, where remote entanglement between ions in different modules is achieved using a probabilistic interaction through photons [36, 37], although this can involve a slow interaction rate. An alternative approach is to use fast ion transport to connect individual modules. This method is part of the proposed blueprint for a long-wavelength radiation trapped ion quantum computer by Lekitsch *et al.* [38]. In this architecture, individual modules are composed of 1296 microfabricated X-junction ion traps, and ions are shuttled to different zones in the X-junction for different operations. Separate modules are then precisely aligned by mounting on precision machined steel frames and using XYZ piezo actuators. This allows ions to be directly shuttled between modules in order to perform operations on large numbers of ions. This proposal for a modular quantum computer is the framework for the research within our group.

1.5 Thesis focus and structure

The focus of this thesis is to demonstrate quantum logic gates which are suitable for use in a scalable architecture. The hyperfine ground state of the ion $^{171}Yb^{+}$ is used as a qubit, placed in a static magnetic field gradient in order to perform multi-qubit operations using long-wavelength radiation. The work is motivated by the concept for a scalable quantum computer proposed by Weidt *et al.* [28] to use global radiation fields for quantum logic, as part of the blueprint for a quantum computer proposed by Lekistch *et al.* [38].

The technique of randomised benchmarking is used to measure the single qubit gate fidelity on the dressed state qubit, a qubit which makes high fidelity operations possible using long-wavelength radiation in static magnetic fields. I then demonstrate a novel two qubit gate which protects against multiple error sources. This gate could be used in laser or long-wavelength based implementations, and is particularly suitable for realistic experimental environments in a large scale quantum computer, which may become noisier and less stable. In particular, these gates protect against errors due to heating of the ions, which is likely to become increasingly important in scalable architectures where microfabricated ion traps are used with higher heating rates due to the smaller ion-electrode distance. I finally present work towards demonstrating the principle of position-dependent quantum logic for a scalable quantum computing architecture, where qubits are moved between positions to perform different gates. The outline of the chapters is presented below.

Chapter 2 summarises the background to using trapped ions as qubits, including the method used to trap ions, as well as methods used to photo-ionise, Doppler cool, initialise, and detect. I also present the theory behind using microwaves for both single and multi-qubit operations.

Chapter 3 presents the experimental setup used for work in this thesis, as well as initial experiments including basic qubit manipulation, state preparation and detection, and driving motional sidebands of the ion transition using long-wavelength radiation.

Chapter 4 explains the theory behind dressed states, and shows an experimental demonstration of their preparation and detection, as well as a measurement of the coherence time and lifetime. There is also a discussion of the possible sources of decoherence.

Chapter 5 presents the results of a randomised benchmarking experiment used to measure the error of single qubit gates performed on the dressed state qubit, and analyses the dominant sources of infidelity contributing to this overall error.

Chapter 6 begins with a presentation of the theory behind a two qubit Mølmer-Sørensen gate using long-wavelength radiation, and an experimental demonstration of this. I then build upon this to explain the theory behind a new gate technique, multi-tone Mølmer-Sørensen gates, which protect against multiple errors include heating and some gate frequency errors. I experimentally demonstrate the robustness of this technique against these two different error sources.

Chapter 7 summarises work towards demonstrating a key component of the scalable architecture proposed by Weidt *et al.* Ions are moved between two positions in a magnetic field gradient while preserving qubit information, and a method is presented that allows

characterisation of the phase of two qubit gates in order to implement a CNOT gate.

Chapter 8 concludes the work in this thesis, summarising results and presenting an outlook for future experiments.

Chapter 2

Ytterbium ions as qubits

2.1 Introduction

In this chapter, I give an overview to the use of trapped $^{171}Yb^{+}$ ions as qubits. I first describe the method used for trapping ions, and the motion and heating of multiple ions in an ion trap. I then describe ionisation, cooling, preparation, and detection of the $^{171}Yb^{+}$ ions used in this thesis. I show that the hyperfine ground state of $^{171}Yb^{+}$ can be used as a qubit, using microwave and radiofrequency radiation for manipulation of the qubit and to implement single qubit gates. Finally, I show that by combining long-wavelength radiation with a magnetic field gradient, the spin and motional states of the ion are coupled allowing multi-qubit operations to be performed, analogously to when using lasers for qubit manipulation.

2.2 Trapped ion background

2.2.1 Ion traps

Earnshaw's theorem states that a charged particle cannot be confined in three dimensions using static electric fields. This is a direct consequence of Gauss' law, which states that in free space the divergence of the electric field should equal zero. A confining potential in three dimensions would equate to a negative divergence. There are two common trapping methods used to circumvent this problem: Penning traps and Paul traps. Penning traps make use of a combination of static electric and magnetic fields to achieve three-dimensional confinement. In this work, a type of Paul trap is used, which uses a combination of static and oscillating electric fields to trap ions.

A schematic of a linear Paul trap is shown in figure 2.1(a), consisting of four elongated

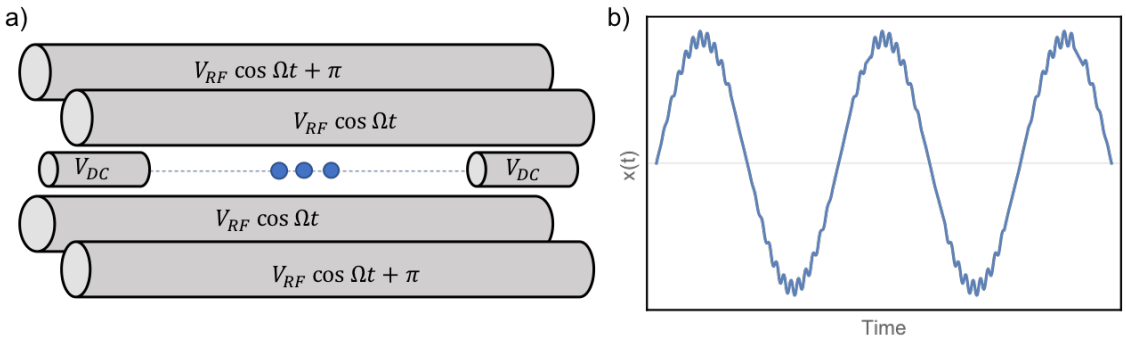

Figure 2.1: a) Schematic of a linear ion trap. The four elongated electrodes have RF potentials of amplitude V_{RF} applied as indicated, and the two endcaps are held at static voltages V_{DC}. The z-axis, along which ions are trapped, is indicated by the blue dashed line. b) The ion's motion in the x and y directions. Intrinsic micromotion is observed, as the superposition of a small oscillation at the trap RF frequency Ω_{RF} with the slower radial secular frequency ν_r.

electrodes. This is an RF quadrupole ion trap, which achieves confinement in the $x-y$ plane using oscillating electric fields. A potential of the form $V_{\mathrm{RF}}\cos(\Omega_{\mathrm{RF}}t)$ is applied to two diagonally opposite electrodes, and the same potential but with a phase offset of π is applied to the remaining two electrodes. An ion that is initially offset from the RF minimum will feel a confining force towards the centre. As the fields invert phase, the force will become anti-confining, but will be of a lesser magnitude as the ion is closer to the centre. The net effect over many cycles is a confining potential. The form of the instantaneous potential created by these RF fields is

$$\phi_{\mathrm{RF}}(x,y,t) = \eta_{\mathrm{RF}} V_{\mathrm{RF}} \left(\frac{x^2-y^2}{2d_r^2}\right)\cos(\Omega_{\mathrm{RF}}t) \tag{2.1}$$

where η_{RF} is a geometric factor which is equal to one for perfect hyperbolic electrodes, and d_r is the distance from the centre of the trap to the RF electrodes.

In order to confine the ion in the third dimension, a static potential is applied to two 'endcap' electrodes. This gives a potential of the form

$$\phi_{\mathrm{DC}}(x,y,z,t) = \eta_{\mathrm{DC}} V_{\mathrm{DC}} \left(\frac{2z^2-(x^2+y^2)}{2d_z^2}\right) \tag{2.2}$$

where η_{DC} is again a geometrical factor and d_z is the distance from the centre of the trap to the endcap electrodes.

Using these potentials, it is possible to find the ion motion using the equation for the

force on the ion, $\vec{F} = -e\vec{\nabla}V$. In the z direction, this gives an equation of motion

$$\frac{\partial^2 z}{\partial t^2} = -\frac{2e\eta_{\mathrm{DC}}V_{\mathrm{DC}}}{md_z^2}z. \tag{2.3}$$

This is the equation of motion for a harmonic oscillator with frequency

$$\nu_z = \sqrt{\frac{2e\eta_{\mathrm{DC}}V_{\mathrm{DC}}}{md_z^2}}. \tag{2.4}$$

This frequency is known as the axial secular frequency, and defines the motion of the ion in the z-direction, which is that of a quantized harmonic oscillator. In order to control the secular frequency for a given ion trap, the applied DC voltages should therefore be adjusted.

For motion in the x direction, the equation of motion is

$$\frac{\partial^2 x}{\partial t^2} = -\frac{e}{m}\left(\frac{\eta_{\mathrm{RF}}V_{\mathrm{RF}}}{d_r^2}\cos\left(\Omega_{\mathrm{RF}}t\right) - \frac{\eta_{\mathrm{DC}}V_{DC}}{d_z^2}\right)x. \tag{2.5}$$

By making the substitutions

$$\begin{aligned} q &= \frac{2e\eta_{\mathrm{RF}}V_{\mathrm{RF}}}{m\Omega_{\mathrm{RF}}^2 d_r^2} \\ a &= -\frac{4e\eta_{\mathrm{DC}}V_{\mathrm{DC}}}{m\Omega_{\mathrm{RF}}^2 d_z^2} \end{aligned} \tag{2.6}$$

this becomes a standard Matthieu differential equation. Solving in the limit $q \ll 1$ and $a \ll q$, it can be shown that the motion takes the approximate form [39, 40]

$$x(t) = x_0\cos\left(\nu_r t\right)\left(1 + \frac{q}{2}\cos\left(\Omega_{\mathrm{RF}}t\right)\right) \tag{2.7}$$

where

$$\nu_r = \frac{\Omega_{\mathrm{RF}}}{2}\sqrt{\frac{q^2}{2} - \frac{2\nu_z^2}{\Omega_{\mathrm{RF}}^2}}. \tag{2.8}$$

This is the radial secular frequency. An equivalent solution can be found in the y-direction and, for a perfectly symmetric system, the radial secular frequency should have the same value in both the x and the y directions. From equation 2.7, it can be seen that there are two superimposed frequencies of motion in the radial direction, at ν_r and Ω_{RF}. For stable trapping, the condition $\Omega_{\mathrm{RF}}/\nu_r \geq 2\sqrt{2}/0.9 \approx 3.14$ must be met [41]. This type of stable motion is shown in figure 2.1(b), and the fast oscillations are known as the intrinsic micromotion. If $\nu_r \ll \Omega_{\mathrm{RF}}$, the fast rotating term can be ignored and the system is simply a harmonic oscillator. Any stray constant force causes a displacement of the ion's

motion so that the average position is no longer at the RF nil. In this case, the magnitude of the fast oscillations becomes larger, and this is known as excess micromotion and is problematic for high fidelity quantum operations. Stray electric fields can cause this effect by displacing the ion, so must be compensated for.

2.2.2 Quantised normal modes

The above derivation considered a single ion in an ion trap. However, when multiple ions are trapped, as well as the harmonic potential from the trap there is also a force due to Coulomb repulsion between ions. Generally, parameters are set so that $\nu_z \ll \nu_r$. This means that multiple ions will form a linear string along the z-axis, and that it is a good approximation to consider axial and radial motion separately. In this work, axial motion will be used for work involving motional states. The ion-spacing along the z axis can be calculated by considering the balance of forces due to the trapping potential and the Coulomb repulsion. The total potential generalised to multiple ions is [42]

$$V = \sum_{i=1}^{N} \frac{1}{2} m\nu_z^2 z_i(t) + \sum_{i \neq j}^{N} \frac{e^2}{8\pi\epsilon_0 |z_i(t) - z_j(t)|}. \tag{2.9}$$

The equilibrium position of the ions can be calculated by finding the minimum in the potential for each ion. This is done by equating the differential of the potential with respect to each ion position to zero, so that $\partial V/\partial z_i = 0$. For the case of two ions, this results in a pair of coupled equations, which can be solved to give an ion-ion spacing of

$$\Delta z = \left(\frac{e^2}{2\pi\epsilon_0 m\nu_z^2} \right)^{1/3}. \tag{2.10}$$

The spacing of ions can therefore be controlled by adjusting the axial secular frequency, with a higher secular frequency reducing the spacing within the ion string.

The motion of N ions trapped in a linear chain can be described by N normal modes along each of the three axes. This allows us to write the displacement of the nth ion in a chain from its equilibrium position as

$$\vec{r}_n = \sum_{l=\{x,y,z\}} \sum_{j=1}^{N} \vec{q}_l S_{j,n}^l z_{l,j}^0 (a_{l,j} + a_{l,j}^\dagger) \tag{2.11}$$

where the first sum is a sum over the principal axes and the second is a sum over the normal modes. The operators $a_{l,j}$ and $a_{l,j}^\dagger$ are the ladder operators for normal mode j in direction l, and $z_{l,j}^0$ is the extent of the ground state wavefunction of a normal mode,

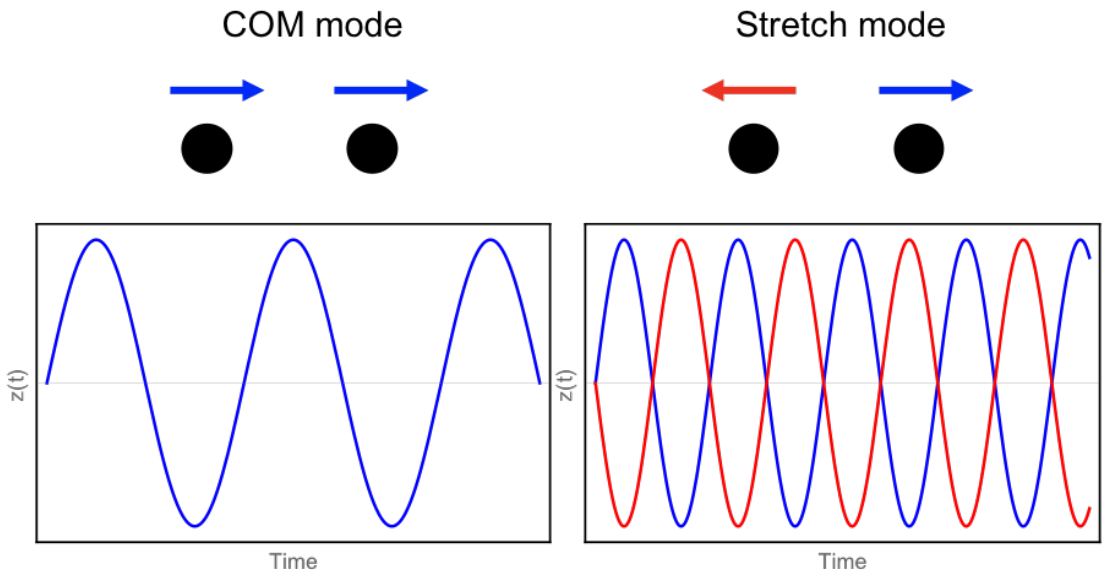

Figure 2.2: Depiction of the two normal modes of motion for two ions trapped in a harmonic potential, where graphs show the displacement $z(t)$ from each ion's equilibrium position over time. Left: The centre of mass (COM) mode where both ions oscillate in phase and with equal frequency, ν_z, and amplitude around their respective equilibrium positions. Right: The stretch mode, where ions move out of phase at a higher frequency equal to $\sqrt{3}\nu_z$. This mode is sometimes called the 'breathing mode'.

given by $z^0_{l,j} = \sqrt{\hbar/2m\nu_{l,j}}$, where $\nu_{l,j}$ is the frequency of that mode. The vector $\vec{q}_l$ is the unit vector along the principal axis l. The term of the normal mode matrix $S^l_{j,n}$ describes the motion of the nth ion for mode j in the l direction. This is normalised such that $\sum_n \left(S^l_{j,n}\right)^2 = 1$ [42].

For a single ion, there is one motional mode along each principal axis, the centre of mass (COM) mode. For two ions, there are equivalently two modes in each direction. In the axial direction, these are the COM and the stretch mode, with normal mode coordinates $S^z_{11} = S^z_{12} = \frac{1}{\sqrt{2}}$ and $S^z_{21} = -S^z_{21} = \frac{1}{\sqrt{2}}$ respectively. The COM mode exhibits motion with both ions moving in phase at the same amplitude and trap frequency $\nu_1 = \nu_z$. In the stretch mode, ions move out of phase with the same amplitude at a higher frequency, $\nu_2 = \sqrt{3}\nu_z$. These two modes are depicted in figure 2.2. In the radial directions x and y, the normal coordinates are the same as for the two modes in the z direction, and represent the COM and the rocking modes.

2.2.3 Ion heating

The mean motional phonon number $\bar{n}$ of a trapped ion will increase at a constant rate of $\dot{\bar{n}}$, usually measured in phonons per second, known as the heating rate. This can be a major source of infidelity for multi-qubit gates, since it causes decoherence of the motional

mode which is used during these types of operations. A low heating rate is therefore desirable. The underlying mechanism behind heating is not fully understood, since the experimentally observed scaling of heating rate with trap distance of around $\dot{\bar{n}} \propto d^{-4}$ [32] does not fit with a uniform noise model [32]. This heating is therefore classified as 'anomalous heating', and is thought to derive from noise on the surface of the electrodes, such as fluctuating electric patch potentials [43]. Factors such as electrical noise from electrode voltage sources also affect the heating rate, and significant work on reducing noise on the experimental system used in this work has previously led to a reduction in the measured heating rate [44].

The heating rate can be written in terms of the spectral density of the electric field noise $S_E(\nu_z)$ at the ion's position, and for the COM mode is given by [45]

$$\dot{\bar{n}}_C(\nu_z) = \frac{e^2}{4m\hbar\nu_z} S_E(\nu_z). \tag{2.12}$$

Previous experiments have indicated that $S_E(\nu_z) \propto \nu_z^{-1}$ [46], which allows an independent parameter to be calculated, $\nu_z S_E(\nu_z)$, from a measured heating rate. This allows heating rates to be extrapolated at different secular frequencies, and gives a dependence of heating rate on secular frequency of $\dot{\bar{n}} \propto \nu_z^{-2}$. This is a reasonable assumption, although it should be noted that this is only an approximation, and some measurements have given different scalings of $S_E(\nu_z)$ with ν_z (for example [47]).

For the COM mode, since both ions move in phase, a uniform electric field can excite the motional mode and therefore cause heating. However, for the stretch mode (and higher order modes in the case of more ions), only a differential field (i.e. a field gradient) can excite the motion of the ions. While equation 2.12 is true for the stretch mode as well as the COM mode, the spectral noise density for these field gradient terms differs from that for uniform field noise. The heating rate for the stretch mode can be expressed in terms of the scaled spectral noise density for the COM mode $\nu_z S_E(\nu_z)$ as [48]

$$\begin{aligned} \dot{\bar{n}}_S(\nu_S) &= \frac{e^2}{4m\hbar\nu_s^2} \frac{\nu_z S_E(\nu_z)}{d_r^2} \Delta z^2 \\ &= \frac{e^2}{4m\hbar\nu_s^{10/3}} \frac{\nu_z S_E(\nu_z)}{d_r^2} \left(\frac{3e^2}{2\pi\epsilon_0 m}\right)^{2/3} \end{aligned} \tag{2.13}$$

where we have used $\nu_s = \sqrt{3}\nu_z$, d_r is the distance to the nearest electrode, and Δz is the ion spacing which has been substituted in from equation 2.10. However, this equation is an approximation, since it assumes a scaling of the noise spectrum with the inverse

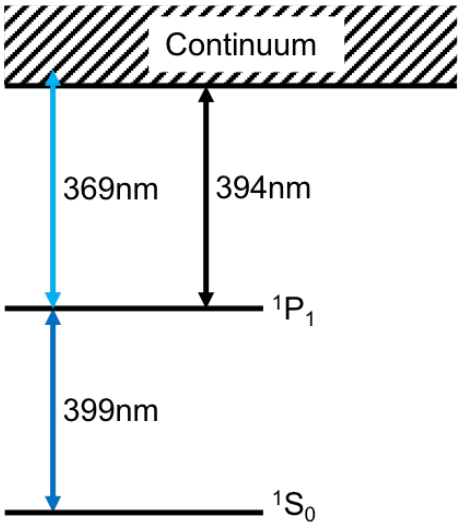

Figure 2.3: Relevant energy levels within ytterbium for photoionisation. While a single stage process could be used to promote an electron directly from the ground state $^1S_0$ to the continuum, a two stage process is used, which allows for isotope selectivity.

of frequency, and also assumes that noise is uncorrelated. In order to obtain more accurate heating rates, they should be measured directly for the COM and stretch modes individually, as will be described in section 4.3.3.

2.3 Ytterbium

There are various elements that have suitable properties to be used for trapping ions, based on a series of considerations. These include the commercial availability of lasers that address the ion's atomic transition energies, and the availability of the relevant isotopes. In this thesis, ytterbium ions are used. In particular, the odd isotope $^{171}Yb^+$ is trapped, where the internal states are split in energy by the hyperfine interaction in the presence of a magnetic field. This produces hyperfine levels which can be used for a qubit transition. In this section, the trapping and cooling of $^{171}Yb^+$ will be discussed, as well as the hyperfine ground state energy levels which are used as the qubit subspace.

2.3.1 Photo-ionisation

In order to trap an ytterbium ion, neutral ytterbium is injected into the trapping position by a thermal beam from an atomic oven. The ionisation energy of ytterbium is 6.25 eV which corresponds to a wavelength of 198 nm. While ionisation could be achieved using a single laser at this UV wavelength, a multi-photon process is used instead. Primarily, this allows for isotope selective trapping. Furthermore, deep UV lasers are more difficult

to obtain and hazardous to operate, and the higher energy photons mean they are more likely to cause charge build up on electrodes. This would cause stray electric fields at the ion position, resulting in excess micromotion.

First, a 399 nm laser is used to promote a valence electron from $^1S_0$ to $^1P_1$, as shown in figure 2.3. The exact frequency of this transition is isotope dependent [49]. A second laser is then needed with wavelength below 394 nm to promote this electron to the continuum. In this experiment, a laser of wavelength 369 nm is available due to its use for Doppler cooling of the ion (as discussed in the next section), so this is used for the final step. An ion is therefore trapped when both lasers are focussed onto the trapping position while a current is being passed through the atomic ovens to generate a thermal beam of neutral ytterbium atoms.

2.3.2 Doppler cooling

Doppler cooling of the ion is achieved by addressing the energy transition with a laser slightly 'red' detuned from the resonant transition, so at a lower frequency than the resonant frequency. This means that there is an asymmetry in absorption of photons, as the ion is more likely to absorb photons when it is moving towards the laser source than away from it, due to the Doppler shift. This results in a net force on the ion opposing motion, and thus lowers the kinetic energy. The trapping potential provides the required restoring force.

Doppler cooling is performed on the transition $^2S_{1/2}, F = 1 \leftrightarrow^2 P_{1/2}, F = 0$ using a single red detuned 369 nm laser. However, this is not a closed cycle so microwave fields and two extra lasers are required, as illustrated in figure 2.4. Once excited to the $^2P_{1/2}, F = 0$ state by the 369 nm laser, population decays to the $^2S_{1/2}, F = 1$ state at a rate of $\Gamma/2\pi = 19.6$ MHz. Off-resonant excitation can occur, resulting in excitation to the state $^2P_{1/2}, F = 1$, which then decays to $^2S_{1/2}, F = 0$. Population can be transferred back to $^2S_{1/2}, F = 1$ using a microwave field at the hyperfine splitting, 12.6 GHz.

0.5% of the time, population in $^2P_{1/2}$ decays to $^2D_{3/2}$. A 935 nm laser is resonant with the transition $^2D_{3/2} \leftrightarrow^3 [3/2]_{1/2}$, from where it decays back to $^2S_{1/2}$. In the experimental setup used in this thesis, the 935 nm laser is at high power and broadened over the hyperfine transitions in $^2D_{3/2}$ and $^3[3/2]_{1/2}$, although it is possible to instead add sidebands to the laser light. Occasionally, on the order of once a day, a background collision results in the transition $^2D_{3/2} \leftrightarrow^2 D_{5/2}$, which then decays to $^2F_{7/2}$. A 638 nm laser is used to excite the transition $^2F_{7/2} \leftrightarrow^1 [5/2]_{5/2}$, from where it decays back to $^2D_{3/2}$ or $^2D_{5/2}$. Since

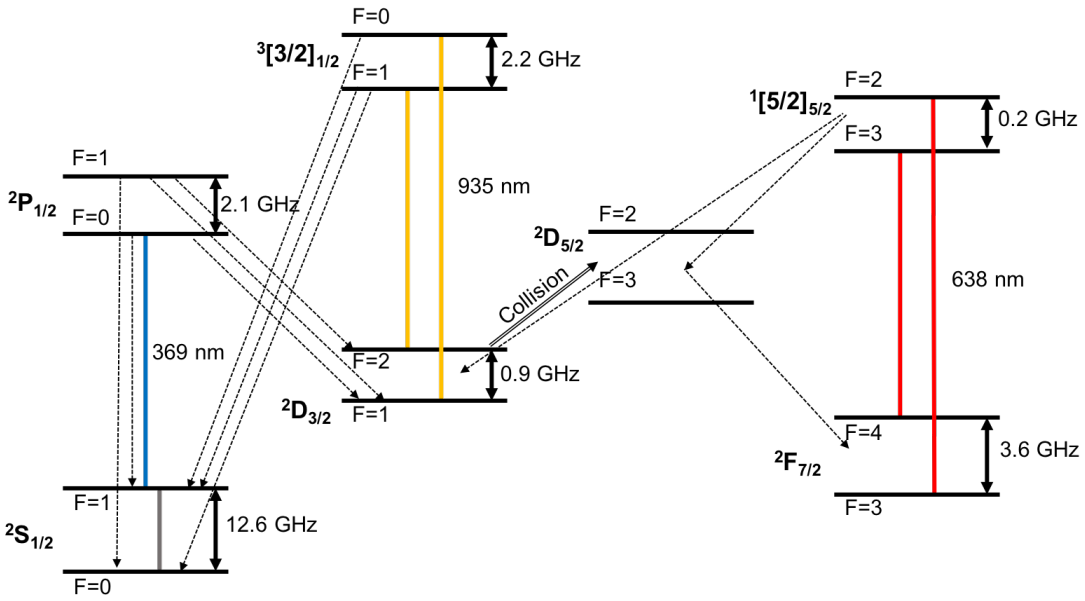

Figure 2.4: Relevant energy levels in $^{171}Yb^+$ showing the transitions used to form a closed Doppler cooling cycle. The thick coloured lines indicate transitions driven by lasers, with the thick grey line showing a microwave transition. The dashed lines are the decay channels possible from each level.

background collisions do not happen regularly, the 638 nm laser can be slowly scanned over the hyperfine levels.

Spontaneous emission of photons during Doppler cooling results in a limit in the minimum energy achievable, which is given by $\hbar\Gamma/2$, where $\Gamma = 19.6\,\mathrm{MHz}$ is the natural linewidth of the cooling transition $^2S_{1/2} \leftrightarrow {}^2P_{1/2}$. This gives a Doppler temperature limit of [50]

$$T = \frac{\hbar\Gamma}{2k_B} \tag{2.14}$$

which in this case is equal to 471 μK. From this temperature, a minimum mean phonon number of the quantised motion of the harmonic oscillator can be found. After Doppler cooling, the ion occupies a thermal distribution of motional states, and the density matrix describing this is

$$\rho_{th} = \sum_{n=1}^{\infty} p_n \left|n\right\rangle \left\langle n\right| \tag{2.15}$$

where $|n\rangle$ are the quantised motional harmonic oscillator states, and p_n is the probability of being in motional state $|n\rangle$. This probability is given by a Boltzmann distribution, with

$$p_n = \frac{1}{1+\bar{n}} \left(\frac{\bar{n}}{1+\bar{n}}\right)^n \tag{2.16}$$

where $\bar{n}$ is the average phonon number. From the Doppler temperature limit, the average

phonon number can be calculated as

$$\bar{n} = \frac{k_B T}{\hbar \nu_l} \tag{2.17}$$

where ν_l is the frequency of the motional mode of interest. In practice, this Doppler temperature limit is generally not reached after Doppler cooling of the ion, for example due to mis-set cooling parameters and the Zeeman structure in the $^2S_{1/2}$ manifold.

2.3.3 State preparation and detection

In order to use $^{171}Yb^+$ as a qubit, a method is required to initialise the ion in a known state, and to distinguish between different states. The ion is prepared in state $^2S_{1/2}, F = 0$ by optical pumping. The frequency of the 369 nm laser used for Doppler cooling is shifted so that it is resonant with the transition $^2S_{1/2}, F = 1 \leftrightarrow^2 P_{1/2}, F = 1$. From $^2P_{1/2}, F = 1$, the only allowed decay is to the state $^2S_{1/2}, F = 0$, and there is no laser resonant with any transitions from this energy level. By application of this shifted 369 nm laser for a period of time, all of the population is therefore transferred into the $^2S_{1/2}, F = 0$ state. This process can be achieved with high fidelity since off-resonant excitation from the $^2S_{1/2}, F = 0$ state is small.

In order to detect the state of the ion, the 369 nm laser is used to distinguish between ions in state $^2S_{1/2}, F = 0$ and $^2S_{1/2}, F = 1$. The laser is set to the resonant frequency of the $^2S_{1/2}, F = 1 \leftrightarrow^2 P_{1/2}, F = 0$ transition. After excitation to the state $^2P_{1/2}, F = 0$, the population can only decay to $^2S_{1/2}, F = 1$, where it can be excited again. This is therefore a closed cycle, so when the ion is in state $^2S_{1/2}, F = 1$ it will scatter multiple photons. However, when it is in state $^2S_{1/2}, F = 0$, there is no resonant light so the ion will not scatter photons. The measurement process therefore involves application of the 369 nm laser light for a period of time, during which photons are collected. By counting these photons, it is possible to distinguish between the two sub-manifolds $^2S_{1/2}, F = 0$ and $^2S_{1/2}, F = 1$. The limit to the fidelity of this detection process is largely due to off-resonant excitation of the laser light causing excitation from $^2S_{1/2}, F = 1$ to $^2P_{1/2}, F = 1$, since the laser is only detuned from this transition by 2.1 GHz. From this state it can decay to $^2S_{1/2}, F = 0$, and so will not scatter photons.

2.3.4 Hyperfine ground state

The internal electronic states of the hyperfine ground state of the $^{171}Yb^{+}$ ion are used as a qubit. There are four states in this manifold, which for simplicity will be labelled as:

$$\begin{aligned} {}^2S_{1/2}, F = 0, m_F = 0 &\rightarrow |0\rangle \\ {}^2S_{1/2}, F = 1, m_F = -1 &\rightarrow |-1\rangle \\ {}^2S_{1/2}, F = 1, m_F = 0 &\rightarrow |0'\rangle \\ {}^2S_{1/2}, F = 1, m_F = +1 &\rightarrow |+1\rangle \end{aligned} \tag{2.18}$$

during this thesis. If there is no magnetic field applied, the three $F = 1$ states are degenerate, and the splitting between the $F = 0$ and $F = 1$ states is $\omega_{\mathrm{hf}}/2\pi = 12.6428121\,\mathrm{GHz}$ [51]. When an offset magnetic field is applied, the three $F = 1$ states are split in frequency by the Zeeman effect. The transition frequencies can be derived from the Breit-Rabi formula [52]. Defining the frequencies as ω_+ for $|0'\rangle \leftrightarrow |+1\rangle$, ω_- for $|-1\rangle \leftrightarrow |0'\rangle$, and ω_0 for $|0\rangle \leftrightarrow |0'\rangle$, as depicted in figure 2.5, we have

$$\begin{aligned} \omega_+ &= \frac{\omega_{\mathrm{hf}}}{2}\left(1 + \frac{g_J\mu_B B}{\hbar\omega_{\mathrm{hf}}} - \sqrt{1 + \left(\frac{g_J\mu_B B}{\hbar\omega_{\mathrm{hf}}}\right)^2}\right) \\ \omega_- &= -\frac{\omega_{\mathrm{hf}}}{2}\left(1 - \frac{g_J\mu_B B}{\hbar\omega_{\mathrm{hf}}} - \sqrt{1 + \left(\frac{g_J\mu_B B}{\hbar\omega_{\mathrm{hf}}}\right)^2}\right) \\ \omega_{0'} &= \omega_{\mathrm{hf}}\sqrt{1 + \left(\frac{g_J\mu_B B}{\hbar\omega_{\mathrm{hf}}}\right)^2} \end{aligned} \tag{2.19}$$

where g_J is the Landé g factor which is $g_J = 2$, μ_B is the Bohr magneton, and B is the magnitude of the applied magnetic field. In small B fields, the value of $g_F\mu_B B/\hbar\omega_{\mathrm{hf}}$ is small, so it can be approximated that the frequency of the $|0\rangle \leftrightarrow |\pm 1\rangle$ transitions vary linearly with the applied magnetic field. However, while the frequency splitting due to the second order Zeeman shift is small, it is experimentally significant. An offset magnetic field of approximately 10 G is typically applied in our experimental setup, giving frequencies $\omega_+/2\pi \approx -\omega_-/2\pi \approx 14\,\mathrm{MHz}$, and $(\omega_{0'} - \omega_{\mathrm{hf}})/2\pi = 31\,\mathrm{kHz}$.

2.4 Trapped ion hyperfine qubits

The hyperfine ground state manifold of the $^{171}Yb^{+}$ qubit, as discussed in section 2.3.4, can be used to form a qubit. Transitions between qubit states could be driven by a pair of Raman beams, but in this case the transition is driven directly using long-wavelength

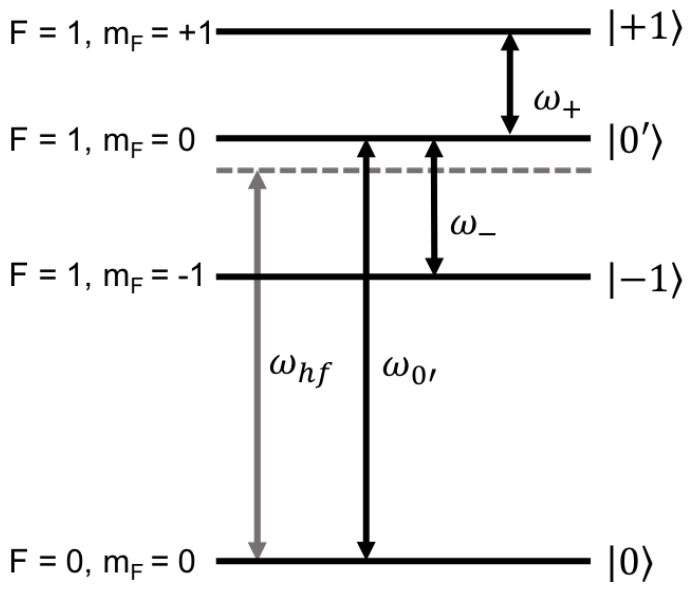

Figure 2.5: Hyperfine ground state of the $^{171}Yb^{+}$ ion (not to scale). The grey arrow labelled ω_{hf} shows the energy transition in zero B field, when the $F = 1$ states are energetically degenerate. The black arrows indicate the energy transitions when the $F = 1$ states are separated due to Zeeman splitting.

radiation resonant with the hyperfine splitting. Single qubit gates using this method are discussed in section 2.4.1. In order to drive multi-qubit operations, however, the long-wavelength radiation must be combined with a magnetic field gradient in order to achieve the required coupling between spin and motional states of the ion. This is discussed in section 2.4.2, where first a derivation for spin-motion coupling using lasers is presented, and then it is shown that the use of microwaves and magnetic field gradients is analogous to this. The derivations in this section in general follow Randall [53].

2.4.1 Single qubit operations

A trapped ion can be used as a qubit by defining two of the internal states as the qubit states $|\downarrow\rangle$ and $|\uparrow\rangle$. In this work, these qubit states are defined within the hyperfine manifold $^2S_{1/2}$ of the $^{171}Yb^+$ ion. The Hamiltonian describing these energy levels is

$$H_0 = \frac{\hbar\omega_0}{2}(|\uparrow\rangle\langle\uparrow| - |\downarrow\rangle\langle\downarrow|) \tag{2.20}$$

where ω_0 is the frequency describing the energy splitting of the $|\downarrow\rangle$ and $|\uparrow\rangle$ states. When electromagnetic radiation is applied to the ion, the interaction is described by a magnetic dipole coupling. The Hamiltonian describing the interaction is

$$H_I = \vec{\mu}.\vec{B} \tag{2.21}$$

where $\vec{\mu}$ is the magnetic moment, and $\vec{B}$ is the applied magnetic field. This magnetic field can be written as

$$\vec{B} = \frac{\vec{B_0}}{2}\left(e^{i(\omega t - \vec{k}.\vec{r} - \phi)} + e^{-i(\omega t - \vec{k}.\vec{r} - \phi)}\right) \tag{2.22}$$

where ω, $\vec{k}$ and ϕ are the frequency, wavevector and phase of the applied radiation respectively, and $\vec{r}$ is the position of the ion. When the applied radiation is near the resonant frequency of the hyperfine qubit (in the case of $|0\rangle \leftrightarrow |\pm 1\rangle$, for example, this is around 12.6 GHz), the magnetic dipole approximation can be made. Since the wavelength of this applied radiation is much larger than the spatial extent of the ion's waveform, we can approximate $e^{i\vec{k}.\vec{r}} \approx 1$. Then, rewriting the Hamiltonian H_I in terms of its matrix elements and using the fact that $\langle\downarrow|\,\vec{\mu}.\vec{B_0}\,|\uparrow\rangle = \langle\uparrow|\,\vec{\mu}.\vec{B_0}\,|\downarrow\rangle$, we can write

$$H_I = \frac{\hbar\Omega_0}{2}\left(|\uparrow\rangle\langle\downarrow| + |\downarrow\rangle\langle\uparrow|\right)\left(e^{i(\omega t - \phi)} + e^{-i(\omega t - \phi)}\right) \tag{2.23}$$

where we have defined the Rabi frequency $\Omega_0 = \langle\downarrow| \vec{\mu}.\vec{B_0} |\uparrow\rangle / \hbar$. We can then transform to the interaction picture with respect to the Hamiltonian describing the internal energy states H_0 using the relation $H_I' = e^{iH_0 t/\hbar} H_I e^{-iH_0 t/\hbar}$, which gives the interaction Hamiltonian

$$H_I' = \frac{\hbar\Omega_0}{2} \left(|\uparrow\rangle \langle\downarrow| e^{i\omega_0 t} + |\downarrow\rangle \langle\uparrow| e^{-\omega_0 t} \right) \left(e^{i(\omega t - \phi)} + e^{-i(\omega t - \phi)} \right). \tag{2.24}$$

This Hamiltonian contains terms rotating at $\omega_0 + \omega$ and $\delta = \omega - \omega_0$. Since $\omega_0 + \omega \gg \delta$, we can disregard these fast terms, making the rotating wave approximation, which gives the Hamiltonian

$$H_I' = \frac{\hbar\Omega_0}{2} \left(|\uparrow\rangle \langle\downarrow| e^{-i(\delta t - \phi)} + |\downarrow\rangle \langle\uparrow| e^{i(\delta t - \phi)} \right). \tag{2.25}$$

This Hamiltonian describes population transfer between the $|\downarrow\rangle$ and $|\uparrow\rangle$ states. In order to understand the behaviour of ion population over time, the equivalent unitary operator can be found by substituting this Hamiltonian into the time-dependent Schrödinger equation, $i\hbar\frac{\partial}{\partial t} |\psi\rangle = H_I' |\psi\rangle$. This results in two coupled first order differential equations. These can be solved with the appropriate boundary conditions for each state, giving a unitary matrix of the form

$$U(\delta, \Omega_0, \phi, t) = \begin{pmatrix} e^{i\delta t}[\cos(\Omega_\delta t/2) - \frac{i\delta}{\Omega_\delta} \sin(\Omega_\delta t/2)] & -\frac{i\Omega_0}{\Omega_\delta} e^{i\delta t/2} e^{-i\phi} \sin(\Omega_\delta t/2) \\ -\frac{i\Omega_0}{\Omega_\delta} e^{-i\delta t/2} e^{i\phi} \sin(\Omega_\delta t/2) & e^{-i\delta t}[\cos(\Omega_\delta t/2) + \frac{i\delta}{\Omega_\delta} \sin(\Omega_\delta t/2)] \end{pmatrix} \tag{2.26}$$

where $\Omega_\delta = \sqrt{\Omega_0^2 + \delta^2}$. If the applied radiation is set to resonance with the transition, so that $\delta = 0$, this simplifies to

$$U(\Omega_0, \phi, t) = \begin{pmatrix} \cos(\Omega_0 t/2) & -ie^{-i\phi} \sin(\Omega_0 t/2) \\ -ie^{i\phi} \sin(\Omega_0 t/2) & \cos(\Omega_0 t/2) \end{pmatrix}. \tag{2.27}$$

It can be seen that by correctly setting the parameters, different single qubit rotations in the x and y bases can be performed. For example,

$$U\left(\Omega_0, 0, \frac{\pi}{\Omega_0}\right) = \begin{pmatrix} 0 & -i \\ -i & 0 \end{pmatrix} = -i\sigma_x \tag{2.28}$$

and

$$U\left(\Omega_0, \frac{\pi}{2}, \frac{\pi}{\Omega_0}\right) = \begin{pmatrix} 0 & -1 \\ 1 & 0 \end{pmatrix} = -i\sigma_y \tag{2.29}$$

where σ_x and σ_y are the Pauli matrices.

Using this unitary, the probability for an ion interacting with applied radiation to be

in state $|\uparrow\rangle$ after it has been initialised in $|\downarrow\rangle$ can be calculated. For an arbitrary Rabi frequency Ω_0, time t and detuning δ, this is

$$P_{\uparrow}(\Omega_0, t, \delta) = \frac{\Omega_0^2}{\Omega_0^2 + \delta^2} \sin^2\left(\frac{\sqrt{\Omega_0^2 + \delta^2}\mathrm{t}}{2}\right). \tag{2.30}$$

There are two simplifications of this probability function which correspond to commonly performed experiments. The first is for the case of applying a pulse of fixed time $t = \pi/\Omega_0$ with a varying detuning δ. The probability function then becomes

$$P_{\uparrow}(\delta, \Omega_0) = \frac{\pi^2}{4} \mathrm{sinc}^2\left(\frac{\sqrt{\Omega_0^2 + \delta^2}\pi}{2\Omega_0}\right). \tag{2.31}$$

The width of the peak depends on the Rabi frequency of the applied radiation, as illustrated in figure 2.6. This type of varying detuning experiment can be performed in order to accurately obtain the frequency of a transition. The other simplification of interest is that for a varying time t and fixed detuning $\delta = 0$. This gives

$$P_{\uparrow}(t, \Omega_0) = \sin^2\left(\frac{\Omega_0 t}{2}\right). \tag{2.32}$$

In this case, oscillations between the two states are seen at frequency Ω_0. This type of experiment is used to find the exact Rabi frequency of applied radiation. When resonant radiation is applied for a time $t = \pi/\Omega_0$, full population transfer to the state $|\uparrow\rangle$ is achieved, and this is called a π pulse. When resonant radiation is applied for half this time, so $t = \pi/2\Omega_0$, a superposition of the two states of the form $(|\downarrow\rangle + e^{i\phi}|\uparrow\rangle)/\sqrt{2}$ is created, where ϕ depends on the phase of the radiation. This is known as a $\pi/2$ pulse.

2.4.2 Multi-qubit operations

In order to perform multi-qubit operations, a method for changing the internal state of one ion dependent on the internal state of another is required. This is achieved through the shared motional mode of the ion string, described in section 2.2.2, which is referred to as the 'bus' mode. To use this shared mode for communication between ions, it is necessary for there to be a coupling between the internal and motional states of each ion. This coupling can be produced using lasers, as outlined in the first part of this section, where the momentum of the optical photon is large enough to alter the motional state while causing a transition between internal states. However, when using long-wavelength radiation, the photon momentum is much smaller, making the coupling strength using this

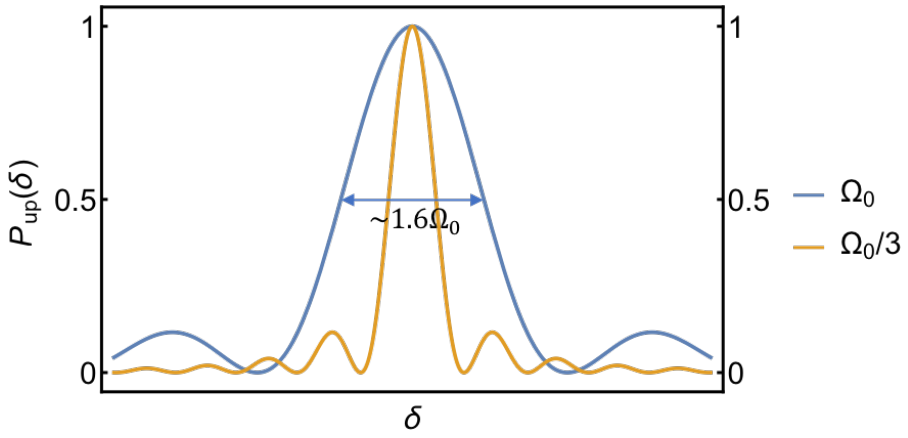

Figure 2.6: Probability of ion being in state $|\uparrow\rangle$ after initialising in $|\downarrow\rangle$ and applying a pulse of radiation at detuning δ for time $t = \pi/\Omega$, shown for two different Rabi frequencies, $\Omega = \Omega_0$ and $\Omega = \Omega_0/3$. The width of the sinc^2 peak is defined by the Rabi frequency, so lower Rabi frequencies can be used to more accurately characterise a transition frequency.

method vanishingly small. A method has been developed to overcome this problem by combining long-wavelength radiation with a static or an oscillating magnetic field gradient [23, 29], which allows for an analogous coupling between spin and motional states. The static magnetic field gradient scheme is used in this thesis, and this method is outlined in the second part of this section.

Coupling spin and motion using lasers

In the previous section, the magnetic dipole approximation was made to ignore the effect of the photon momentum of long-wavelength radiation. Here, we consider the second term in the expansion of $e^{i\vec{k}.\vec{r}}$ which, for optical radiation, is essential for describing the coupling between spin and motion necessary for multi-qubit operations. The following derivation uses the labelling of states $|\downarrow\rangle \equiv |0'\rangle$ and $|\uparrow\rangle \equiv |+1\rangle$, but it can be generalised to other pairs of states.

The Hamiltonian describing an ion with internal energy states defined, as before, as $|\uparrow\rangle$ and $|\downarrow\rangle$, confined in a harmonic potential with secular frequency ν_z can be written as the sum of two terms

$$H_0 = H_B + H_m. \tag{2.33}$$

H_B describes the internal energy levels of an ion in a constant magnetic field. Ignoring second order Zeeman effects, this energy splitting can be written as

$$H_B = \frac{\hbar\omega_0}{2}\left(|\uparrow\rangle\langle\uparrow| - |\downarrow\rangle\langle\downarrow|\right) + \mu_B B\,|\uparrow\rangle\langle\uparrow| \tag{2.34}$$

where B is the magnetic field strength, $\mu_B = e\hbar/2m_e$ is the Bohr magneton, and the frequency splitting can be written as $\omega_B = \omega_0 + \mu_B B/\hbar$. H_m describes the motional state of the ion, and is written as

$$H_m = \hbar\nu_z a^\dagger a \tag{2.35}$$

where $a^\dagger$ and a are the raising and lowering operators for the axial motional mode of trap frequency ν_z. Without the magnetic dipole approximation, which was made in the previous section to describe interactions with radiation close to the frequency of the hyperfine qubit, the full Hamiltonian to describe the interaction with radiation is given by

$$H_I = \frac{\hbar\Omega_0}{2}\left(|\uparrow\rangle\langle\downarrow| + |\downarrow\rangle\langle\uparrow|\right)\left(e^{i(\omega t - kz - \phi)} + e^{-i(\omega t - kz - \phi)}\right). \tag{2.36}$$

This describes the interaction with a wave propagating along the trap axis, in the z-direction, so that $\vec{k}.\vec{r} = kz$, where $k = |\vec{k}|$. The ion position can be expanded in terms of the ladder operators, $z = z_0(a + a^\dagger)$, where z_0 is the position spread of the ground state wavefunction of the ion, given by $z_0 = \sqrt{\hbar/2m\nu_z}$, where m is the mass of the ion. The Lamb-Dicke parameter is the ratio of the spread of the ion's ground state wavefunction to the wavelength of the incoming radiation, defined as

$$\eta = kz_0 = k\sqrt{\frac{\hbar}{2m\nu_z}}. \tag{2.37}$$

This allows us to write $kz = \eta(a + a^\dagger)$. Moving to the interaction picture with respect to H_0 gives an interaction Hamiltonian

$$H_I' = \frac{\hbar\Omega_0}{2}\left(|\uparrow\rangle\langle\downarrow| e^{i(\omega_B - \omega)t} e^{i\phi} e^{i\eta(ae^{-i\nu_z t} + a^\dagger e^{i\nu_z t})} + H.c.\right). \tag{2.38}$$

As the ion is cooled, the Lamb-Dicke regime is reached where the following criterion applies

$$\eta^2(2n+1) \ll 1. \tag{2.39}$$

Within this regime, sidebands that result from terms higher than the first order in the expansion of equation 2.38 around $e^{i\eta(ae^{-i\nu_z t} + a^\dagger e^{i\nu_z t})}$ can be ignored. The zeroth order is given by

$$H_c = \frac{\hbar\Omega_0}{2}\left(|\uparrow\rangle\langle\downarrow| e^{-i(\delta_c t - \phi)} + |\downarrow\rangle\langle\uparrow| e^{i(\delta_c t - \phi)}\right) \tag{2.40}$$

where δ_c is the detuning from the carrier transition. This Hamiltonian is identical to equation 2.25, and describes population transfer between states $|\downarrow\rangle$ and $|\uparrow\rangle$ with no effect

on the motional states $|n\rangle$. In order to resolve individual sidebands, $\Omega_0 \ll \nu_z$ must be satisfied. In that case, the two first order terms can be written independently as

$$H_r = \frac{i\hbar\eta\Omega_0}{2}\left(e^{-i\delta_r t}e^{i\phi}a\,|\uparrow\rangle\langle\downarrow| + e^{i\delta_r t}e^{-i\phi}a^\dagger\,|\downarrow\rangle\langle\uparrow|\right) \tag{2.41}$$

and

$$H_b = \frac{i\hbar\eta\Omega_0}{2}\left(e^{-i\delta_b t}e^{i\phi}a^\dagger\,|\uparrow\rangle\langle\downarrow| + e^{i\delta_b t}e^{-i\phi}a\,|\downarrow\rangle\langle\uparrow|\right). \tag{2.42}$$

These are known as the red and blue sideband transitions respectively. The detunings are defined as $\delta_r = \omega - (\omega_B - \nu_z)$ and $\delta_b = \omega - (\omega_B + \nu_z)$. The red sideband acts to remove a phonon while exciting the internal state of the ion, whereas for the blue sideband a phonon is added when the internal state of the ion is excited. The magnitude of the Rabi frequencies of the coupling to the red and blue motional sidebands is dependent on η, with

$$\Omega_r = \sqrt{n}\eta\Omega_0 \tag{2.43}$$

and

$$\Omega_b = \sqrt{n+1}\eta\Omega_0 \tag{2.44}$$

respectively. It is therefore important to have a sufficiently large value of η for a strong sideband coupling rate. For a transition frequency of 12.6 GHz and an axial trap frequency of $\nu_z/2\pi = 460\,\text{kHz}$ (approximately the secular frequency used for experimental demonstration of two qubit operations in chapter 6), the Lamb-Dicke parameter is only 2.1×10^{-6}. Optical radiation can instead be used, which gives a significantly larger Lamb-Dicke parameter on the order of 0.1 due to the shorter wavelength, by use of a two photon Raman process. However, an alternative method for coupling which does not depend on the wavelength of the driving radiation is presented in the next section.

Coupling spin and motion using a magnetic field gradient

In order to achieve a sufficient level of coupling between the ions' internal and motional states for multi-qubit operations, a static magnetic field gradient can be used in conjunction with long-wavelength radiation [23]. This will be shown in the following derivation, which again follows Randall [53]. The magnetic field at the ion's position can then be written as

$$B(z) = B_0 + \frac{\partial B}{\partial z}z = B_0 + \frac{\partial B}{\partial z}z_0(a + a^\dagger), \tag{2.45}$$

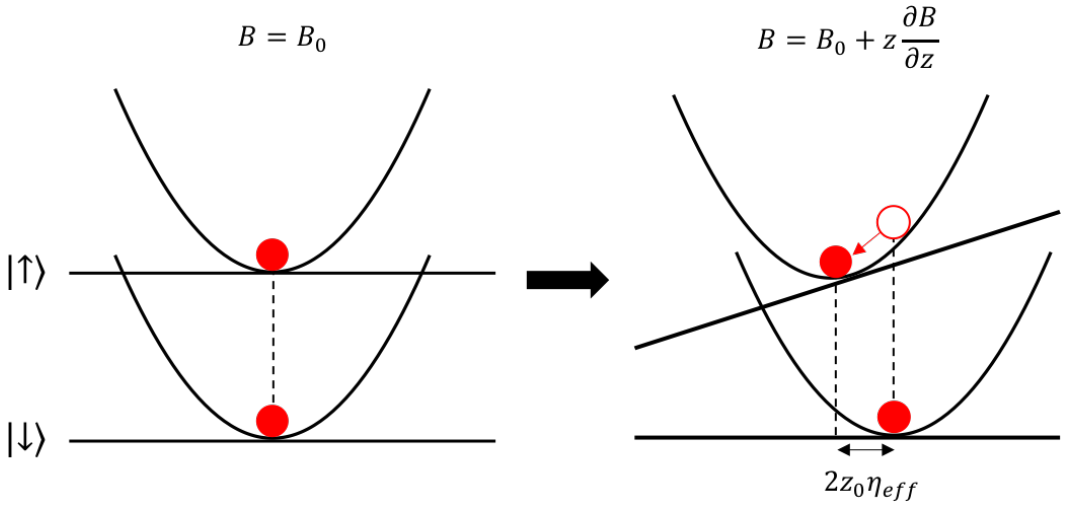

Figure 2.7: Schematic of coupling between spin and motion using a magnetic field gradient. The effect of the addition of a gradient is to cause a displacement in the harmonic oscillator describing the motional states of $|\uparrow\rangle$. This corresponds to a displacement of $2z_0\eta_{\text{eff}}$ in ion equilibrium position, along with a constant energy offset of $-\hbar\nu_z\eta_{\text{eff}}^2$.

where we have expressed the ion position in terms of the ground state position and the ladder operators, $z = z_0(a + a^\dagger)$. The Hamiltonian describing the state of the ion is again given by $H = H_B + H_m$, where H_B describes the internal energy states and H_m describes the motional states. The first term is the same as in the previous section and is

$$H_B = \frac{\hbar\omega_0}{2}(|\uparrow\rangle\langle\uparrow| - |\downarrow\rangle\langle\downarrow|) + \mu_B B\,|\uparrow\rangle\langle\uparrow|\,. \tag{2.46}$$

The motional Hamiltonian, however, now incorporates a term that is dependent on the magnetic field gradient, and is given by

$$H_m = \mu_B \frac{\partial B}{\partial z} z_0(a + a^\dagger)\,|\uparrow\rangle\langle\uparrow| + \hbar\nu_z a^\dagger a. \tag{2.47}$$

The second term in this Hamiltonian describes a normal harmonic oscillator, but the first term of H_m shows an intrinsic coupling between the internal and motional states of the ion. We can rewrite this motional Hamiltonian as the sum of the matrix elements for the two spin states

$$H_m = H_m^\downarrow\,|\downarrow\rangle\langle\downarrow| + H_m^\uparrow\,|\uparrow\rangle\langle\uparrow|\,. \tag{2.48}$$

The motional Hamiltonian acting on the state $|\downarrow\rangle$ reduces to that for a harmonic oscillator with eigenstates $|n\rangle$, and is given by

$$H_m^{\downarrow} = \langle\downarrow| H_m |\downarrow\rangle = \hbar\nu_z a^\dagger a. \tag{2.49}$$

It therefore remains unaffected by the gradient. However, for the state $|\uparrow\rangle$, the extra term dependent on the gradient remains, and the Hamiltonian is

$$H_m^{\uparrow} = \langle\uparrow| H_m |\uparrow\rangle = \mu_B \frac{\partial B}{\partial z} z_0 (a + a^\dagger) + \hbar\nu_z a^\dagger a. \tag{2.50}$$

In order to simplify this expression, we can define a new parameter

$$\eta_{\text{eff}} = \frac{\mu_B}{\hbar\nu_z} \frac{\partial B}{\partial z} z_0, \tag{2.51}$$

as well as new ladder operators,

$$\begin{aligned} b &= a + \eta_{\text{eff}} \\ b^\dagger &= a^\dagger + \eta_{\text{eff}}. \end{aligned} \tag{2.52}$$

The Hamiltonian can then be re-expressed as

$$H_m^{\uparrow} = \hbar\nu_z b^\dagger b - \hbar\nu_z \eta_{\text{eff}}^2. \tag{2.53}$$

This is another harmonic oscillator Hamiltonian but with a constant energy offset of $-\hbar\nu_z\eta_{\text{eff}}^2$. There is a new position basis for the states of this shifted harmonic oscillator, where

$$z' = z_0(b^\dagger + b) = z + 2z_0\eta_{\text{eff}}. \tag{2.54}$$

The state $|\uparrow\rangle$ therefore experiences a harmonic oscillator with a shift in position basis and a corresponding constant energy offset. A schematic of this effect is shown in figure 2.7. The eigenstates of this displaced harmonic oscillator system are the Fock states $|n'\rangle$, which can be written in terms of the original harmonic oscillator states as displaced Fock states, $|n'\rangle = D(-\eta_{\text{eff}})\,|n\rangle$. The overall effect of the field gradient is therefore to state-dependently cause a displacement of the harmonic oscillator.

In order to understand the effect of radiation on the ion, it is useful to define a basis where the states share harmonic oscillator states. This is possible using 'polaron' states,

where the internal energy states incorporate the displacement. These are

$$\begin{aligned} |\downarrow_p\rangle |n_p\rangle &= |\downarrow\rangle |n\rangle \\ |\uparrow_p\rangle |n_p\rangle &= e^{-\eta_{\text{eff}}(a^\dagger - a)} |\uparrow\rangle |n\rangle . \end{aligned} \tag{2.55}$$

These states cannot be expressed separably in the original basis. The corresponding ladder operators are

$$a_p^{(\dagger)} = a^{(\dagger)} |\downarrow\rangle \langle\downarrow| + b^{(\dagger)} |\uparrow\rangle \langle\uparrow| = a^{(\dagger)} + \eta_{\text{eff}} |\uparrow\rangle \langle\uparrow| . \tag{2.56}$$

For long-wavelength radiation applied near the resonant frequency of the hyperfine transition, the magnetic dipole approximation can again be made to ignore the effect of the term e^{ikz}. The Hamiltonian for the interaction with applied radiation is then

$$H_{LW} = \frac{\hbar\Omega_0}{2} \left(|\uparrow\rangle \langle\downarrow| e^{i(\omega t - \phi)} + |\uparrow\rangle \langle\downarrow| e^{-i(\omega t - \phi)} \right) \tag{2.57}$$

which can be written in the polaron state basis as

$$H_{LW} = \frac{\hbar\Omega_0}{2} \left(e^{\eta_{\text{eff}}(a_p^\dagger - a_p)} |\uparrow_p\rangle \langle\downarrow_p| + e^{-\eta_{\text{eff}}(a_p^\dagger - a_p)} |\downarrow_p\rangle \langle\uparrow_p| \right) \left(e^{i(\omega t - \phi)} + e^{-i(\omega t - \phi)} \right) . \tag{2.58}$$

As before, we will go into the interaction picture with respect to the Hamiltonian describing the internal energy states H_0 and use the rotating wave approximation to ignore fast rotating terms, giving

$$H'_{LW} = \frac{\hbar\Omega_0}{2} \left(e^{i(\omega_B - \omega)t} e^{i\phi} e^{\eta_{\text{eff}}(a_p^\dagger e^{i\nu_z t} - a_p e^{-i\nu_z t})} |\uparrow_p\rangle \langle\downarrow_p| + H.c. \right) \tag{2.59}$$

where $\omega_B = \omega_0 + \mu_B B_0/\hbar - \nu_z \eta_{\text{eff}}^2$ is the qubit transition frequency. This Hamiltonian takes exactly the same form as equation 2.38, which describes the coupling between internal and motional states using laser radiation, with η_{eff} replacing η. We can therefore consider η_{eff} as the effective Lamb-Dicke parameter, determining the strength of the coupling between the internal and the motional states. However, in this case the parameter is not dependent on the wavelength of the radiation, but is instead given by

$$\eta_{\text{eff}} = \frac{\mu_B}{\sqrt{2\hbar m \nu_z^3}} \frac{\partial B}{\partial z}. \tag{2.60}$$

The effective Lamb-Dicke parameter, and therefore the strength of the coupling, can therefore be increased by using a larger magnetic field gradient, and by operating at lower secular frequencies.

In the same way as in section 2.4.2, the Lamb-Dicke regime is defined as where $\eta_{\text{eff}}^2 n_p \ll 1$. We can then expand this Hamiltonian to first order to give carrier and sideband terms:

$$\begin{aligned} H_c &= \frac{\hbar\Omega_0}{2}\left(e^{-i\delta_c t}e^{i\phi}\left|\uparrow_p\right\rangle\left\langle\downarrow_p\right| + e^{i\delta_c t}e^{-i\phi}\left|\downarrow_p\right\rangle\left\langle\uparrow_p\right|\right) \\ H_r &= -\frac{\hbar\eta_{\text{eff}}\Omega_0}{2}\left(e^{-i\delta_r t}e^{i\phi}a_p\left|\uparrow_p\right\rangle\left\langle\downarrow_p\right| + e^{i\delta_r t}e^{-i\phi}a_p^\dagger\left|\downarrow_p\right\rangle\left\langle\uparrow_p\right|\right) \\ H_b &= \frac{\hbar\eta_{\text{eff}}\Omega_0}{2}\left(e^{-i\delta_b t}e^{i\phi}a_p^\dagger\left|\uparrow_p\right\rangle\left\langle\downarrow_p\right| + e^{i\delta_r t}e^{-i\phi}a_p\left|\downarrow_p\right\rangle\left\langle\uparrow_p\right|\right). \end{aligned} \tag{2.61}$$

Similarly, the red and blue sideband transitions allow for a change in internal energy state coupled to a change in motional state. There is a phase difference from equations 2.41 and 2.42, where the spin motion coupling is achieved through photon momentum using optical fields, but this can be compensated for if necessary by changing the phase of the driving fields. For a gradient of 24.5 T/m (as used experimentally in this work) and a secular frequency of 460 kHz, the effective Lamb-Dicke parameter is approximately 0.006 - much larger than that achieved through photon momentum coupling. This is sufficiently large to perform multi-qubit operations, and forms the basis of the multi-qubit work presented in this thesis. From here on, the effective Lamb-Dicke parameter described in equation 2.60 will be relabelled as $\eta_{\text{eff}} \Rightarrow \eta$.

This theory of spin-motion coupling with a magnetic field gradient can be generalised to multiple ions in a trap. In this case, there are multiple normal modes as described in section 2.2.2, and the sidebands can be addressed individually providing $\Omega_0 \ll |\nu_k - \nu_{k\pm1}|$, where ν_k is the frequency of each mode. Furthermore, the effective Lamb-Dicke parameter for ion j and mode k becomes

$$\eta_{jk} = \frac{S_{jk}\mu_B}{\hbar\nu_k}\frac{\partial B}{\partial z}z_{0k} \tag{2.62}$$

where S_{jk} is the normal mode coefficient. For two ions, there are two normal modes: the COM mode at ν_z and the stretch mode at $\sqrt{3}\nu_z$. The normal mode coefficient for the COM mode is $S_{11}^z = S_{12}^z = 1/\sqrt{2}$, and for the stretch it is $S_{21}^z = -S_{22}^z = -1/\sqrt{2}$.

There is also an extra term which comes from expanding the motional Hamiltonian for multiple ions. As well as individual energy shifts on each ion, there are terms which express collective pairwise energy shifts. This Hamiltonian for ions i and j is

$$H_{ss} = -\sum_{i\neq j}^{N}\hbar J_{ij}(\left|\uparrow_i\right\rangle\left\langle\uparrow_i\right| \times \left|\uparrow_j\right\rangle\left\langle\uparrow_j\right|) \tag{2.63}$$

where

$$J_{ij} = \sum_{k=1}^{N}\nu_k\eta_{ik}\eta_{jk}. \tag{2.64}$$

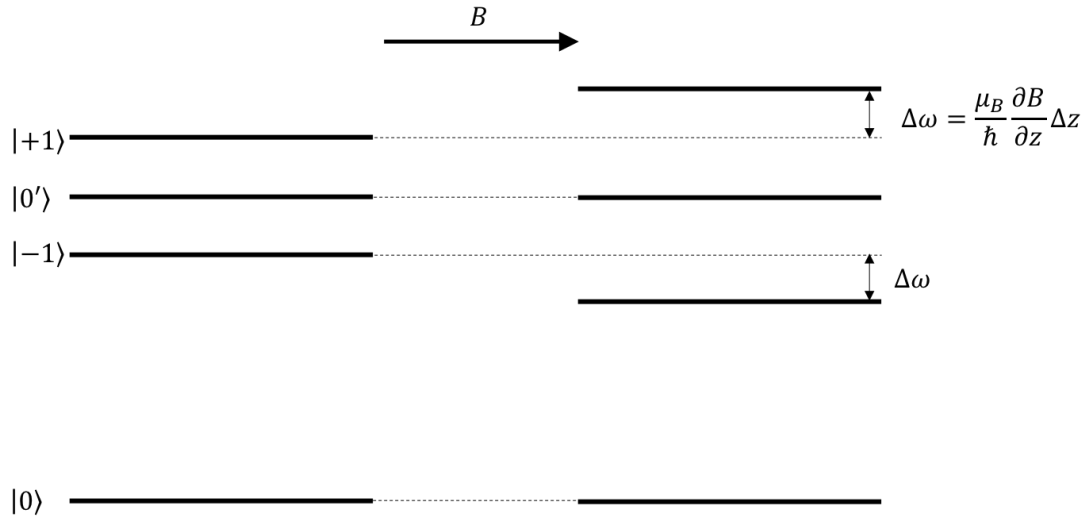

Figure 2.8: Schematic of the frequency splitting of the hyperfine states of two ions in a magnetic field gradient, ignoring second order Zeeman effects, where Δz is the spacing between the ions.

There is therefore an implicit spin-spin coupling between ions, which can be used for conditional logic operations, which has been demonstrated experimentally [25]. However, for the gradient used in this work, the strength of the coupling is low and therefore the gate time is longer than the decoherence time of the qubit. This limits the gate fidelity, so this particular gate scheme is not suitable for two qubit logic operations in our system. This type of coupling does not affect the gate we implement, demonstrated in chapter 6.

2.4.3 Individual addressing

When using lasers for coherent operations it is necessary to individually address ions spatially. This places strict requirements on the lasers beam, such as on the beam waist and the beam pointing stability. Microwaves cannot individually address ions spatially due to the longer wavelength. However, when placed in a magnetic field gradient, the frequency splitting of the ion transitions becomes position-dependent. Ignoring the second order Zeeman shift, the frequency of the transition $|0\rangle \leftrightarrow |+1\rangle$ for ion i at position z_i is

$$\omega_i = \omega_0 + \frac{\mu_B}{\hbar}\left(B_0 + z_i \frac{\partial B}{\partial z}\right) \tag{2.65}$$

which gives a frequency difference of

$$\Delta\omega = \frac{\mu_B}{\hbar}\frac{\partial B}{\partial z}\Delta z \tag{2.66}$$

where Δz is the splitting between the ions, given for two ions by equation 2.10. This is shown in figure 2.8. It is therefore possible to individually address all ions with long-wavelength radiation, since ions are individually addressed in frequency space. The cross talk defines how well ions can be individually addressed, and is given by the amount of population transferred in a neighbouring ion after a pulse of duration t on a given ion. This can be calculated from equation 2.31, and taking the time average of this gives

$$C_{ij} = \frac{\Omega_0^2}{2(\Omega_0^2 + \Delta\omega^2)} \approx \frac{\Omega_0^2}{2\Delta\omega^2}. \tag{2.67}$$

There is therefore a trade-off between the Rabi frequency and the level of of cross talk. A higher Rabi frequency is generally desirable to perform faster quantum operations and lessen the effects of decoherence, but this may result in higher levels of cross talk. This can be reduced by the use of pulse shaping, or by increasing the magnetic field gradient in order to create a larger frequency splitting between ions.

The second order Zeeman shift has been ignored in this analysis, since the frequencies of the $|0\rangle \leftrightarrow |\pm 1\rangle$ transitions are dominated by the first order term. However, this second order is significant for the transition $|0\rangle \leftrightarrow |0'\rangle$ (known as the clock transition), as it allows for individual addressing of this transition also. In a typical field of 10 G, the frequency splitting between clock transitions for two ions is typically on the order of 10 kHz. Again, there is a trade-off between the Rabi frequency of the transition and the cross talk, with a higher limitation placed on this transition due to the smaller frequency splitting. However, the frequency splitting is sufficient to allow for accurate individual addressing of ions.

Chapter 3

Experimental setup and initial experiments

In this chapter, the experimental setup used for the work in this thesis is described. The core of the experiment consists of a macroscopic ion trap in an ultra-high vacuum system, with access for the necessary lasers, microwaves and RF radiation. This experimental setup builds on the work of multiple PhD students, and various aspects have been described in detail elsewhere, as referenced. More in depth discussion is provided where adaptations or improvements have been made. Various initial experiments are then presented which form the basis of work throughout this thesis, demonstrating much of the theory described in chapter 2.

3.1 Ion trap

3.1.1 Macroscopic ion trap

This work uses a macroscopic linear blade Paul trap, a variation of the theory described in 2.2.1, and a schematic of this trap is shown in figure 3.1. Further information on the design of this trap can be found in [54]. The trap consists of four blades made of stainless steel with a 50 μm gold coating. RF voltage is applied to two of the four blades, and provides radial confinement in the $x-y$ plane. Static DC voltages are applied to the other two blades. Each of these DC blades is segmented into three electrodes, and the two outer electrodes on each blade act as endcaps to provide confinement along the z-axis. There are also three cylindrical compensation rods, two of which are electrically connected, and along with the centre electrodes on the DC blades these allow for movement of the ion in the $x-y$ plane. This is necessary to ensure that the ions sit along the RF nil line, which ensures there is no

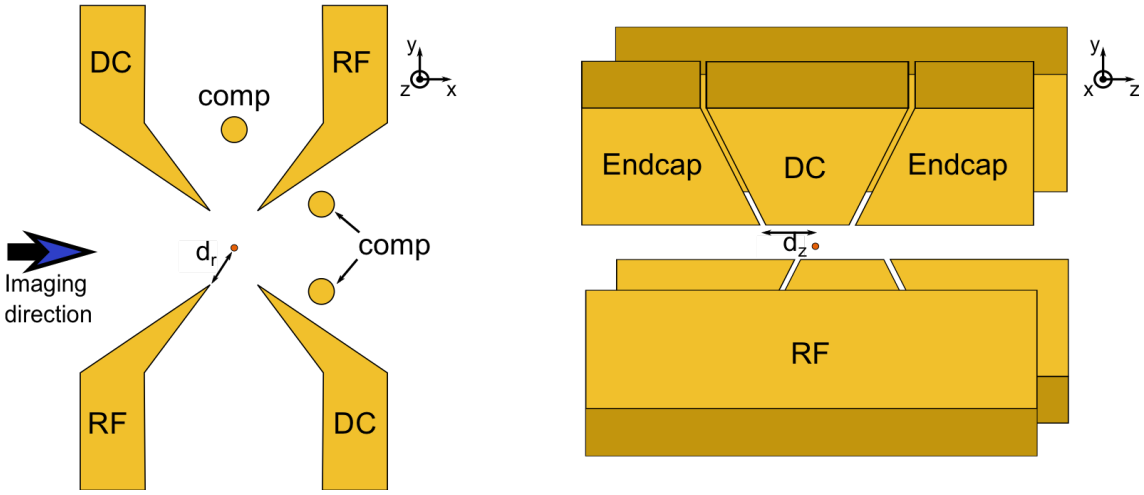

Figure 3.1: A schematic of the macroscopic linear Paul trap used in this work. The trap consists of four blade electrodes and three compensation rods (omitted in the right diagram for clarity). RF voltage is applied to two of the blades. DC voltages are applied to the other two blades, which are each segmented into three electrodes, as well as to the compensation rods. The ion-electrode distances are $d_r = 310(10)\,\mu$m and $d_z \approx 500\,\mu$m. Figure adapted with permission from [53].

excess micromotion present which can cause problems for high fidelity operations. One of the endcaps is unintentionally electrically connected to a compensation rod, but this is not problematic given the number of electrodes available. The distance to the endcaps in the z direction is $d_z \approx 500\,\mu$m, and the nearest ion-electrode distance is $d_r = 310(10)\,\mu$m. The relatively large dimensions of the trap have two consequences: low heating rates compared with surface traps, and small amounts of scattering of 369 nm Doppler cooling laser. This low scattering rate helps with ion readout, and reduces the possibility of the photoelectric effect producing patch charges on electrodes, which can produce increased micromotion. Using typical electrode voltages, the change in ion position with voltage was simulated to be 17.8 nm/mV for the electrode that had the largest effect on the ion position. An atomic oven enriched with $> 95\%$ ^{171}Yb is used to produce a thermal beam of neutral Yb atoms for trapping, requiring a current of 6.2 A.

3.1.2 DC and RF voltages

DC voltages are applied to the trap using a highly stable low noise voltage supply which is controlled by a PC control programme via USB (Stahl BS series, HV40-16, 16 channel). The maximum output voltage of each channel is 40 V. The DC voltages then pass through a low-pass filter designed by Dr David Murgia [40], a schematic of which is shown in figure 3.2. This filter has a cut-off frequency of 30.5 Hz, below mains frequency, and uses SMA input connections. A box was designed to sit directly on the vacuum system, with the

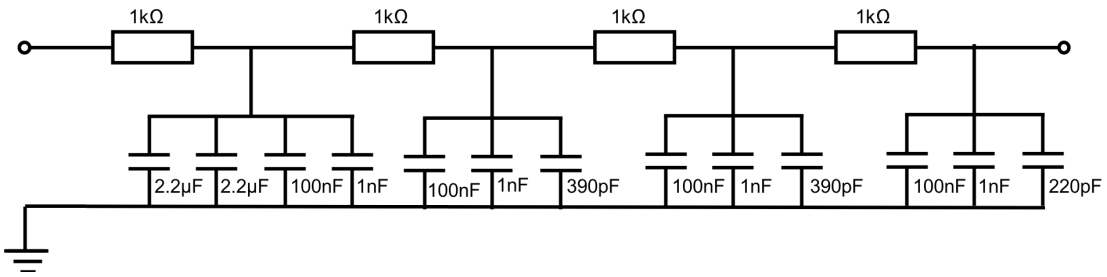

Figure 3.2: Schematic of the filter for the DC voltages which are applied to the trap electrodes. This a low pass filter with a cut-off frequency of 30.5 Hz.

filter output connected to the DC feedthroughs to the vacuum system via a routing PCB.

The trapping RF is supplied by a signal generator (HP8640) and amplified by 47 dB (NP Technologies NP-541). A helical resonator then impedance matches this signal to the ion trap and provides further amplification of the voltage. This high Q factor resonator allows higher voltages to be applied and also filters out noise at unwanted frequencies. When attached to the ion trap, the resonator was measured to have a Q factor of $Q = 200(20)$ at a resonant frequency of 19.212 MHz. This allows the applied RF voltage to be found using the equation $V_{\text{ac}} = \kappa\sqrt{2PQ}$ where P is the RF power applied to the ion trap, $\kappa = (L/C)^{1/4}$, and L and C are the inductance and capacitance of the ion trap resonator system respectively. This has been measured experimentally as $\kappa = 13(1)$ [55]. For the work presented in this thesis, 1.6 W of RF power is typically applied, giving an RF voltage of $V_{\text{ac}} \approx 330\,\text{V}$.

3.1.3 Magnetic field gradient

When using long-wavelength radiation, a magnetic field gradient is required in order to generate the spin-motion coupling needed for two qubit gates, as explained in section 2.4.2. While a large magnetic field gradient is required, it is also important that the absolute magnetic field is low, as high magnetic fields can have undesired effects such as reducing detection fidelity, and increased second order zeeman shifts which lead to higher sensitivity of the $|0\rangle \leftrightarrow |0'\rangle$ transition to magnetic field fluctuations. This is achieved through the use of permanent samarium cobalt (SmCo) rare earth magnets retrofitted to the ion trap, as shown in figure 3.3. The north poles of each pair of magnets face each other to achieve a high gradient that is well approximated as linear at the ion position, and a low absolute magnetic field. Magnets are partially coated with three layers (nickel, copper, and nickel) in order to reduce outgassing during the baking procedure, but this has been found to lower the gradient produced. Further information of the magnet design can be found in

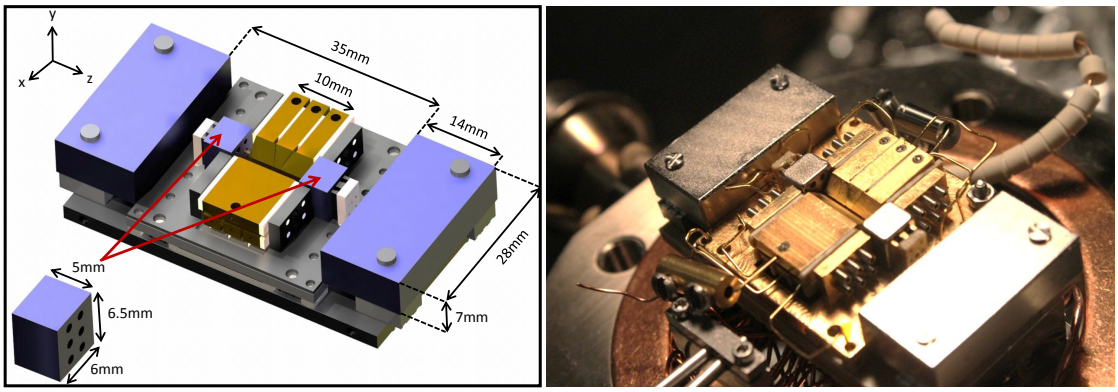

Figure 3.3: Diagram (left) of the trap with magnets (shown in purple) positioned either side to produce a magnetic field gradient. Two magnets of different size are positioned either side of the trap, to ensure that the required magnetic field gradient along the z-axis as well as a low magnetic field offset is produced. A photo of the magnets fitted onto the trap is shown on the right. Figure reproduced with permission from [53].

[56]. These magnets produce a gradient of $\partial B/\partial z = 24.5(1)\,\mathrm{T/m}$.

Although the absolute magnetic field should theoretically be low at the ion position, magnets are only coarsely aligned so an undesired offset field occurs. Additional permanent magnets are positioned outside the vacuum system to reduce this. Three pairs of Helmholtz coils are also used outside the vacuum system, one aligned along each spatial axis. Each coil has 185 turns of 1.08 mm copper wire. A current within the range 1-2 A is required to achieve an offset field of approximately 10 G.

3.1.4 Vacuum system

The ion trap is housed in an ultra-high vacuum environment, at around 10^{-11} Torr. Further details of the vacuum system can be found in [57]. Feedthroughs allow for 50 DC and 1 RF connection to the ion trap and 6 DC connections to atomic ovens. Ultra high vacuum is maintained using an ion pump (Varian StarCell 9191145) and measured using an ion gauge (Varian 9715015). The vacuum system is placed inside a Faraday cage which is not in use due to adverse temperature effects when it is fully closed.

3.2 Optical setup

3.2.1 Lasers

Although microwave and RF radiation is used for coherent manipulation of the ion, three lasers are required for Doppler cooling (369 nm, 935 nm, 638 nm) and one for photoionisa-

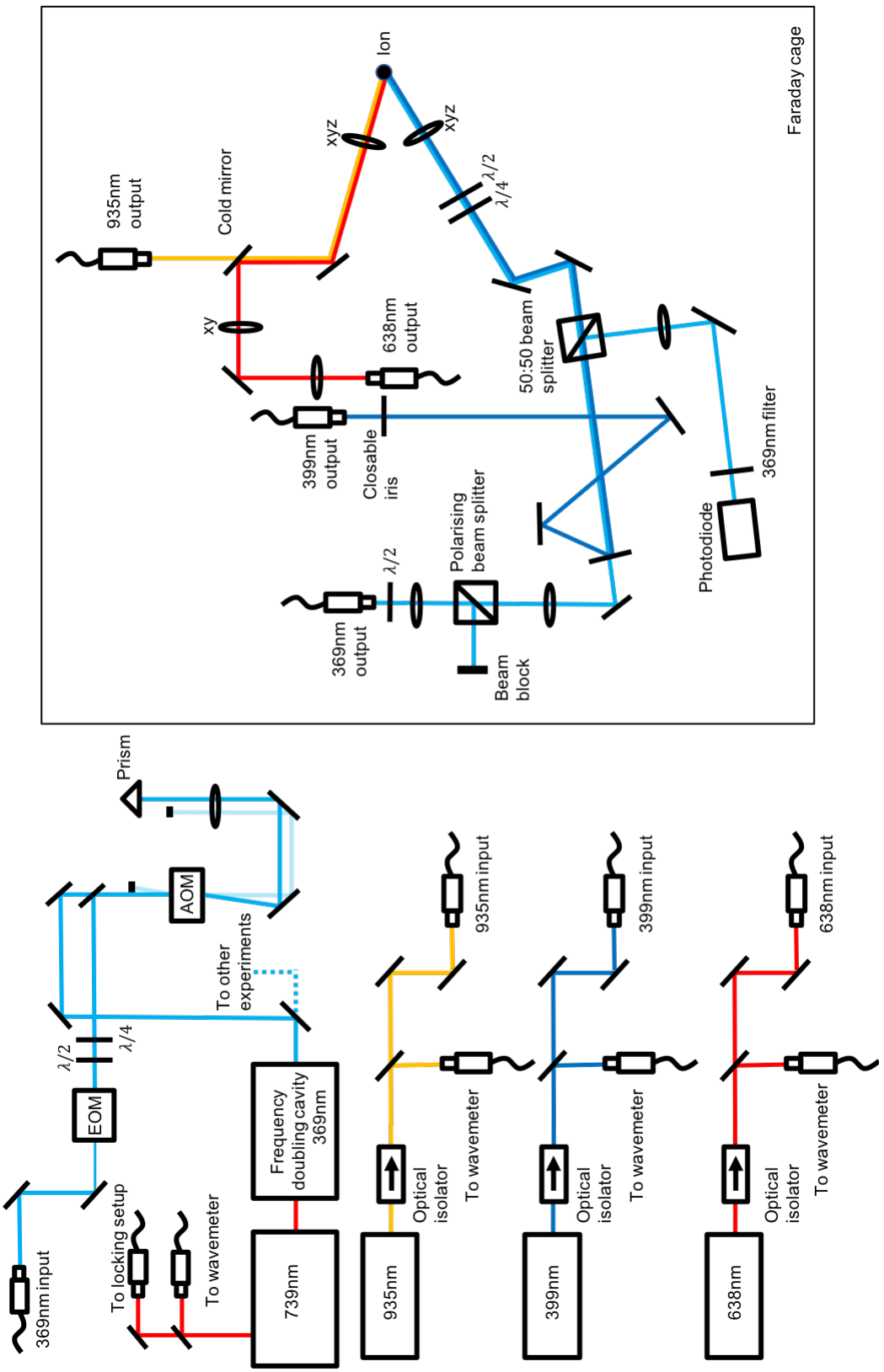

Figure 3.4: Schematic of the optical layout of the four lasers required for trapping, cooling, preparing and detecting $^{171}Yb^{+}$ ions. The 399 nm laser is used only for trapping and is blocked during experiments.

tion (399 nm). The 369 nm laser used for cooling, preparation and detection of the ion is an MSquared Ti:Sapphire laser (SOLSTIS CW). This produces light at 739 nm, which is then frequency doubled to around 1.5 W of 369 nm using a bow tie cavity with a second harmonic generation crystal (ECD-X). The other three of these lasers (the 935 nm, 638 nm and 399 nm) are home built external cavity diode lasers (ECDL), as described in [58]. In order to scan the hyperfine transitions described in section 2.3.4, a modulation frequency of approximately 1 Hz is applied simultaneously to the diode current and the piezo voltage of the 638 nm laser.

A schematic of the optical layout is shown in figure 3.4. Optical fibres are used to pass lasers through the walls of the Faraday cage and to decouple the pointing stability through the vacuum system from the lasers themselves. Outside of the cage, the beam paths of the 935 nm, 399 nm and 638 nm are similar. They pass through an optical isolator, followed by a beam picker which diverts some light to the wavemeter, and steering mirrors for coupling into an optical fibre. The 369 nm beam path is more complex. The beam passes first through a double pass acousto-optical modulator (AOM) setup, which allows light to be turned on and off on the timescale of less than 1 μs, and to control the frequency and the power of the light using an analogue output from the experimental computer FPGA. The AOM (Isomet 1206C-833) is driven by an RF signal between 100 MHz and 130 MHz (Isomet AOM driver) which is added to the laser frequency. In order to achieve full extinction of light, a switch (Mini-circuits ZASW-2-50DR+) is placed after the AOM driver since it was found that the AOM driver internal switch did not fully block the RF signal. After the AOM setup, the beam passes through an EOM (Qubig EO-T1055M3, driven by Qubig E2.13I3) which adds sidebands at approximately 1 GHz. The light is coupled into the optical fibre.

Once inside the Faraday cage, the lasers are directed to the ion trap through two viewports on the vacuum system. The 935 nm and 638 nm beams are overlapped using a cold mirror (Thorlabs M254C45) which, when placed at 45°, transmits light of wavelength $\gtrsim$ 700 nm and reflects light of a lower wavelength. The overlap is finely adjusted using a lens in an x-y translation stage in the 638 nm beam path before this cold mirror. Both beams are then positioned on the ion using a lens in an x-y-z translation stage fitted with digital micrometers.

The 369 nm laser passes through a polarising beam splitter (Eksma 430-1157) after the fibre output which only transmits horizontally polarised light. This transforms polarisation fluctuations and drifts from the fibre into amplitude fluctuations and drifts. After steering

mirrors, the beam then passes through a 50:50 beam splitter (Eksma 355-1105). One of the outputs of the beamsplitter is sent to a photodiode through a 369 nm bandpass filter which minimises the effect on the photodiode measurement of background light. The signal from the photodiode is used to monitor the power of the laser when the AOM is set to high power, and to stabilise the power of the laser beam when the AOM is set to low laser power using a digital PID circuit in LabVIEW which alters the RF power sent to the AOM (setup designed by Dr Tomas Navickas and Tom Crane). During experiments, the 399 nm beam is blocked at the fibre output using an adjustable iris, but when trapping it is overlapped with the 369 nm beam. This is achieved using a bandpass filter (Semrock FF01-3701/36-25) with centre frequency 370 nm and bandwidth 36 nm, which allows the 369 nm light through and reflects the 399 nm light. These beams pass through a half and a quarter waveplate to control the polarisation and finally through a lens in an x-y-z translation stage with digital micrometers to focus the beam on the ion.

3.2.2 Frequency stabilisation

In order to effectively and repeatably Doppler cool, prepare, and detect the ion, the frequency of the 369 nm laser needs to be stabilised. For the majority of the work in this thesis, a three stage lock is used, which is described in detail in [59]. A 780 nm laser beam (Moglabs, Cateye External Cavity Diode Laser) passes through a Rubidium cell and, using saturation absorption spectroscopy, is locked to the $5^2S_{1/2} \leftrightarrow 5^2P_{3/2}$ transition of the Rubidium vapour. The 780 nm beam is then directed through a cavity, the length of which is locked to this stabilised laser. The 739 nm beam passes through and is locked to the same cavity. An AOM is used in the beam path for the 780 nm light allowing the frequency of the 780 nm, and therefore the 739 nm, to be fine tuned. For later work, shown in chapter 7, a new locking setup was used, installed by Dr. Tomas Navickas [59]. The 739 nm is locked directly to a low-drift passive cavity of length approximately 10 cm. The cavity is isolated in a vacuum system with acoustic shielding and temperature stabilised.

The 935 nm laser is locked using the wavemeter, which supplies the wavelength of the laser to the LabVIEW experimental control program. This then generates feedback to the piezo of the 935 nm laser using the experimental computer FPGA. This protects against slow drifts in the frequency which cause preparation and detection to become less effective. Other lasers are left unstabilised, since they are not used for sensitive operations and are generally only used for short periods of time over which stability is not an issue.

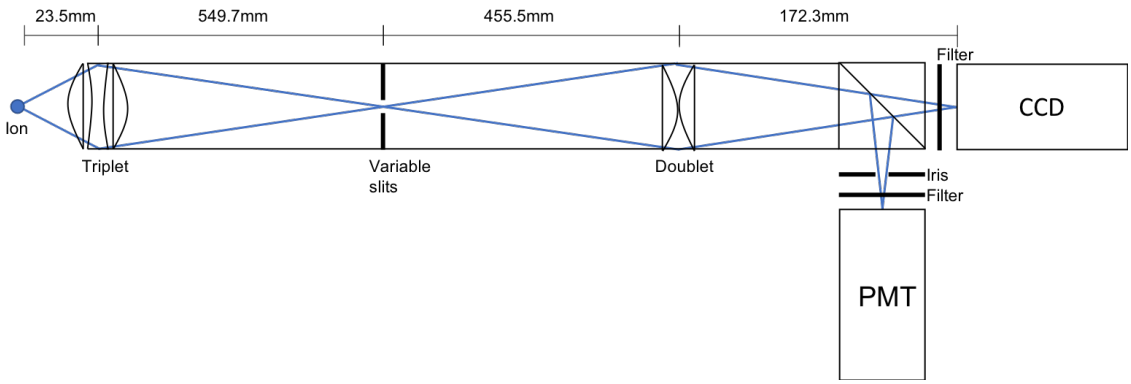

Figure 3.5: Schematic of the imaging setup designed to reduce the magnification of the ions on to the CCD camera (not to scale). A removable mirror allows the photon path to be directed either to the PMT or the CCD camera for detection.

3.2.3 Imaging

In order to detect an ion, 369 nm light scattered by the ion is collected and magnified by a series of lenses, which is then detected either by a CCD camera (Andor iXon Ultra) or a photomultiplier tube (PMT, Hamamatsu H8259-01). Typically, the camera is used for aligning lasers to the ion position and trapping ions, and the PMT is used for collection of photons during experiments. For a single ion, the method of counting photons on the PMT gives good contrast between when the ion is dark and when the ion is bright. When measuring two ions, however, there are various limitations on the effectiveness of using the PMT for detection. There is significant overlap in the distributions in the number of photons counted for one ion bright or two ions bright during a detection event, as discussed in section 3.4.2, which significantly reduces the detection fidelity. The extent of this overlap is affected by any drifts in laser frequency or power. Furthermore, using a PMT it is only possible to distinguish three cases: no ions bright, one ion bright, or both ions bright. It is therefore desirable to use the camera instead to detect during experiments involving two ions. This means that instead of detecting two ions together, two single ions are effectively being detected simultaneously, assuming there is little cross talk, which reduces the problem of overlap in number of photons collected. It also allows the possibility of distinguishing four experimental results: $\{d, d\}$, $\{b, d\}$, $\{d, b\}$ and $\{b, b\}$, where b represents bright and d represents dark.

In order to provide the ability to detect on the camera, the imaging setup described in detail in [60] was altered to provide lower magnification. The original magnification of the setup was $M_{tot} = 35.1$ [55], which resulted in ions imaged onto a large number of pixels. For optimal efficiency of camera detection, the photons scattered from an ion should instead be focussed primarily onto one pixel, to maximise the signal to noise ratio. The

imaging setup consists of a triplet and a doublet lens positioned in a lens tube to reduce background light, and is shown in figure 3.5. The triplet lens is positioned 23.5 mm from the ion and provides a magnification of $M_{tr} = -17.5$, resulting in an image at 549.7 mm. This is the result of a simulation [60], since the thin lens approximation does not hold for the triplet lens.

The total required magnification of the system, $M_{tot} = M_{tr}M_d$, can be calculated by finding the ratio between the diffraction limit of the triplet lens (1.13 μm) and the pixel size of the camera (8 μm $\times$ 8 μm). This gives a total magnification $M_{tot} \approx 7$, giving a required doublet magnification of $M_d = -0.4$. Given the length constraint between the ion image from the triplet and the CCD/PMT, we can define $s_{tot} = s_{di} - s_{do}$ where s_{tot} is the total length, s_{di} is the distance to the image and s_{do} is the distance to the object. The image and object distance of the doublet can then be calculated using

$$M_d = \frac{s_{di}}{s_{do}} \tag{3.1}$$

which gives $s_{do} = -455.5$ mm and $s_{di} = 172.3$ mm. Using the thin lens approximation

$$f_d = \left(\frac{1}{-s_{do}} + \frac{1}{s_{di}} \right)^{-1} \tag{3.2}$$

we find the required focal length of the doublet to be 125 mm. For a doublet consisting of two lens with focal lengths f_1 and f_2 placed in close proximity, the focal length is given by

$$f_d = \left(\frac{1}{f_1} + \frac{1}{f_2} \right)^{-1}. \tag{3.3}$$

We use two lenses of focal length 250 mm (Thorlabs LA1461-A) to give the required focal length.

The lens tube is placed in an x-y-z translation stage with digital micrometers. At the ion image position after the triplet, two variable slits (Thorlabs VA100C) are placed at right angles which can be used to block light scatter from electrodes, allowing for individual control in the x and y direction. The end of the imaging tube is connected by bellows (to allow for free movement of the triplet lens) to a cage cube. This cage cube allows easy access for removing and repeatably replacing a mirror, used to swap between use of the camera and the PMT. With no mirror in place, the light from the ion continues to the camera, and with the mirror in place it is reflected by 90° to the PMT. A 369 nm bandpass filter is placed directly in front of both the camera and the PMT. There is an additional adjustable iris in front of the PMT to block scatter and background light. For experiments

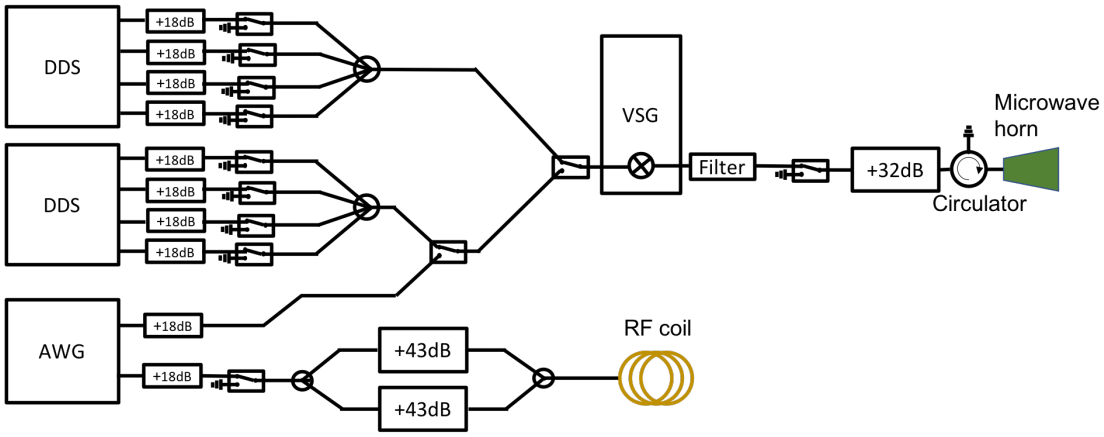

Figure 3.6: Schematic of the setup used to broadcast RF and microwave radiation to the ion. To generate the required microwaves, RF frequencies are mixed with a microwave signal from the VSG. Two DDS boards are in use for the microwave setup, although the majority of coherent manipulation is done using the AWG. The RF setup uses only the AWG to generate the required frequencies.

in this thesis, PMT detection is used, but work is ongoing to introduce camera detection for ion readout.

3.3 Microwave and radiofrequency generation

Microwave and radiofrequency (RF) radiation is required to drive transitions within the $^2S_{1/2}$ manifold of the $^{171}Yb^+$ ion. The setup for generating this radiation has been described in detail in [53], but various adjustments have been made which will be described here. A schematic of the setup is shown in figure 3.6. For both microwave and RF radiation, multiple frequency tones are required to address various transitions within the hyperfine manifold simultaneously. Multiple ions require further frequencies since the magnetic field gradient means that the Zeeman splitting of the hyperfine states differs between ions, as described in section 2.4.3.

3.3.1 Microwave generation

Microwave fields with controllable frequency, phase and amplitude are generated by using a controllable RF source and mixing with a fixed microwave signal. Initially, this RF was produced using Analog Devices AD9959 evaluation boards. These are four channel direct digital synthesis (DDS) boards that, with a clock input of 25 MHz, can produce frequencies of up to 500 MHz with a maximum amplitude of 700 mV_{pp}. The frequency, phase and amplitude are all controllable from the experimental computer. Further details of this setup can be found in [61], although an adjustment has been made to communicate directly be-

tween the computer and the boards via USB, rather than through an Arduino. Each board produces four signals, each of which is then amplified by +18 dB (Mini-Circuits ZFL-750+) and passed through a switch (Mini-Circuits ZASWA-2-50DR+) which is controlled using a TTL signal from the FPGA controlled by the experimental computer. The four frequencies are combined using a four way combiner (Mini Circuits ZMSC-4-3+). There are two boards in use for the microwave setup, producing 8 individually controllable channels, with a switch placed after the two combiners to switch between boards.

To replace some of these frequencies, one channel of a two channel arbitrary waveform generator (AWG) is used (Keysight M8190A 12 GSa/s). Using this advanced AWG allows an unlimited number of frequency tones to be produced, all with controllable amplitude and phase. It also allows for more complex waveforms to be generated, incorporating features such as pulse amplitude shaping and time-varying frequencies. Generating and uploading these complex and often long waveforms to the AWG can be computationally intense and therefore time-consuming. It is important that this process is as fast as possible as the waveforms need to be updated dynamically between each step of the experimental sequence. A separate dedicated AWG computer is therefore used, which communicates with the main experimental computer via ethernet. The waveform samples are calculated using C++ Accelerated Massive Parallelism (C++AMP) which runs on a graphics (GPU) card. The AWG control system was implemented by Adam Lawrence and is fully described in [62]. The maximum memory per AWG channel is 2 GSa. The waveforms are uploaded to the AWG via a PCIe interface, which allows the entire memory to be uploaded in seconds, if it is already stored in the computer memory. At present, the AWG runs at 500 MSa/s, a sample rate high enough for the microwave signals to be produced (which are typically 100 MHz-150 MHz). Using this sample rate gives a total playtime per channel of approximately 4 s. This is sufficient for current experiments, but in order to minimise use of memory and time for generation and upload of waveforms in the future, sequencing can be used. This allows multiple segments to be stored in the AWG memory, which can be labelled and individually triggered. Furthermore, this AWG offers the possibility of infinite playtime via streaming. The waveform can be split into multiple segments and used as a ring buffer- as soon as the AWG moves onto the next segment, the previous one is updated. The bandwidth of this is limited by waveform generation and upload time.

The AWG is currently used for most coherent manipulation during the experimental sequence, while DDS channels are still used for Doppler cooling in the experimental sequence and between experiments. The transition from DDS to AWG should soon be

complete so that the AWG produces all microwave frequencies with no need for the DDS boards. The AWG is clocked at 10 MHz, and triggered using a TTL output from the experimental computer FPGA. A switch is used to alternate between the AWG and DDS boards.

The microwave signal at approximately 12.6 GHz is produced using a vector signal generator (VSG, Keysight E8267D) at power 16 dBm, and the RF signal is combined with this using the internal mixer of the VSG. The microwave frequency is set to be 100 MHz below the resonant frequency of the hyperfine microwave transition in no magnetic field. Only the positive sidebands produced by the mixer and this signal are used, which means that the negative sidebands and the carrier frequency are far off resonant from the transitions being addressed. These are filtered out with a custom passband filter (A1 Microwave WQ18) with a narrow frequency band, before passing through a final switch (AMC SWN-218-2DT). The signal is amplified by +32 dB (Microwave Amps AM25-12-13-30-33) (use of the VSG, which is capable of producing higher powers than previous microwave sources, has eliminated the need for a pre-amplifying stage before this amplifier). The signal then passes through a circulator, which ensures that any reflections are dissipated into a 50 Ω resistive load rather than reflected back to the amplifiers, which could cause damage. The signal is finally sent to a microwave horn (Flann Microwave 18240-10) which emits horizontally polarised radiation. This is positioned at 45° to the z-axis and is rotated by 45° in order to contain σ_-, σ_+, and π components. This positioning is fine-tuned by optimising the Rabi frequencies of the ion transitions.

3.3.2 RF generation

RF frequencies can be directly generated since the frequencies are low enough to not require mixing. Two further DDS boards were previously used for this, and for the initial two qubit gate experiments shown in chapter 6 an AWG (Agilent 33522A) was used. However, the RF radiation is now solely produced by the second channel of the AWG used as part of the microwave setup (M8190A). As with the microwaves, this allows for an unlimited number of individually controllable frequency tones to be produced, with complex waveform manipulation. A switch is placed after the AWG output, and the signal is then split two ways (Mini-Circuits ZFSC-2-1-S+) and passed through two +43 dB amplifiers (Mini-Circuits LZY-22X+). A high power combiner (Werlatone D1635-102) recombines these two amplified signals, and the resultant signal is sent to an RF coil (3 turns, wire diameter 3.55 mm, radius 51 mm) placed outside the vacuum window through

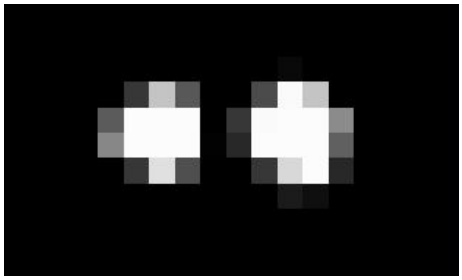

Figure 3.7: Picture of two trapped ions taken on the CCD camera.

which the ion is imaged.

3.4 Initial experiments

3.4.1 Trapping

All lasers are aligned to the centre of the ion trap with powers of approximately 50 μW for the 369 nm, 200 μW for the 399 nm, 1 mW for the 638 nm, and 6 mW for the 935 nm. The 935 nm laser power is high since this laser power broadens over the transitions in the $^2D_{3/2}$ and $^3[3/2]_{1/2}$ manifolds. Microwaves are also turned on to address the $^2S_{1/2}$ hyperfine manifold. A current of 6.2 A is run through the atomic ovens to produce a beam of neutral ytterbium atoms, and ions are usually trapped within a timescale of minutes. A picture of two trapped ions from the CCD camera is shown in figure 3.7. When trapped, the axial and radial secular frequencies of the ions can be measured by applying an RF field through the RF coil and scanning the frequency. When resonant with a secular frequency, the RF field will excite the motion of the ions, and this excitation can be observed on the camera or in the fluorescence on the PMT when precise measurement is needed.

3.4.2 Cooling, state preparation, and state detection

For most experimental sequences, there are four main steps. First, the ions are Doppler cooled. Secondly, the ions are initialised by preparing in state $|00\rangle$. Following this, some coherent manipulation generally takes place. This consists of pulses of RF and microwave radiation, and varies depending on what type of experiment is being performed. Finally, the state of the ions is detected. Whilst the coherent manipulation varies between experiments, the cooling, preparation and detection steps are the same for each experiment. These will therefore be described in this section. A schematic which summarises the experimental requirements for each step is shown in figure 3.8.

The AOM allows for extinction of the laser, as well as for fast control of the frequency

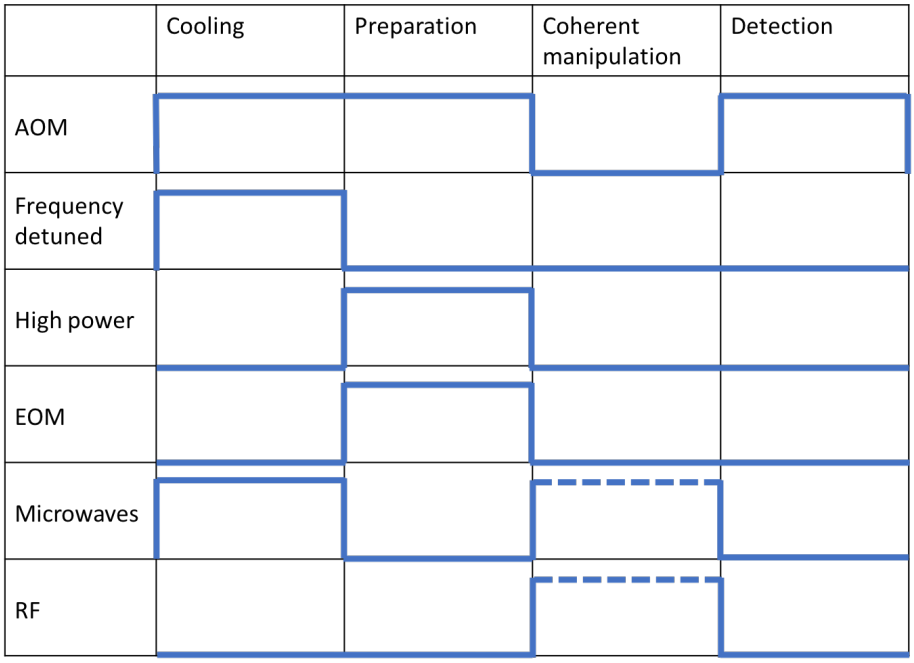

Figure 3.8: Schematic of the settings required for each step of the experimental sequence. When the AOM is off, the laser is blocked. When the AOM is on, the frequency can be adjusted between two levels: red detuned from the resonant frequency of the cooling transition, or at this resonant frequency. The laser can also be set to two power levels, high or low. The EOM and microwaves can also be controlled during the experimental sequence. During coherent manipulation, a combination of microwaves and RF pulses may be used, depending on the specific experiment being performed.

and power. The frequency is set so that the AOM can switch between two frequencies: the resonant frequency for the $^2S_{1/2}, F = 1 \leftrightarrow ^2 P_{1/2}, F = 0$ transition, or 12 MHz red detuned from this frequency. The laser power is set to switch between approximately 2.6 μW, which is near the saturation intensity of the transition, and 50 μW. Doppler cooling of the ion is performed at low power, and red detuned from resonance by approximately 12 MHz.

State preparation is performed by optically pumping the ion to the state $^2S_{1/2}, F = 0 \equiv |0\rangle$, as described in section 2.3.3. A sideband 2.1 GHz from the carrier is added to the 369 nm laser frequency using the EOM, which makes it resonant with the $^2S_{1/2}, F = 1 \leftrightarrow ^2 P_{1/2}, F = 1$ transition. From $^2P_{1/2}, F = 1$, the ion can only decay to $^2S_{1/2}, F = 0$, and there is no laser resonant with any transitions from this energy level. Within μs's, population is pumped to this state.

For state detection, the laser is turned on with the AOM set to low power and at the resonant frequency, and the number of photons on the PMT is counted. When population is in the $^2S_{1/2}, F = 1$ manifold, the laser is resonant with a cycling transition so the ion will scatter photons and fluoresce, and therefore record a 'bright' result. When the ion is in the state $^2S_{1/2}, F = 0$, there is no resonant laser so the ion will not scatter photons and will record a 'dark' result. When the ion is in the 'dark' state, some photons are still counted due to scatter of 369 nm light from the trap electrodes. A threshold number of photons between the bright and dark states can therefore be determined, and the hyperfine states distinguished using this threshold.

The limit to the effectiveness of this method of detecting the ion's state is the off-resonant coupling of the 369 nm laser to other levels in both $^2S_{1/2}$ and $^2P_{1/2}$. In particular, the laser is only detuned by approximately 2.1 GHz from the $^2S_{1/2}, F = 1 \leftrightarrow ^2 P_{1/2}, F = 1$ transition. The likelihood of this off-resonant coupling occurring increases over time, which places a limit on the detection time. However, since the imaging setup only collects a small proportion of scattered photons, with a collection efficiency measured of 0.1% [55], a longer detection time is desirable to decrease the chance of collecting no photons when the ion is in the bright state. There is therefore a tradeoff in the detection time between the need to collect enough photons to properly distinguish the states, and the off-resonant coupling of the laser to other transitions. A specially designed detection setup was shown by Noek *et al.* [63] to increase the collection efficiency to 10%, which allows for an increased detection fidelity.

The combined error due to imperfect preparation and detection of the ion is known as the SPAM (state preparation and measurement) error. In order to determine this

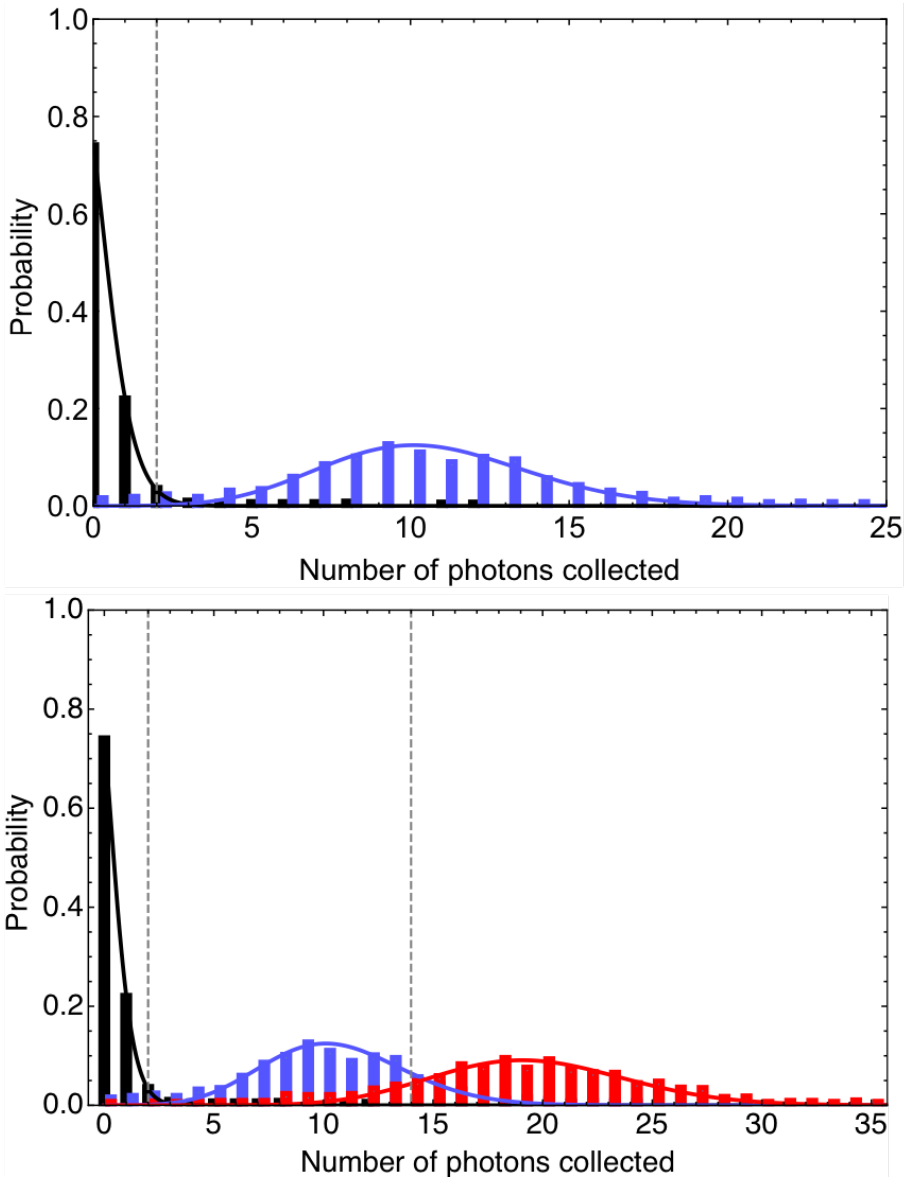

Figure 3.9: Top: state detection measurement for a single ion, where the ion is prepared in the dark state $|0\rangle$ and measured, and then a microwave pulse transfers the population to the bright state $|0'\rangle$ and it is measured. Each measurement consists of 1000 repetitions, and this allows the mean number of photons collected to be calculated for each state. A threshold of $t_1 = 2$ gives a state detection fidelity of 0.970. Bottom: State detection measurement for two ions. Three measurements are taken, to distinguish between the cases no ions bright, one ion bright, and both ions bright. Considerable overlap can be seen between the histograms for one and two ions bright. Thresholds of $t_1 = 2$ and $t_2 = 14$ give a state detection fidelity of 0.879.

error and to determine the threshold between bright and dark measurements, a state detection measurement is performed. For a single ion, this involves two measurements. The ion is first prepared into the state $|0\rangle$, and measured. Then, after being prepared in $|0\rangle$, a microwave pulse is used to transfer population to $|0'\rangle$, and this is measured. Each measurement is repeated multiple times (typically 1000 or more), and this allows statistics for the number of photons collected in each case to be gathered. A typical measurement for a single ion is shown in figure 3.9. The resultant measurement should display Poissonian statistics, so that a histogram with mean photon number μ can be fitted in each case. For a threshold t_1, a dark measurement is classified as one where $n \leq t_1$, where n is the number of photons collected. If $n > t_1$, this is classified as a bright measurement. From this threshold, the state detection measurement can be used to write a matrix that describes the measurement probabilities (b or d) in terms of the true state probabilities ($|\downarrow\rangle \equiv^2 S_{1/2}, F = 0$ or $|\uparrow\rangle \equiv^2 S_{1/2}, F = 1$):

$$\begin{pmatrix} P(b) \\ P(d) \end{pmatrix} = \begin{pmatrix} P(b|\uparrow) & P(b|\downarrow) \\ P(d|\uparrow) & P(d|\downarrow) \end{pmatrix} \begin{pmatrix} P(\uparrow) \\ P(\downarrow) \end{pmatrix} \tag{3.4}$$

The value of the threshold t_1 is chosen to maximise the mean of the diagonal elements of this 2×2 matrix. An experimental data set with measured probabilities $P(b)$ and $P(d)$ can then be multiplied by the inverse of this matrix in order to normalise out SPAM errors and calculate the true probabilities of states $|\uparrow\rangle$ and $|\downarrow\rangle$.

For two ions, there are four possible experimental results: $\{\downarrow,\downarrow\}, \{\uparrow,\downarrow\}, \{\downarrow,\uparrow\}, \{\uparrow,\uparrow\}$. However, using the PMT it is only possible to distinguish between three cases, since $\{\uparrow,\downarrow\}$ and $\{\downarrow,\uparrow\}$ should scatter the same number of photons and therefore record the same result. Similarly as for a single ion, a state detection measurement is taken, with the result shown in figure 3.9. The results of three measurements are recorded: the ions both prepared in $|0\rangle$, a microwave pulse to transfer the population in one ion to $|0'\rangle$, and a microwave pulse on both ions to transfer population to $|0'\rangle$. This allows two threshold numbers of photons to be determined, t_1 and t_2, where t_1 is the threshold between no ions bright and one ion bright, and t_2 is the threshold between one ion bright and two ions bright. From the experimental result, it can be seen that there is a large overlap between the histograms for one ion bright and two ions bright. This reduces the detection fidelity by a significant amount. This overlap is also sensitive to drifts in laser power or frequency, so it is necessary to take more frequent state detection measurements to ensure that SPAM error is being accurately normalised out. The same method is used for this error normalisation as for a

single ion, where the inverse of the experimentally determined 3×3 matrix which describes the measured probabilities in terms of the real probabilities is used.

3.5 Coherent manipulation

3.5.1 Rabi oscillations

As described in section 2.4.1, transitions within the hyperfine manifold of the ion can be performed by applying radiation at the resonant frequency. By scanning the frequency of the applied radiation and measuring the population at each step, it is possible to determine the exact frequency of a transition, as shown in figure 3.10. An ion is cooled and prepared in state $|0\rangle$. A pulse of microwave radiation of around 12.6 GHz is applied on the transition $|0\rangle \leftrightarrow |0'\rangle$, after which the state of the ion is detected. The data is normalised using the method described in section 3.4.2, and a fit of equation 2.31 is shown in figure 3.10. This 'clock' transition is insensitive to the magnetic field to first order. The frequency shift of approximately 29 kHz from the frequency of the transition at zero field, $\omega_{\mathrm{hf}}/2\pi$, is due to the second order Zeeman shift.

A Rabi oscillation on this transition is also shown in figure 3.10. After the ion is cooled and prepared in state $|0\rangle$, a pulse of microwave radiation is applied for increasing pulse lengths, after which the population is measured. The frequency of this oscillation depends on the magnetic field amplitude of the applied oscillating field. No decay in amplitude is seen due to the insensitivity of the transition to magnetic field noise to first order.

3.5.2 Experimental stabilisation

Unlike the states composing the clock transition shown in figure 3.10, the states $|-1\rangle$ and $|+1\rangle$ are dependent on magnetic field strength to first order. Any change in the magnetic field at the ion position therefore causes a significant change in the transition frequency involving these states. This change in magnetic field strength can result from a change in ambient magnetic field in the environment, or, since there is a magnetic field gradient present in this setup, a change in ion position. As described in section 3.1.1, a change in voltage on one of the trap DC electrodes can cause a change in position of the ion along the z-axis of 17.8 nm/mV. In the magnetic field gradient used in this setup, this corresponds to a change in frequency of approximately 25 Hz/mV for the insensitive clock transition $|0\rangle \leftrightarrow |0'\rangle$, and 6.26 kHz/mV for the sensitive transition $|0\rangle \leftrightarrow |+1\rangle$.

In order to perform high fidelity quantum operations, it is essential that frequencies are

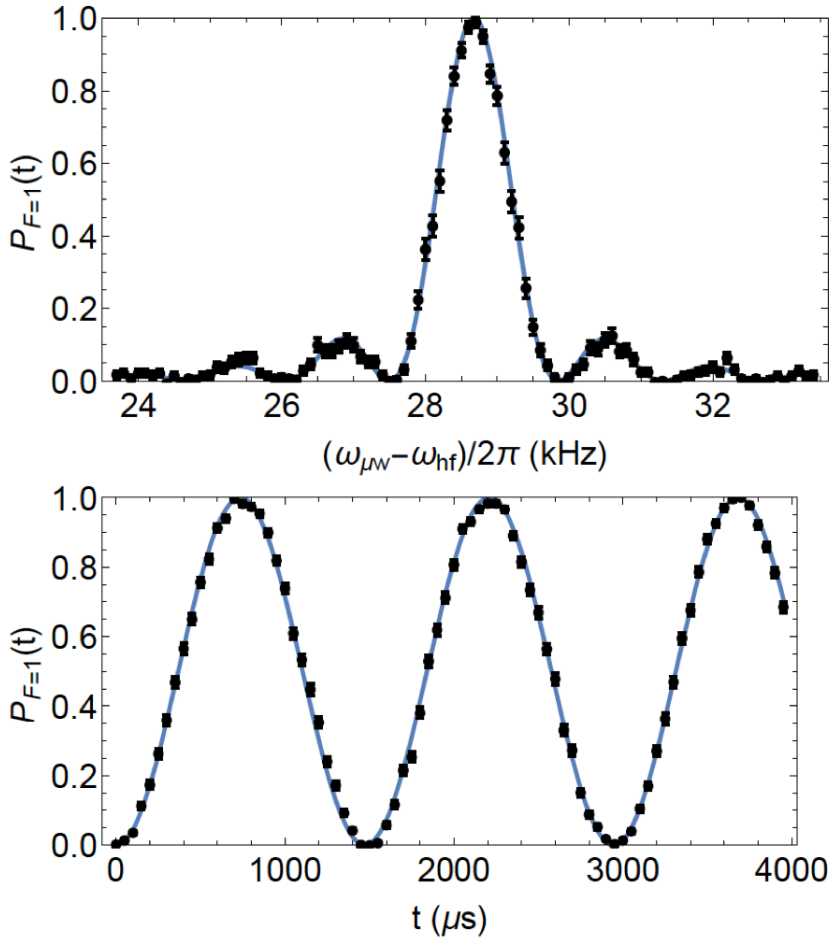

Figure 3.10: Top: Population in ${}^2S_{1/2}, F = 1$ after a pulse of microwave radiation of length π/Ω is applied around the frequency of the transition $|0\rangle \leftrightarrow |0'\rangle$, where Ω is the Rabi frequency. Each point is the result of 300 repetitions, and SPAM error is normalised out using a state detection measurement, as described in 3.4.2. The fit is a fit of equation 2.31 and gives a centre frequency of $(\omega - \omega_{hf})/2\pi = 28.675(3)$ kHz, where ω is the resonant frequency of the transition and ω_{hf} is the frequency of the transition at zero magnetic field. Bottom: A Rabi oscillation on the same transition, where the microwave radiation set to the resonant frequency ω. Each point is a result of 1000 repetitions, and again the data is normalised. A fit of equation 2.32 gives a Rabi frequency of $\Omega/2\pi = 679.0(4)$ Hz. Figure reproduced with permission from [53].

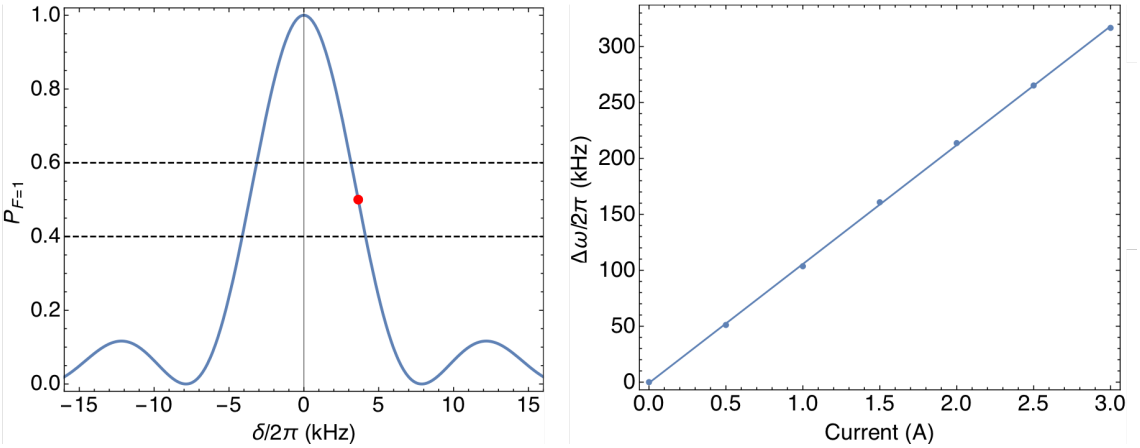

Figure 3.11: Left: The magnetic field stabilisation sequence is calibrated so that a microwave pulse on the transition $|0\rangle \leftrightarrow |+1\rangle$ should give the result $P(F = 1) = 0.5$, as indicated by the red point. If the result is between 0.4 and 0.6, shown by the grey dashed lines, the main experiment proceeds. Right: Frequency of the transition $|0\rangle \leftrightarrow |+1\rangle$ as a function of the current in a small coil used for feedback for magnetic field stabilisation. The frequency change is calculated with respect to the frequency at 0 mA through the coil.

accurately known, and any drift in frequency generally induces error. We therefore stabilise the frequency by running an auxiliary experimental sequence between experimental steps. During this auxiliary experimental sequence, a microwave pulse of 110 μs is applied on the transition $|0\rangle \leftrightarrow |+1\rangle$ of an ion. The frequency of this pulse is chosen so that it should give a result of $P(F = 1) = 0.5$, as shown in figure 3.11. The measured probability $P(F = 1)$ is used to calculate an error signal, which allows feedback to be applied to the current in a small coil situated approximately 30 cm from the ion on the z-axis. This adjusts the magnetic field strength at the ion, and moves the $|0\rangle \leftrightarrow |+1\rangle$ transition by 106 kHz/A. If the measured result is between $P(F = 1) = 0.4$ and $P(F = 1) = 0.6$, the main experiment proceeds, but if outside of this range the auxiliary sequence is run again to compensate further. Using these limits, the $|0\rangle \leftrightarrow |+1\rangle$ transition is stabilised for slow drifts to within approximately 1 kHz, which corresponds to a stability of approximately 5 Hz on the $|0\rangle \leftrightarrow |0'\rangle$ transition and a magnetic field stability of 0.7 mG. If more than one ion is trapped, this auxiliary sequence is performed on a single ion, as it is assumed that any change in B field is primarily a uniform change across the ion string, and the difference between ions in feedback from the coil is negligible. By compensating for long term drifts in frequency on one ion, we are therefore stabilising the B field across the whole ion string. Typically over a day the current can drift by on order 100 mA, although this varies depending on the experimental environment.

A Rabi oscillation on the transition $|0\rangle \leftrightarrow |+1\rangle$ is shown in figure 3.12, with and without

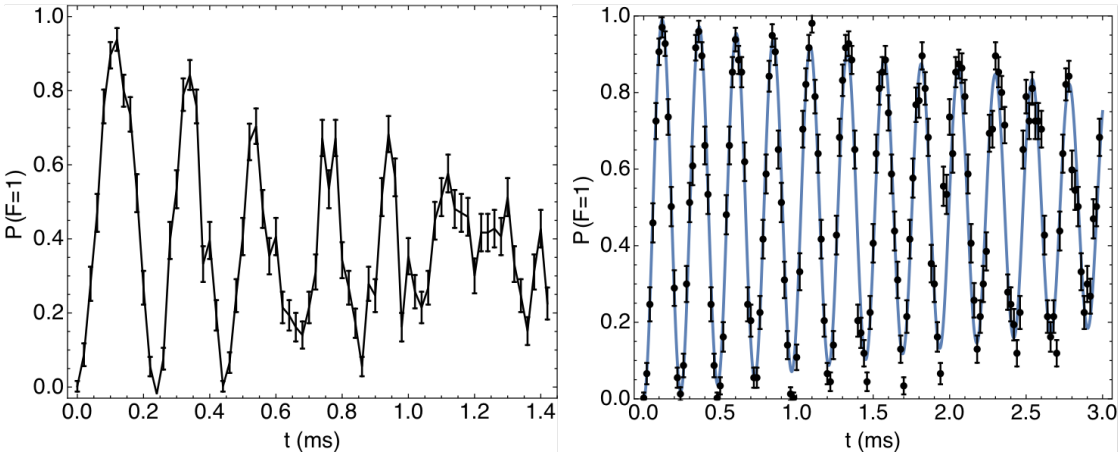

Figure 3.12: Left: Rabi oscillations with no stabilisation quickly decay, as shown here. An exponential decay is not a good fit to this type of decay, which is dependent on slow drift of magnetic field. Right: With the stabilisation sequence, the Rabi oscillations last for longer. The amplitude decay is due to dephasing caused by higher frequency magnetic field noise, and an exponential fit gives a decay time of 6.4(6) ms.

magnetic field stabilisation. It can be seen that without stabilisation the oscillations quickly decay, whereas with magnetic field stabilisation the oscillations continue for over double the time. However, a clear exponential decay in amplitude is still displayed, unlike for the clock transition in figure 3.10. This is due to dephasing caused by fast magnetic field noise, which is not compensated for by the stabilisation method. An exponential fit to this Rabi oscillation gives a decay time of 6.4(6) ms.

We have also experimentally observed that the fluorescence of the ion can drift over long experiments, which alters the numbers of photons scattered during state detection. This is particularly problematic for two ions, since the threshold between one and two ions bright is sensitive to any change in ion fluorescence. Although there are many factors which could cause this change, it is assumed to be primarily associated with a change in the frequency of the cooling 369 nm laser due to an imperfect frequency lock. A change in the beam power of the 369 nm laser is discounted as a cause, since it would result in a change in the maximum photon counts observed when the frequency of the laser was scanned over the resonant transition, which is not observed. Drifts in polarisation of the 369 nm beam from the optical fibre are eliminated through the use of a polarising beam splitter after the fibre. A change in the frequency of the repump 935 nm laser could also cause a change in fluorescence, but since this is locked on the wavemeter and a high laser power is applied to the ion this is assumed to be negligible. We therefore compensate for changes in fluorescence by altering the frequency applied to the AOM for the 369 nm laser. An auxiliary sequence is run between experimental steps, at the same time as the magnetic

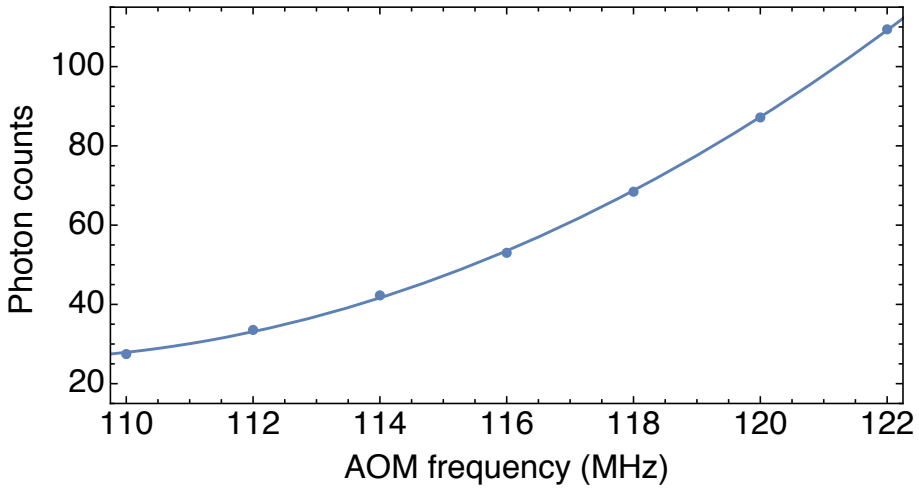

Figure 3.13: Plot of the average photons counted on the PMT scattered from the ion during Doppler cooling against the AOM frequency. The measured photon counts are used to feed back to the AOM frequency during an auxiliary sequence to stabilise the ion fluorescence. A second order polynomial is fitted to the data.

field stabilisation sequence. The photons counts during Doppler cooling are measured, and feedback is sent to the set frequency of the AOM. The dependence of photon counts on AOM frequency is shown in figure 3.13. If the measurement is ± 2 from the set value, the experiment proceeds, but if it is outside of this range then the auxiliary sequence is performed again. Typically, the AOM frequency changes by a maximum of 2 MHz over a period of 1 hour.

3.5.3 Individual addressing

As described in section 2.4.3, an advantage of applying a magnetic field gradient to multiple ions is that the frequency of the transitions becomes position dependent, and therefore ions can be individually addressed in frequency space while long-wavelength radiation is broadcast to all ions. This is demonstrated for two ions in figure 3.14, with ion-ion separation of $\Delta z = 6.1\,\mu$m at secular frequency $\nu_z \approx 428$ kHz. A π-pulse on the $|0\rangle \leftrightarrow |+1\rangle$ transition for each ion at Rabi frequency 2.5 kHz is shown, with separation of approximately 2 MHz. The cross talk for these parameters can be calculated from equation 2.67 as 7×10^{-9}, which could be further reduced by lowering the Rabi frequency.

3.5.4 Microwave sidebands

As described in section 2.4.2, microwave and radiofrequency can be used in conjunction with a magnetic field gradient to couple spin and motional states. This is demonstrated in figure 3.15, where two ions are prepared in state $|00\rangle$ and a microwave pulse is applied for

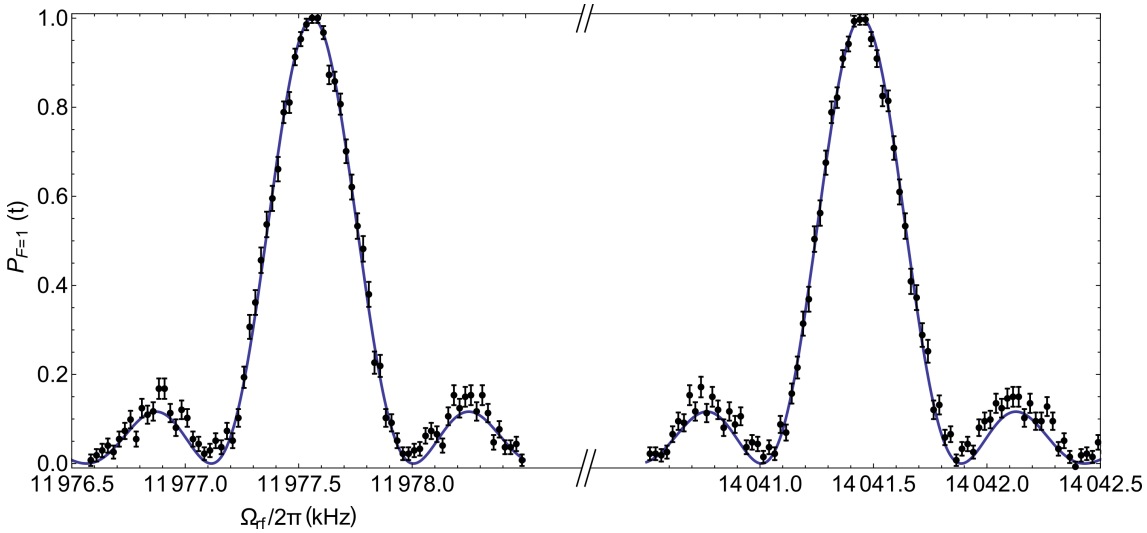

Figure 3.14: Resonant frequencies for the $|0\rangle \leftrightarrow |+1\rangle$ transitions for two ions separated by approximately 2 MHz, showing the individual addressing capabilities that are a direct consequence of using a magnetic field gradient.

200 μs. The frequency is scanned over five transitions - the carrier, and the red and blue sidebands for both the COM and the stretch modes. The COM and stretch mode sidebands are separated from the carrier transition by ν_z and $\sqrt{3}\nu_z$ respectively, where $\nu_z/2\pi = 265$ kHz. There is an additional Stark shift which reduces the frequency separation from the carrier by 9 kHz for the COM mode and 4 kHz for the stretch mode. The coupling strength to the sidebands is defined by the magnitude of the effective Lamb-Dicke parameter, which for the COM mode is $|\eta_1| = 0.009$ and for the stretch mode is $|\eta_2| = 0.004$.

3.5.5 Measuring ion temperature

As described in section 2.4.2, after Doppler cooling the ion occupies a thermal distribution of states described by the density matrix in equation 2.15. The average phonon number $\bar{n}$ of this thermal distribution can be measured by applying radiation resonant with either the red or blue sideband. At typical temperatures achieved after Doppler cooling, where $\bar{n} \gg 1$, the red and blue sidebands exhibit a nearly identical response to resonant driving radiation, since $\Omega_{n,n-1} = \sqrt{n}\eta\Omega_0 \approx \Omega_{n,n+1} = \sqrt{n+1}\eta\Omega_0$. For the red sideband, the probability to transfer from n to $n-1$ when driving the sideband resonantly is

$$P_{n,n-1}(t) = \frac{1}{2} - \frac{1}{2}\cos\Omega_{n,n-1}t. \tag{3.5}$$

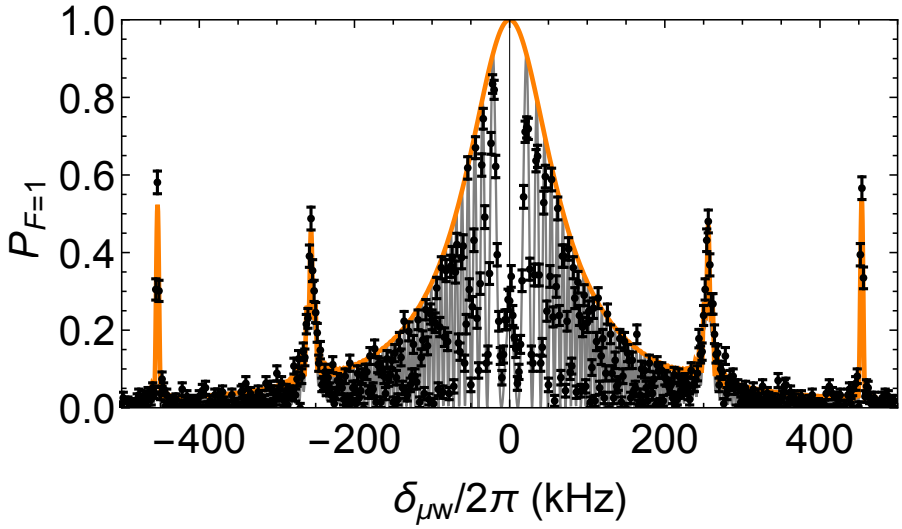

Figure 3.15: Microwave driven motional sidebands for two ions on transition $|0\rangle \leftrightarrow |+1\rangle$. Probability for an ion to be in $F = 1$ after a microwave pulse of 200 μs is plotted against the detuning from the carrier transition. Two sidebands are seen corresponding to the COM mode at $\nu_z/2\pi = 265$ kHz and the stretch mode at $\sqrt{3}\nu_z/2\pi = 459$ kHz. The orange line plots the carrier envelope with the sideband terms, and the black line plots the fine structure resulting from the applied pulse time and Rabi frequency, which is randomly sampled by data points. Figure reproduced with permission from [53].

Assuming a thermal state ρ_{th}, the probability to make a transition on the red sideband is then

$$P_{rsb}(t) = \sum_{n=0}^{\infty} p_n P_{n,n-1}(t). \tag{3.6}$$

where the probabilities p_n are given by $p_n = \frac{1}{1+\bar{n}} \left(\frac{\bar{n}}{1+\bar{n}}\right)^n$. This therefore allows us to determine the value of $\bar{n}$ by measuring the response of the red (or blue) sideband to driving radiation at increasing times and fitting this probability distribution.

The result of an experiment of this type is shown in figure 3.16. Two ions are initialised in state $|00\rangle$ and microwave radiation is applied on the red sideband on the transition $|0\rangle \leftrightarrow |+1\rangle$ of one ion. A stretch mode sideband is used, at secular frequency $\sqrt{3}\nu_z/2\pi = 461$ kHz. The Rabi frequency of the driving radiation is measured as $\Omega_0/2\pi = 57$ kHz by addressing the $|0\rangle \leftrightarrow |+1\rangle$ transition resonantly. A fit to the sideband then gives a mean motional mode of $\bar{n} = 53(4)$. This is above the Doppler cooling limit of $\bar{n} = 37$, probably due to imperfectly set experimental cooling parameters. This could also be due to an increased linewidth from power broadening of the laser and the Zeeman structure of the $^2S_{1/2}$ manifold.

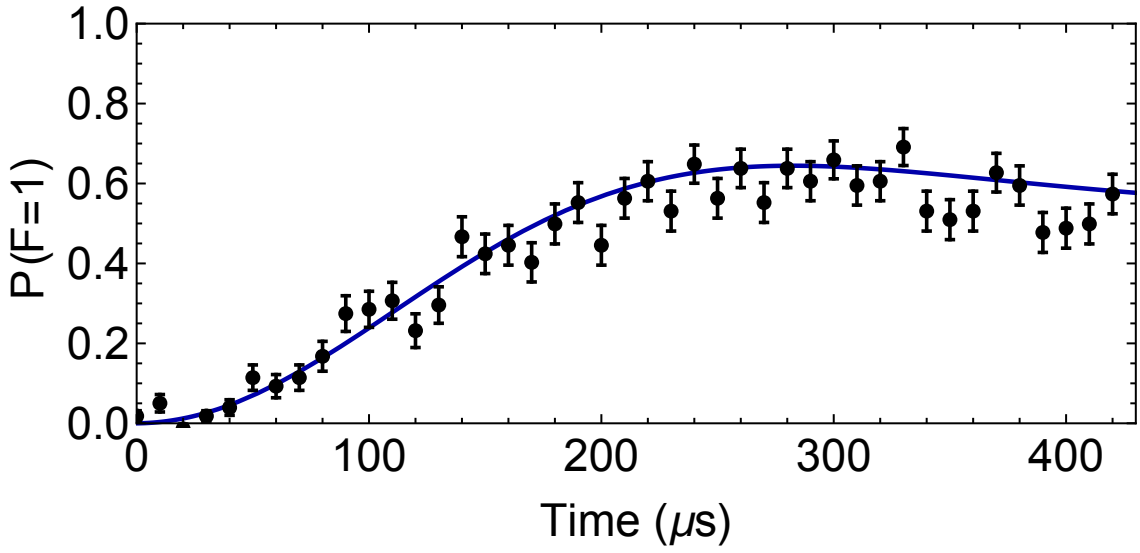

Figure 3.16: Probability of an ion being in $F = 1$ after the stretch mode red sideband on the transition $|0\rangle \leftrightarrow |+1\rangle$ is driven resonantly. Assuming a thermal distribution, a fit of equation 3.6 to the data gives a mean motional mode of $\bar{n} = 53(4)$.

Chapter 4

Dressed states

4.1 Introduction

As shown in section 2.4.2, it is possible to use long-wavelength radiation to drive multi-qubit operations by combining it with a magnetic field gradient. However, this method involves the use of magnetic field sensitive states, which have a low coherence time due to the first order sensitivity to magnetic field noise, as shown in section 3.5.2. In this chapter, I explain and demonstrate a method to overcome this problem by dressing the qubit manifold with microwave radiation, as first described by Timoney *et al.* [27], in order to produce a qubit state that has a long coherence time but retains its sensitivity to the magnetic field. By pairing one of these dressed states with a state which is insensitive to the magnetic field to first order, we have a qubit which is ideal for performing quantum logic using long-wavelength radiation.

4.2 Dressed states

In this section, I will discuss the theory behind the dressed state basis, and explain and demonstrate a method for preparing and detecting this qubit. I will then present measurements of the lifetime and coherence time of the qubit, and discuss potential sources of decoherence. I will finish by showing that this qubit is compatible with performing multi-qubit operations in a static magnetic field gradient using long-wavelength radiation.

4.2.1 Dressed state basis

The hyperfine manifold of $^{171}Yb^{+}$ in an offset magnetic field consists of four states: two states which are insensitive to first order to magnetic fields, $|0\rangle$ and $|0'\rangle$, and two states

which are sensitive to first order to magnetic fields, $|+1\rangle$ and $|-1\rangle$. These sensitive states dephase quickly in a magnetic field due to magnetic field noise, as can be seen in figure 3.12. By dressing two of the sensitive transitions with electromagnetic radiation, it is possible to produce a state which retains sensitivity to magnetic field gradients but is robust to magnetic field noise. This will be demonstrated here by using radiation to address the microwave transitions $|0\rangle \leftrightarrow |+1\rangle$ and $|0\rangle \leftrightarrow |-1\rangle$, but the theory also applies to a system where the radiofrequency transitions $|0'\rangle \leftrightarrow |+1\rangle$ and $|0'\rangle \leftrightarrow |-1\rangle$ are addressed.

The Hamiltonian describing the energy levels of the states $|0\rangle$, $|-1\rangle$ and $|+1\rangle$ is given by

$$H_0 = -\hbar\omega_0 |0\rangle\langle 0| + \hbar\omega_+ |+1\rangle\langle +1| - \hbar\omega_- |-1\rangle\langle -1| \tag{4.1}$$

where $\omega_- = \omega_+ + \Delta\omega_z$ and $\Delta\omega_z$ is the second order Zeeman shift, and we have defined energy levels with respect to the energy of the state $|0'\rangle$. Two microwave fields are applied continually to the transitions $|0\rangle \leftrightarrow |+1\rangle$ and $|0\rangle \leftrightarrow |-1\rangle$, which produces the Hamiltonian

$$H_{\mu w} = \frac{\hbar\Omega_+}{2}(e^{i(\omega_0+\omega_++\delta_+)t}e^{-i\phi_+} |0\rangle\langle +1| + H.c.) + \frac{\hbar\Omega_-}{2}(e^{i(\omega_0-\omega_-+\delta_-)t}e^{-i\phi_-} |0\rangle\langle -1| + H.c.). \tag{4.2}$$

Transforming to the interaction picture with respect to the Hamiltonian H_0 and making the rotating wave approximation gives the interaction Hamiltonian

$$H'_{\mu w} = \frac{\hbar\Omega_+}{2}(e^{i\delta_+ t}e^{-i\phi_+} |0\rangle\langle +1| + H.c.) + \frac{\hbar\Omega_-}{2}(e^{i\delta_- t}e^{-i\phi_-} |0\rangle\langle -1| + H.c.). \tag{4.3}$$

By assuming that there is no detuning for either transition so that $\delta_+ = \delta_- = 0$, the dressing Rabi frequencies are set to be equal so that $\Omega_+ = \Omega_- = \Omega_{\mu w}$, and the phases are set to be $\phi_+ = \phi_- = 0$, this Hamiltonian reduces to

$$H'_{\mu w} = \frac{\hbar\Omega_{\mu w}}{2}(|0\rangle\langle +1| + |0\rangle\langle -1| + |+1\rangle\langle 0| + |-1\rangle\langle 0|). \tag{4.4}$$

There are three eigenstates of this Hamiltonian, which are superpositions of the bare states

$$\begin{aligned} |D\rangle &= \frac{1}{\sqrt{2}}(|+1\rangle - |-1\rangle) \\ |u\rangle &= \frac{1}{2}|+1\rangle + \frac{1}{2}|-1\rangle + \frac{1}{\sqrt{2}}|0\rangle \\ |d\rangle &= \frac{1}{2}|+1\rangle + \frac{1}{2}|-1\rangle - \frac{1}{\sqrt{2}}|0\rangle . \end{aligned} \tag{4.5}$$

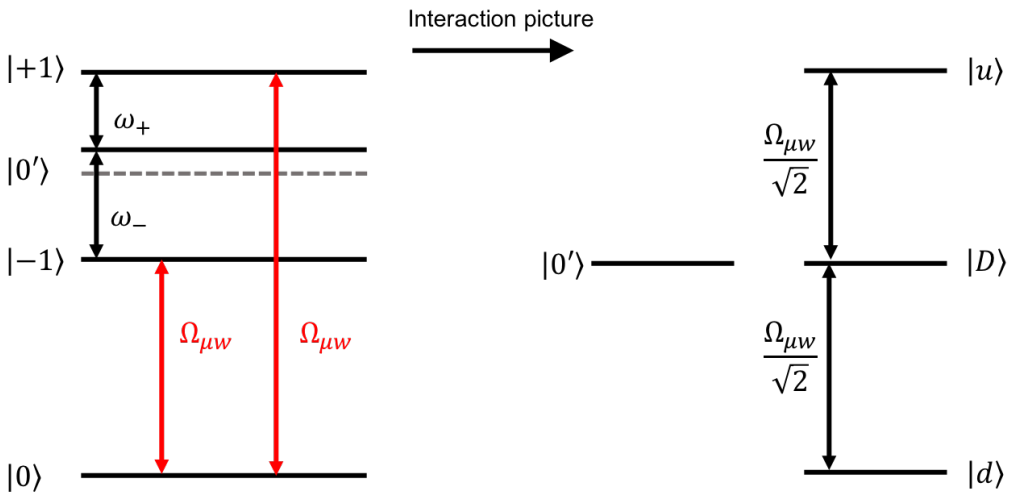

Figure 4.1: Left: Schematic of the energy levels in the $^{171}Yb^{+}$ hyperfine manifold with microwave fields (indicated by red arrows) dressing the transitions $|0\rangle \leftrightarrow |\pm 1\rangle$ with Rabi frequency $\Omega_{\mu w}$. Right: Energy states in the resultant dressed state basis, where the three dressed states $|u\rangle$, $|D\rangle$, and $|d\rangle$ are separated in energy by $\Omega_{\mu w}/\sqrt{2}$.

We can then re-express the dressing Hamiltonian $H'_{\mu w}$ in terms of these eigenstates, as

$$H'_{\mu w} = \frac{\hbar\Omega_{\mu w}}{\sqrt{2}}(|u\rangle\langle u| - |d\rangle\langle d|). \tag{4.6}$$

From this Hamiltonian, it can be seen that the energies of these three dressed states are $\epsilon_D = 0$, $\epsilon_u = \frac{\hbar\Omega_{\mu w}}{\sqrt{2}}$ and $\epsilon_d = -\frac{\hbar\Omega_{\mu w}}{\sqrt{2}}$, as shown in figure 4.1. The energies of the states $|u\rangle$ and $|d\rangle$ depend on the Rabi frequency of the microwave dressing fields $\Omega_{\mu w}$, while the energy of the state $|D\rangle$ is independent of $\Omega_{\mu w}$.

We now look at the effect of noise on this dressed state system. Noise on the magnetic field sensitive bare states can be written as

$$H_{noise} = \mu_B \Delta B(t)(|+1\rangle\langle +1| - |-1\rangle\langle -1|). \tag{4.7}$$

Qubits involving the bare states $|+1\rangle$ and $|-1\rangle$ therefore quickly dephase under the influence of this noise. Expressing this noise Hamiltonian in terms of the dressed states, we obtain

$$H_{noise} = \frac{\mu_B \Delta B(t)}{\sqrt{2}}(|u\rangle\langle D| + |d\rangle\langle D| + H.c.). \tag{4.8}$$

From this it can be seen that the effect of noise is to drive population between states $|D\rangle$, and $|u\rangle$ and $|d\rangle$. Considering noise at a frequency ω_f, so that $\Delta B(t) = B_f \cos(\omega_f t + \phi_f)$,

we can transform equation 4.8 to the interaction picture with respect to the dressing Hamiltonian equation 4.6. By making the rotating wave approximation that $\mu_B B_f/\hbar \ll \Omega_{\mu w}/\sqrt{2}$, the noise Hamiltonian becomes

$$H'_{noise} = \frac{\mu_B B_f}{2\sqrt{2}}(|u\rangle\langle D| e^{-i(\omega_f - \frac{\Omega_{\mu w}}{\sqrt{2}})t} + |d\rangle\langle D| e^{i(\omega_f - \frac{\Omega_{\mu w}}{\sqrt{2}})t} + H.c.). \tag{4.9}$$

From this Hamiltonian, it can be seen that noise at and around the dressed state splitting frequency $\Omega_{\mu w}/\sqrt{2}$ drives population between the dressed states, whereas noise at other frequencies has no effect. The effect of magnetic field noise is therefore suppressed, since only noise at this specific frequency determined by the power of the dressing microwaves has an effect. Assuming a noise spectrum of $\sim 1/f$, where the amplitude of the noise decreases with frequency, it is desirable to set higher dressing field Rabi frequencies. Since the energies of states $|u\rangle$ and $|d\rangle$ depend on this Rabi frequency, noise on $\Omega_{\mu w}$ causes dephasing of these states. However, the energy of state $|D\rangle$ is independent of this Rabi frequency, so it is well-protected against both magnetic field noise and Rabi frequency noise. We therefore pair the state $|D\rangle$ with the insensitive state $|0'\rangle$, which is not involved in the dressed state interaction, as a qubit which is well-protected against noise. In order to use the states $|u\rangle$ and $|d\rangle$, potentially to form a qutrit, it should be ensured that the Rabi frequency of the dressing fields is stabilised.

4.2.2 Manipulation of the dressed state qubit

In the original proposal for use of dressed states in $^{171}Yb^+$ by Timoney *et al.* [27], a radiofrequency field which couples all three of the $F = 1$ states was used to manipulate the dressed states. In this method, the coupling strength between the states is determined by the phase of the RF field, which places a limit on the achievable Rabi frequency, and only σ_y couplings are possible. Webster *et al.* [64] developed a method which exploited the second order Zeeman shift $\Delta\omega_z$ to allow arbitrary single qubit rotations to be performed with axes defined by the phase of the radiofrequency field. This method will be described and used in this work.

In order to manipulate the qubit, a radiofrequency field is applied near resonance with the $|0'\rangle \leftrightarrow |-1\rangle$ or the $|0'\rangle \leftrightarrow |+1\rangle$ transition. These two transitions are separated in frequency by the second order Zeeman shift, $\Delta\omega_z$. By defining δ_{rf} as the detuning from the $|0'\rangle \leftrightarrow |+1\rangle$ transition, we can write the Hamiltonian describing the radiofrequency

field's interaction with the bare states as

$$H_{\mathrm{rf}} = \frac{\hbar\Omega_{\mathrm{rf}}}{2}(|+1\rangle \langle 0'| e^{-i\delta_{\mathrm{rf}}t}e^{i\phi_{\mathrm{rf}}} + |-1\rangle \langle 0'| e^{i(\delta_{\mathrm{rf}}-\Delta\omega_z)t}e^{-i\phi_{\mathrm{rf}}} + H.c.) \tag{4.10}$$

where we have simplified the Hamiltonian by setting the dressing field phases as $\phi_+ = \phi_- = 0$. By re-expressing this in terms of the dressed states and transforming to the interaction picture with respect to the dressing Hamiltonian, equation 4.6, this becomes

$$\begin{aligned} H_{\mathrm{rf}} = \frac{\hbar\Omega_{\mathrm{rf}}}{2\sqrt{2}}[&|D\rangle \langle 0'| (e^{-i\delta_{\mathrm{rf}}t}e^{i\phi_{\mathrm{rf}}} - e^{i(\delta_{\mathrm{rf}}-\Delta\omega_z)t}e^{-i\phi_{\mathrm{rf}}}) \\ &\frac{1}{\sqrt{2}}|u\rangle \langle 0'| (e^{-i(\delta_{\mathrm{rf}}-\frac{\Omega_{\mu w}}{\sqrt{2}})t}e^{i\phi_{\mathrm{rf}}} + e^{i(\delta_{\mathrm{rf}}-\Delta\omega_z+\frac{\Omega_{\mu w}}{\sqrt{2}})t}e^{-i\phi_{\mathrm{rf}}}) \\ &\frac{1}{\sqrt{2}}|d\rangle \langle 0'| (e^{-i(\delta_{\mathrm{rf}}+\frac{\Omega_{\mu w}}{\sqrt{2}})t}e^{i\phi_{\mathrm{rf}}} + e^{i(\delta_{\mathrm{rf}}-\Delta\omega_z-\frac{\Omega_{\mu w}}{\sqrt{2}})t}e^{-i\phi_{\mathrm{rf}}}) + H.c.]. \end{aligned} \tag{4.11}$$

This corresponds to six separate transitions, two to each of the dressed states. The separation into two transitions for each dressed state is a result of the second order Zeeman shift $\Delta\omega_z$, and corresponds either to connecting to the dressed state via the $|0'\rangle \leftrightarrow |+1\rangle$ or the $|0'\rangle \leftrightarrow |-1\rangle$ transition. In order to address only one transition, it should be ensured that the Rabi frequency of the addressing radiation is much less than the frequency splittings, both the second order Zeeman shift, $\Omega_{\mathrm{rf}} \ll \Delta\omega_z$, and the dressed state splitting defined by the microwave Rabi frequency, $\Omega_{\mathrm{rf}} \ll \Omega_{\mu w}/\sqrt{2}$. In this case, all off-resonant terms can be disregarded. In order to separably address all transitions, it should also be ensured that the Rabi frequency of the dressing fields and the second order Zeeman shift do not cause overlaps in state frequencies. For example, in the case that $\Delta\omega_z \approx \Omega_{\mu w}/\sqrt{2}$, transitions to $|u\rangle$ and $|D\rangle$ are overlapped.

If we set $\delta_{\mathrm{rf}} = 0$ and assume that the Rabi frequency is low enough that all other off-resonant transitions can be ignored, the Hamiltonian becomes

$$H_{\mathrm{rf}} = \frac{\hbar\Omega_{\mathrm{rf}}}{2\sqrt{2}}(|D\rangle \langle 0'| e^{i\phi_{\mathrm{rf}}} + |0'\rangle \langle D| e^{-i\phi_{\mathrm{rf}}}). \tag{4.12}$$

The states $|0'\rangle$ and $|D\rangle$ therefore form a qubit where single qubit rotations can be performed around an arbitrary axis defined by the phase of the applied RF field, and with a Rabi frequency defined by the power of the RF field as $\Omega_D = \Omega_{\mathrm{rf}}/\sqrt{2}$. For the states $|u\rangle$ and $|d\rangle$, the Rabi frequency is $\Omega_{\mathrm{ud}} = \Omega_{\mathrm{rf}}/2$.

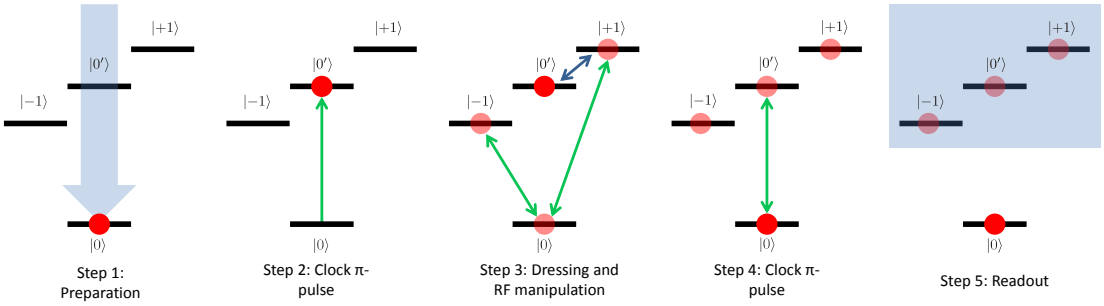

Figure 4.2: Schematic demonstrating a simple method to prepare and detect dressed states, from [65]. This method is an experimental simplification of previous methods, and uses states which are insensitive to magnetic field noise, reducing decoherence.

4.2.3 Preparation and detection

In the original proposal [27], a partial stimulated Raman adiabatic passage (STIRAP) process was used to prepare and detect the dressed state qubit. A new method was demonstrated by Randall *et al.* [65] which eliminated the need for STIRAP. The advantages of this new method are primarily the experimental simplification provided, and the use of only states which are insensitive to magnetic field noise to first order, reducing decoherence. This method is described and demonstrated here, and is the primary method used for preparation and detection of the dressed state qubit in this thesis.

The method used to prepare and detect the dressed state qubit is summarised in the schematic in figure 4.2. After an ion is prepared in state $|0\rangle$, a clock π pulse is used to transfer population to the state $|0'\rangle$. Since this is outside of the dressed state subspace, the dressing fields can be instantaneously turned on without affecting the ion population. This prepares the dressed state qubit.

In order to measure the resultant population after any manipulation of this qubit has been completed, the microwave dressing fields are instantaneously turned off and a final clock π pulse on the transition $|0'\rangle \leftrightarrow |0\rangle$ is performed. This transfers population from the qubit state $|0'\rangle$ to $|0\rangle$. Any population that was in the qubit state $|0'\rangle$ is mapped to $|0\rangle$. Any population in the dressed state manifold $\{|-1\rangle, |0\rangle, |-1\rangle\}$ will be mapped to the $F = 1$ manifold $\{|-1\rangle, |0'\rangle, |-1\rangle\}$. The normal detection method can then be used to distinguish between the $F = 0$ and $F = 1$ states, with the qubit state $|0'\rangle$ resulting in a dark measurement and the qubit state $|D\rangle$ resulting in a bright measurement. This is a simple experimental method for measuring the population within the dressed state qubit which relies on a single microwave field applied to an insensitive transition. This method can be extended to distinguish between other dressed states by using a series of pulses, as described in [65].

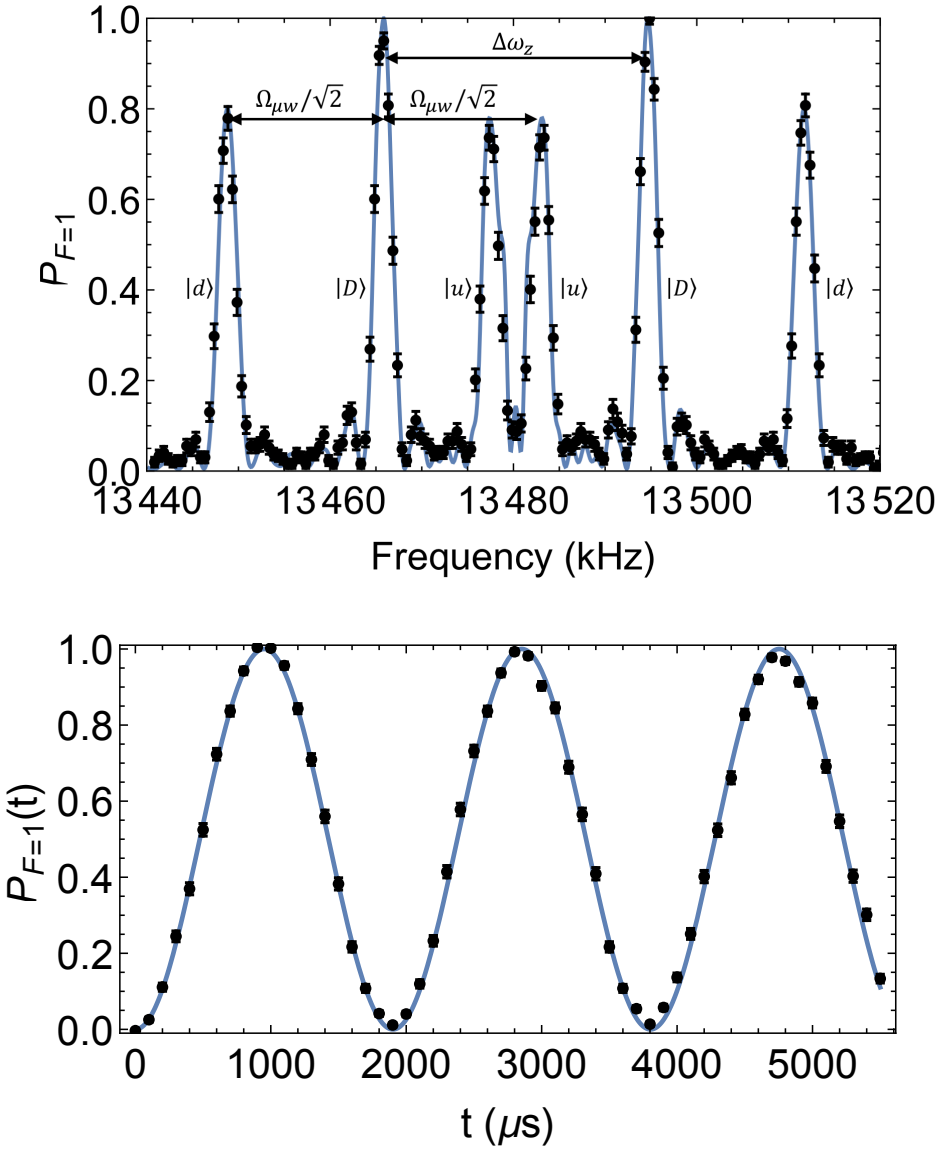

Figure 4.3: Top: Experimental preparation of all dressed states, with the dressed state corresponding to each peak and frequency separations labelled. Dressing fields of Rabi frequency $\Omega_{\mu w}/2\pi = 28.68\,\text{kHz}$ and an RF pulse of time $365\,\mu\text{s}$ with frequency around the $|0'\rangle \leftrightarrow |\pm 1\rangle$ were applied. The second order Zeeman shift was measured as $\Delta\omega_z/2\pi = 28.68\,\text{kHz}$. The theory curve is a result of a numerical simulation of the dressing and RF Hamiltonians. Bottom: Rabi oscillations on the transition $|0'\rangle \leftrightarrow |D\rangle$, via the state $|+1\rangle$. The fit of the theory curve gives a Rabi frequency of $\Omega_D/2\pi = 0.5258(4)\,\text{kHz}$. Data and fits reproduced with permission from [53].

This method of preparation and manipulation of the dressed state qubit has been demonstrated experimentally, as shown in figure 4.3. A single ion is used where the second order Zeeman shift is measured to be $\Delta\omega_z/2\pi = 28.68\,\text{kHz}$. The ion was prepared in state $|0\rangle$ and a single π pulse was used to transfer population to $|0'\rangle$. The dressing fields were turned on with a measured Rabi frequency of $\Omega_{\mu w}/2\pi = 28.68\,\text{kHz}$. An RF field was applied with frequency around $|0\rangle \leftrightarrow |\pm 1\rangle$, for the experimentally measured time of a π pulse on the transition $|0'\rangle \leftrightarrow |D\rangle$, $365\,\mu\text{s}$. This accounts for the lower peak heights for states $|u\rangle$ and $|d\rangle$, since the Rabi frequency is different so this time does not correspond to a full π pulse. After this RF pulse, the dressing fields were turned off and a final π pulse on the transition $|0\rangle \leftrightarrow |0'\rangle$ was performed. By repeating the experiment while scanning the applied RF field frequency, the population spectrum can be measured, as shown in figure 4.3. Six distinguishable peaks can clearly be seen, with frequency separations labelled for clarity. A Rabi flop on the transition $|0'\rangle \leftrightarrow |D\rangle$ is also shown. The frequency of the RF radiation was set to the measured value for the $|0'\rangle \leftrightarrow |D\rangle$ transition via the $|+1\rangle$ state. The time of the pulse was increased for each experimental step, and the result is shown in figure 4.3, where a theory curve has been fitted giving a Rabi frequency of $\Omega_D/2\pi = 0.5258(4)\,\text{kHz}$. No decay is seen over this time period, in marked contrast with the flop on $|0\rangle \leftrightarrow |+1\rangle$ shown in section 3.5.2.

The method described above is a simple and fast method to map populations from the dressed state qubit to the bare states which does not require the use of magnetic field sensitive states with short coherence times. However, it cannot be used when mapping of both the population and phase of the dressed state qubit is required. This may be necessary, for example, for information storage in an insensitive qubit during ion shuttling. Methods for high fidelity mapping have been developed by Randall *et al.* [66], and one such method will be described and demonstrated in chapter 7.

4.2.4 T_1 and T_2 measurements

To demonstrate the increased robustness to the adverse effects from magnetic field noise of the dressed states, a lifetime (T_1) and coherence time (T_2) measurement are performed. The lifetime is a measure of the rate at which population leaks from the measured state to other states in the qubit, while the decoherence time is a measure of the rate of loss of coherence in a qubit. Magnetic field noise around the dressed state separation frequency $\Omega_{\mu w}/\sqrt{2}$ causes population transfer between the dressed states, which limits the lifetime. The coherence time can be limited by noise on the Rabi frequency and the detuning of the

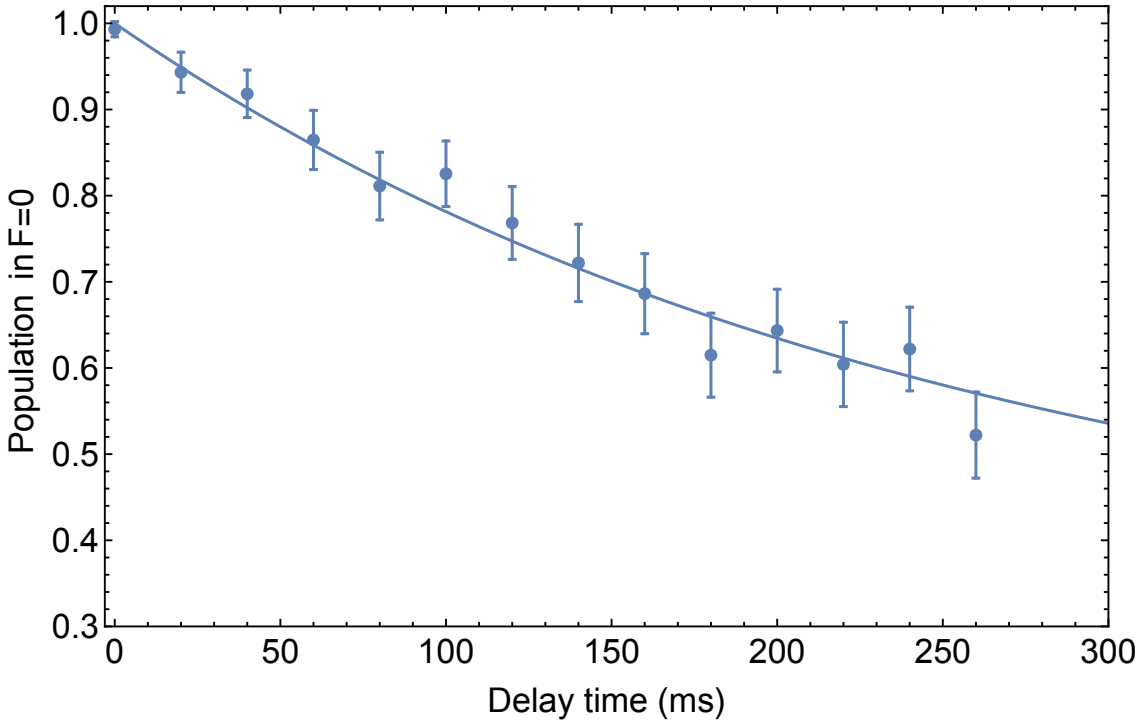

Figure 4.4: Lifetime measurement for the state $|D\rangle$. A π pulse on the transition $|0'\rangle \leftrightarrow |D\rangle$ is followed by a variable length delay and a final π pulse to transfer population back to $|0'\rangle$. Using the detection method, the population should therefore be measured in $F = 0$, but depolarising from the state $|D\rangle$ to other states during the delay time reduces this probability. An exponential fit decaying to 1/3 gives a lifetime $T_1 = 0.25(1)\,\mathrm{s}$.

dressing fields, as well as the second order sensitivity to magnetic field noise of the state $|0'\rangle$ and imperfectly set parameters, as discussed in the next section.

In order to measure the lifetime, the state $|D\rangle$ is prepared as in the previous section, using a π pulse on the state $|0'\rangle$. A variable delay time is then introduced, during which the dressing fields remain constant, followed by a final π pulse to transfer population back to $|0'\rangle$. The qubit is then measured using the method demonstrated in the previous section. By stepping the delay time, a decay is observed in the population measured in $F = 0$ due to population transfer between the dressed states caused by noise at the splitting frequency, $\Omega_{\mu w}/\sqrt{2}$. This is experimentally demonstrated in figure 4.4, where a π pulse of time $945\,\mu\mathrm{s}$ was used and a delay of up to 260 ms performed, with dressing field Rabi frequencies of approximately $\Omega_{\mu w} = 17\,\mathrm{kHz}$. There are three dressed states, so an exponential decay to 1/3 is fitted to the measurements, giving a lifetime of $T_1 = 0.25(1)\,\mathrm{s}$.

A Ramsey measurement is used to determine the coherence time. Once the qubit is prepared in $|0'\rangle$, the dressing fields are turned on and a $\pi/2$ pulse is performed to transfer half of the population to $|D\rangle$, so that a superposition $\frac{1}{\sqrt{2}}(|0'\rangle + e^{i\phi}|D\rangle)$ is prepared. A delay is then introduced, during which the dressing fields remain on. Halfway through

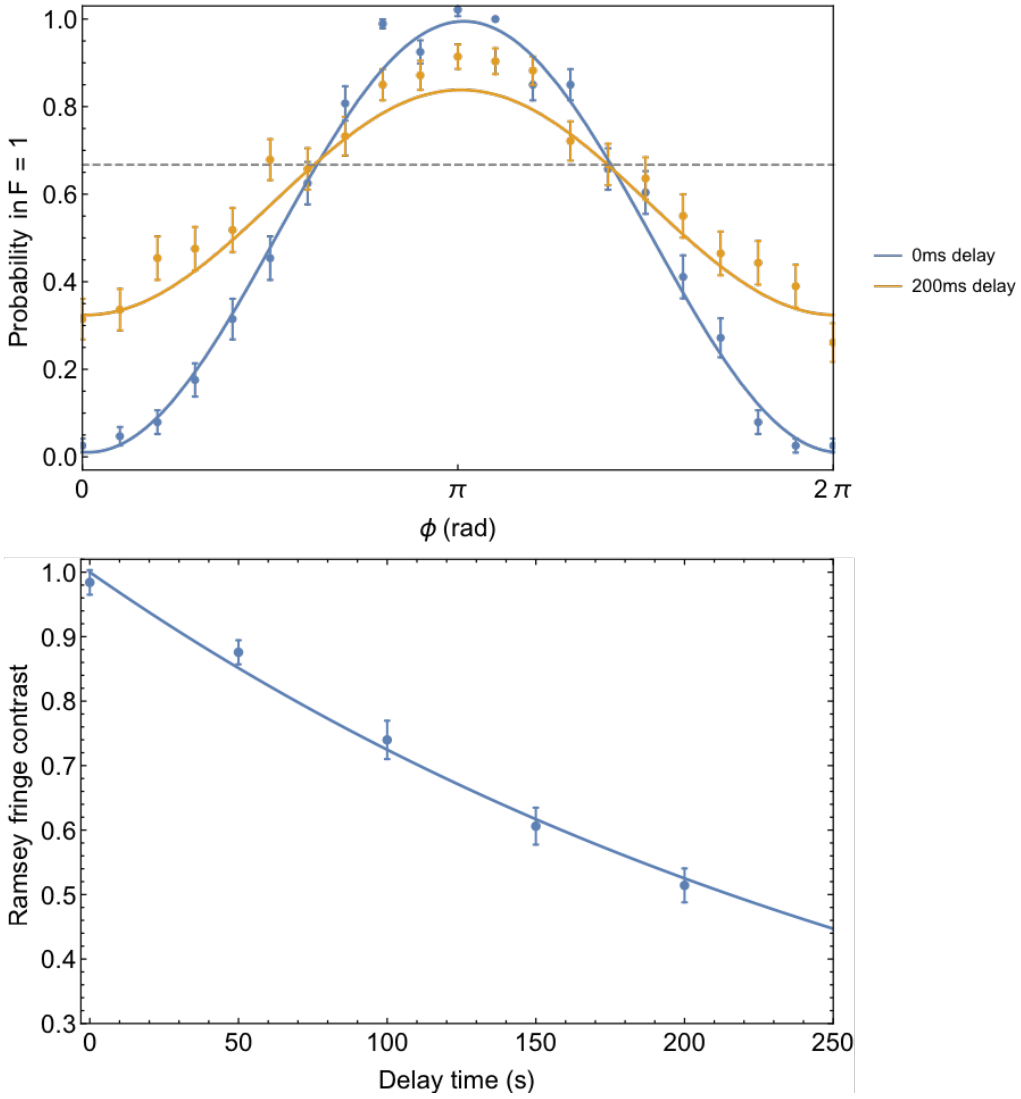

Figure 4.5: Top: Ramsey measurements on the dressed state qubit $|0'\rangle \leftrightarrow |D\rangle$ for delay times 0 ms and 200 ms. A $\pi/2$ pulse is applied on the qubit transition with phase $\phi = 0$, followed by a delay and a final $\pi/2$ pulse with phase ϕ. A spin echo pulse is applied halfway through the delay time. Decoherence during the delay reduces the amplitude of the resultant fringe, as can be clearly seen for the two delay times shown above. The amplitude decays to 2/3, shown by the dashed grey line. Bottom: Fitted Ramsey fringe amplitudes for different delay times. A fit of an exponential decay gives a coherence time of $T_2 = 0.31(1)$ s.

the delay, a spin echo pulse is performed, which consists of a π pulse with fixed phase on the transition $|0'\rangle \leftrightarrow |D\rangle$. After the delay is complete, a second $\pi/2$ pulse on the qubit transition is performed, the phase of which is stepped relative to the initial $\pi/2$ pulse. This results in a sinusoidal fringe, which for a 'perfect' Ramsey measurement with no dephasing has an amplitude of one. However, the effect of dephasing during the delay is to reduce this amplitude. The spin echo pulse removes the effect of slow drifts, so this observed decay in amplitude is due to noise faster than half of the delay time. The fitted fringes for delay times 0 ms and 200 ms are shown in figure 4.5, where a $\pi/2$ pulse of time 473 μs was used with dressing field Rabi frequencies of approximately 17 kHz. Since depolarising is also occurring during this time, the probability measured in the $F = 1$ manifold decays exponentially to approximately 2/3. The amplitude fits of Ramsey fringes with multiple delay times is also shown in figure 4.5. A fit of an exponential decay function gives a coherence time of $T_2 = 0.31(1)$ s. This is almost two orders of magnitude higher than the decoherence time of 6.4(6) ms on the magnetic field sensitive state $|0\rangle \leftrightarrow |+1\rangle$ shown in chapter 3. Since the decoherence time is approximately the same as the T_1 time, it is likely that depolarising is the dominant and therefore limiting process.

Both of these results are lower than the previously measured value of $T_1 \approx T_2 \approx 0.65$ s [53]. Further investigation is required to determine the cause of this decrease, which could be a result of higher levels of noise on the DC electrodes from an alteration in the filtering setup. Due to this variation, the lifetime and decoherence time for each experiment in subsequent chapters will be stated.

4.2.5 Decoherence of the dressed state qubit

When parameters are correctly set, dressed states protect well against magnetic field noise, as shown in section 4.2.1. However, if parameters are incorrect, the sensitivity to noise begins to increase, which will cause dephasing of superpositions of the qubit and decrease the T_2 time. In particular, if the Rabi frequencies of the dressing fields are mismatched, so that $\Omega_+ \neq \Omega_-$, a considerable increase in sensitivity to noise is seen. If the dressing Rabi frequencies are mismatched but the detunings are correct so that $\delta_+ = \delta_- = 0$, the dressing Hamiltonian from equation 4.3 can be simplified to

$$H_{\mu w} = \frac{\hbar}{2}(\Omega_+ |0\rangle \langle +1| + \Omega_- |0\rangle \langle -1| + \Omega_+ |+1\rangle \langle 0| + \Omega_- |-1\rangle \langle 0|). \tag{4.13}$$

The eigenstates of this Hamiltonian are then

$$\begin{aligned}
|D\rangle &= \frac{1}{\sqrt{\Omega_+^2+\Omega_-^2}}(\Omega_- |+1\rangle - \Omega_+ |-1\rangle) \\
|u\rangle &= \frac{1}{\sqrt{2}}\left(\frac{\Omega_+}{\sqrt{\Omega_+^2+\Omega_-^2}}|+1\rangle + \frac{\Omega_-}{\sqrt{\Omega_+^2+\Omega_-^2}}|-1\rangle + |0\rangle\right) \\
|d\rangle &= \frac{1}{\sqrt{2}}\left(\frac{\Omega_+}{\sqrt{\Omega_+^2+\Omega_-^2}}|+1\rangle + \frac{\Omega_-}{\sqrt{\Omega_+^2+\Omega_-^2}}|-1\rangle - |0\rangle\right),
\end{aligned} \tag{4.14}$$

which reduce to the eigenstates in equation 4.5 for the case where $\Omega_+ = \Omega_- = \Omega_{\mu w}$. The energy for the eigenstate $|D\rangle$ remains at the same value as the $|0'\rangle$ energy, but energies for the eigenstates $|u\rangle$ and $|d\rangle$ are $\pm\frac{\hbar}{2}\sqrt{\Omega_+^2+\Omega_-^2}$. By re-expressing the noise Hamiltonian in equation 4.7 as a function of these eigenstates, we can understand the effect of noise in this case. The noise Hamiltonian becomes

$$\begin{aligned}
H_{\text{noise}} = \frac{\mu_B \Delta B(t)}{\sqrt{2}}\Bigg[&\frac{2\Omega_+\Omega_-}{\Omega_+^2+\Omega_-^2}(|u\rangle\langle D| + |d\rangle\langle D| + |D\rangle\langle u| + |D\rangle\langle d|) \\
&+\frac{\Omega_+^2-\Omega_-^2}{\sqrt{2}(\Omega_+^2+\Omega_-^2)}(|u\rangle\langle u| + |d\rangle\langle d| + |u\rangle\langle d| + |d\rangle\langle u| - 2|D\rangle\langle D|)\Bigg].
\end{aligned} \tag{4.15}$$

If Rabi frequencies are matched, the effect of the noise is therefore to drive transitions between the dressed states as before, so that only noise resonant with this frequency splitting has an effect. However, in the case of a mismatch, there is a term $|D\rangle\langle D|$ which is dependent on the magnitude of this mismatch. The energy shift for the bare states resulting from a change in magnetic field can be calculated as $|\langle \pm 1| H_{\text{noise}} |\pm 1\rangle| = \mu_B \Delta B(t)$, which is the sensitivity to noise. We can define a fractional sensitivity for the dressed states with mismatched Rabi frequencies compared to the bare states as

$$\frac{|\langle D| H_{\text{noise}} |D\rangle|}{|\langle \pm 1| H_{\text{noise}} |\pm 1\rangle|} = \frac{|\Omega_+^2 - \Omega_-^2|}{|\Omega_+^2 + \Omega_-^2|}. \tag{4.16}$$

By defining the average dressing field Rabi frequency as $\Omega_{\mu w} = (\Omega_+ + \Omega_-)/2$ and the difference as $\Delta\Omega_{\mu w} = \Omega_+ - \Omega_-$, this fractional sensitivity can be expressed in the limit of small mismatches as $|\Delta\Omega_{\mu w}|/\Omega_{\mu w}$. We therefore see a linear increase in sensitivity with the proportional mis-set of the dressing fields. Similarly, the states $|u\rangle$ and $|d\rangle$ become sensitive to magnetic field noise, but the sensitivity is a factor of two less than for the state $|D\rangle$.

In order to ensure that the dressing field powers are matched to a high degree of

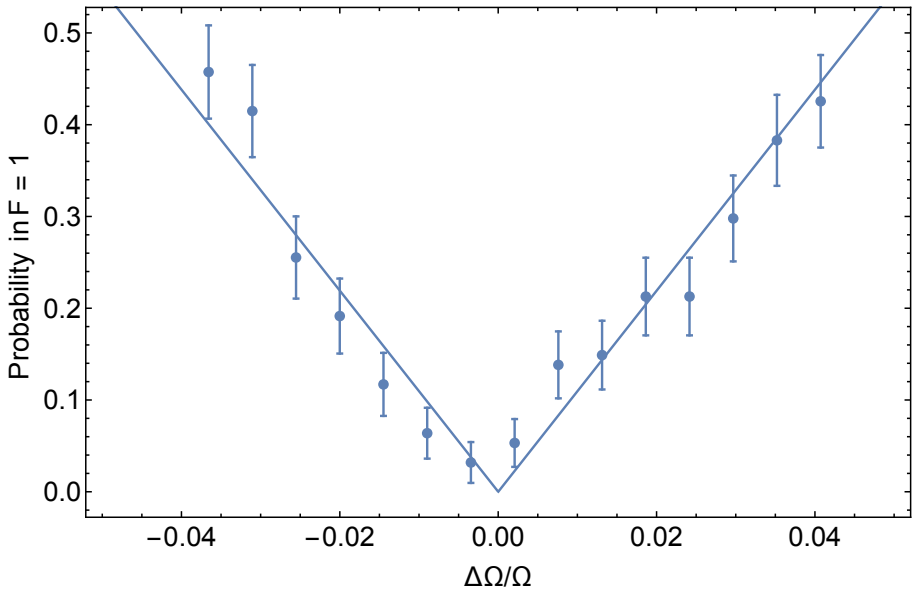

Figure 4.6: Results of an experiment to finely match dressing field powers to ensure minimum sensitivity to magnetic field noise. A Ramsey measurement with a fixed delay time of 50 ms and fixed phase on both $\pi/2$ pulses of $\phi = 0$ is applied (with a spin echo pulse halfway through the delay), which should result in a measurement of $F = 0$. The power of the $|0\rangle \leftrightarrow |-1\rangle$ dressing field is scanned relative to the power of the $|0\rangle \leftrightarrow |+1\rangle$ dressing field. When the Rabi frequencies are mismatched, sensitivity to magnetic field noise increases, so the probability of measuring $F = 1$ also increases due to decoherence during the delay. A linear fit to $|\Delta\Omega_{\mu w}|/\Omega_{\mu w}$ enables the matched dressing field powers to be found, with an error of approximately 0.1% in fractional power.

accuracy to avoid decoherence resulting from magnetic field noise, an experimental method using a Ramsey experiment is used to calibrate them. After preparing an ion in state $|0'\rangle$, a $\pi/2$ pulse on the transition $|0'\rangle \leftrightarrow |D\rangle$ is performed. A 50 ms delay is then implemented, with the dressing fields remaining on. Halfway through this delay, a π spin echo pulse on the transition $|0'\rangle \leftrightarrow |D\rangle$ is performed to eradicate the effect of slow frequency noise. Finally, a $\pi/2$ pulse with the same phase as the initial $\pi/2$ pulse is performed. In the case of no decoherence, the measurement should yield a result where all population is in the $|0'\rangle$ state, so that $F = 0$ is measured. However, in the presence of decoherence the probability of measuring $F = 1$ increases. By stepping the power of one dressing field relative to the other, a minimum in the measurement should be observed, corresponding to where the powers are well matched and there is therefore little decoherence. This type of experiment is demonstrated in figure 4.6, where the probability $P(F = 1)$ is plotted against the fractional Rabi frequency error $|\Delta\Omega_{\mu w}|/\Omega_{\mu w}$, with $\Omega_{\mu w} \approx 17\,\text{kHz}$. A linear fit to this data allows the optimal power to be found, with an error of approximately 0.1% in the fractional detuning. Over the course of a day, dressing field Rabi frequencies have been measured to change by up to 1%, leading to a 1% sensitivity compared to the bare states. These Rabi frequencies are therefore generally calibrated up to twice a day.

The detunings of the dressing fields can also be incorrect, but numerical simulations have shown that this effect is smaller than for a dressing field Rabi frequency mis-set. For the case where the detuning is equal for the two dressing fields, or equal and opposite, there is no change in sensitivity of $|D\rangle$. There is a quadratic dependence on the proportional detuning $(|\delta|/\Omega_{\mu w})^2$ for a detuning on only one dressing field [53]. As discussed in section 3.5.2, the experimental method used to stabilise the magnetic field keeps the sensitive transitions to within approximately 1 kHz, and repeated measurements of the $|0\rangle \leftrightarrow |+1\rangle$ transition frequency over the course of several hours have confirmed this. A change of 1 kHz would lead to a fractional sensitivity of 0.25% compared to the bare states, assuming typical dressing field Rabi frequencies of 20 kHz. An additional feature of the qubit is that it is insensitive to first order to drifts in the absolute magnetic field. This type of drift would cause the detuning of the dressing fields to be equal and opposite, so that $\delta_+ = -\delta_- = \delta$. In such a system, the detuning of the transition $|0'\rangle \leftrightarrow |D\rangle$ from the transition frequency $|0'\rangle \leftrightarrow |+1\rangle$ is equal to δ, which is equivalent to the original RF frequency. We therefore find that the RF field is still resonant with $|0'\rangle \leftrightarrow |D\rangle$, although there is a small reduction in the Rabi frequency of this applied RF field.

Decoherence of the qubit $\{|0'\rangle, |D\rangle\}$ can also occur due to the second order sensitivity

of the $|0'\rangle$ state to magnetic field noise. The Hamiltonian for noise on the state $|0'\rangle$ can be written approximately as

$$H_{\text{noise}} = \frac{4\mu_B^2}{\hbar\omega_{\text{hf}}} B_0 \Delta B(t) \left|0'\right\rangle \left\langle 0'\right| \tag{4.17}$$

where B_0 is the offset magnetic field applied to the ion. The fractional sensitivity with respect to the bare states can be written as

$$\frac{|\left\langle 0'\right| H_{\text{noise}} \left|0'\right\rangle|}{|\left\langle \pm 1\right| H_{\text{noise}} \left|\pm 1\right\rangle|} = \frac{4\mu_B B_0}{\hbar\omega_{\text{hf}}} \tag{4.18}$$

which, for a typical offset magnetic field of 10 G, is equal to approximately 2×10^{-4}. Dephasing due to the second order sensitivity of $|0'\rangle$ is therefore a small effect at the magnetic fields used in this experimental setup.

4.2.6 Multi-qubit dressed state operations

The dressed state transition frequency is determined by the transition frequency of $|0'\rangle \leftrightarrow |\pm 1\rangle$, and is therefore magnetic field dependent to first order. In a static magnetic field gradient, the transition frequency becomes position dependent, and so dressed states can be used for multi-qubit operations using long-wavelength radiation, as described in 2.4.2. The Hamiltonian describing a four level system corresponding to the hyperfine ground state of $^{171}\text{Yb}^+$ in a magnetic field gradient is

$$\begin{aligned} H_0 &= H_B + H_m \\ H_B &= \hbar\omega_+ \left|+1\right\rangle \left\langle +1\right| - \hbar\omega_- \left|-1\right\rangle \left\langle -1\right| - \hbar\omega_0 \left|0\right\rangle \left\langle 0\right| \\ H_m &= \hbar\nu_z \eta \sigma_z (a + a^\dagger) + \hbar\nu_z a^\dagger a \end{aligned} \tag{4.19}$$

where we have defined the zero energy as the energy of the state $|0'\rangle$, and σ_z is the Pauli matrix, $\sigma_z = \left|+1\right\rangle \left\langle +1\right| - \left|-1\right\rangle \left\langle -1\right|$. The effect of the magnetic field gradient is to displace the harmonic oscillator for the states $|+1\rangle$ and $|-1\rangle$ in opposite directions, with polaron states

$$\begin{aligned} \left|0_p\right\rangle \left|n_p\right\rangle &= \left|0\right\rangle \left|n\right\rangle \\ \left|0'_p\right\rangle \left|n_p\right\rangle &= \left|0'\right\rangle \left|n\right\rangle \\ \left|+1_p\right\rangle \left|n_p\right\rangle &= e^{-\eta(a^\dagger - a)} \left|+1\right\rangle \left|n\right\rangle \\ \left|-1_p\right\rangle \left|n_p\right\rangle &= e^{\eta(a^\dagger - a)} \left|-1\right\rangle \left|n\right\rangle . \end{aligned} \tag{4.20}$$

The corresponding polaron ladder operators are given by $a_p^{(\dagger)} = a^{(\dagger)} + \eta\sigma_z$. Dressed states in a magnetic field gradient can then be described in the same way as in the absence of a gradient, except using these polaron spin and motional states.

Using these definitions, the Hamiltonian for an RF field in the interaction picture with respect to H_0 can be written in the polaron basis as

$$H'_{\mathrm{rf}} = \frac{\hbar\Omega_{\mathrm{rf}}}{2}\left(|+1_p\rangle\langle 0'_p| e^{-i\delta_{\mathrm{rf}}t}e^{i\phi_{\mathrm{rf}}}e^{\eta(\tilde{a}_p^\dagger - \tilde{a}_p)} + |-1_p\rangle\langle 0'_p| e^{i(\delta_{\mathrm{rf}}+\Delta\omega_z)t}e^{-i\phi_{\mathrm{rf}}}e^{-\eta(\tilde{a}_p^\dagger - \tilde{a}_p)} + H.c.\right) \tag{4.21}$$

where we have defined $\tilde{a}_p = a_p e^{-i\nu_z t}$. This can be written in the dressed basis, similarly to section 4.2.2, after the polaron transformation as

$$\begin{aligned} H_{\mathrm{rf}} = \frac{\hbar\Omega_{\mathrm{rf}}}{2\sqrt{2}}\Big(& |D\rangle\langle 0'| \left(e^{-i\delta_{\mathrm{rf}}t}e^{i\phi_{\mathrm{rf}}}e^{\eta(\tilde{a}_p^\dagger - \tilde{a}_p)} - e^{i(\delta_{\mathrm{rf}}-\Delta\omega_z)t}e^{-i\phi_{\mathrm{rf}}}e^{-\eta(\tilde{a}_p^\dagger - \tilde{a}_p)}\right) \\ & \frac{1}{\sqrt{2}}|u\rangle\langle 0'| \left(e^{-i(\delta_{\mathrm{rf}}-\frac{\Omega_{\mu w}}{\sqrt{2}})t}e^{i\phi_{\mathrm{rf}}}e^{\eta(\tilde{a}_p^\dagger - \tilde{a}_p)} + e^{i(\delta_{\mathrm{rf}}-\Delta\omega_z+\frac{\Omega_{\mu w}}{\sqrt{2}})t}e^{-i\phi_{\mathrm{rf}}}e^{-\eta(\tilde{a}_p^\dagger - \tilde{a}_p)}\right) \\ & \frac{1}{\sqrt{2}}|d\rangle\langle 0'| \left(e^{-i(\delta_{\mathrm{rf}}+\frac{\Omega_{\mu w}}{\sqrt{2}})t}e^{i\phi_{\mathrm{rf}}}e^{\eta(\tilde{a}_p^\dagger - \tilde{a}_p)} + e^{i(\delta_{\mathrm{rf}}-\Delta\omega_z-\frac{\Omega_{\mu w}}{\sqrt{2}})t}e^{-i\phi_{\mathrm{rf}}}e^{-\eta(\tilde{a}_p^\dagger - \tilde{a}_p)}\right) + H.c.\Big). \end{aligned} \tag{4.22}$$

The zeroth order term is the Hamiltonian for transitions on the carrier dressed states, and is identical to equation 4.11. The first order terms are the terms for the red and blue sidebands, given by

$$\begin{aligned} H^r_{\mathrm{rf}} = -\frac{\hbar\eta\Omega_{\mathrm{rf}}}{2\sqrt{2}}\Big(& |D\rangle\langle 0'| \left(e^{-i\delta_{\mathrm{r}}t}e^{i\phi_{\mathrm{rf}}}a - e^{i(\delta_{\mathrm{r}}-\Delta\omega_z)t}e^{-i\phi_{\mathrm{rf}}}a^\dagger\right) \\ & \frac{1}{\sqrt{2}}|u\rangle\langle 0'| \left(e^{-i(\delta_{\mathrm{r}}-\frac{\Omega_{\mu w}}{\sqrt{2}})t}e^{i\phi_{\mathrm{rf}}}a + e^{i(\delta_{\mathrm{r}}-\Delta\omega_z+\frac{\Omega_{\mu w}}{\sqrt{2}})t}e^{-i\phi_{\mathrm{rf}}}a^\dagger\right) \\ & \frac{1}{\sqrt{2}}|d\rangle\langle 0'| \left(e^{-i(\delta_{\mathrm{r}}+\frac{\Omega_{\mu w}}{\sqrt{2}})t}e^{i\phi_{\mathrm{rf}}}a + e^{i(\delta_{\mathrm{r}}-\Delta\omega_z-\frac{\Omega_{\mu w}}{\sqrt{2}})t}e^{-i\phi_{\mathrm{rf}}}a^\dagger\right) + H.c.\Big) \end{aligned} \tag{4.23}$$

and

$$\begin{aligned} H^b_{\mathrm{rf}} = \frac{\hbar\eta\Omega_{\mathrm{rf}}}{2\sqrt{2}}\Big(& |D\rangle\langle 0'| \left(e^{-i\delta_{\mathrm{b}}t}e^{i\phi_{\mathrm{rf}}}a^\dagger - e^{i(\delta_{\mathrm{b}}-\Delta\omega_z)t}e^{-i\phi_{\mathrm{rf}}}a\right) \\ & \frac{1}{\sqrt{2}}|u\rangle\langle 0'| \left(e^{-i(\delta_{\mathrm{b}}-\frac{\Omega_{\mu w}}{\sqrt{2}})t}e^{i\phi_{\mathrm{rf}}}a^\dagger + e^{i(\delta_{\mathrm{b}}-\Delta\omega_z+\frac{\Omega_{\mu w}}{\sqrt{2}})t}e^{-i\phi_{\mathrm{rf}}}a\right) \\ & \frac{1}{\sqrt{2}}|d\rangle\langle 0'| \left(e^{-i(\delta_{\mathrm{b}}+\frac{\Omega_{\mu w}}{\sqrt{2}})t}e^{i\phi_{\mathrm{rf}}}a^\dagger + e^{i(\delta_{\mathrm{b}}-\Delta\omega_z-\frac{\Omega_{\mu w}}{\sqrt{2}})t}e^{-i\phi_{\mathrm{rf}}}a\right) + H.c.\Big). \end{aligned} \tag{4.24}$$

There are therefore six red and six blue sidebands, corresponding to the sidebands for the six transitions shown in figure 4.3. Due to the energy ordering of the states, the red sideband for the dressed state transitions via $|0'\rangle \leftrightarrow |-1\rangle$ involves the addition of a phonon to the motional state, rather than the removal of a phonon. Likewise, for the blue sideband

these transitions correspond to a removal rather than an addition of a phonon.

The presence of these sidebands for dressed states in a magnetic field gradient shows that dressed states are suitable for implementing multi-qubit quantum logic using long-wavelength radiation, by providing a long coherence time as well as allowing spin-motion coupling. As in the case of bare states, ions can be individually addressed in frequency space due to the position dependence of the frequency of the transition $|0'\rangle \leftrightarrow |\pm 1\rangle$ in a magnetic field gradient.

4.3 Sideband cooling

In section 2.3.2, the limits of Doppler cooling were discussed. In order to reach ion temperatures below this limit, a sideband cooling process can be used, which involves reducing the motional state of an ion by making transitions on the red sideband. Low ion temperatures are useful for multi-qubit operations as described in the following chapter since, although the operation does not depend on the initial ion temperature, the sensitivity to incorrectly set parameters greatly increases with higher ion temperatures. This sideband cooling technique has been used to cool an ion to the ground state of vibration with probability up to 99.9% [67]. Sideband cooling can be achieved with long-wavelength radiation [44] using either bare states or dressed states, as discussed in the next section. The method of sideband thermometry to measure the mean motional mode of the ion is then demonstrated. This method requires the long coherence time provided by dressed states to accurately measure the temperature, and can also be used to measure heating rates.

4.3.1 Sideband cooling process

As has been demonstrated, using long-wavelength radiation coupled with a magnetic field gradient, it is possible to couple the spin and motional states of an ion, and spectrally resolve the sidebands. This makes it possible to implement sideband cooling, which involves two processes. First, a spectrally resolvable red sideband is driven to transfer population from the motional state $|n\rangle$ to state $|n-1\rangle$. Second, a fast dissipative 'repump' process is required to transfer the spin state back to the original without affecting the motional state.

The first of these steps can be implemented on the red sideband of a bare state, for example $|0\rangle \leftrightarrow |+1\rangle$, or of a dressed state, $|0'\rangle \leftrightarrow |D\rangle$. Using bare states is experimentally simpler, but there is a limit to achievable temperatures due to the short decoherence time, which reduces the effectiveness of transferring population for each sideband cooling

pulse. Using the dressed state $|0'\rangle \leftrightarrow |D\rangle$ provides the possibility of achieving lower ion temperatures, but requires more RF and microwave fields and pulses.

In either case, the pulse times are generated using Python code (written by Andrea Rodriguez) which calculates the transition time for $|n\rangle \rightarrow |n-1\rangle$ for consecutive decreasing values of n from $n_{\max}$ to $n = 1$. The number of pulses determines the value $n_{\max}$ from which these transition times start. For each value of n, the transition time is $t_n = \pi/\sqrt{n}\eta\Omega_0$, where Ω_0 is the carrier transition Rabi frequency.

The repump is performed using the same optical pumping process used to prepare the ion in state $|0\rangle$. The 369 nm laser with modulation of approximately 2 GHz is applied to the ion for 6 μs. This is resonant with the transition $^2S_{1/2}, F = 1 \rightarrow^2 P_{1/2}, F = 1$, from where it can decay to $^2S_{1/2}, F = 0$, which is the desired spin state. Since the population can also decay to $^2S_{1/2}, F = 1$, there is some photon scatter before the desired spin state is reached. This photon scatter imparts recoil energy to the ion, which effectively heats the ion and places a limit on the achievable ground state occupation. For 6 μs of radiation, this scatter is found to be on average 3 photons using the rate equations (code written by Dr Simon Webster), which corresponds to an increase in mean motional mode number of $\Delta n_{\text{recoil}} \approx 0.006$.

When using dressed states for cooling, additional steps are required in the repump process. After each pulse on the red sideband, the dressing fields are turned off and a pulse on the transition $|0'\rangle \leftrightarrow |0\rangle$ is performed, to transfer the population in $|D\rangle$ into the $F = 1$ subspace. This ensures that the repump process is only applied to the population which made a spin state transition, thereby limiting photon scatter. After the repump, another clock π pulse is performed on $|0'\rangle \leftrightarrow |0\rangle$ and the dressing fields are turned on again for the next red sideband pulse. This additional complexity increases the repump time by twice the time required for a clock π pulse.

4.3.2 Measuring temperature

A method for measuring the temperature after Doppler cooling was discussed in section 3.5.5. However, this method assumed a high value of $\bar{n}$, so that $\Omega_{n,n+1} \approx \Omega_{n,n-1}$, where the sideband Rabi frequencies are given by $\Omega_{n,n+1} = \sqrt{n+1}\eta\Omega_0$ and $\Omega_{n,n-1} = \sqrt{n}\eta\Omega_0$. For ion temperatures with $\bar{n} < 1$, sideband thermometry is a more accurate method for measuring the temperature. As before, we assume a thermal state occupation of the ion

motional modes, with the probability for occupying each state $|n\rangle$ given by

$$p_n = \frac{1}{\bar{n}+1}\left(\frac{\bar{n}}{\bar{n}+1}\right)^n. \tag{4.25}$$

Assuming a resonant interaction, so that $\delta_r = \delta_b = 0$, the probability to make a transition on each sideband is then given by

$$\begin{aligned} P^{\uparrow}_{rsb}(t) &= \sum_{n=0}^{\infty} p_n P^{\uparrow}_{n,n-1}(t) \\ P^{\uparrow}_{bsb}(t) &= \sum_{n=0}^{\infty} p_n P^{\uparrow}_{n,n+1}(t) \end{aligned} \tag{4.26}$$

where the transition probability for each value of n is given by

$$\begin{aligned} P^{\uparrow}_{n,n-1}(t) &= \frac{1}{2}(1-\cos(\Omega_{n,n-1}t)) \\ P^{\uparrow}_{n,n+1}(t) &= \frac{1}{2}(1-\cos(\Omega_{n,n+1}t)). \end{aligned} \tag{4.27}$$

Using these transition probabilities and occupation probabilities, it can be shown [13] that

$$P^{\uparrow}_{rsb}(t) = \frac{\bar{n}}{\bar{n}+1}P^{\uparrow}_{bsb}(t). \tag{4.28}$$

By defining the ratio between the two sidebands amplitudes as $R = P^{\uparrow}_{rsb}(t)/P^{\uparrow}_{bsb}(t)$, we can therefore calculate the mean motional state as

$$\bar{n} = \frac{R}{1-R}. \tag{4.29}$$

By applying a pulse of radiation resonantly to each sideband that maximises the sideband height, the mean occupational number can therefore be measured. This measurement should be performed in the dressed state qubit, since the long coherence time means that the sideband heights can be more accurately measured.

An experiment of this type is shown in figure 4.7, where both sideband cooling and spectroscopy was performed on the dressed state $|0\rangle \leftrightarrow |D\rangle$. Dressing fields of Rabi frequency $\Omega_{\mu w}/2\pi = 32\,\text{kHz}$ were applied to each ion, and the axial trap frequency was measured to be $\nu_z/2\pi = 426.7(1)\,\text{kHz}$. The temperature after 4 ms of Doppler cooling was measured as $\bar{n} = 65(5)$, after which 500 sideband pulses were applied, with time totalling 71 ms. The carrier Rabi frequency was measured as $\Omega_D/2\pi = 61.2\,\text{kHz}$ by applying an RF pulse with equal and opposite detunings to the transitions $|0'\rangle \leftrightarrow |\pm 1\rangle$. Since $\Omega_{\mu w} \gg \Delta\omega_z$,

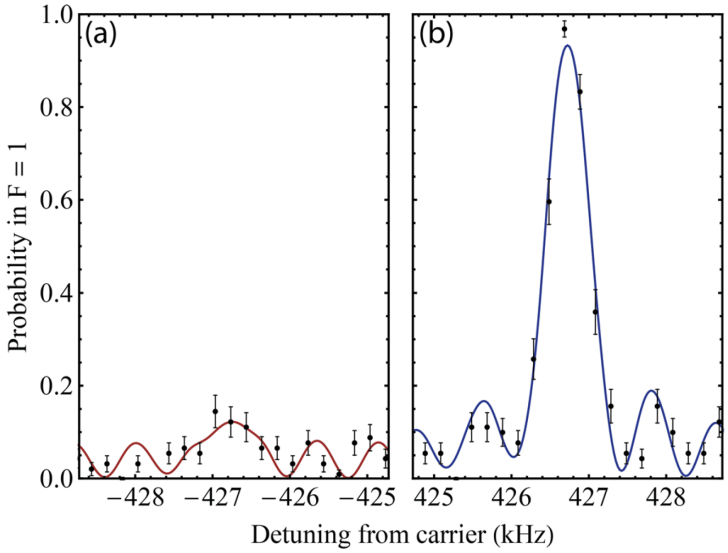

Figure 4.7: Sideband scans on the red and blue sideband of the dressed state $|D\rangle$, using an RF pulse on the transition $|0'\rangle \leftrightarrow |D\rangle$ for a time 1270 μs, after sideband cooling for 71 ms. The ratio of the sideband heights allows the mean occupation of the motional mode to be found, giving $\bar{n} = 0.13(4)$ or equivalently a ground state occupation of $p_0 = 0.88(7)$. Figure from [44].

where the second order Zeeman shift is measured as $\Delta\omega_z/2\pi = 34\,\text{kHz}$, the ion oscillates between the states $|0'\rangle$ and $\frac{1}{\sqrt{2}}(|+1\rangle + e^{i\phi}\,|-1\rangle)$ at frequency $\sqrt{2}\Omega_{\text{rf}}$. The Rabi frequency on the state $|D\rangle$ can be then be calculated from $\Omega_D = \Omega_{\text{rf}}/\sqrt{2}$. Due to the additional complexity of the dressed states, the mean occupational number was calculated using a numerical simulation (written by Dr Joe Randall [53]), shown by the solid lines in figure 4.7. The resulting curves from integrating over the Hamiltonian for different values n in initial state $|0', n\rangle$ were assigned weights p_n. These were then fitted to the experimental data to give a mean phonon number of $\bar{n} = 0.13(4)$, corresponding to a ground state occupation of $p_0 = 0.88(7)$. The limit to the lowest possible mean phonon number for the ion is dephasing of the red sideband transition, off-resonant excitation to the carrier, and heating of the motional mode.

The shared motional mode of two ions can similarly be sideband cooled by applying pulses to the red sideband of one of the ions for performing multi-qubit operations. In this case, there are two different possible modes to cool - the COM mode ν_z and the stretch mode $\nu_s = \sqrt{3}\nu_z$.

4.3.3 Measuring heating rates

Using sideband thermometry, heating rates can also be measured. The ion is sideband cooled and, before the temperature is measured, a delay is added to the sequence. After

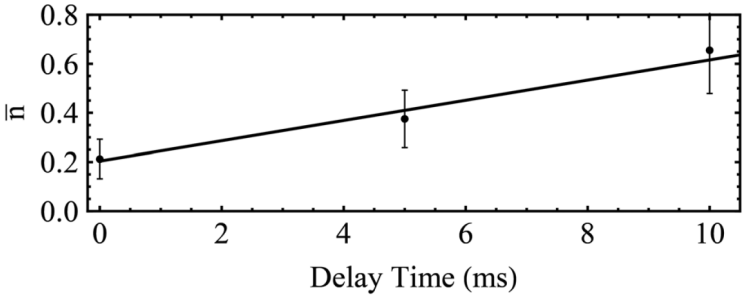

Figure 4.8: Heating rate for a single ion, measured by introducing a variable delay time between sideband cooling and measuring the temperature of the ion. Heating during this delay time causes an increase in $\bar{n}$, allowing a heating rate to be measured using a linear fit, giving $\dot{\bar{n}} = 41(7)\,\mathrm{s}^{-1}$ for a secular frequency of 426.7(1) kHz. Figure from [44].

this delay, both sidebands are scanned so that $\bar{n}$ can be calculated. During this delay, the ion is heating at a rate of $\dot{\bar{n}}$, so by varying the length of this delay time, the heating rate can be measured. Data for a single ion is shown in figure 4.8, using the same parameters as for the cooling demonstrated in section 4.3.2. By using a linear fit, a heating rate of $\dot{\bar{n}} = 41(7)\,\mathrm{s}^{-1}$ is calculated for the mode with secular frequency 426.7(1) kHz.

This method can also be applied to measure the heating rate of the COM and stretch mode for two ions. Due to the lower heating rate of the stretch mode, no significant increase in phonon number was observed for delays up to approximately 100 ms. This allowed a limit of $1\,\mathrm{s}^{-1}$ to be placed on the heating rate of the stretch mode at 461 kHz. This is lower than previously measured heating rates, which is attributed to the replacement of the electrode DC voltage supply from a home-built supply to a commercial supply.

Chapter 5

Randomised benchmarking of single qubit gates

5.1 Introduction

For a large scale quantum processor, quantum logic gates with an infidelity below the fault tolerant threshold for quantum error correction are required. The usefulness of a gate must therefore be determined with a method that can measure the error in a realistic computational scenario. Quantum process tomography (QPT) [68, 69] can be used in order to fully characterise a quantum gate, where measurements are performed on a set of input states to fully reconstruct the process matrix. However, this method has various limitations. Primarily, the gate error is generally very small, and therefore hard to measure. Error due to state preparation and detection (SPAM) is often larger than the gate error, so will dominate the measurement process.

Randomised benchmarking is an alternative method for measuring gate fidelity proposed by Knill *et al.* [70] which has since been widely used experimentally (for example [71, 72, 17]). It involves performing multiple sequences of randomly chosen computational gates and measuring the accumulated error. Using long sequences of gates gives an accumulated error much larger than the error on a single gate, which is therefore easier to measure. From the correlation between sequence length and average error it is possible to extract the average error for a single computational gate. This method also gives a more realistic error estimate, since it involves long sequences of gates with unknown initial states such as would be involved in computations, and does not rely on accurate state preparation and measurement.

There are, however, limitations to the randomised benchmarking approach, and varia-

tions of the standard randomised benchmarking technique have been proposed to overcome them. It is only possible to extract an average error per gate using randomised benchmarking, and not to diagnose errors on specific quantum gates. Interleaved benchmarking can be used to overcome this issue by interleaving the gate of interest with random gates [73]. An extension of this technique uses interleaved benchmarking sequences for optimisation of specific quantum gates [74]. The largest problem, however, that randomised benchmarking faces is insensitivity to coherent errors. Coherent errors depend on the specific sequences, and the worst case error that can occur is important for certifying gate errors below the fault-tolerant threshold. Randomised benchmarking measures the average error, and the best bound that can be placed on the worst case error without further information on the noise in the system is the square root of the average error. A variation on the randomised benchmarking protocol can be used to estimate the coherence of the noise in the system [75]. Techniques also exist which allow for tailoring coherent noise into stochastic noise, so worst case errors are equivalent to the average error directly measured using randomised benchmarking [76]. An alternative technique is to instead use gate set tomography [77]. This technique uses specifically designed pulse sequences which amplify different errors rather than random sequences. The selection of periodic sequences ensures that at least one sequence gives the worst-case for every coherent error, and therefore allows for optimisation of gates and stricter certification of gates below the fault-tolerant threshold.

Despite these limitations, in this chapter we implement the technique of randomised benchmarking, since it is an experimentally simple and widely used (and therefore comparable) measure of the average gate infidelity. It may however be interesting to investigate the implementation of alternative methods to gain additional knowledge of the sources of error. As demonstrated in chapter 4, the dressed state qubit $\{|0'\rangle, |D\rangle\}$ is useful for implementing quantum logic using long-wavelength radiation, since it exhibits long coherence times as well as a sensitivity to a magnetic field gradient, allowing for multi-qubit operations. I demonstrate randomised benchmarking of single qubit gates using this dressed state qubit. I begin by describing the randomised benchmarking protocol and experimental implementation. I then present the experimentally measured result and analyse the sources of error.

5.2 Randomised benchmarking protocol

A randomised benchmarking experiment consists of measuring the outcome of a sequence of L random gates, and comparing this result to the expected outcome. From this comparison, an accumulated error can be calculated, which is larger and therefore easier to measure than the error on a single gate. The accumulated error depends on the specific sequence performed, so multiple different randomised sequences of the same length are used to give an average error. A relatively small number of random sequences is required to converge to the average error over all sequences. By repeating this process for different values of L, it is possible to distinguish between the error due to single qubit gates and the error due to SPAM. The average error per gate can then be calculated.

The exact method used here to implement randomising benchmarking closely follows the method used by Dr Thomas Harty [17], which is a minor modification from the original proposal [70]. The randomised benchmarking protocol is as follows. For a sequence length L, randomly choose a sequence of L computational gates, chosen from the set of $\pi/2$ pulses around the $\{\pm x, \pm y\}$ axes. Repeat this N_g times to generate N_g sequences of computational gates. For each of these sequences, randomise N_r times by inserting a π pulse from the set $\{\pm x, \pm y, \pm z, I\}$ before each $\pi/2$ pulse. This choice of pairs of π and $\pi/2$ pulses ensures that the error is of order one times the computational gate error. This produces $N_r N_g$ sequences of randomised computational gates. For each sequence, calculate the expected outcome for a system free from experimental error, and choose randomly one of the two operators from the set of $\pi/2$ pulses $\{\pm x, \pm y, \pm z\}$ which will bring the ion back into an eigenstate of σ_z for measurement. Append a final randomisation π pulse from the set $\{\pm x, \pm y, \pm z, I\}$. The code to generate these sequences was written by Dr Simon Webster. Each of these $N_r N_g$ sequences is implemented experimentally N_e times, and the error calculated by comparing the experimental result to the expected result. The average error for sequence length L is then calculated from this set of errors. This experimental process is illustrated in figure 5.1.

This process is repeated for different values of L. In the original proposal [70], the protocol to generate a set of randomised sequences was followed for the largest value of L and truncated for shorter sequence lengths. Here, as in [17], this process is repeated independently for increasing values of L computational gates. This should have no effect on the outcome. Once the average error for each length of sequence L has been experimentally

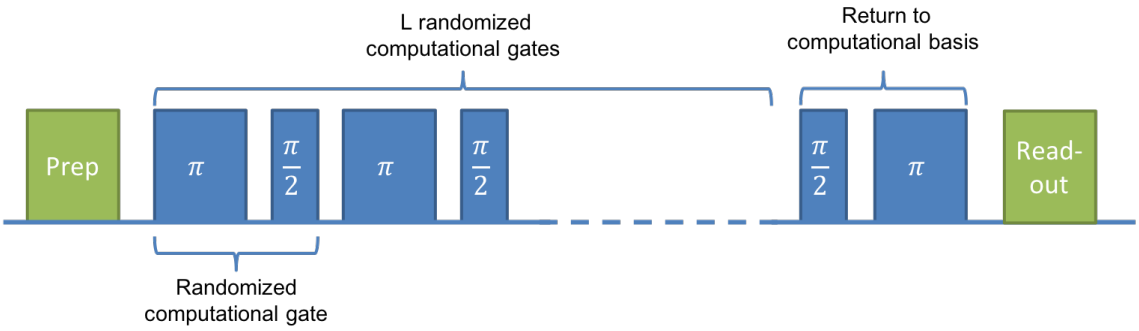

Figure 5.1: An illustration of the randomised benchmarking experimental protocol. Each sequence consists of L randomised computational gates, followed by a $\pi/2$ pulse to bring the qubit state back to the z-basis for measurement and a final randomisation π pulse. For each value of L, there are $N_g N_r$ sequences resulting from N_g sets of computational gates interleaved with N_r randomisation pulses.

measured, this set of data can then be fitted to the model

$$e_L = \frac{1}{2} - \frac{1}{2}(1 - 2e_{\text{spam}})(1 - 2e_{\text{gate}})^L, \tag{5.1}$$

allowing the error due to imperfect state preparation and measurement, e_{spam}, and the error per randomised computational gate, e_{gate}, to be extracted.

5.3 Experimental implementation

The qubit used in this implementation is comprised of the dressed states $\{|0'\rangle, |D\rangle\}$, as explained in chapter 4. The method described in section 4.2.3 is used for preparation and readout of the dressed state qubit. After initialisation in $|0\rangle$, a π pulse on the clock transition transfers ion population to $|0'\rangle$. The dressing fields are instantaneously turned on at a Rabi frequency of $\Omega_{\mu w}/2\pi = 20.7\,\text{kHz}$. Once all manipulation of the qubit is complete, the dressing fields are turned off and a final clock π pulse transfers any population in $|0'\rangle$ back to $|0\rangle$. Population in the state $|0'\rangle$ therefore results in a $F = 0$ dark measurement, and population in $|D\rangle$ gives an $F = 1$ bright measurement. The qubit transition frequency and π time were approximately measured using experiments like those shown in figure 4.3.

In order to accurately measure the frequency of the $|0'\rangle \leftrightarrow |D\rangle$ transition, a Ramsey experiment was used. A $\pi/2$ pulse of time $t = \pi/2\Omega_D$, where Ω_D is the Rabi frequency of the RF field on the $|0'\rangle \leftrightarrow |D\rangle$ transition, is applied with frequency ω and phase $\phi = 0$. A delay of 10 ms is performed, after which a second $\pi/2$ pulse with the same frequency and phase is applied. By stepping the frequency ω around the resonant frequency, Ramsey fringes are measured, with the centre fringe produced around the $|0'\rangle \leftrightarrow |D\rangle$ transition.

This allows the transition frequency to be accurately measured. A Ramsey experiment with a delay is used instead of a low power π pulse since it gives a higher resolution of the frequency for a given time. The full width at half maximum for a π pulse applied around the resonant frequency is given by approximately $\Delta f \approx 0.8/t_\pi$, where t_π is the time of the π pulse, as can be calculated from equation 2.31. For a Ramsey fringe, the full width at half maximum is given by $\Delta f = 1/2T$, where T is the delay time [41]. This therefore provides greater resolution of the frequency for a fixed interaction time. The frequency was scanned in steps of 2 Hz, and a fit to the resultant peak gave a frequency of $\omega_D = 12349.176(1)$ kHz.

In many previous implementations of randomised benchmarking, π pulses were implemented as two $\pi/2$ pulses, since square pulses were used with constant amplitude [70, 72, 17]. However, our pulses use a $\sin^2$ ramp in amplitude at the beginning and end of the pulse. This is used to counteract the effect of off-resonant coupling of the gate field to unwanted transitions outside of the qubit subspace, which incurs infidelity. This will be discussed in greater depth in section 5.5.1. The pulse shaping time used is a significant proportion of the overall gate time, which means that the time for two $\pi/2$ pulses is significantly longer than the time for a π pulse. We therefore implemented π and $\pi/2$ pulses as distinct operations.

A pulse shaping time of 100 μs for the ramp at the beginning and end of the pulse was used. This pulse-shaping time was experimentally measured to sufficiently reduce off-resonant coupling error, and this measurement will be discussed in section 5.5.1. In order to accurately measure the time for a π pulse, the frequency was set to the measured transition frequency and 21 π pulses of time t were performed consecutively, which should result in ion population in state $|D\rangle$. The time of the applied pulse was varied, and the resultant peak was centred around the correct π time, t_π. Similarly, to accurately measure the time for a $\pi/2$ pulse $t_{\pi/2}$, 34 consecutive $\pi/2$ pulses were performed, which should result in ion population in state $|D\rangle$. In both cases, the pulse time was stepped in increments of 1 μs. An example of this experiment for $\pi/2$ pulses is shown in figure 5.2. The Rabi frequency of the RF field was $\Omega_D = 592$ Hz, and the measured pulse times were $t_\pi = 943.0(5)$ μs and $t_{\pi/2} = 523.0(5)$ μs.

Between implementing each set of sequences, these routines for measuring the frequency and pulse times were repeated to ensure the transition frequency was being effectively stabilised, and to identify and compensate for any change in the unstabilised pulse time. A change in pulse length was measured of 2 μs for a π pulse and 1 μs for a $\pi/2$ pulse,

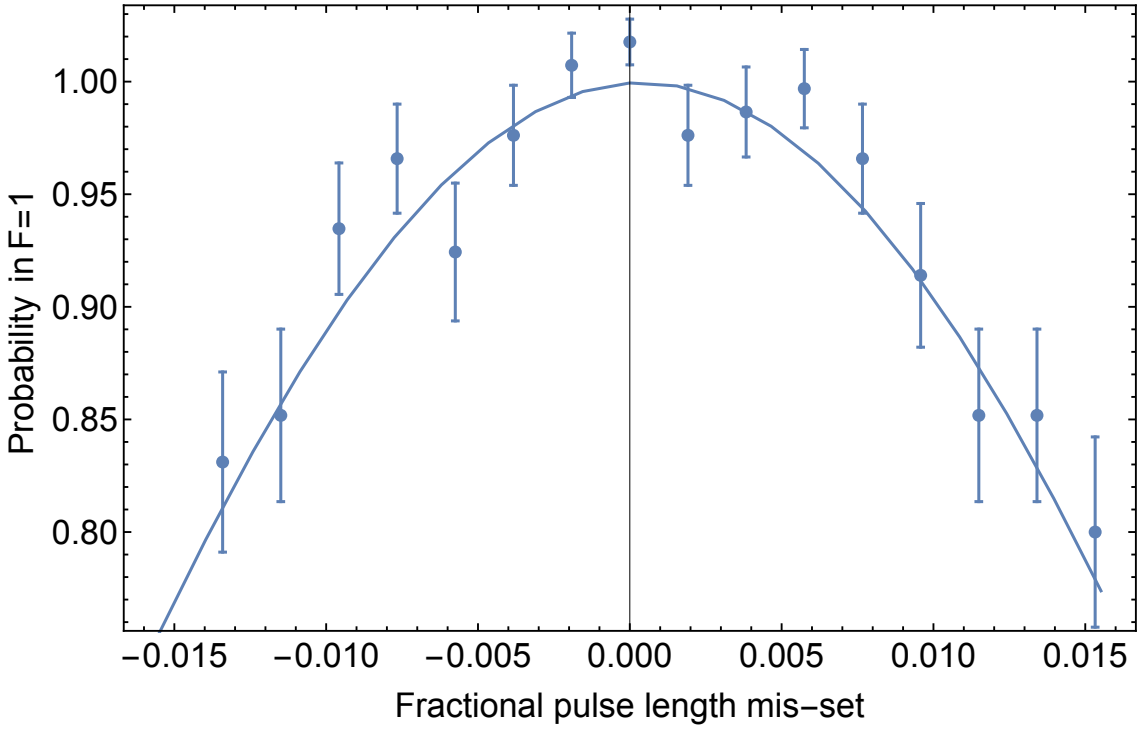

Figure 5.2: Result of an experiment to determine the pulse area of a $\pi/2$ pulse. 34 $\pi/2$ pulses with a pulse shaping ramp time of 100 μs are applied to the qubit, and the $\pi/2$ pulse time is stepped. Measuring the population in $F = 1$ allows a pulse time of 523 μs to be determined. The solid line is a result of a numerical simulation of the full dressed state system.

or equivalently 0.2% of the total pulse length in both cases.

For each value of L, $N_g = 5$ and $N_r = 5$ were used to give a total of 25 randomised sequences. Each sequence was repeated $N_e = 100$ times experimentally. Gates around the $\{\pm x, \pm y\}$ axes were implemented by setting the phase of the applied RF radiation. Identity pulses were implemented using a delay of the same time as a computational gate. To perform a σ_z gate, an identity pulse was used followed by a change of frame for all subsequent pulses. Between implementing each sequence, the magnetic field and fluorescence were monitored and compensated for to ensure stability, as explained in section 3.5.2.

5.4 Result

Figure 5.3 shows the result of randomised benchmarking of the qubit $\{|0'\rangle, |D\rangle\}$. The pale grey data points show the result of $N_g N_r = 25$ sequences performed for each sequence length L. Each point shows the average error over $N_e = 100$ experimental repeats. Since the model used, given in equation 5.1, takes into account SPAM error, the usual method of normalising out error by matrix inversion, as described in section 3.4.2, is not used. Instead, a threshold is used to discriminate between the $F = 0$ and $F = 1$ states.

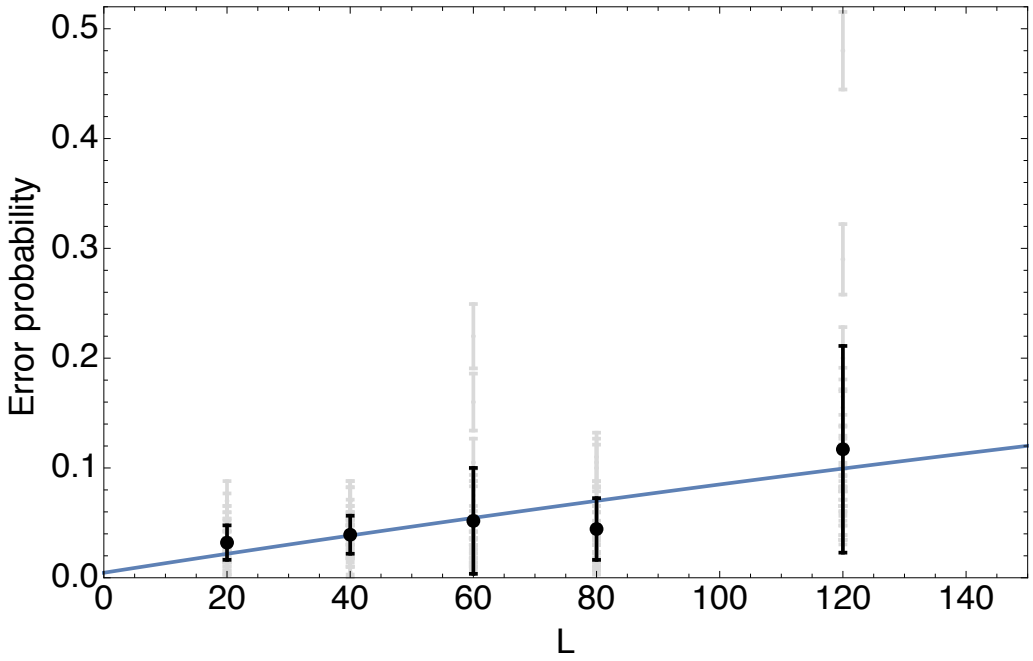

Figure 5.3: Randomised benchmarking of the $\{|0'\rangle, |D\rangle\}$ qubit, giving an error per gate of $9(3) \times 10^{-4}$. Black data points are the average of the measured error probability on 25 randomised sequences of length L, and results of these individual sequences are shown in grey. The blue line shows the fit of the model given in equation 5.1 to the experimental data.

This threshold was measured to be 1 photon, where results of ≤ 1 were recorded as a a dark measurement and > 1 a bright measurement. The same error per gate result is obtained within error if matrix inversion is used. The black data points are the mean error probability for each value of L, given by the mean of the individual sequence results. The error bar indicates the standard deviation of the data set. The solid blue line is the fit from equation 5.1. The SPAM error given by the fit is $e_{\text{spam}} = 5(20) \times 10^{-3}$, which agrees with a state detection measurement fidelity taken at the time of the randomised benchmarking implementation of 1.8×10^{-2}. The error per gate is $e_{\text{gate}} = 9(3) \times 10^{-4}$, or equivalently a fidelity of 0.9991(3).

5.5 Sources of error

We now look at the dominant sources of error contributing towards the experimentally measured error per gate.

5.5.1 Off-resonant coupling

When we calculated the Hamiltonian for making single qubit rotations in the dressed system in section 4.2.2, we made the assumption that the Rabi frequency of the RF field

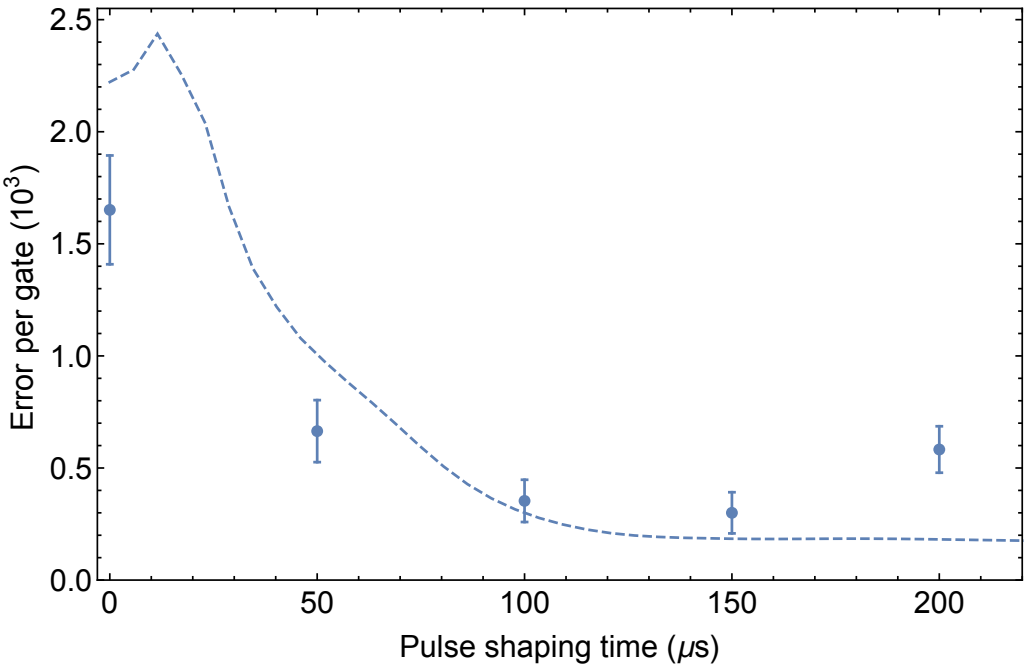

Figure 5.4: Error from off-resonant coupling as a function of pulse shaping time. Experimental points are the average of 36 sequences of $L = 40$ randomised computational gates, averaged to error per individual gate. The Rabi frequency gives a square shaped pulse π time of approximately 845 μs. The dashed line shows the result of a numerical simulation of 20 randomly chosen pairs of π and $\pi/2$ pulses from the gate sets used to generate the benchmarking sequences for an approximate guide, although this is not a full model of the experiment.

was much less than the frequency splittings to the other dressed states, so that other dressed state transitions could be ignored. This corresponds to two assumptions. The first is that $\Omega_D \ll \Delta\omega_z$, where ω_z is the second order Zeeman shift which defines the splitting between the two $|0'\rangle \leftrightarrow |D\rangle$ transitions. The second is that $\Omega_D \ll \Omega_{\mu w}/\sqrt{2}$, where $\Omega_{\mu w}/\sqrt{2}$ is the separation in frequency between the transition $|0'\rangle \leftrightarrow |D\rangle$ and the transitions $|0'\rangle \leftrightarrow |u\rangle$ and $|0'\rangle \leftrightarrow |d\rangle$, which is defined by the Rabi frequency of the dressing fields $\Omega_{\mu w}$. However, in this implementation these frequency splittings are $\Delta\omega_z/2\pi = 24.65\,\text{kHz}$ and $\Omega_{\mu w}/\sqrt{2} = 14.6\,\text{kHz}$. This therefore places a stringent condition on the Rabi frequency Ω_D. In the case that Ω_D is not low enough, the RF field off-resonantly couples to other dressed state transitions outside of the qubit subspace, causing unwanted excitations and therefore a significant error.

In order to reduce this error and therefore alleviate the limit on Ω_D, pulse shaping is used. By ramping the pulse amplitude at the beginning and end of the pulse using a $\sin^2$ shape with envelope time t_r, much of the off-resonant excitation can be eliminated. The pulse shaping ramp time t_r must be sufficient to fulfil the condition for adiabaticity, which is that $\Delta^2 \gg |d\Omega(t)/dt|$ [78], where Δ is the frequency separation to the nearest off-resonant transition which is on order 10 kHz. This does, however, increase the overall pulse time in order to keep the pulse area constant. For a pulse ramp of the form $\Omega_D \sin^2(\pi t/2t_r)$ between times $t = 0$ and $t = t_r$, the pulse area is given by half the equivalent area for a square pulse of amplitude Ω_D over this ramp time. This means that for a π pulse, the pulse length increases to $t_\pi = t^0_\pi + t_r$, and for a $\pi/2$ pulse to $t_{\pi/2} = t^0_{\pi/2} + t_r$, where t^0_π and $t^0_{\pi/2}$ are the pulse lengths with no pulse shaping. This means that other errors such as depolarisation and parameter drift, which are discussed in the following sections, become increasingly important.

For the Rabi frequency used in this experiment of $\Omega_D = 592\,\text{Hz}$, a pulse ramp time of $t_r = 100\,\mu\text{s}$ at the beginning and end of the pulse was found to be sufficient to largely eliminate off-resonant effects. This was determined by experimentally measuring the error per gate for different pulse shaping times at this Rabi frequency, using 36 sequences of 40 randomised computational gates. For each pulse shaping ramp time, the overall pulse length was optimised using methods discussed in 5.3. The resultant data points are shown in figure 5.4. In this figure is also the result of a full dressed state simulation incorporating off-resonant effects, using the same Rabi frequency. The dashed line shows the average infidelity for a set of 20 pairs of π and $\pi/2$ pulses, randomly chosen from the set used to generate the randomised sequences. This simulation does not emulate exactly the experi-

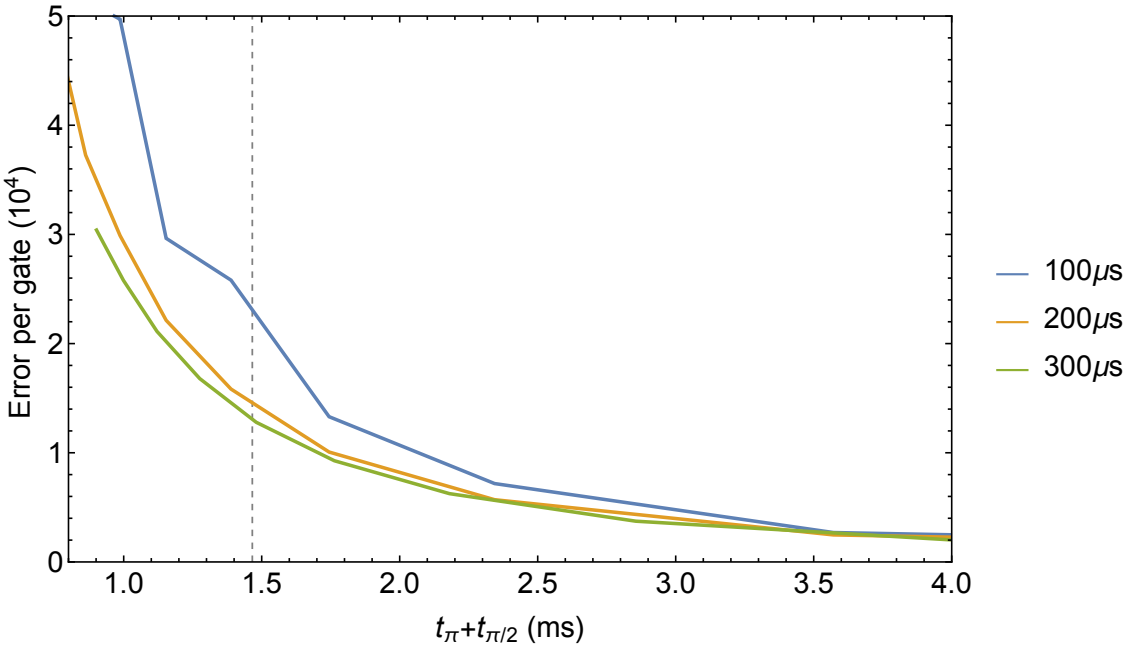

Figure 5.5: Simulation of 20 randomly chosen pairs of π and $\pi/2$ pulses for a varied Rabi frequency. The error per gate due to off-resonant coupling is plotted against the total time for a π and $\pi/2$ pulse for three different pulse shaping times. The vertical grey dashed line marks where the experimental data was taken with a 100 μs ramp time, showing that an improvement at this gate time would be possible with a longer pulse ramp time. This improvement for longer pulse ramp times becomes even more significant for faster gates.

mental process, but since the full set of experimental sequences was too computationally intense this result is shown for an approximate reference instead. At low pulse shaping times, when there is a high level of off-resonant coupling, there is a larger uncertainty on the result of the simulation due to oscillatory effects which depend on the exact timing of the gates and detunings of the off-resonant transitions. The cause of the discrepancy for the data point at a pulse shaping time of 200 μs is unknown, although at longer pulse times we do expect some sources of error to become worse. This simulation indicates that at a pulse shaping time of 100 μs there is an infidelity of 2.7×10^{-4}, although this is an approximation due to the difficulty of simulating the full system for longer sequences.

In order to investigate the limit to the effectiveness of pulse shaping, a simulation at the experimental parameters used above for different pulse shaping times was performed for varied Rabi frequency. The results of this simulation are shown in figure 5.5, where the error per gate due to off-resonant coupling is plotted against the total time for a π and a $\pi/2$ pulse, $t_\pi + t_{\pi/2}$. For any pulse shaping ramp time, there is a limit to the minimum achievable gate time, since $t_{\pi/2} \geq 2t_r$ must be true in order to perform a full $\pi/2$ pulse, or equivalently $t^0_{\pi/2} \geq t_r$. It can be seen that there is a trade-off between total time and off-resonant coupling error, with longer times leading to lower errors. The grey dashed line

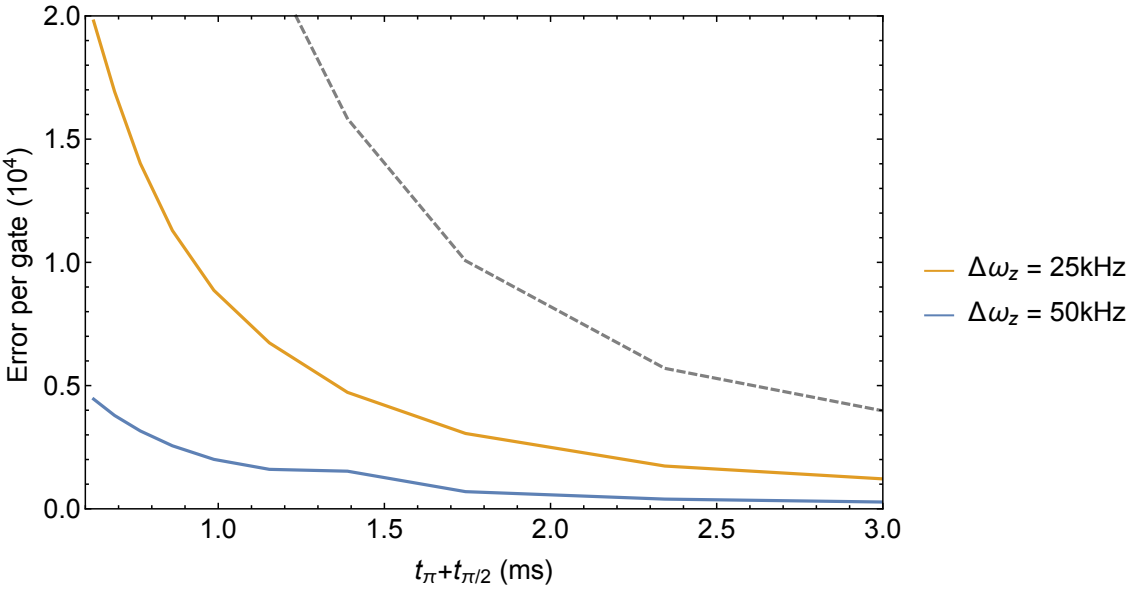

Figure 5.6: Simulation of the same 20 randomly chosen pairs of π and $\pi/2$ pulses as in figure 5.5, for a varied Rabi frequency with a pulse shaping time of 200 μs. The simulation is performed with microwave Rabi frequencies ten times the value used for the experimental implementation, to show the possible reduction of off-resonant coupling error. The simulation is shown for two different values of second order Zeeman shift, with the higher value resulting in even larger reduction of off-resonant coupling error. The grey dashed line shows the result for the current experimental parameters for reference, with lower microwave Rabi frequencies and a second order Zeeman shift of $\Delta\omega_z = 25\,\text{kHz}$.

is plotted at the experimental gate time implemented, where a 100 μs ramp time was used, suggesting that a longer pulse-shaping time could have reduced the off-resonant coupling error.

Figure 5.6 shows the result of the same simulation with dressing fields at ten times the Rabi frequency, so that $\Omega_{\mu w}/\sqrt{2} = 146\,\text{kHz}$. The ability to produce Rabi frequencies of ten times the current limit corresponds to one hundred times the currently available power, so would require a significant experimental upgrade. A pulse shaping time of 200 μs is used, since there is little difference in error between different pulse shaping times at these parameters. The simulation was performed for two different values for the second order Zeeman shift: $\Delta\omega_z = 25\,\text{kHz}$, as in the current experimental setup, and $\Delta\omega_z = 50\,\text{kHz}$. The grey dashed line shows the result of the simulation shown in figure 5.5 of the current experimental parameters, $\Omega_{\mu w}/\sqrt{2} = 14.6\,\text{kHz}$ and $\Delta\omega_z = 25\,\text{kHz}$, for reference. Higher dressing field Rabi frequencies and second order Zeeman shifts can clearly be seen to reduce the error significantly, as expected. However, there is a limit to how high the second order Zeeman shift can be since high absolute magnetic fields can cause problems, such as reduced detection fidelity and increased dephasing of the clock qubit due to higher second order sensitivity. Use of Blackman shaped pulses [66] instead of $\sin^2$ shaped pulses

was found to have little effect on the error.

5.5.2 Frequency mis-set

If the frequency of the transition $|0'\rangle \leftrightarrow |D\rangle$ is incorrectly set, either due to a systematic mis-set or an undetected change in parameters, an error is induced on gates. To first order, the frequency of the $|0'\rangle \leftrightarrow |D\rangle$ transition is insensitive to magnetic field drifts. However, second order effects can cause transition frequency error. There are several mechanisms leading to magnetic field fluctuations, some of which are unique to our magnetic gradient system. In addition to fluctuations in the ambient magnetic field environment of the trap, ion movement in the magnetic field gradient causes a change of transition frequency. The magnetic field at the ion position is experimentally stabilised, using an auxiliary sequence which involves measuring the frequency of the $|0\rangle \leftrightarrow |+1\rangle$ transition, as described in section 3.5.2. This stabilises the $|0\rangle \leftrightarrow |0'\rangle$ transition to within 5 Hz, so a stability of approximately 2.5 Hz can be assumed on the $|0'\rangle \leftrightarrow |D\rangle$ transition frequency.

In order to simulate the effect of a frequency mis-set, the unitary matrix describing single qubit gate rotations in a two level system is used, which is given by

$$U(\delta, \Omega_0, \phi, t) = \begin{pmatrix} e^{i\delta t}[\cos(\Omega_\delta t/2) - \frac{i\delta}{\Omega_\delta}\sin(\Omega_\delta t/2)] & -\frac{i\Omega_0}{\Omega_\delta}e^{i\delta t/2}e^{-i\phi}\sin(\Omega_\delta t/2) \\ -\frac{i\Omega_0}{\Omega_\delta}e^{-i\delta t/2}e^{i\phi}\sin(\Omega_\delta t/2) & e^{-i\delta t}[\cos(\Omega_\delta t/2) + \frac{i\delta}{\Omega_\delta}\sin(\Omega_\delta t/2)] \end{pmatrix} \tag{5.2}$$

from section 2.4.1, where $\Omega_\delta = \sqrt{\Omega_0^2 + \delta^2}$. A set of 36 sequences of $L = 40$ randomised computational gates is simulated, corresponding to $N_r = 6$ and $N_g = 6$. The average error per gate over this set of sequences is represented by the solid line in figure 5.7. The equivalent experimental process for the same set of randomised sequences of gates was performed, and the resulting average error per gate is shown by the data points in figure 5.7. A clear frequency offset was seen between simulation and the experimental nominal zero detuning, which was identified by the Ramsey frequency measurement. A fit of the data to the simulated result gave this offset as 2.7 Hz.

This systematic misset could be the result of imperfect measurement processes. The Ramsey detuning scan used to measure the transition frequency does not take into account any AC Stark effects caused by the applied RF field of Rabi frequency Ω_D. Although AC Stark shifts associated with the dressed states connected to $|0'\rangle$ via $|+1\rangle$ cancel out due to symmetry, there is still an AC Stark shift associated with the dressed states connected

to $|0'\rangle$ via $|-1\rangle$. This is given by

$$\begin{aligned}\Delta\omega_{|0'\rangle\leftrightarrow|D\rangle} &= -\frac{\Omega_D^2}{2\Delta\omega_z} - \frac{\Omega_{\mathrm{ud}}^2}{4(\Delta\omega_z - (\Omega_{\mu w}/\sqrt{2}))} - \frac{\Omega_{\mathrm{ud}}^2}{4(\Delta\omega_z + (\Omega_{\mu w}/\sqrt{2}))} \\ &= -\frac{\Omega_D^2}{2}\left(\frac{1}{\Delta\omega_z} + \frac{1}{8(\Delta\omega_z - (\Omega_{\mu w}/\sqrt{2}))} + \frac{1}{8(\Delta\omega_z + (\Omega_{\mu w}/\sqrt{2}))}\right)\end{aligned} \tag{5.3}$$

where $\Delta\omega_z$ is the second order Zeeman shift, $\Omega_{\mu w}$ is the Rabi frequency of the dressing fields, and Ω_{ud} is the Rabi frequency of the dressed states $|u\rangle$ and $|d\rangle$, which is given by $\Omega_{\mathrm{ud}} = \Omega_D/\sqrt{2}$. For the experimental parameters used here, this gives a Stark shift of approximately $-10\,\mathrm{Hz}$. The reason for the discrepancy between the calculated AC Stark shift and the measured frequency offset is unknown, although four level dressed state simulations which incorporate effects of off-resonant coupling, pulse shaping, and AC Stark shifts show similar low frequency offsets.

As well as constant frequency mis-sets, faster frequency fluctuations cause gate error, but the timescale of these fluctuations is not easy to measure. The effect of these errors is a random sampling of the average error per gate shown in figure 5.7, which could be the reason for the clear rounding of the data around the zero detuning in this graph. Since the auxiliary sequence stabilises the transition to within 2.5 Hz, it will be assumed that this is the magnitude of the fluctuations. With a systematic offset of 2.7 Hz, the linear nature of the gate infidelity with detuning mis-set means that a random sampling of magnitude 2.5 Hz around this systematic offset averages to the gate error at 2.7 Hz. This gives a theoretical error of 2.4×10^{-4}.

5.5.3 Pulse area mis-set

An offset in the pulse area for π pulses or $\pi/2$ pulses will also cause gate error. This offset could be due to a systematically mis-set pulse time or Rabi frequency resulting from imperfect calibration. It could also be a result of an undetected change in experimental parameters over time. Calibration measurements showing a maximum drift of $2\,\mu$s on the pulse time of the π pulse between each set of sequences corresponds to a pulse area drift of approximately 0.002. As with frequency fluctuations, the timescale of Rabi frequency noise is not known, but it will be assumed that the dominant error results from a slow change. Faster noise will be assumed to be a secondary effect, as in [71, 31].

Figure 5.8 shows the simulated effect of a pulse area mis-set in a two level system, with error per gate averaged after 36 sequences of 40 randomised gates plotted against the fractional pulse area error. The simulation is performed using the unitary matrix

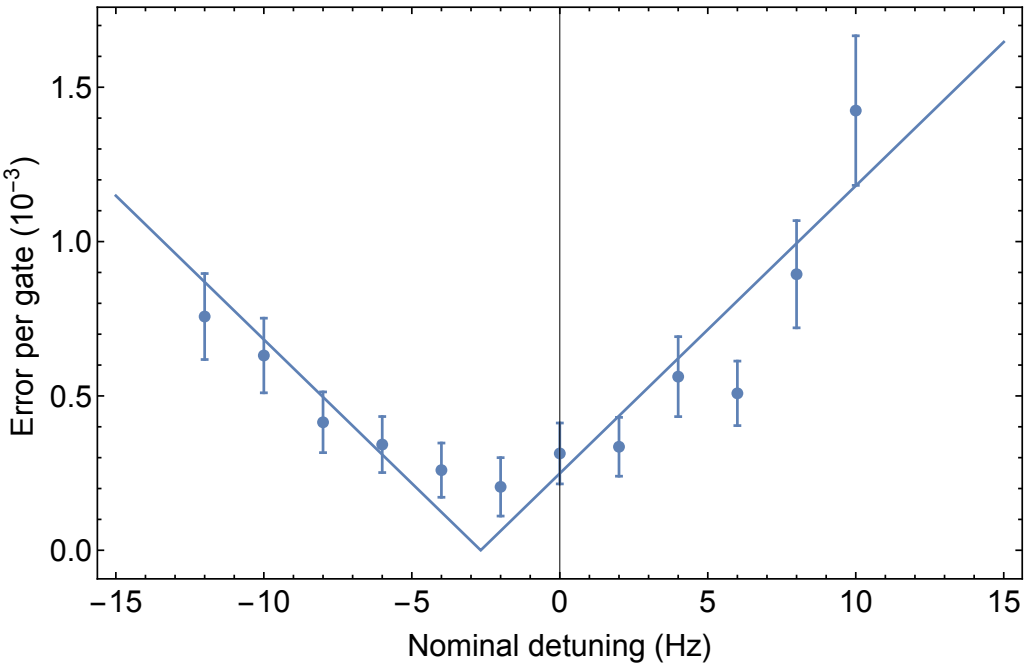

Figure 5.7: Error per randomised computational gate for a frequency detuning. The solid line is the result of a simulation of 36 sequences of length $L = 40$ in a two level qubit. The data points are the experimentally measured average error per gate from the same set of sequences. A clear offset is seen for the experimental data from the nominal 0 Hz detuning, and a fit to the simulated results gives this offset as 2.7 Hz.

describing single qubit rotations, as in section 5.5.2. A fractional drift in pulse area as observed in calibration measurements would correspond to an error of approximately 1.7×10^{-4}. This is the same magnitude as the error due to the systematic frequency mis-set.

5.5.4 Dephasing and depolarising

The dressed state qubit should be well protected against magnetic field noise. However, as discussed in section 4.2.5, dephasing and depolarising of the qubit can occur as a result of imperfectly set parameters, second order sensitivity to magnetic fields, and frequency noise at the dressed state splitting $\Omega_{\mu w}/\sqrt{2}$. This dephasing and depolarising can be modelled using a master equation of the form

$$\frac{d}{dt}\rho = -i[H, \rho] + L(\rho), \tag{5.4}$$

where H is the Hamiltonian of the single qubit gate acting on the ion, ρ is the density operator describing the ion's state, and the Lindblad operator is of the form

$$L(\rho) = -\frac{1}{2}\sum_m (C_m^\dagger C_m \rho + \rho C_m^\dagger C_m) + \sum_m C_m \rho C_m^\dagger. \tag{5.5}$$

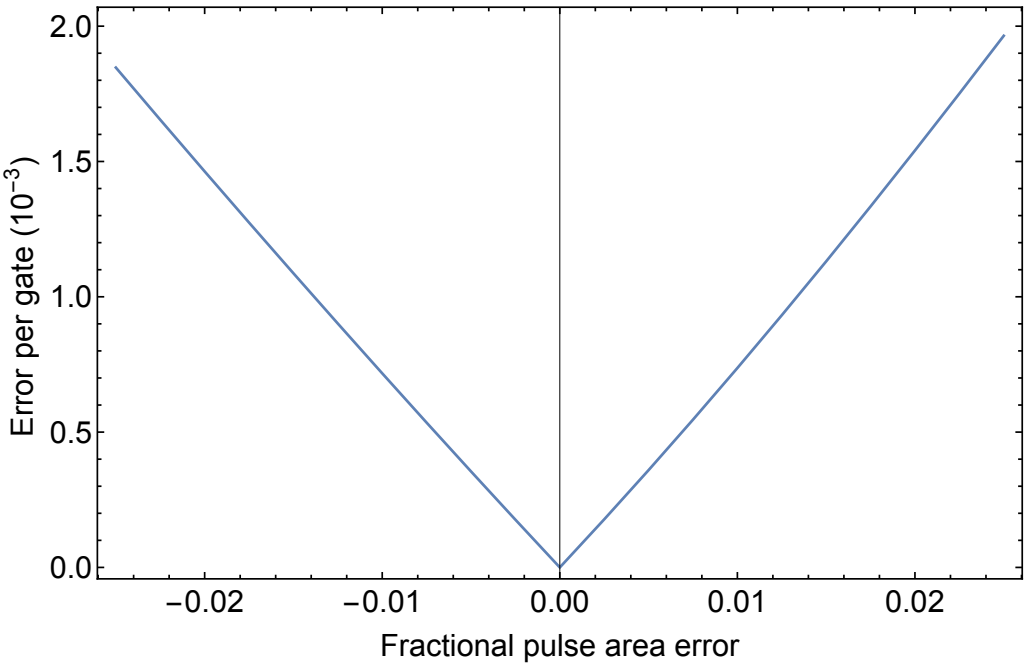

Figure 5.8: Error per gate for a fractional pulse area offset. The solid line is a result of a simulation of 36 sequences of length $L = 40$.

The operators C_m depend on the noise source being considered.

Dephasing becomes problematic when the detunings and the Rabi frequencies of the dressing fields are set incorrectly. Its effect can be described by the operator:

$$C = \sqrt{\frac{\Gamma}{2}}(|D\rangle\langle D| - |0'\rangle\langle 0'|) \tag{5.6}$$

where $\Gamma = 1/T_2$ and T_2 is the coherence time. At the time of the randomised benchmarking experiment, this was measured as approximately $T_2 = 600\,\text{ms}$. This model, however, is a simplification of the decoherence process. A simple estimate from the ratio of the gate time to the coherence time would give an error per gate of 2.3×10^{-3}, but this is an over-estimate. The error resulting from dephasing in a randomised benchmarking sequence is hard to estimate (both using a master equation and a simple estimate), since the noise frequency spectrum causing this dephasing is not known. For low frequency noise, which is likely to be a large contributory factor to the dephasing of the qubit, the effect of randomised pulses is to partially refocus the qubit since noise is correlated between pulses. We have therefore not made a numerical estimate, but will assume this error is non-negligible.

Depolarising is caused by magnetic field noise resonant with the frequency splitting of the dressed states. During this experiment, the lifetime was measured as $T_1 = 2.6\,\text{s}$ [53]. Both the T_1 and T_2 times are longer than the more recent measurements shown in section

4.2.4. For depolarising there are 6 relevant operators corresponding to σ_x, σ_y and σ_z type interactions which drive population between $|D\rangle$ and $\{|u\rangle, |d\rangle\}$ [53]:

$$\begin{aligned}
C_1 &= \sqrt{\frac{\gamma_1}{6}}(|u\rangle\langle D| + |D\rangle\langle u|) \\
C_2 &= \sqrt{\frac{\gamma_1}{6}}(|d\rangle\langle D| + |D\rangle\langle d|) \\
C_3 &= \sqrt{\frac{\gamma_1}{6}}(i|u\rangle\langle D| - i|D\rangle\langle u|) \\
C_4 &= \sqrt{\frac{\gamma_1}{6}}(i|d\rangle\langle D| - i|D\rangle\langle d|) \\
C_5 &= \sqrt{\frac{\gamma_2}{6}}(|u\rangle\langle u| - |D\rangle\langle D|) \\
C_6 &= \sqrt{\frac{\gamma_2}{6}}(|d\rangle\langle d| - |D\rangle\langle D|)
\end{aligned} \tag{5.7}$$

The σ_z type interactions shown in C_5 and C_6 are caused by fluctuations in the relative energies of the dressed state energies, for example by fluctuations in the dressing field Rabi frequency which defines the splitting between $|D\rangle$ and $\{|u\rangle, |d\rangle\}$. We can ignore this effect, assuming that the most significant error is caused by resonant magnetic field noise driving population transfer between states, and therefore set $\gamma_1 = 1/T_1$ where T_1 is the lifetime and $\gamma_2 = 0$.

In order to estimate the effect this depolarising will have on a single qubit computational gate, we simulate the effect of the depolarising terms on states with no Hamiltonian acting over the time for approximately 100 randomised computational gates (i.e. 100 π and $\pi/2$ pulses) . This is shown by the solid lines in figure 5.9 for the states $|D\rangle$ (blue) and $\frac{1}{\sqrt{2}}(|0'\rangle + |D\rangle)$ (orange). We can estimate the effect on a single gate by calculating the error on the state $|D\rangle$ during the time for a single gate and halving, since over a randomised sequence we can assume that each qubit state is occupied for approximately half the time. This gives an error of approximately 1.9×10^{-4}.

5.6 Conclusion

Randomised benchmarking of the dressed state qubit $\{|0'\rangle, |D\rangle\}$ has allowed an error of $9(3) \times 10^{-4}$ to be measured, which is an order of magnitude below a fault-tolerant threshold of 1×10^{-2} [5]. A summary of the error estimations from each of the sources discussed above is shown in table 5.1. These errors are in general approximations due to the difficulty of modelling the exact system and understanding the sources of error fully, but these estimates give the right order of magnitude for the measured error. The error

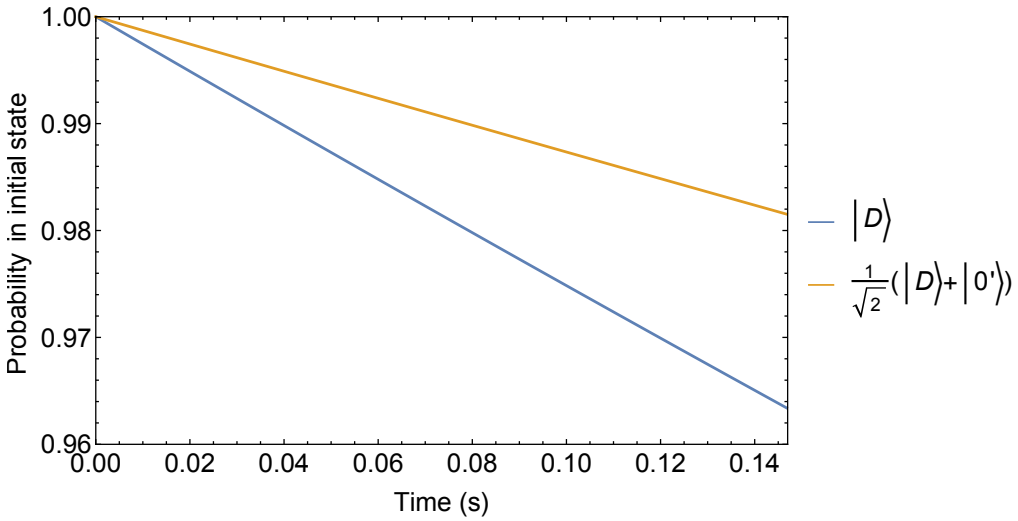

Figure 5.9: Depolarisation of the states $|D\rangle$ and $\frac{1}{\sqrt{2}}(|0'\rangle + |D\rangle)$ over the time for 100 randomised computational gates, as a result of population being driven from the qubit subspace $\{|0'\rangle, |D\rangle\}$ to the other dressed states $\{|u\rangle, |d\rangle\}$.

Error source	Error approximation
Off-resonant coupling	2.7×10^{-4}
Frequency mis-set	2.4×10^{-4}
Pulse area mis-set	1.7×10^{-4}
Depolarisation	1.9×10^{-4}
Total	8.7×10^{-4}

Table 5.1: Summary of the error approximations calculated for each error source considered above.

due to dephasing is also likely to be non-negligible, although a numerical estimate cannot be made without information on the frequency spectrum causing the dephasing.

A large contribution to this total error results from the systematic frequency mis-set experimentally measured in figure 5.7. Further work to determine this frequency offset more exactly could reduce this error, through use of randomised benchmarking sequences to calibrate the qubit transition frequency initially. Driving faster gates would also reduce sensitivity to an incorrectly set frequency, either resulting from this systematic mis-set or an undetected change in parameters. The error resulting from depolarisation would also decrease if gate times become shorter. More advanced randomised benchmarking techniques can also be used to determine and optimise for major sources of error [74].

The limit, however, to the speed of gates is due to the off-resonant coupling error. Analysis in section 5.5.1 suggests that by using a higher pulse shaping time, it would be possible to drive faster gates while maintaining the same off-resonant coupling error at current experimental parameters. However, in order to reduce the off-resonant coupling infidelity to significantly lower than the current value, simulations indicate that lower Rabi

frequencies resulting in longer pulse times will be required. Increasing the Rabi frequency of the dressing fields and the second order Zeeman shift would relax these limitations allowing faster gates, which will be an important step forward for reducing the overall error of single qubit gates performed on this qubit.

An alternative to using the dressed state qubit would be to use the clock qubit $\{|0\rangle, |0'\rangle\}$ for single qubit gates, since sensitivity to magnetic field gradients is not required for single qubit operations. The information stored in the clock qubit could then be mapped to the dressed state basis for multi-qubit operations [66]. A method for this mapping will be described in the next chapter. The current experimental setup does not allow for use of the clock qubit for single qubit gates, since it is not possible to control the phase of the microwave fields, which are generated by mixing a phase-controllable RF signal with a microwave frequency of unknown phase. However, an improvement to the microwave setup could make this possible, for example by using a high frequency AWG, or by frequency doubling or quadrupling a lower frequency phase-controllable source. Use of this clock qubit would help alleviate the error caused by off-resonant coupling. For multiple ions in a trap, the nearest transition would be defined by the difference in second order Zeeman shifts for multiple ions, which is on the order of 10 kHz. There is still therefore a limit on the achievable Rabi frequency in order to keep cross talk to a minimum. However, for small numbers of ions in a confining potential, there are fewer off-resonant transitions than for the dressed state qubit, which can off-resonantly couple to the states $|D\rangle$, $|u\rangle$ and $|d\rangle$. The clock qubit also exhibits a considerably longer lifetime, so the infidelity resulting from depolarising will become negligible at the level of error discussed here.

Chapter 6

Robust two qubit gates

6.1 Introduction

In order to implement universal quantum computation, a two ion entangling gate is required as well as a set of single qubit gates, which were demonstrated in the previous chapter. Two qubit gates have been demonstrated on pairs of trapped ions with high fidelity using optical fields [18, 19], and long-wavelength radiation gates are demonstrating increasing fidelities [28, 30]. However, maintaining these fidelities while scaling to a large quantum computer will require gates that are more robust. Many proposed trapped ion architectures require ions to be trapped close to the surface of a microfabricated chip [35, 36, 38, 79]. This could result in increased gate infidelities due to heating and dephasing of the ions' motion caused by voltage fluctuations in the electrodes of the chip [80], since the heating rate scales unforgivingly with d^{-4}, where d is the ion-electrode distance [32]. Additionally, it is likely that parameters will slowly change, either from position to position on the chip or due to drift over time. This problem is exacerbated at higher values of the initial mean excitation of the motional mode, $\bar{n}$, which, for example, could be induced by heating during ion shuttling processes required in many architectures [35, 36, 38]. A quantum computer will therefore require gate operations that are both high fidelity and resilient to imperfect experimental environments.

The Mølmer-Sørensen (MS) gate [14, 15] is a widely used geometric phase gate where states are driven in circular trajectories in phase space and state dependently pick up a phase. The resilience to infidelity caused by heating on these gates can be improved by performing multiple smaller circles in phase space. However, this has an adverse effect on the gate time, which scales as the number of circles completed. As in the previous chapter, many sources of infidelity become increasingly important over longer gate times,

such as parameter drift and dephasing/depolarising. Hayes *et al.* experimentally demonstrated a similar technique as a method of reducing the effect of a 'symmetric' detuning error [81], such as caused by a drift in trap frequency. Recent theoretical work [82] has proposed a novel method to protect against errors due to heating and symmetric detuning errors by tracing out more complicated paths in phase space. In this chapter, I experimentally demonstrate these new Multi-Tone Mølmer-Sørensen (MTMS) gates, and show their resilience to heating and symmetric detuning errors by comparing to standard MS gates. Sections 6.2-6.4 present a standard two qubit Mølmer-Sørensen gate and the dominant error sources causing infidelity. In section 6.5, I introduce MTMS gates and show theoretically and experimentally how they mitigate many of these sources of gate infidelity.

6.2 Spin-motion entanglement in a single ion

In order to understand the Mølmer-Sørensen interaction for two ions, it is useful first to derive the entanglement of the spin and motion for a single ion as this is the driving mechanism for two ion entanglement. As shown in section 2.4.2, red and blue sideband interactions with the ion driven by long-wavelength radiation have the following Hamiltonians:

$$H_{\mathrm{r}} = -\frac{\hbar\eta\Omega_0}{2}(\sigma_+ a e^{-i\delta_r t}e^{i\phi_r} + \sigma_- a^\dagger e^{i\delta_r t}e^{-i\phi_r}) \tag{6.1}$$

$$H_{\mathrm{b}} = \frac{\hbar\eta\Omega_0}{2}(\sigma_+ a^\dagger e^{-i\delta_b t}e^{i\phi_b} + \sigma_- a e^{i\delta_b t}e^{-i\phi_b}) \tag{6.2}$$

where η is the effective Lamb-Dicke parameter, Ω_0 is the carrier Rabi frequency, δ_r and δ_b are the detunings from the red and blue sidebands, and ϕ_r and ϕ_b are the phases of the fields applied to the red and blue sidebands.

A Mølmer-Sørensen interaction involves off-resonantly driving both the red and blue sidebands of an ion, with equal and opposite detuning so that $\delta_r = -\delta_b = \delta$. This gives a Hamiltonian

$$H_{\mathrm{MS}} = \frac{\hbar\eta\Omega_0}{2}[e^{i\delta t}a^\dagger(\sigma_+ e^{i\phi_b} - \sigma_- e^{-i\phi_r}) - e^{-i\delta t}a(\sigma_+ e^{i\phi_r} - \sigma_- e^{-i\phi_b})]. \tag{6.3}$$

We can define spin and motional phases

$$\begin{aligned}\phi_{\mathrm{s}} &= \frac{1}{2}(\phi_r + \phi_b)\\ \phi_{\mathrm{m}} &= \frac{1}{2}(\phi_r - \phi_b)\end{aligned} \tag{6.4}$$

which allows us to factorise the Hamiltonian into spin and motional parts

$$H_{\mathrm{MS}} = -\frac{i\hbar\eta\Omega_0}{2} S_\phi [e^{i\delta t} a^\dagger e^{-\phi_m} - e^{-i\delta t} a e^{i\phi_m}], \tag{6.5}$$

where we have defined the Mølmer-Sørensen spin operator

$$S_\phi = i(\sigma_+ e^{i\phi_s} - \sigma_- e^{-i\phi_s}). \tag{6.6}$$

This spin operator has eigenstates that are superpositions of the basis states, $|{\leftarrow_\phi}\rangle = \frac{1}{\sqrt{2}}(|{\downarrow}\rangle + ie^{i\phi_s}|{\uparrow}\rangle)$ and $|{\rightarrow_\phi}\rangle = \frac{1}{\sqrt{2}}(|{\downarrow}\rangle - ie^{i\phi_s}|{\uparrow}\rangle)$ and so can be written as $S_\phi = |{\leftarrow_\phi}\rangle\langle{\leftarrow_\phi}| - |{\rightarrow_\phi}\rangle\langle{\rightarrow_\phi}|$.

This Mølmer-Sørensen Hamiltonian is time-dependent, and in order to understand the evolution of states in time we can use the Magnus expansion. This is a method used to find an approximation of the time-dependent Schrödinger equation that is unitary to any order, described in [83]. The Magnus expansion allows the unitary operator to be written as

$$U(t, t_0) = \exp\left\{\left[\sum_k O_k\right]\right\}. \tag{6.7}$$

The first term of this expansion can be calculated as

$$\begin{aligned} O_1 &= -\frac{i}{\hbar}\int_0^t dt' H(t') \\ &= S_\phi(\alpha(t)a^\dagger - \alpha^*(t)a), \end{aligned} \tag{6.8}$$

where we have defined

$$\alpha(t) = \frac{i\eta\Omega_0}{2\delta} e^{-i\phi_m}(e^{i\delta t} - 1). \tag{6.9}$$

The second term in the Magnus expansion is given by

$$\begin{aligned} O_2 &= -\frac{1}{2\hbar^2}\int_0^t \int_0^{t'} dt'' dt' [H(t'), H(t'')] \\ &= iS_\phi^2 \chi(t), \end{aligned} \tag{6.10}$$

where we have defined

$$\chi(t) = \frac{\eta^2\Omega^2}{4\delta^2}(\delta t - \sin\delta t). \tag{6.11}$$

In this case, the Magnus expansion gives an exact solution since all higher order terms are equal to zero. Third order terms and above involve nested commutators, such as $[H(t), [H(t'), H(t'')]]$, which are all equal to zero.

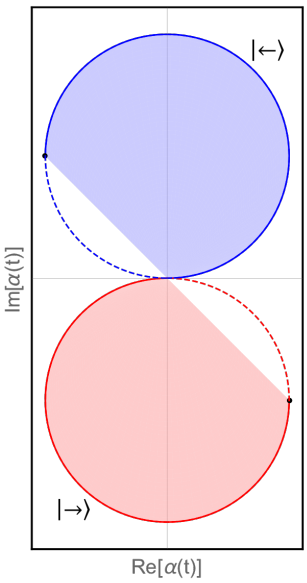

Figure 6.1: States $|\leftarrow_\phi\rangle$ and $|\rightarrow_\phi\rangle$ are driven in circles in phase space in opposite directions, as indicated by the blue and red lines, plotted here for an ion starting in motional state $|n=0\rangle$, which is equivalent to the coherent state with $\alpha = 0$. When the states are removed from the origin, the spin and motional states of the ion are entangled. At times $\tau = 2\pi q/\delta$, the circles in phase space close and there is no spin-motion entanglement. The states acquire a phase equal to twice the area of the circles in phase space, which for the single ion case is global but for two ion entanglement is crucial.

The time evolution unitary operator can then be written as:

$$\begin{aligned} U_{\mathrm{MS}}(t) &= \exp\Big\{\big(S_\phi(\alpha(t)a^\dagger - \alpha^*(t)a)\big)\Big\}\exp\big\{(i\chi(t)S_\phi^2)\big\} \\ &= e^{i\chi(t)}(|\leftarrow_\phi\rangle\langle\leftarrow_\phi| D(\alpha(t)) + |\rightarrow_\phi\rangle\langle\rightarrow_\phi| D(-\alpha(t))) \end{aligned} \tag{6.12}$$

where $D(\alpha(t)) = e^{\alpha(t)a^\dagger - \alpha^*(t)a}$ is the displacement operator.

From this unitary, we can see that a spin dependent force is exerted on the ions, with states $|\leftarrow_\phi\rangle$ and $|\rightarrow_\phi\rangle$ being displaced in opposite senses. The form of $\alpha(t)$ (equation 6.9) shows that the states move in a circular trajectory in phase space, moving with radius $R = \frac{\eta\Omega_0}{2\delta}$ around centre $C_\pm = \pm\frac{i\eta\Omega_0}{2\delta}e^{-i\phi_m}$. This is shown in figure 6.1, a phase space plot of the real and imaginary parts of $\alpha(t)$, where states $|\leftarrow_\phi\rangle$ and $|\rightarrow_\phi\rangle$ move in circles in opposite directions. At times $\tau = 2\pi q/\delta$ the states return to the origin and the circles close, where q is an integer defining the number of circles performed. However, despite returning to their initial motional state, the states have acquired a phase. This is known as the geometric phase, and is given by $\chi(\tau) = q2\pi R^2$, which is equal to twice the area of the circle(s) completed in phase space. For the single ion case, this phase is global and so can be disregarded, but it becomes crucial for two ion entanglement.

Entanglement between the spin and motional states of the ion can be generated by preparing it in a superposition of the spin eigenstates, such as $|\downarrow\rangle = \frac{1}{\sqrt{2}}(|\leftarrow_\phi\rangle + |\rightarrow_\phi\rangle)$. For an ion prepared in the motional ground state $|\downarrow\rangle|n=0\rangle$, the state evolves with time t as

$$|\psi(t)\rangle = \frac{1}{\sqrt{2}}(|\leftarrow_\phi\rangle|\alpha(t)\rangle + |\rightarrow_\phi\rangle|-\alpha(t)\rangle). \tag{6.13}$$

The two states move in opposite circular trajectories in phase space, as shown in figure 6.1. When the motional states are separated in phase space, there is entanglement between the spin and motional states, and at times τ the states return to the origin. Importantly, the displacement and phases are not dependent on the ion's initial motional state. While shown above for the initial motional state $|n=0\rangle$, this can be extended to any initial motional state, and spin eigenstates will still move in circles in phase space and return to the same initial state.

6.3 Two ion entanglement

This entanglement between the spin and motional states of a single ion is crucial for the entanglement of the spin states of two ions. Instead of applying detuned fields to the sidebands of a single ion, we apply them to both ions simultaneously, and the result is an interaction where phase is acquired spin-dependently, thus allowing the possibility of entanglement.

6.3.1 Theory

We can generalise the Mølmer-Sørensen interaction to two ions, so that we have a Hamiltonian of the form

$$H_{\mathrm{MS}} = H^1_{\mathrm{MS}} + H^2_{\mathrm{MS}}. \tag{6.14}$$

Assuming that the detuning δ and the Rabi frequency Ω_0 is the same for both ions, and that we are only interacting with a single mode, we can write the Hamiltonians for each ion, i, as

$$H^i_{\mathrm{MS}} = -\frac{i\hbar\eta_i\Omega_0}{2}S_{\phi i}(a^\dagger e^{i\delta t}e^{-i\phi_{mi}} - ae^{-i\delta t}e^{i\phi_{mi}}). \tag{6.15}$$

For two ions, there are two motional modes that may be used- the centre of mass (COM) mode and the stretch mode, as described in 2.2.2. For the COM mode, the effective Lamb-Dicke parameters for each ion are $\eta_1 = \eta_2 = \eta_c$, and for the stretch mode they are $\eta_1 = -\eta_2 = \eta_s$. Following the same procedure as for the single ion case, we can find the

effect of this time-dependent Hamiltonian by using the Magnus expansion to express it as a unitary operator. The first order term, O_1, is separable since it only involves first order Hamiltonian terms in the integral, so can be expressed simply as the sum of the terms given by equation 6.8 for each ion, with

$$\alpha_i(t) = \frac{i\eta_i\Omega_0}{2\delta}e^{-i\phi_{mi}}(e^{i\delta t} - 1). \tag{6.16}$$

The second order term, however, contains the commutator $[H_{MS}(t'), H_{MS}(t'')]$, so there are cross terms between the two ions. The second term, given for the single ion case by equation 6.10, becomes

$$O_2 = \sum_{i,j=1}^{2} i\chi_{ij}(t)S_{\phi i}S_{\phi j}, \tag{6.17}$$

and we can define

$$\chi_{ij}(t) = \frac{\eta_i\eta_j\Omega_0^2}{4\delta^2}(\delta t\cos(\Delta\phi_{mij}) - \sin(\Delta\phi_{mij}) - \sin(\delta t - \Delta\phi_{mij})) \tag{6.18}$$

where $\Delta\phi_{mij} = \phi_{mi} - \phi_{mj}$. The time evolution unitary can then be written as

$$U_{\mathrm{MS}}(t) = \exp\left\{\left(\sum_{i=1}^{2} S_{\phi i}(\alpha_i(t)a^\dagger - \alpha_i^*(t)a)\right)\right\}\exp\left\{\left(-\sum_{i,j=1}^{2} i\chi_{ij}(t)S_{\phi i}S_{\phi j}\right)\right\}. \tag{6.19}$$

By setting the phases $\phi_{s1} = \phi_{s2} = \phi_{m1} = \phi_{m2} = 0$, we can write this as

$$\begin{aligned} U_{\mathrm{MS}}(t) =& e^{-i(\chi_{11}+\chi_{22}+\chi_{12}+\chi_{21})}D(\alpha_1+\alpha_2)\left|{\leftarrow\leftarrow}\right\rangle\left\langle{\leftarrow\leftarrow}\right| \\ &+e^{-i(\chi_{11}+\chi_{22}+\chi_{12}+\chi_{21})}D(-\alpha_1-\alpha_2)\left|{\rightarrow\rightarrow}\right\rangle\left\langle{\rightarrow\rightarrow}\right| \\ &+e^{-i(\chi_{11}+\chi_{22}-\chi_{12}-\chi_{21})}D(\alpha_1-\alpha_2)\left|{\leftarrow\rightarrow}\right\rangle\left\langle{\leftarrow\rightarrow}\right| \\ &+e^{-i(\chi_{11}+\chi_{22}-\chi_{12}-\chi_{21})}D(-\alpha_1+\alpha_2)\left|{\rightarrow\leftarrow}\right\rangle\left\langle{\rightarrow\leftarrow}\right| \end{aligned} \tag{6.20}$$

where, for simplicity of notation, we have dropped the time dependence of $\chi_{ij}(t)$ and $\alpha_i(t)$ For the COM mode, since $\eta_1 = \eta_2$, we find $\chi_{11} = \chi_{22} = \chi_{12} = \chi_{21} = \chi_c$ and $\alpha_1 = \alpha_2 = \alpha_c$. This means that the displacements for $|{\leftarrow\rightarrow}\rangle$ and $|{\rightarrow\leftarrow}\rangle$ cancel out, while $|{\leftarrow\leftarrow}\rangle$ and $|{\rightarrow\rightarrow}\rangle$ are displaced by $2\alpha_c(t)$. For the stretch mode, since $\eta_1 = -\eta_2$, we find $\chi_{11} = \chi_{22} = -\chi_{12} = -\chi_{21} = \chi_s$ and $\alpha_1 = -\alpha_2 = \alpha_s$. This means that the opposite to the COM case is true – the displacements cancel for $|{\leftarrow\leftarrow}\rangle$ and $|{\rightarrow\rightarrow}\rangle$, and $|{\leftarrow\rightarrow}\rangle$ and $|{\rightarrow\leftarrow}\rangle$ are displaced by $2\alpha_s(t)$. In both cases, a relative phase of $4\chi(t)$ is accumulated between the sets of states, where $\chi(t)$ is $\chi_s(t)$ or $\chi_c(t)$ depending on the mode being used. It is

this geometric phase that allows entanglement to be produced.

If ions are prepared in state $|\downarrow\downarrow\rangle\,|n=0\rangle \equiv \frac{1}{\sqrt{2}}(|\leftarrow\leftarrow\rangle+|\rightarrow\rightarrow\rangle+|\leftarrow\rightarrow\rangle+|\rightarrow\leftarrow\rangle)\,|n=0\rangle$, then, for COM mode entanglement, our state evolves in time as

$$\begin{aligned}|\psi_c(t)\rangle =& e^{-4i\chi_c(t)}\,|\leftarrow\leftarrow\rangle\,|2\alpha_c(t)\rangle \\ &+e^{-4i\chi_c(t)}\,|\rightarrow\rightarrow\rangle\,|-2\alpha_c(t)\rangle \\ &+|\leftarrow\rightarrow\rangle\,|n=0\rangle \\ &+|\rightarrow\leftarrow\rangle\,|n=0\rangle\,,\end{aligned} \tag{6.21}$$

and for the stretch mode

$$\begin{aligned}|\psi_s(t)\rangle =& |\leftarrow\leftarrow\rangle\,|n=0\rangle \\ &+|\rightarrow\rightarrow\rangle\,|n=0\rangle \\ &+e^{-4i\chi_s(t)}\,|\leftarrow\rightarrow\rangle\,|2\alpha_s(t)\rangle \\ &+e^{-4i\chi_s(t)}\,|\rightarrow\leftarrow\rangle\,|-2\alpha_s(t)\rangle\,.\end{aligned} \tag{6.22}$$

As for the single ion case, full circles in phase space are completed when $\alpha(\tau)=0$ at times $\tau = 2\pi q/\delta$, where q is an integer which defines the number of complete circles performed. At these times, there is no residual entanglement between the spin and motional modes. In order to create a maximally entangled state, we need to ensure the relative phase acquired $4\chi(\tau)$ is equal to $\pi/2$. This can be achieved by setting

$$\delta = \pm 2\sqrt{q}\eta\Omega_0. \tag{6.23}$$

By setting the detuning appropriately, it is therefore possible to generate maximally entangled states.

For an ion initialised in spin state $|\downarrow\downarrow\rangle$ but in a thermal state with mean number $\bar{n}$ rather than in the ground state $|n=0\rangle$, the density matrix can be used to understand the evolution of state probabilities. This can be defined as

$$\rho_{\mathrm{th}}(t) = \sum_{n=0}^{\infty} p_n\,|\psi_n(t)\rangle\,\langle\psi_n(t)|\,, \tag{6.24}$$

where the thermal coefficients are defined as $p_n = (1/(1+\bar{n}))(\bar{n}/(1+\bar{n}))^n$ and the state $|\psi_n(t)\rangle$ is

$$|\psi_n(t)\rangle = e^{4i\chi(t)}(|\leftarrow\leftarrow\rangle+|\rightarrow\rightarrow\rangle)\,|n\rangle+|\leftarrow\rightarrow\rangle\,D(2\alpha(t))\,|n\rangle+|\rightarrow\leftarrow\rangle\,D(-2\alpha(t))\,|n\rangle\,. \tag{6.25}$$

We are using $\alpha(t)$ and $\chi(t)$ to represent either the COM or stretch mode functions, since the following analysis is equivalent for both. The reduced density matrix is found by tracing over the motional states. This describes only the spin degree of freedom, and is given by

$$\rho_{\mathrm{th}}^{(s)}(t) = \sum_{m=0}^{\infty} \langle m| \rho_{\mathrm{th}}(t) |m\rangle . \tag{6.26}$$

This reduced density matrix can be used to find expressions for the evolution of the probabilities of the states $|\uparrow\uparrow\rangle$, $|\downarrow\downarrow\rangle$, $|\downarrow\uparrow\rangle$ and $|\uparrow\downarrow\rangle$:

$$P(\uparrow\uparrow) = \frac{1}{8}(3 + e^{-16|\alpha(t)|^2(\bar{n}+\frac{1}{2})} - 4\cos(4\chi(t))e^{-4|\alpha(t)|^2(\bar{n}+\frac{1}{2})}), \tag{6.27}$$

$$P(\downarrow\downarrow) = \frac{1}{8}(3 + e^{-16|\alpha(t)|^2(\bar{n}+\frac{1}{2})} + 4\cos(4\chi(t))e^{-4|\alpha(t)|^2(\bar{n}+\frac{1}{2})}), \tag{6.28}$$

$$P(\uparrow\downarrow) = P(\downarrow\uparrow) = \frac{1}{8}(1 - e^{-16|\alpha(t)|^2(\bar{n}+\frac{1}{2})}). \tag{6.29}$$

At the gate time τ, when $\alpha(\tau) = 0$, the spin state of the ion should be entirely composed of the states $|\uparrow\uparrow\rangle$ and $|\downarrow\downarrow\rangle$.

To find the fidelity of the state produced at the gate time τ, we can calculate the overlap with the ideal Bell state, given by $|\psi_\phi\rangle = \frac{1}{\sqrt{2}}(|\downarrow\downarrow\rangle + e^{i\phi}|\uparrow\uparrow\rangle)$. This gives

$$\mathrm{F_{Bell}} = \langle\psi_\phi| \rho |\psi_\phi\rangle = \frac{1}{2}(\rho_{\uparrow\uparrow,\uparrow\uparrow} + \rho_{\downarrow\downarrow,\downarrow\downarrow} + \mathrm{e}^{\mathrm{i}\phi}\rho_{\downarrow\downarrow,\uparrow\uparrow} + \mathrm{e}^{-\mathrm{i}\phi}\rho_{\uparrow\uparrow,\downarrow\downarrow}) \tag{6.30}$$

where $\rho_{\uparrow\uparrow,\uparrow\uparrow} = P(\uparrow\uparrow)$ is given in equation 6.27 and $\rho_{\downarrow\downarrow,\downarrow\downarrow} = P(\downarrow\downarrow)$ is given in equation 6.28. The specific phase ϕ of the Bell state is usually unimportant as it can be corrected for using single qubit rotations. By calculating the relevant density matrix elements for the Bell state $|\psi\rangle = (|\downarrow\downarrow\rangle + i|\uparrow\uparrow\rangle)/\sqrt{2}$, we can use equation 6.30 to find the theoretical fidelity as a function of time, given by

$$\mathrm{F_{Bell}} = \frac{1}{8}(3 + \mathrm{e}^{-16|\alpha(\mathrm{t})|^2(\bar{\mathrm{n}}+\frac{1}{2})} + 4\sin(4\chi(\mathrm{t}))\mathrm{e}^{-4|\alpha(\mathrm{t})|^2(\bar{\mathrm{n}}+\frac{1}{2})}) \tag{6.31}$$

which gives a fidelity $\mathrm{F_{Bell}} = 1$ at the gate time τ, indicating a maximally entangled two qubit state. While this method has been demonstrated here for two ions, it can be generalised to higher numbers of ions.

6.3.2 Measuring the fidelity

The fidelity of a two qubit gate can be characterised by measuring the overlap of the final state with a Bell state, as defined in equation 6.30. The first two terms, $\rho_{\downarrow\downarrow,\downarrow\downarrow}$ and

$\rho_{\uparrow\uparrow,\uparrow\uparrow}$, can be found by simply measuring the populations of the ions after a gate pulse, allowing the probability $P(\downarrow\downarrow) + P(\uparrow\uparrow)$ to be calculated. In order to find the off-diagonal elements of the density matrix, we perform a parity measurement. A $\pi/2$ pulse is applied to both ions simultaneously with the same phase, so that each ion experiences a rotation $R(\pi/2, \phi_p)$, where ϕ_p is the phase of the pulse. We then define the parity as

$$\begin{aligned}\Pi &= P(\uparrow\uparrow) + P(\downarrow\downarrow) - P(\uparrow\downarrow) - P(\downarrow\uparrow) \\ &= 2|\rho_{\uparrow\downarrow,\downarrow\uparrow}| \cos(\phi_{\uparrow\downarrow,\downarrow\uparrow}) - 2|\rho_{\uparrow\uparrow,\downarrow\downarrow}| \cos(\phi_{\uparrow\uparrow,\downarrow\downarrow} + 2\phi_p).\end{aligned} \tag{6.32}$$

where $|\rho_{\uparrow\downarrow,\downarrow\uparrow}|$ and $|\rho_{\uparrow\uparrow,\downarrow\downarrow}|$ are the amplitudes of the complex matrix elements, and $\phi_{\uparrow\downarrow,\downarrow\uparrow}$ and $\phi_{\uparrow\uparrow,\downarrow\downarrow}$ are the arguments. By scanning the phase of the parity pulse ϕ_p, we find that the parity oscillates at a rate $2\phi_p$, and therefore by fitting a cosine function to the resultant measurement, we can find the value of $|\rho_{\uparrow\uparrow,\downarrow\downarrow}|$. Taking the average of the population and parity measurement gives us the total fidelity.

6.3.3 Two ion entanglement using the dressed state qubit

As discussed in chapter 4, the dressed state qubit can be used to reduce the susceptibility of a qubit to magnetic field noise while maintaining the sensitivity to magnetic fields which allows for coupling between spin and motional states. We therefore use a dressed state qubit to perform two ion entanglement, using the pair of states $\{|0'\rangle, |D\rangle\}$ as the qubit so that for the derivation shown above $|\downarrow\rangle \equiv |0'\rangle$ and $|\uparrow\rangle \equiv |D\rangle$. The gate Rabi frequency Ω_0 is given by $\Omega_0 = \Omega_{\mathrm{D}} = \Omega_{\mathrm{rf}}/\sqrt{2}$. The different transition frequencies of the two ions in the magnetic field gradient mean that four distinct gate fields are required, corresponding to two for each ion.

Due to the nature of our dressed state qubit, when performing an MS gate there is an AC Stark shift present that does not exist in a two level system. AC Stark effects resulting from the gate fields on the dressed states connected to $|0'\rangle$ via $|+1\rangle$ are cancelled out due to symmetry. However, AC Stark shifts on the dressed states connected to $|0'\rangle$ via $|-1\rangle$

result in a shift in the qubit transition frequency $\omega_{0'\leftrightarrow \mathrm{D}}$. This is given by

$$\begin{aligned}\Delta\omega_{0'\leftrightarrow \mathrm{D}} = &\frac{\Omega_{\mathrm{D}}^2}{2}\left(\frac{1}{-\Delta\omega_z+\nu_z}+\frac{1}{-\Delta\omega_z-\nu_z}\right)\\ &+\frac{\Omega_{\mathrm{ud}}^2}{4}\left(\frac{1}{-\Delta\omega_z+\nu_z-\Omega_{\mu\mathrm{w}}/\sqrt{2}}+\frac{1}{-\Delta\omega_z+\nu_z+\Omega_{\mu\mathrm{w}}/\sqrt{2}}\right.\\ &\left.+\frac{1}{-\Delta\omega_z-\nu_z-\Omega_{\mu\mathrm{w}}/\sqrt{2}}+\frac{1}{-\Delta\omega_z-\nu_z+\Omega_{\mu\mathrm{w}}/\sqrt{2}}\right)\\ &\approx \frac{3\Omega_0^2\Delta\omega_z}{2\nu_z^2}\end{aligned} \tag{6.33}$$

where $\Delta\omega_z$ is the second order Zeeman shift, $\Omega_{\mu\mathrm{w}}$ is the dressing field Rabi frequency, $\Omega_{\mathrm{ud}} = \Omega_{\mathrm{D}}/\sqrt{2}$ is the Rabi frequency of the $|0'\rangle \leftrightarrow |u\rangle$ and $|0'\rangle \leftrightarrow |d\rangle$ transitions, and we have made the approximations $|\delta_0+\nu_z| \approx |\nu_z|$ and $|\nu_z| \gg \Omega_{\mathrm{D}}, \Omega_{\mu\mathrm{w}}$. This Stark shift can be compensated for by shifting the frequencies of the gate fields to $\delta_b = -\delta + \Delta\omega_{0'\leftrightarrow \mathrm{D}}$ and $\delta_r = \delta + \Delta\omega_{0'\leftrightarrow \mathrm{D}}$ so that they are symmetric around the Stark shifted carriers. The AC Stark shifts are different for each ion due to the different values of the second order Zeeman shift.

6.3.4 Experimental demonstration

We demonstrate a long-wavelength driven two qubit gate using the dressed state qubit, as presented in [28]. The stretch mode of the two ions was used with a frequency of $\nu_s/2\pi = 459.34(1)\,\mathrm{kHz}$, and the ions were sideband cooled using microwave radiation on the $|0\rangle$ to $|+1\rangle$ red sideband transition to cool the ion to $\bar{n} \approx 0.14$. The ions were prepared in the state $|0'0'\rangle$ by first optically pumping to $|00\rangle$ and then using π pulses on the clock transition $|0\rangle \leftrightarrow |0'\rangle$ for each ion. Microwave dressing fields of Rabi frequency $\Omega_{\mu\mathrm{w}1}/2\pi = 20.5\,\mathrm{kHz}$ and $\Omega_{\mu\mathrm{w}2}/2\pi = 21.6\,\mathrm{kHz}$ were applied to the $|0\rangle \leftrightarrow |-1\rangle$ and $|0\rangle \leftrightarrow |+1\rangle$ transitions for each ion respectively. The dressing field Rabi frequencies for each ion are set to different values in order to suppress the spin-spin coupling due to the static magnetic field gradient which drives population between $|DD\rangle$ and $(|ud\rangle + |du\rangle)/\sqrt{2}$ [53], therefore causing error. The qubit transition frequency $|0'\rangle \leftrightarrow |D\rangle$ was measured using a π pulse of 2 ms, and the gate power was set to $\Omega_0/2\pi = 45.4\,\mathrm{kHz}$. The gate time was 2.7 ms and the gate pulse was ramped over a time of $10\,\mu\mathrm{s}$ at the beginning and the end of the gate pulse with a $\sin^2$ shape. The measured evolution of the states over twice the gate time is shown in figure 6.2, where solid lines show the theoretical evolution of the population probabilities $P(0'0')$, $P(DD)$, and $P(0'D)+P(D0')$. Good agreement is seen between the experimental data and the theory curves, with a small deviation at the end of the time scan which may

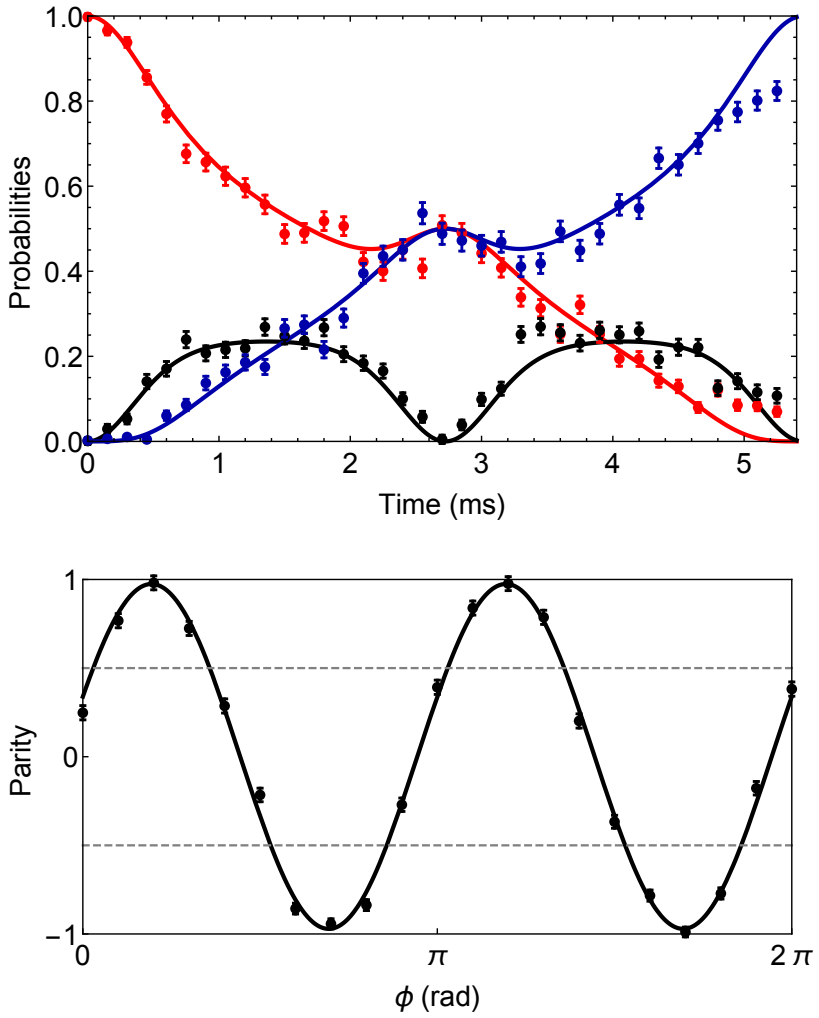

Figure 6.2: Single loop Mølmer-Sørensen gate performed in the dressed state basis, with stretch mode frequency $\nu/2\pi$ =459.34(1) kHz, gate field Rabi frequency $\Omega_0/2\pi$ =45.4 kHz and gate time τ =2.7 ms. A gate time scan is shown (top) where solid lines show theoretical population probabilities $P(0'0')$ (red), $P(DD)$ (blue), and $P(0'D)+P(D0')$ (black). A parity oscillation at the gate time is shown (bottom) with fitted amplitude P=0.972(17). The parity oscillation and a separate population measurement give a fidelity F_{Bell} =0.985(12). Figure from [28]

be due to an incorrectly set AC Stark shift or a drift of gate parameters. The population at the gate time was measured to be $P(0'0') + P(DD)$=0.997(8) using 1300 repetitions. A parity curve is shown below the population time scan, and a fit to this gives $P = 0.972(17)$. These two measurements give a gate fidelity of $F_{\text{Bell}} = 0.985(12)$. The sources of error contributing to the infidelity will be discussed in the next section.

6.4 Gate errors

Two qubit gates are subject to various sources of errors which limit the fidelity. These errors can be classed into two broad categories: errors that are due to the fundamental nature of the system (such as heating and depolarisation), and errors due to experimental mis-set, drift or noise (such as detuning mis-set). In order to optimise gate parameters, all these errors must be taken into account. The error budget for the gate experimentally demonstrated in the previous section is shown in table 6.1. This budget agrees within experimental error to the measured infidelity. In this section, I will explain these leading error terms, as well as errors that arise from parameter mis-set.

Source	Infidelity (10^{-2})
Motional heating	0.96
Depolarisation	0.27
Carrier coupling	$< 10^{-4}$
Kerr coupling	0.08
Total	1.31

Table 6.1: Error budget for the experimental implementation of the MS gate shown in figure 6.2.

6.4.1 Heating

Although there is no entanglement between spin and motional states at the end of the gate operation, heating of the motional mode during the gate process while the spin and motional states are entangled induces error. In order to understand the effect of this heating, we can model the evolution of the density matrix using a Master equation [14]. This approach was used for studying the effects of depolarising on single qubit gates in section 5.5.4. The Master equation is

$$\frac{d}{dt}\rho = -i[H_{\text{MS}}, \rho] + L(\rho) \tag{6.34}$$

where the Lindbladian $L(\rho)$ is of the form

$$L(\rho) = -\frac{1}{2}\sum_m (C_m^\dagger C_m \rho + \rho C_m^\dagger C_m) + \sum_m C_m \rho C_m^\dagger. \tag{6.35}$$

For heating, the Lindblad operators are $C_1 = \sqrt{\dot{\bar{n}}}a$ and $C_2 = \sqrt{\dot{\bar{n}}}a^\dagger$, where $\dot{\bar{n}}$ is the heating rate in quanta per second. Moving to the interaction picture with respect to the gate Hamiltonian H_{MS} so that heating is the only interaction, we find that the operators C_1 and C_2 transform as

$$\tilde{C}_1 = \sqrt{\dot{\bar{n}}}(a - i\alpha^*(t)S_\phi) \tag{6.36}$$

$$\tilde{C}_2 = \sqrt{\dot{\bar{n}}}(a^\dagger + i\alpha(t)S_\phi) \tag{6.37}$$

which is a formal representation of the fact that heating during the gate operation affects the qubit states. These expressions can be substituted into the Master equation, and by tracing over the motional states we find an equation for the elements of the reduced density matrix

$$\dot{\rho}_{M_\phi, M'_\phi}(t) = -\dot{\bar{n}}|\alpha(t)|^2(M_\phi - M'_\phi)^2 \rho_{M_\phi, M'_\phi}(t) \tag{6.38}$$

where M_ϕ and M'_ϕ are the eigenvalues corresponding to $S_\phi \rho_{M_\phi, M'_\phi}(t)$ and $\rho_{M_\phi, M'_\phi}(t) S_\phi$ respectively. Substituting in the expression for $\alpha(t)$ and integrating gives the reduced density matrix at the gate time τ

$$\rho_{M_\phi, M'_\phi}(\tau) = \rho_{M_\phi, M'_\phi}(0) \exp\left\{\left(-\dot{\bar{n}}\frac{(M_\phi - M'_\phi)^2}{8q}\tau\right)\right\}. \tag{6.39}$$

In this interaction picture, the density matrix is ideally constant and the exponential term represents the detrimental effect of heating. We can then move back to the lab frame where we find that this heating effect causes elements of the gate density matrix to decohere at different rates, depending on the S_ϕ eigenvalues. Finding the fidelity at the gate time using the expression in equation 6.30 gives an infidelity due to heating of

$$\epsilon_{\mathrm{heating}} = 1 - \frac{1}{8}(3 + 4e^{-\frac{\dot{\bar{n}}\tau}{2q}} + e^{-\frac{2\dot{\bar{n}}\tau}{q}}) \tag{6.40}$$

which, for small infidelities, approximates as

$$\epsilon_{\mathrm{heating}} = \frac{4\dot{\bar{n}}\tau}{q}. \tag{6.41}$$

Increasing the number of loops q can therefore reduce the infidelity caused by heating. However, the gate time increases with $\sqrt{q}$ so other errors will become increasingly important.

6.4.2 Dephasing and depolarising

Following the approach taken in section 5.5.4 for the dephasing and depolarising of the dressed state qubit, we can model this process using a Master equation. Measurements of the lifetime and coherence time at the time of the two qubit gate implementation gave equal results of approximately $T_1 \approx T_2 \approx 0.65\,\mathrm{s}$. This suggests that the dominant process is depolarising, where population is driven between $|D\rangle$ and $\{|u\rangle, |d\rangle\}$. This effect has been simulated by Dr J. Randall [53], taking the worst case scenario by preparing the two ions in a Bell state and simulating the effect of the depolarising noise terms over the gate time. An exponential decay analytical expression was found to fit the results well, giving

$$\epsilon_{\mathrm{depolarisation}} = (1 - F_0)(1 - e^{-\frac{\gamma_0 \tau}{T_1}}), \tag{6.42}$$

where T_1 is the lifetime of the qubit, measured as $T_1 = 0.63(4)\,\mathrm{s}$, and $F_0 = 0.2778$ and $\gamma_0 = 0.92$ were found to give good agreement on timescales similar to the gate time. Reducing the gate time τ is therefore the only way to decrease the depolarising error for a fixed lifetime T_1.

6.4.3 Off-resonant coupling

We have assumed so far that gate fields only interact with the sideband they are addressing. This is a good approximation in the limit $\Omega_0 \ll \nu$ where Ω_0 is the Rabi frequency of the gate fields and ν is the secular frequency of the motional mode used for the gate, and so is approximately the frequency splitting between the gate fields and the carrier transition. However, as Ω_0 becomes larger, the off-resonant excitation also increases. Since higher gate power to drive faster gates is generally desirable, this effect becomes important. The excitation caused by the gate fields interacting with off-resonant transitions is oscillatory in behaviour at a frequency equal to the detuning from the carrier, $\nu + \delta$. This behaviour is coherent, so if the gate time is set at a multiple of the oscillation period we should not see any adverse effects on the gate fidelity. However, such time accuracy is difficult to obtain. Furthermore, in our dressed state system, we have multiple concurrent off-resonant excitations, and finding a time which minimises all oscillations would be challenging.

We therefore see the introduction of an infidelity given approximately by Ω^2/Δ^2 [14].

This can be understood from equation 2.30, where the amplitude of the oscillations is given by $\Omega^2/(\Omega^2+\Delta^2)$, which for $\Omega \ll \Delta$ can be approximated as Ω^2/Δ^2. For the dressed state system, there are six off-resonant carrier excitations due to the six dressed states. For the two $|D\rangle$ excitations, the Rabi frequency is given by $\Omega_{\mathrm{D}} = \Omega_0$ and for the $|u\rangle$ and $|d\rangle$ terms the Rabi frequency is $\Omega_{\mathrm{ud}} = \Omega_0/\sqrt{2}$. We can approximate that all of the dressed states are detuned from the gate fields by the secular frequency ν, since $\delta \ll \nu$ and $\Omega_{\mu w}/\sqrt{2} \ll \nu$. We therefore have a total error term of

$$\epsilon_{\mathrm{c}} \approx 2\frac{\Omega_{\mathrm{D}}^2}{\nu^2} + 4\frac{\Omega_{\mathrm{ud}}^2}{\nu^2} = \frac{4\Omega_0^2}{\nu^2}. \tag{6.43}$$

This error term becomes large as the gate Rabi frequency Ω_0 becomes comparable to the motional mode frequency ν.

This error can be significantly reduced, however, by introducing pulse shaping [84], where instead of instantaneously turning the gate fields on or off, the RF field amplitude is ramped up or down at the beginning and end of the gate pulse over a time t_{ramp} using a $\sin^2$ shape, as in section 5.5.1. This is demonstrated in figure 6.3, a two level simulation of a two qubit gate at secular frequency $\nu/2\pi = 460\,\mathrm{kHz}$ of total time 3.4 ms, which includes off-resonant coupling to the carrier. For the case where there is no pulse shaping, the population $P(\uparrow\downarrow) + P(\downarrow\uparrow)$ oscillates and, depending on the exact timing of the gate, the average error would be approximately 2.5%. However, with a ramp time of $10\,\mu$s, which is a fraction of 0.3% of the total gate time, this source of error is almost completely removed.

Figure 6.4 shows the fidelity as a function of the Rabi frequency, when the Rabi frequency is expressed as a proportion of the secular frequency (i.e. the detuning between the gate field and the off-resonant carrier excitation transition). The secular frequency is again 460 kHz. Two qubit gate simulations are shown with pulse shaping times $0\,\mu$s and $10\,\mu$s. In general, the limit $\Omega_0/\nu \leq 0.1$ is imposed, which is equivalent to keeping the off-resonant coupling error to on the order of 10^{-4} or less, which makes the error negligible in this implementation. Longer ramp times are not used since they would affect the character of the gate as they become significant compared to the gate time.

6.4.4 Symmetric detuning

A gate error is induced if the magnitude of the detuning from the sideband for each ion is incorrect, so that $\delta_r = \delta + \Delta$ and $\delta_b = -\delta - \Delta$, where $\delta = 2\sqrt{q}\eta\Omega$ is the correct detuning and Δ is a small detuning mis-set. This symmetric detuning would typically be the same for both ions by ensuring that the frequency splitting between the two gate fields is the

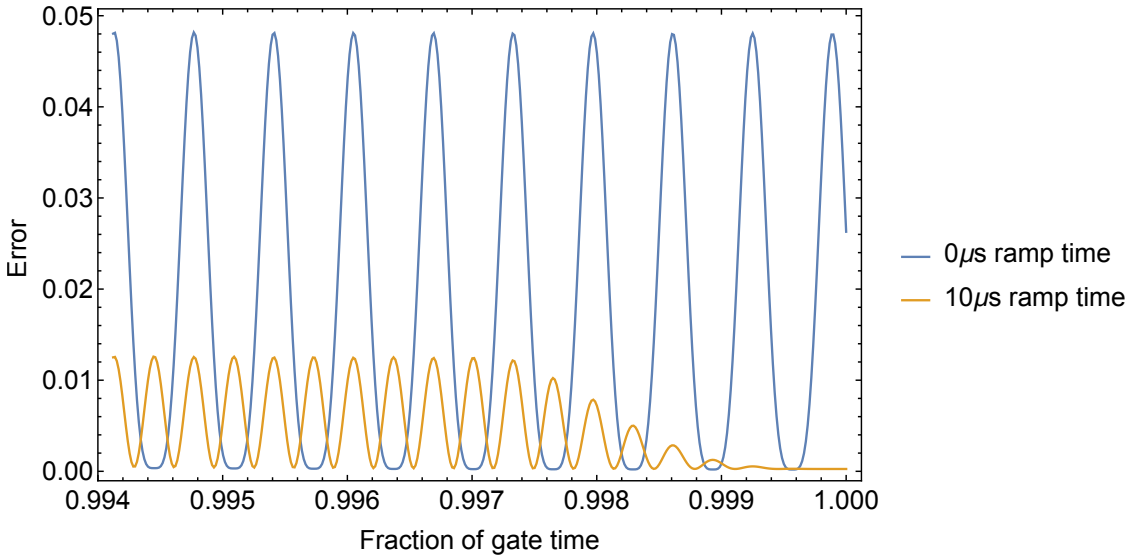

Figure 6.3: Off-resonant coupling to a carrier transition for a two level system is simulated for a two qubit gate driven at $\Omega_0 \approx 0.08\nu$, where $\nu/2\pi = 460\,\text{kHz}$. The error in the final $20\,\mu\text{s}$ is shown. The blue line shows the gate with no pulse-shaping, and the error can be seen to oscillate between around 0 and 5%. The orange line shows a gate with a $10\,\mu\text{s}$ ramp time at the beginning and end of the gate, and it can be seen that the error ramps down to approximately zero as the populations adiabatically follow the ramped pulse.

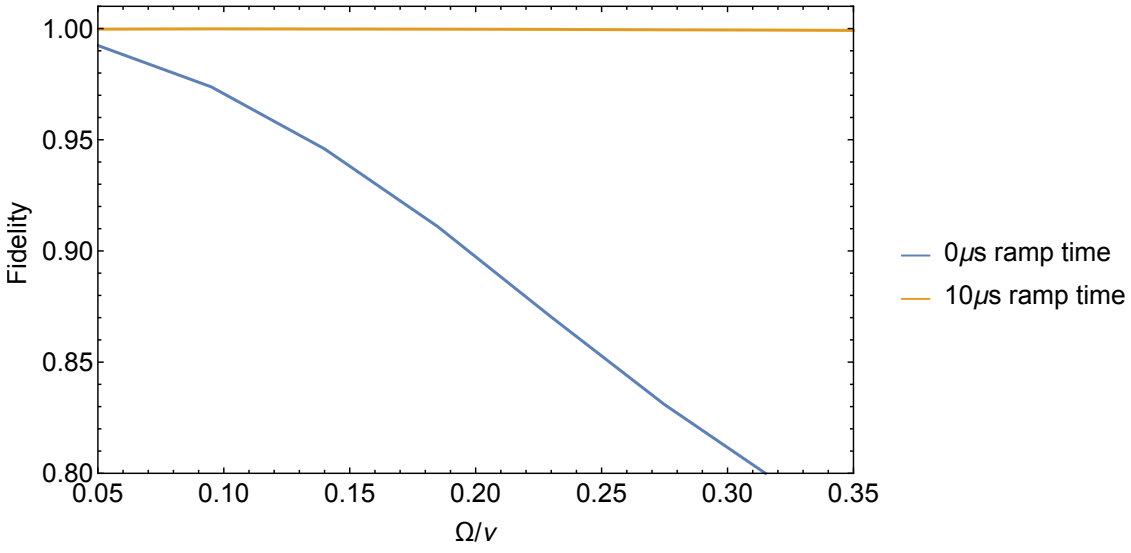

Figure 6.4: The fidelity of a gate is simulated with off-resonant coupling to a carrier transition with increasing ratio Ω/ν, where $\nu/2\pi = 460\,\text{kHz}$. The blue line is a gate with no pulse shaping, and it can be seen that the fidelity (averaged over 2 oscillations) quickly decreases. The orange line is with a $10\,\mu\text{s}$ ramp time, which can be seen to protect against this error.

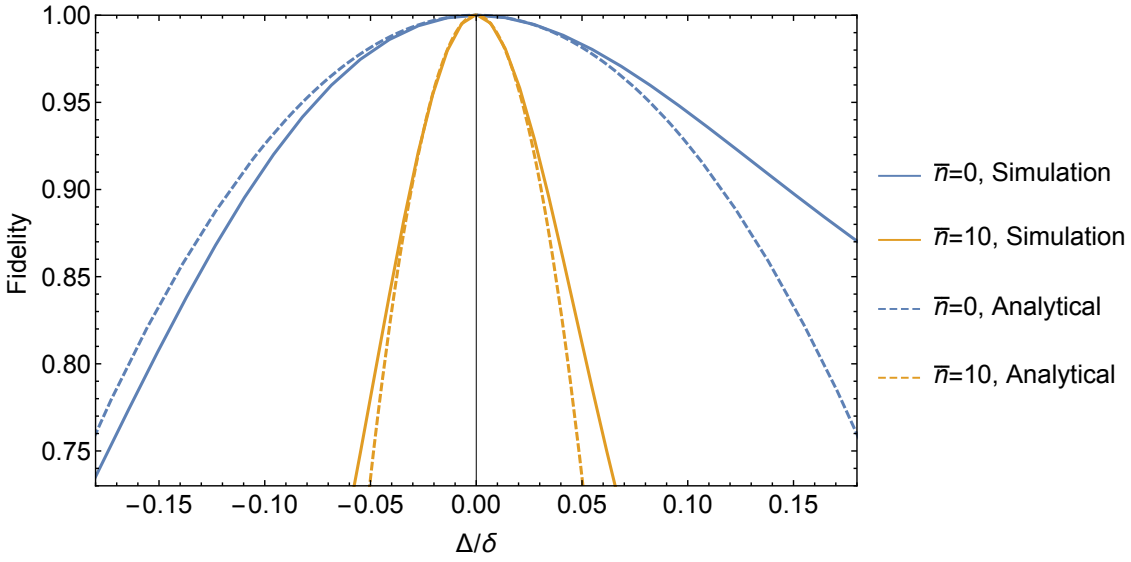

Figure 6.5: The fidelity with a symmetric detuning mis-set Δ is simulated and shown by solid lines for $\bar{n} = 0$ (blue) and $\bar{n} = 10$ (orange). The analytical approximations are also shown for both initial mean motional states by dashed lines, with good agreement seen at low values of Δ/δ. A high increase in sensitivity to symmetric detuning is seen for the higher value of $\bar{n}$.

same for each ion. This kind of error can occur if the parameters are initially mis-set due to an incorrect measurement of the secular frequency, or if there is an undetected change in secular frequency over time (for example due to a drift in the voltage of the trapping DC electrodes).

This mis-set in detuning means that loops in phase space do not completely close, leaving residual entanglement between the spin and motional states of the ion at the end of the gate operation. Furthermore, the accumulated phase is no longer equal to $\pi/2$, the phase required to generate a maximally entangled state. Starting from equation 6.31 for the fidelity of a two qubit gate, we can find an analytical expression for the error caused by a symmetric detuning mis-set Δ by expanding around the fidelity F = 1. This gives

$$\epsilon_\Delta = \frac{2q(2\bar{n}+1)+1}{4}\pi^2\left(\frac{\Delta}{\delta}\right)^2 \tag{6.44}$$

up to $O(\Delta^2)$.

Numerical simulations of gate infidelity as a function of fractional symmetric detuning mis-set at initial mean motional states $\bar{n} = 0$ and $\bar{n} = 10$ are shown in figure 6.5 (solid lines). The fidelity of the detuned state is calculated with respect to the Bell state produced at zero detuning, to account for any unknown change in phase of the entangled state. The asymmetry seen for higher positive fractional detunings shows the introduction of third order and higher terms not included in equation 6.44. A significant increase in

sensitivity is seen with higher $\bar{n}$. This makes performing gates at higher initial mean motional states, such as those achieved after Doppler cooling, challenging due to the high sensitivity to parameter mis-set. This therefore means that near ground state cooling is generally required to reach high fidelities. The analytical approximations from equation 6.44 are also shown (dashed lines), showing good agreement at low fractional symmetric detunings.

6.4.5 Asymmetric detuning

Gate infidelity can also be caused by an asymmetric frequency mis-set, so that $\delta_r = \delta + \Delta_a$ and $\delta_b = -\delta + \Delta_a$. This type of mis-set causes the gate fields to be asymmetrically positioned around the carrier transition, and can be a result of an undetected change in the qubit transition frequency on either ion, $|0'\rangle \leftrightarrow |D\rangle$. It can also be caused by an incorrectly set AC Stark shift. AC Stark shifts are calculated from equation 6.33, but if either the gate powers are incorrectly measured or there is an undetected change in the gate power, an asymmetric detuning is introduced. This type of detuning can be independent for each ion. Due to the difficulty in obtaining an analytical expression for this type of detuning error, we study its effects using numerical simulation as shown in figure 6.6. The blue line shows the simulation results at $\bar{n} = 0$ for an equal asymmetric detuning on both ions such that $\Delta_1 = \Delta_2 = \Delta_a$. The orange line instead is for an asymmetric detuning on only one ion, so that $\Delta_1 = \Delta_a$ and $\Delta_2 = 0$, and shows decreased sensitivity compared to the case where both ions are detuned. The green line is a simulation for $\Delta_1 = \Delta_2 = \Delta_a$ at $\bar{n} = 10$, and, similarly to the symmetric detuning, we see an increase in sensitivity with increased initial motional mode of the ion. Although $\bar{n} = 10$ is still below the Doppler cooling limit, higher values of $\bar{n}$ take a long time to simulate due to the large number of motional states required to form an effectively complete Hilbert space.

6.4.6 Rabi frequency mis-set

Gate infidelity can result from an incorrect gate Rabi frequency, so that for the two ions $\Omega_1 = \Omega_2 = \Omega_0 + \Delta\Omega$. In this case, full circles are still completed in phase space, as $\alpha(\tau) = 0$. However, the phase accumulated during the gate will be incorrect. We can find an expression for the error caused by this as before by expanding the fidelity around F = 1

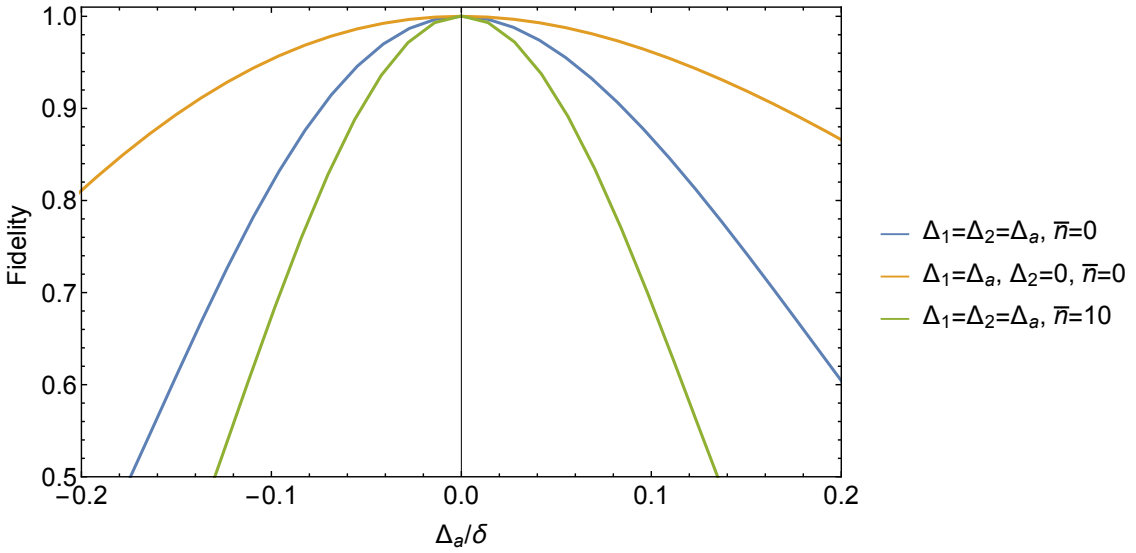

Figure 6.6: Results of a numerical simulation for an asymmetric detuning mis-set Δ_a on the two qubit gate, with fidelity plotted against Δ_a as a fraction of the gate detuning δ. At $\bar{n} = 0$, we consider two cases: an equal asymmetric detuning on both ions (blue), and an asymmetric detuning on only one ion (orange), which exhibits a lower sensitivity. A simulation at $\bar{n} = 10$ is also shown (green), which shows a higher sensitivty to asymmetric detuning.

[85]. Using equation 6.31, we can write the fidelity at the gate time, where $\alpha(\tau) = 0$, as

$$\begin{aligned} F &= \frac{1}{2}(1 + \sin(\frac{\pi}{2} - \Delta\phi)) \\ &\approx 1 - \frac{1}{4}\Delta\phi^2 \end{aligned} \tag{6.45}$$

where $\Delta\phi$ is the error in the acquired phase from the ideal value of $\pi/2$, and the approximation is for small values of $\Delta\phi$. The error can then be written as

$$\epsilon_{\Delta\Omega} \approx \frac{\pi^2}{4}\left(\frac{\Delta\Omega}{\Omega_0}\right)^2. \tag{6.46}$$

There is therefore no dependence on $\bar{n}$, and the overall sensitivity is lower than the sensitivity to symmetric detuning errors.

We can also calculate what happens during the gate when the Rabi frequencies are mismatched, so that $\Omega_1 \neq \Omega_2$. Gate parameters are set using the average value of Rabi frequency, so that $\Omega_0 = \frac{1}{2}(\Omega_1 + \Omega_2)$, and we define $\Delta\Omega_{12} = \frac{1}{2}(\Omega_1 - \Omega_2)$. In this case, ions experience different magnitude forces, and the displacements are not equal since $\alpha_1(t) \neq \alpha_2(t)$. This means that all four two ion states move in circles, since displacement is not completely cancelled, as can be seen from equation 6.20. All of these circles close at the gate time, but the relative phase acquired is imperfect. The phase acquired by each

of the four states can be calculated, using

$$\chi_{ij}(\tau) = \frac{\pi}{8}\frac{\Omega_i\Omega_j}{\Omega_0^2}. \tag{6.47}$$

For the COM mode, the two states which would normally be displaced, $|{\leftarrow}{\leftarrow}\rangle$ and $|{\rightarrow}{\rightarrow}\rangle$, acquire a phase of

$$\begin{aligned}\phi &= \chi_{11}(\tau) + \chi_{22}(\tau) + \chi_{12}(\tau) + \chi_{21}(\tau) \\ &= \frac{\pi}{8}\frac{(\Omega_1+\Omega_2)^2}{\Omega_0^2} = \frac{\pi}{2}.\end{aligned} \tag{6.48}$$

However, the states $|{\leftarrow}{\rightarrow}\rangle$ and $|{\rightarrow}{\leftarrow}\rangle$, which for perfect experimental parameters would remain stationary, also acquire a phase. This is given by

$$\begin{aligned}\Delta\phi &= \chi_{11}(\tau) + \chi_{22}(\tau) - \chi_{12}(\tau) - \chi_{21}(\tau) \\ &= \frac{\pi}{8}\frac{(\Omega_1-\Omega_2)^2}{\Omega_0^2} = \frac{\pi}{2}\left(\frac{\Delta\Omega_{12}}{\Omega_0}\right)^2.\end{aligned} \tag{6.49}$$

There is therefore an error in the acquired relative phase of $-\Delta\phi$. Using equation 6.45, the error can be written as

$$\epsilon_{\Omega_1\neq\Omega_2} = \frac{\pi^2}{16}\left(\frac{\Delta\Omega_{12}}{\Omega_0}\right)^4. \tag{6.50}$$

This error is the same for the stretch mode. The fractional dependence is two orders of magnitude smaller than for error for a Rabi frequency offset on both ions given in equation 6.46, so this error is negligible.

6.4.7 Kerr effect

The non-linear form of the Coulomb repulsion between ions leads to a small inherent anharmonicity in any motional modes that involve relative motion between the ions, such as the stretch mode. This means that the frequency of the mode is dependent on ion separation, and leads to a coupling between modes. The axial stretch mode we use for the gate is then coupled to the radial rocking mode. The form of this coupling is given by [86, 87]

$$H_{\text{kerr}} = \hbar K a_s a_s^\dagger a_r a_r^\dagger \tag{6.51}$$

where a_s and a_r are the ladder operators for the stretch and rocking modes respectively, and the coupling constant is given by

$$K = -\frac{\nu_s}{2}\left(1 + \frac{\nu_s^2}{4\nu_r^2 - \nu_s^2}\right)\left(\frac{\nu_z}{\nu_r}\right)\left(\frac{2\hbar\nu_z}{\alpha^2 mc^2}\right)^{\frac{1}{3}} \tag{6.52}$$

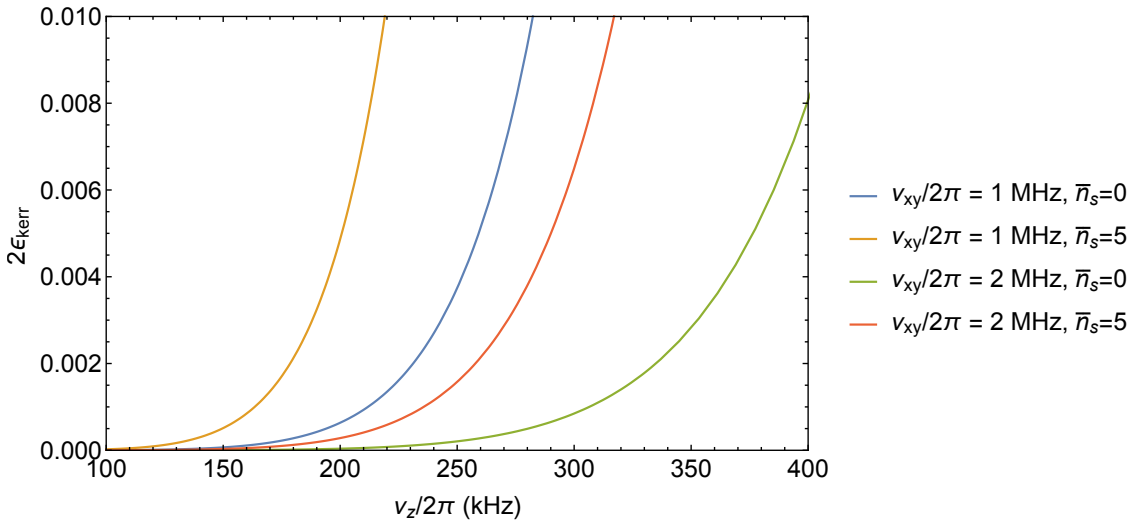

Figure 6.7: Infidelity due to Kerr coupling of the stretch mode used for the gate to the radial modes, plotted against the frequency of the COM mode ν_z for radial modes $\nu_{xy} = 1\,\text{MHz}$ and $\nu_{xy} = 2\,\text{MHz}$, and initial phonon state of the stretch mode $\bar{n} = 0$ and $\bar{n} = 5$.

where ν_z is the axial trap frequency, $\nu_s = \sqrt{3}\nu_z$ is the stretch mode frequency, $\nu_r = \sqrt{\nu_\perp^2 - \nu_z^2}$ is the rocking mode frequency, $\nu_\perp$ is the radial mode frequency (either ν_x or ν_y), and α is the fine structure constant. There is therefore a modification of the stretch mode frequency as a function of the number of phonons in the rocking mode, given by Kn_r where n_r is the initial mean occupation of the radial motional mode, and this leads to a symmetric detuning error. For a thermal occupation of the radial mode, this fluctuation of the symmetric detuning varies between experiments. The error can be calculated by substituting the variance of the thermal occupation number $\text{Var}(\bar{n}_r) = \bar{n}_r(2\bar{n}_r + 1)$ into the equation for symmetric detuning, giving an error [85]

$$\epsilon_{\text{kerr}} = K^2\bar{n}_r(2\bar{n}_r + 1)\left(\frac{\pi^2}{\delta^2}\right)\left(\frac{1 + 2q(1 + 2\bar{n}_s)}{4}\right). \tag{6.53}$$

Since there are two radial modes in the x and y direction with approximately the same frequency, the total error is $2\epsilon_{\text{kerr}}$.

This error is plotted in figure 6.7 for different values of the radial frequency ν_{xy} and initial average axial phonon mode occupancy $\bar{n}_s$. It can be seen that the error is most effectively reduced by increasing the radial mode frequency. A lower initial value of $\bar{n}_s$ also reduces the Kerr error.

6.4.8 Other errors

Whilst there are other errors which may affect the gate, they are negligible in our system compared to the errors discussed above. For example, there is an additional error term from the spin-spin coupling due to the magnetic field gradient which drives population between $|DD\rangle$ and $(|ud\rangle + |du\rangle)/\sqrt{2}$ [53]. However, this effect can be made off-resonant by setting the dressing field Rabi frequency, which defines the splitting between $|D\rangle$ and $\{|u\rangle, |d\rangle\}$, to different values for each ion. A splitting of $\Delta\Omega = 1\,\text{kHz}$ is enough to suppress the error so that it is negligible compared to other errors. Other errors which are often significant for implementations of the Mølmer-Sørensen gate include deviations from the Lamb-Dicke regime and coupling to spectator modes [14]. However, due to the small value of the Lamb-Dicke parameter in our implementation, these errors are unimportant. Furthermore, approximations in the dressed state picture leads to extra error terms, discussed in [88], but these were also found to be negligible in this case.

6.5 Multi-tone two ion entanglement

While gate errors can be small in perfect experimental conditions, it is likely that when moving to large scale quantum computing architectures they will become increasingly important. In particular, heating is likely to become increasingly important due to the smaller ion-electrode distances typical of the microfabricated ion traps used in many architectures [35, 36, 38, 79]. Realistic experimental environments are also likely to be noisier and less stable [89, 90], and gate parameters may slowly change over time or across the surface of the chip. Robust gates that can reach and maintain high fidelities in large scale quantum computing architectures are therefore required. Haddadfarshi *et al.* [82] showed that by using multi-tone Mølmer-Sørensen (MTMS) gates, it was possible to reduce the effect of heating on the gate. In collaboration with Sam Collingbourne and Dr Florian Mintert [91], we found that the same method also protected against symmetric detuning errors, discussed for a standard MS gate in section 6.4.4. Here, I summarise Haddadfarshi *et al.*'s work and show how this also provides protection against symmetric detuning errors, and demonstrate both protection against heating and symmetric detuning experimentally. I also discuss how this method can be used to mitigate the effects of off-resonant coupling and Kerr coupling errors.

6.5.1 Two ion entanglement

In this method, the single field used to address each sideband in standard MS gates is replaced by N fields at detunings $\delta_k = k\delta$ with powers $\Omega_k = c_k\Omega_0$, as depicted in the energy level diagram in figure 6.8. By choosing optimal values of c_k, a maximally entangled state is created while providing protection against multiple sources of error. The Mølmer-Sørensen Hamiltonian in equation 6.15 can be generalised to multiple tones. The two ion Mølmer-Sørensen Hamiltonian for N tones is

$$H_{\mathrm{MS}}^{N} = \sum_{k=1}^{N} H_{\mathrm{MS}}^{1,k} + H_{\mathrm{MS}}^{2,k}, \tag{6.54}$$

where the Hamiltonian for ion i and each tone k is

$$H_{\mathrm{MS}}^{i,k} = \frac{i\hbar\eta_i\Omega_k}{2} S_{\phi i}(a^\dagger e^{ik\delta t}e^{-i\phi_{mi}} - ae^{-ik\delta t}e^{i\phi_{mi}}). \tag{6.55}$$

In order to evaluate the time dependence of the Hamiltonian, the Magnus expansion can be used as for a standard MS gate. The first term is separable for ion i and tone k, so can be generalised from equation 6.8, expressed as the sum of terms for each ion and each tone as

$$O_1 = \sum_{i,k} S_{\phi i}(\alpha_{ik}(t)a^\dagger - \alpha_{ik}^*(t)a) \tag{6.56}$$

with

$$\alpha_{ik}(t) = \frac{i\eta_i\Omega_k}{2k\delta} e^{-i\phi_{mi}}(e^{ik\delta t} - 1). \tag{6.57}$$

The second term, however, contains cross terms due to the commutator so is not separable for each ion. It can be written as a sum over ions i, j and tones m, k as

$$O_2 = \sum_{i,j,m,k} i\chi_{ijmk}(t) S_{\phi i} S_{\phi j}. \tag{6.58}$$

The expression for $\chi_{ijmk}(t)$ differs in the cases $m \neq k$ and $m = k$. Simplifying these expressions by setting $\phi_{mi} = \phi_{mj} = 0$ gives

$$\chi_{ijmk}(t) = \frac{\eta_i\eta_j\Omega_m\Omega_k}{4\delta^2}\left(\frac{1}{k(m-k)}\sin\left(\delta(m-k)t\right) - \frac{1}{mk}\sin\left(\delta mt\right)\right) \tag{6.59}$$

for $m \neq k$, and

$$\chi_{ijkk}(t) = \frac{\eta_i\eta_j\Omega_k^2}{4k^2\delta^2}(k\delta t - \sin\left(k\delta t\right)) \tag{6.60}$$

for $m = k$. The time evolution unitary operator is therefore

$$U_{\mathrm{MS}}(t) = \exp\left(\sum_{i,k} S_{\phi i}(\alpha_{ik}(t)a^\dagger - \alpha^*_{ik}(t)a)\right) \exp\left(-\sum_{i,j,m,k} i\chi_{ijmk}(t)S_{\phi i}S_{\phi j}\right). \quad (6.61)$$

This is the same unitary as for the single tone case discussed in section 6.3.1, but generalised over multiple tones with

$$\alpha_i(t) \Rightarrow \sum_{k=1}^{N} \alpha_{ik}(t) \quad (6.62)$$

and

$$\chi_{ij}(t) \Rightarrow \sum_{m,k=1}^{N} \chi_{ijmk}(t). \quad (6.63)$$

As before, gates are completed at time $\tau = 2\pi/\delta$ when $\alpha_i(\tau) = 0$, and states will accumulate a relative phase, shown for the COM mode in equation 6.21 and the stretch mode in equation 6.22. The amplitudes of the gate tones should be set so that the magnitude of this accumulated phase is $\pi/2$ in order to create a maximally entangled state. For both COM and stretch mode, a relative phase of $4\chi(\tau)$ is acquired, where $\chi(\tau)$ is either $4\chi_c(\tau)$ or $4\chi_s(\tau)$. To find this relative phase for the multiple tone gate, we can drop the ion subscripts i, j and write

$$\chi(\tau) = \sum_{m,k=1}^{N} \chi_{mk}(\tau). \quad (6.64)$$

We find that $\chi_{mk}(\tau) = 0$ for $m \neq k$, so that

$$\chi(\tau) = \frac{\eta^2\Omega_0^2\pi}{2\delta^2} \sum_{k=1}^{n} \frac{c_k^2}{k} = \frac{\pi}{8} \sum_{k=1}^{n} \frac{c_k^2}{k} \quad (6.65)$$

where the magnitude of η depends on the mode used and we have substituted $\Omega_k = c_k\Omega_0$. Imposing the condition $4\chi(\tau) = \pi/2$ gives the condition on the gate tone amplitudes which must be satisfied for generating maximally entangled states:

$$\sum_{k=1}^{N} \frac{c_k^2}{k} = 1. \quad (6.66)$$

This specifies the condition for entanglement, and in the following sections we will derive further conditions on the gate tone amplitudes for maximising protection against heating and symmetric detuning errors.

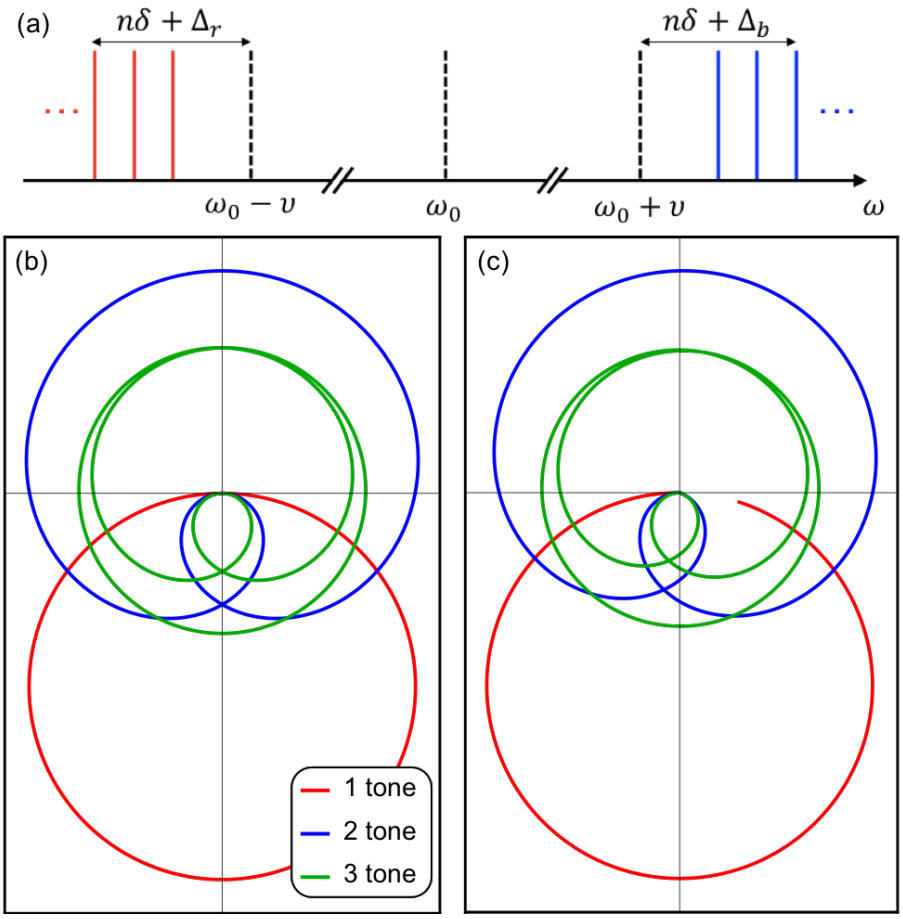

Figure 6.8: (a) A diagram showing multiple gate tones driving the red and blue sideband with a detuning of Δ_r and Δ_b respectively. (b) Phase space trajectories for one (red), two (blue), and three (green) tone gates. For multi-tone gates, the average of the phase space displacement over the duration of the gate is zero. As the number of tones increases the trajectories become closer to circles around the origin, reducing the magnitude of the displacement from the origin. Since it is this displacement which couples the qubit states to motional decoherence, this reduces the effect of heating during the gate. Figure (c) shows incomplete loops resulting from an incorrectly set gate detuning $\delta + \Delta$, which causes error due to the residual entanglement between the spin and motional states of the qubit and the incorrect phase accumulation. For the two and three tone gates, the loops close to first order in Δ, as can be seen in the diagram, and the accumulated phase becomes closer to that required for maximal entanglement, demonstrating the reduction in sensitivity to symmetric detuning errors.

6.5.2 Protection against heating

As discussed in section 6.4.1, decoherence of motional states due to heating during the gate induces an error. This is characterised by the Master equation given in equation 6.34. Integrating this gives a general time dependence of an element of the reduced density matrix

$$\dot{\rho}_{M_x,M'_x}(t) = -\dot{\bar{n}}|\alpha(t)|^2(M_x - M'_x)^2\rho_{M_x,M'_x}(t). \tag{6.67}$$

The heating is therefore characterised by the expression for $\alpha(t)$, which for MTMS gates becomes a summation term $\alpha(t) = \sum_{k=1}^{N}\alpha_k(t)$. Haddadfarshi *et al.* showed that the error due to heating is most effectively minimised by choosing coefficients such that $\langle\alpha(t)\rangle = 0$ and minimising $\langle|\alpha(t)|^2\rangle$ [82]. This can be understood by looking at the displacement operator which characterises the heating error. For MTMS gates, we find

$$|\alpha(t)|^2 = \left(\frac{\eta\Omega_0}{2\delta}\right)^2\left[\sum_{j,k=1}^{n}\frac{c_kc_j}{kj}\cos\left((j-k)\delta t\right) - 2\sum_{k=1}^{n}\frac{c_k}{k}\cos\left(k\delta t\right) - \left(\sum_{k=1}^{n}\frac{c_k}{k}\right)^2\right]. \tag{6.68}$$

Substituting this into equation 6.67, integrating and evaluating at the gate time gives

$$\rho_{M_x,M'_x}(\tau) = \rho_{M_x,M'_x}(0)\exp\left\{\left[-\dot{\bar{n}}(M_x - M'_x)^2\left(\sum_{k=1}^{n}\frac{c_k^2}{k^2} + \left(\sum_{k=1}^{n}\frac{c_k}{k}\right)^2\right)\frac{\tau}{16}\right]\right\}. \tag{6.69}$$

Setting $\sum_{k=1}^{N}\frac{c_k}{k} = 0$ is therefore the first condition for reducing the effect of heating on the gate. The formula for the error is then the same as for a single tone gate, given in equation 6.39, except the heating rate $\dot{\bar{n}}$ is replaced by an effective heating rate $\dot{\bar{n}}_{\text{eff}}$, given by

$$\dot{\bar{n}}_{\text{eff}} = \frac{1}{2}\sum_{k=1}^{N}\frac{c_k^2}{k^2}\dot{\bar{n}}. \tag{6.70}$$

In order to minimise the error due to heating, this effective heating rate coefficient must therefore be minimised. This gives a set of conditions for the coefficients that most effectively protect against heating errors:

$$\min\left(\sum_{k=1}^{N}\frac{c_k^2}{k^2}\middle|\sum_{k=1}^{N}\frac{c_k^2}{k} = 1, \sum_{k=1}^{N}\frac{c_k}{k} = 0\right). \tag{6.71}$$

This allows optimal coefficients to be found, and the resulting formulas are given in [82] as

$$c_j = 4\frac{jb}{1-j\lambda} \tag{6.72}$$

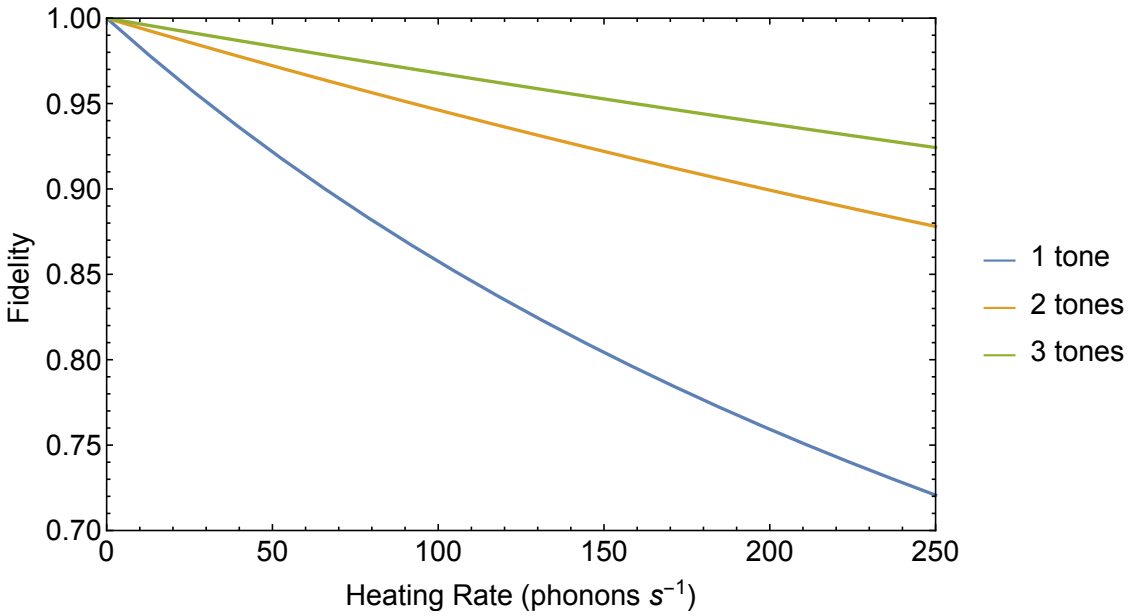

Figure 6.9: Gate fidelity simulation plotted against heating rate (in phonons s^{-1}) for a secular frequency of $\nu/2\pi = 460\,\text{kHz}$, detuning of $\delta_0/2\pi = 292\,\text{Hz}$ and single tone Rabi frequency of $\Omega_0/2\pi = 36\,\text{kHz}$. The gate time τ and first order detuning δ were kept constant for each gate, and no other errors were incorporated in the simulation.

and

$$b = -\frac{1}{4}\left(\sum_{j=1}^{N}\frac{j}{(1-j\lambda)^2}\right)^{-\frac{1}{2}} \tag{6.73}$$

where λ is the smallest root of the equation

$$\sum_{j}^{N}(1-j\lambda)^{-1} = 0. \tag{6.74}$$

From this, we can find the coefficients for $N = \{1, 2, 3\}$ tones when the gate time τ and the first order detuning δ is kept constant, which are shown in table 6.2. The resultant phase

Tones	c_1	c_2	c_3
1	1	0	0
2	$-\frac{1}{\sqrt{3}} \approx -0.576$	$\frac{2}{\sqrt{3}} \approx 1.152$	0
3	-0.132	-0.719	1.474

Table 6.2: Amplitude coefficients for $\{N = 1, 2, 3\}$ tone gates.

space trajectories from these multi-tone coefficients are shown in figure 6.8. At the end of the gate, trajectories are closed and the phase picked up is that required for a maximally entangled state, but the loops performed are more complicated than the simple circles resulting from a single tone.

These coefficients give smaller effective heating rates than for a single tone gate. For

$N = 2$ tones, we find

$$\dot{\bar{n}}_{\text{eff}} = \frac{1}{3}\dot{\bar{n}} \approx 0.333\dot{\bar{n}} \tag{6.75}$$

and for $N = 3$ tones

$$\dot{\bar{n}}_{\text{eff}} \approx 0.193\dot{\bar{n}}. \tag{6.76}$$

This effective heating rate can be substituted into the expression for the error due to heating to give

$$\epsilon_{\text{heating}} = 1 - \frac{1}{8}(3 + 4e^{-\frac{1}{2}\dot{\bar{n}}_{\text{eff}}\tau} + e^{-2\dot{\bar{n}}_{\text{eff}}\tau}). \tag{6.77}$$

The effect of the multi-tone gates on heating can be understood qualitatively by looking at the trajectories in phase space, as depicted in figure 6.8 for $N = \{1, 2, 3\}$ tones. The condition $\sum_{k=1}^{N} c_k/k = 0$ means that the time average of the trajectory during the gate is zero. Furthermore, the minimisation of the term $\sum_{k=1}^{N} c_k^2/k^2$ means that the average magnitude of the displacement from the origin is minimised – as the number of tones increases, the trajectories become more closely approximated by circles around the origin. Since it is this displacement from the origin that couples the qubit states to motional decoherence, this reduced magnitude demonstrates a reduction in sensitivity to heating.

Using the Lindblad equations, the effect of increased heating on the gate can be simulated, as shown in figure 6.9. The fidelity was calculated from the overlap of the final state with the Bell state created with zero heating. A significant improvement can be seen, with the largest improvement seen in going from one to two tones. Simulations and analytical expressions were found to agree exactly, as expected.

6.5.3 Protection again symmetric detuning errors

Using MTMS gates, it is also possible to protect against symmetric detuning mis-set errors [91]. In the following, I show that the same conditions that minimise the heating error for MTMS gates also maximise the protection against symmetric detuning errors. Assuming a symmetric detuning of $\Delta_r = \Delta_b = \Delta$, we can define the displacement term for ion i and tone k at the gate time $\tau = 2\pi/\delta$ as

$$\alpha_{ik}(\tau) = \frac{i\eta_i c_k \Omega_0}{2(k\delta + \Delta)}(e^{i\frac{2\pi\Delta}{\delta}} - 1) \tag{6.78}$$

where we have set $\phi_m = 0$. Expanding this term for small Δ and summing over the tones gives the expression

$$\alpha_i(\tau) = \frac{i\eta_i\Omega_0}{4}\sum_{k=1}^{N}\frac{c_k}{k}\sum_{q=0,p=1}^{\infty}\frac{(i2\pi)^p}{p!n^q}\left(\frac{\Delta}{\delta}\right)^{p+q}. \tag{6.79}$$

In order to minimise residual spin-motion entanglement, we should therefore impose the condition

$$\sum_{k=1}^{N}\frac{c_k}{k} = 0 \tag{6.80}$$

which is the same condition as for the protection against heating. Calculating the magnitude of the geometric phase term at the gate time τ with a small symmetric detuning Δ gives

$$\chi(\tau) = \sum_{m,k}^{N}\frac{\eta_i\eta_j c_m c_k\Omega_0^2}{4(k\delta+\Delta)}\left(\frac{2\pi}{\delta}\delta_{mk} - \frac{\sin\left(\frac{2\pi\Delta}{\delta}\right)}{m\delta+\Delta}\right). \tag{6.81}$$

This can be expanded to first order in Δ, which gives

$$\chi(\tau) = \frac{\pi}{8} - \frac{\pi}{8}\left(\sum_{k=1}^{N}\frac{c_k^2}{k^2} + \left(\sum_{k=1}^{N}\frac{c_k}{k}\right)^2\right)\left(\frac{\Delta}{\delta}\right). \tag{6.82}$$

This results in an incorrect accumulated phase. We can calculate the infidelity by substituting these expressions for the displacement and accumulated phase into equation 6.31. Up to second order in the detuning Δ, this gives an expression

$$\epsilon_\Delta = \frac{\pi^2}{2}\left|\sum_{k=1}^{N}\frac{c_k}{k}\right|^2\left|\frac{\Delta}{\delta}\right|^2(2\bar{n}+1) + \frac{\pi^2}{16}\left(\sum_{k=1}^{N}\frac{c_k^2}{k^2} + \left(\sum_{k=1}^{N}\frac{c_k}{k}\right)^2\right)^2\left(\frac{\Delta}{\delta}\right)^2 \tag{6.83}$$

Since we have imposed the condition $\sum_k c_k/k = 0$, we have eliminated any first order dependence on the initial motional mode $\bar{n}$ of the ions. In order to enhance protection further, the term $\sum_k c_k^2/k^2$ should be minimised. This set of conditions for finding optimal values of c_k to reduce error due to symmetric detuning is identical to the conditions for reducing error due to heating, so MTMS gates simultaneously protect against both effects. Using the coefficients for two tones given in table 6.2, the expression for the symmetric detuning error becomes

$$\epsilon_\Delta = \frac{1}{36}\pi^2\left(\frac{\Delta}{\delta}\right)^2 \simeq 0.028\pi^2\left(\frac{\Delta}{\delta}\right)^2 \tag{6.84}$$

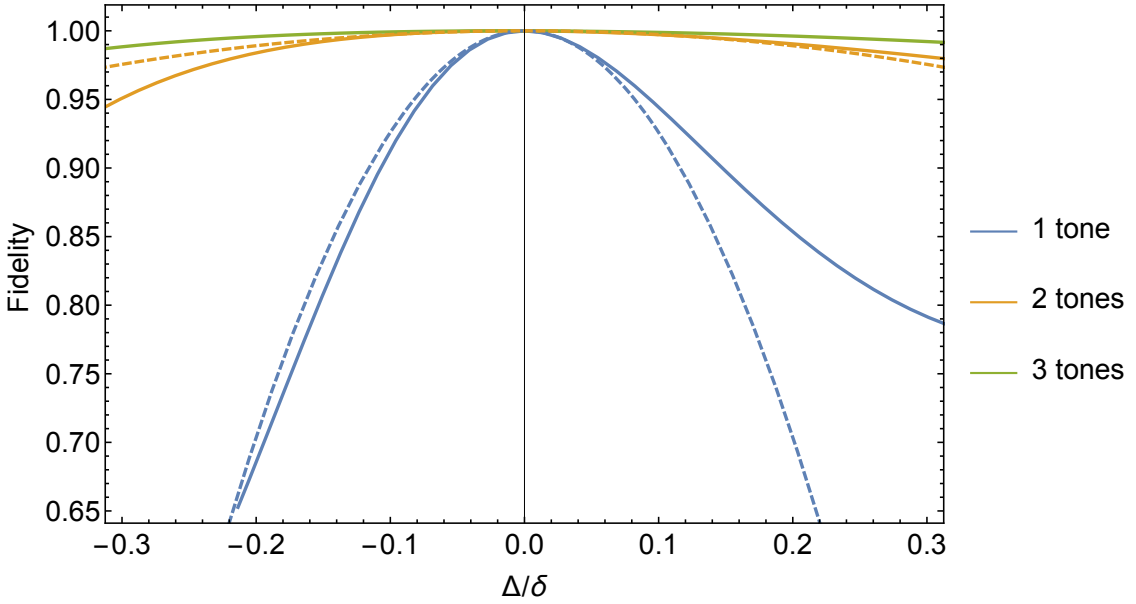

Figure 6.10: Fidelity as a function of symmetric detuning Δ as a proportion of the gate detuning δ. The solid lines show the results of a numerical simulation at $\bar{n} = 0$ for one, two and three tone gates. A large reduction in sensitivity to detuning error can be seen by using multi-tone gates. The analytical expression, which is an approximation up to $O(\Delta^2)$, is plotted for single and two tone gates in dashed lines.

and for three tones

$$\epsilon_\Delta = \frac{39 - 12\sqrt{3}}{1936}\pi^2 \left(\frac{\Delta}{\delta}\right)^2 \simeq 0.0094\pi^2 \left(\frac{\Delta}{\delta}.\right)^2 \tag{6.85}$$

This shows a significant improvement over the single tone gate.

This improvement is shown for $\bar{n} = 0$ in figure 6.10. Solid lines show the result of a numerical simulation for $N = \{1, 2, 3\}$ tones, and dashed lines show the analytical approximation which agrees well for low values of Δ/δ. A large improvement is seen between $N = 1$ and $N = 2$ tones, with slightly further improvement from $N = 2$ to $N = 3$ tones. Furthermore, figure 6.11 shows the significant improvement seen for higher initial values of $\bar{n}$. The analytical approximation for the fidelity is plotted for $N = 1$ and $N = 2$ tones at an initial mean motional mode of $\bar{n} = 20$ and while the two tone gate remains resilient to detuning errors, the single tone gate fidelity drops off very quickly. This protection opens up the possibility of performing gates 'hot', i.e. at higher initial values of $\bar{n}$ achievable through only Doppler cooling.

6.5.4 Asymmetric detuning

Although we do not have an analytical expression for the error resulting from an asymmetric detuning, a numerical simulation is shown in figure 6.12 where an equal asymmetric

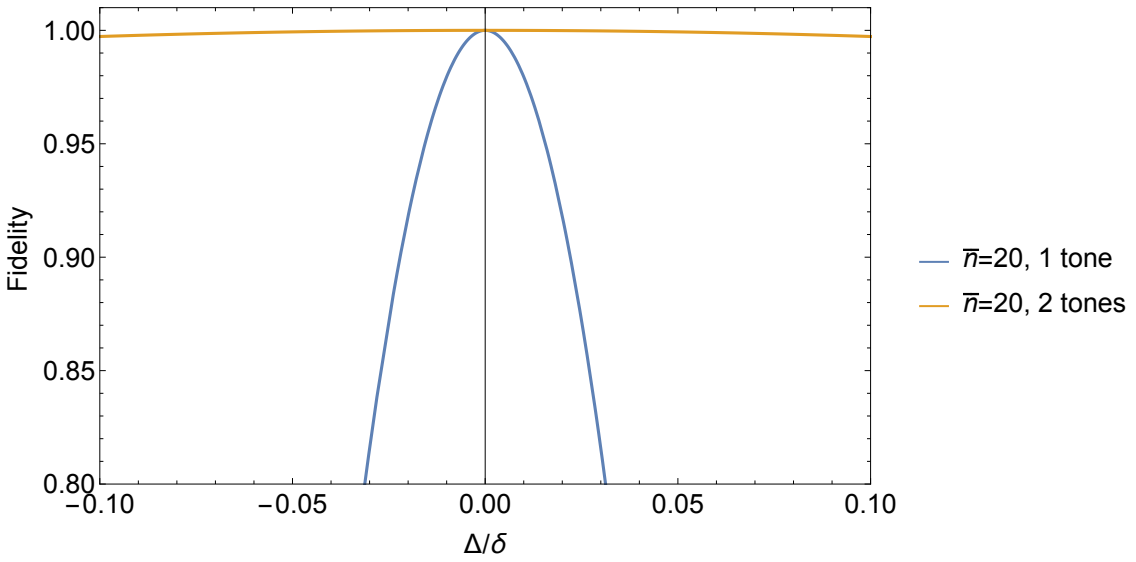

Figure 6.11: A demonstration of the effect of multi-tones at an initial value of $\bar{n} = 20$. The lines are an approximation of the fidelity to lowest order in fractional symmetric detuning error of Δ/δ. To this order, the two tone gate has no temperature dependence, so exhibits the same robustness to detuning seen at $\bar{n} = 0$, whereas for the single tone case it can be seen that the fidelity rapidly falls.

detuning Δ_a is applied to each ion. At $\bar{n} = 0$, an improvement is seen between single and two tone gates, although moving to three tones has a slightly detrimental effect. Dashed lines show a simulation for one and two tones at an initial mean excitation of the motional mode of $\bar{n} = 10$. At this higher value of $\bar{n}$, the improvement becomes marginal. The sensitivity to asymmetric detunings for two tone gates is therefore still dependent on the starting temperature of the ions, unlike the symmetric detuning sensitivity. This may place a limit on achievable fidelities at higher values of $\bar{n}$.

6.5.5 Kerr coupling

Kerr coupling, as explained in section 6.4.7, induces infidelity due to a fluctuating symmetric detuning error caused by the axial stretch mode coupling to a radial mode which has only been Doppler cooled. Since MTMS gates protect against symmetric detuning errors, they therefore also protect against Kerr errors. The expression for the variance of the trap frequency can be substituted into the symmetric detuning error equation for MTMS gates, giving an error

$$\epsilon_{\text{kerr}} = K^2 \bar{n}_r (2\bar{n}_r + 1) \left(\frac{\pi}{4\delta}\right)^2 \left(\sum_{k=1}^{N} \frac{c_k^2}{k^2}\right)^2 . \tag{6.86}$$

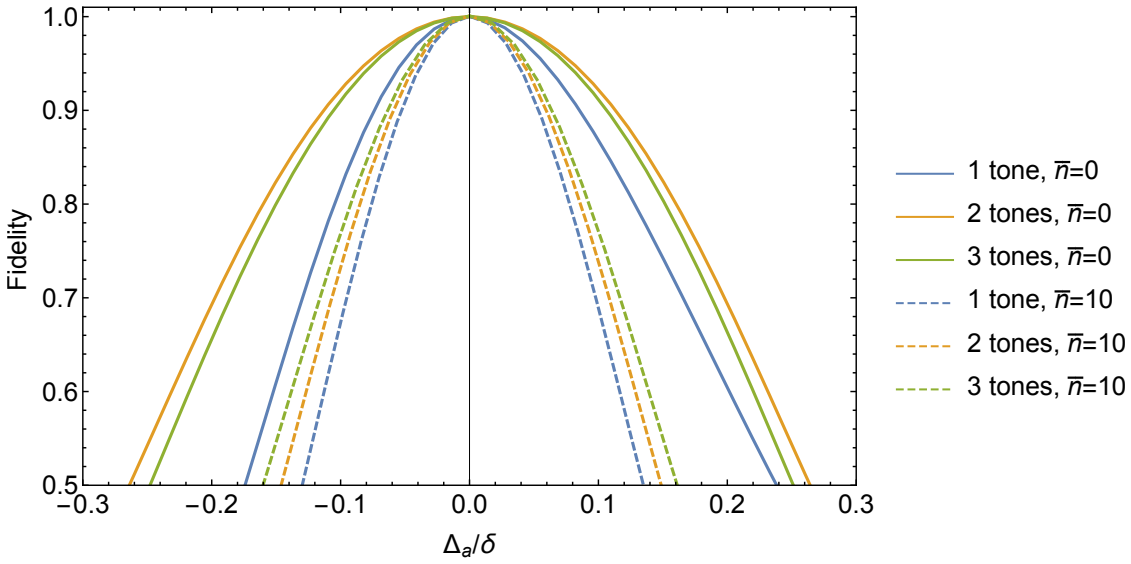

Figure 6.12: A numerical simulation of an equal asymmetric detuning error Δ on both ions is shown, with fidelity plotted against the detuning error Δ as a proportion of the gate detuning δ. At $\bar{n} = 0$ an improvement is seen between single and two tone gates, although a slightly detrimental effect is seen in moving to three tones. At $\bar{n} = 10$, this improvement becomes only marginal.

For two tones, this becomes

$$\epsilon_{\text{kerr}} = 0.028K^2\bar{n}_r(2\bar{n}_r + 1)\left(\frac{\pi}{\delta}\right)^2 \tag{6.87}$$

and for three tones

$$\epsilon_{\text{kerr}} = 0.0094K^2\bar{n}_r(2\bar{n}_r + 1)\left(\frac{\pi}{\delta}\right)^2. \tag{6.88}$$

There is significant improvement from the single tone case, and no dependence on the initial mean motional state of the stretch mode. This effect is shown in figure 6.13, where all lines are plotted for a radial mode frequency of $\nu_{xy} = 1\,\text{MHz}$. This relaxes limits on the secular frequency resulting from the Kerr coupling error. It also removes one of the main limitations on using the stretch mode, which exhibits a lower heating rate than the COM mode, for two qubit gates.

6.5.6 Off-resonant coupling

As discussed in section 6.4.3, off-resonant coupling from the gate fields to the carrier transition and the other dressed states causes an error. Pulse shaping can eliminate this to a certain extent, but a limit of approximately $\Omega/\nu \leq 0.1$ is required to ensure this error is negligible. In order to understand the effect of the two tone gate on off-resonant coupling, we must consider the shape of the gate pulse. Since we have two frequencies

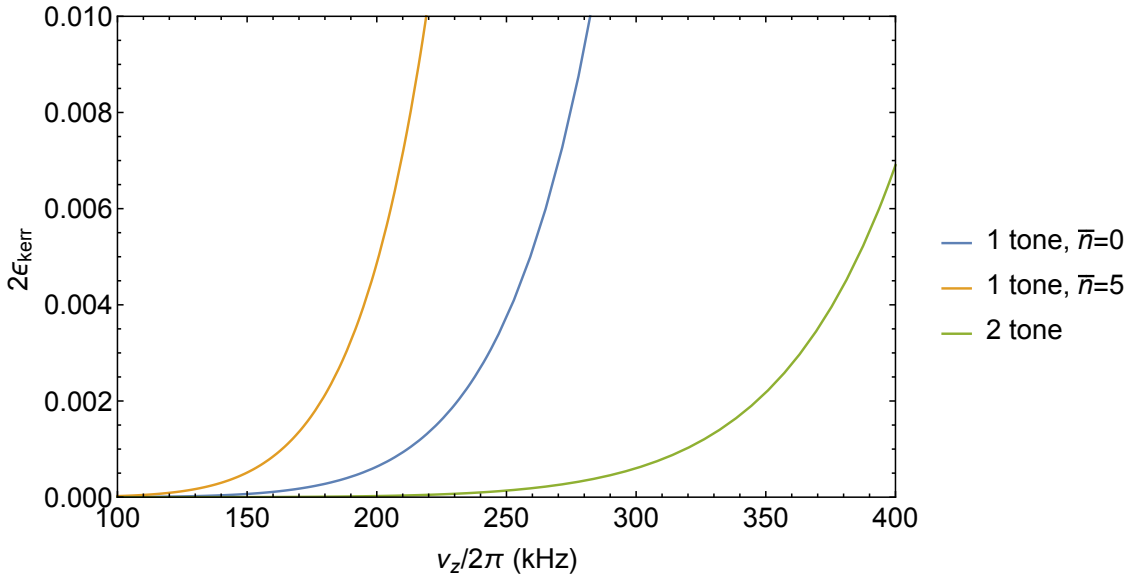

Figure 6.13: Infidelity due to Kerr coupling plotted against the stretch mode secular frequency ν_z for a radial mode frequency $\nu_{xy} = 1\,\text{MHz}$. The resilience to symmetric detuning errors of the two tone gate means that the Kerr error is much lower, and there is no dependence to lowest order in Δ on the initial motional mode of the stretch mode $\bar{n}$.

separated by δ, our signal is of the form

$$\begin{aligned} f(t) &= Ae^{i\omega t} + Be^{i(\omega+\delta)t} \\ &= e^{i\omega t}(A + Be^{i\delta t}). \end{aligned} \tag{6.89}$$

Finding the amplitude modulation of this signal gives

$$|f(t)|^2 = A^2 + B^2 + 2AB\cos(\delta t). \tag{6.90}$$

The two tone gate pulse is therefore sinusoidally modulated, as shown in figure 6.14. The pulse reaches a peak power of $\sqrt{3}\Omega_0$ instantaneously at $\tau/2$, and has a higher average power during the gate. However, the natural sinusoidal modulation of the gate pulse is ideal for mitigating the effect of off-resonant coupling. It provides extra protection when compared with a short ramp and the beginning and end of the gate. Despite the higher total power for two tones, the effect of off-resonant coupling is therefore smaller, as shown in figure 6.15. Numerical simulations show the fidelity with an increasing ratio Ω_0/ν, where $\nu/2\pi = 460\,\text{kHz}$ and both single and two tone gates have a pulse shaping time of $10\,\mu\text{s}$ at the beginning and end of the gate. There is a faster drop off in fidelity for the single tone gate than for the two tone gate. Off-resonant coupling may in some cases place a limit on the maximum Rabi frequency the gate can be driven at, and this limit could be relaxed through the use of two tone gates.

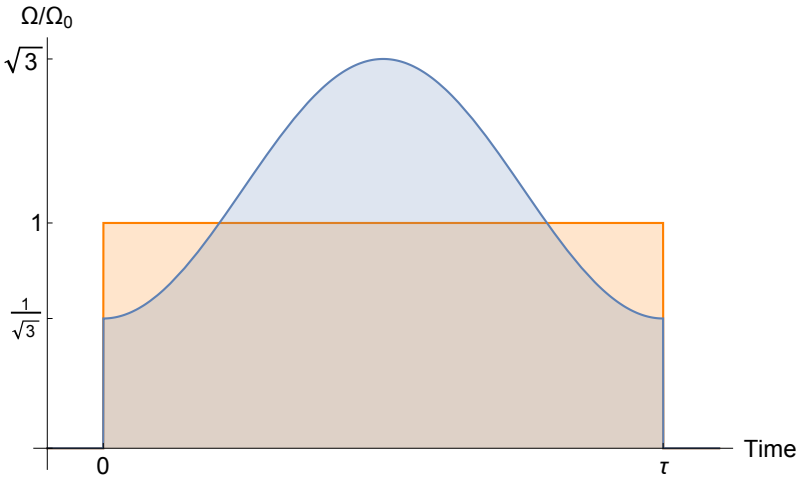

Figure 6.14: The pairs of gate fields for the two tone gate separated by the gate detuning δ mean that the pulse is naturally sinusoidally shaped, at a frequency δ.

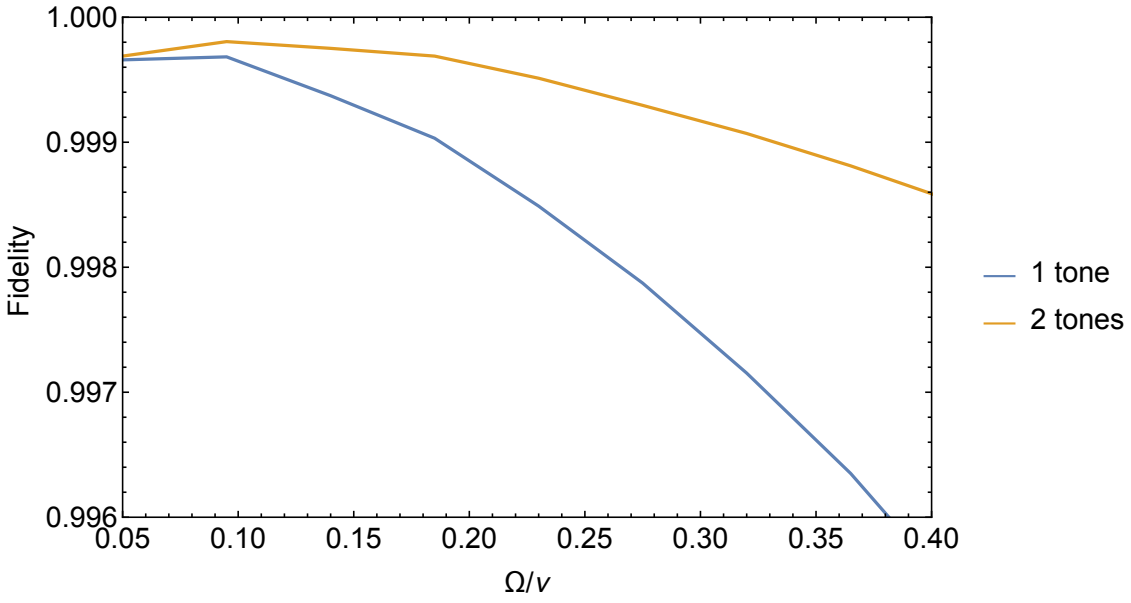

Figure 6.15: The effect of off-resonant coupling in a two level system on the fidelity is simulated. Despite the higher overall power, the infidelity due to off-resonant coupling is lower for the two tone gate due to the natural sinusoidal pulse-shaping of the gate.

6.6 Experimental implementation

Two tone gates were implemented in the dressed state basis in the qubit $\{|0'\rangle, |D\rangle\}$, similarly to the standard MS gate demonstrated in section 6.3.4. The stretch mode of the two ions was used, with a secular frequency of $\nu_s/2\pi = 461\,\text{kHz}$, and the ions were sideband cooled before the gate to approximately $\bar{n} \approx 0.15$. Ions were prepared in $|0'0'\rangle$ by first optically pumping to $|00\rangle$ and then applying a clock π pulse to both ions.

Since two tone gates use a higher peak power than a single tone gate at the same gate time, as discussed in 6.5.6, it was necessary to perform a slower gate compared to the demonstration of the standard MS gate in section 6.3.4, due to limitations in the RF amplifying setup. The maximum gate Rabi frequency Ω_D was determined by measuring the RF Rabi frequency Ω_{rf} at increasing RF powers, until we reached saturation in the amplifiers. The value of Ω_{rf} in each case was measured using a three level Rabi flop, as described in 4.3.2. The RF field is set with equal and opposite detunings to the $|0'\rangle \leftrightarrow |\pm 1\rangle$ transitions, and the ion oscillates between the states $|0'\rangle$ and $\frac{1}{\sqrt{2}}(|+1\rangle + e^{i\phi}|-1\rangle)$ at a rate $\sqrt{2}\Omega_{\text{rf}}$. Once the maximum value of Ω_{rf} was obtained, this allowed the maximum value of Ω_D to be determined as $\Omega_D = \Omega_{\text{rf}}/\sqrt{2}$. The peak gate power of $\sqrt{3}\Omega_0$ was then set to this maximum value, giving a base gate Rabi frequency of $\Omega_0/2\pi = 36\,\text{kHz}$. This corresponds to a gate time of $\tau = 3.4\,\text{ms}$ and a first order detuning of $\delta/2\pi = 292\,\text{Hz}$. Four gate fields were applied per ion of power $\Omega_1 = -\Omega_0/\sqrt{3}$ and $\Omega_2 = 2\Omega_0/\sqrt{3}$ at detunings δ and 2δ respectively. During the implementation of the gate, an imbalance in the populations of $|0'0'\rangle$ and $|DD\rangle$ at the gate time suggested that the power was lower than expected, possibly due to non-linear behaviour in the amplifiers resulting from nearing saturation. By optimising these populations, a factor was introduced to increase the amplitude of the gate fields by up to 5%.

As discussed in section 6.3.3, the nature of the dressed state qubit means that there is a non-zero AC Stark shift due to asymmetry of the gate fields around the dressed states connected through $|-1\rangle$. For the single tone gate, this AC Stark shift was constant. However, as shown in figure 6.14, the amplitude of the two tone gate field varies sinusoidally over the gate time. The AC Stark shift therefore also varies. There is a maximum Stark shift at $t = \tau/2$ when the instantaneous Rabi frequency is $\Omega = \Omega_2 - \Omega_1 = \sqrt{3}\Omega_0$, and a minimum at $t = 0$ and $t = \tau$ when the instantaneous Rabi frequency is $\Omega = \Omega_2 + \Omega_1 = \Omega_0/\sqrt{3}$. The AC Stark shifts are proportional to Ω^2, and for each ion can be calculated from equation 6.33. The frequencies of the gate fields are then sinusoidally varied between the two values to compensate for the changing carrier frequency during the gate. The

second order Zeeman shifts of the two ions were measured as 19.20 kHz and 30.05 kHz, giving AC Stark shifts between approximately 60 Hz and 520 Hz for ion 1, and 90 Hz and 820 Hz for ion 2.

Two tone gates were compared with single tone gates by measuring the effect of heating and symmetric detuning errors. Single tone gates of the same time τ and first order detuning δ were used for comparison, in order to keep the effect of other errors such as depolarisation constant. Other possible comparisons include keeping a constant maximum gate power, or average gate power, and this is discussed in section 6.7.

6.6.1 Heating

In order to verify the resilience to heating of the two tone gates, artificial heating was injected into the trap to increase the heating rate. Random noise with a flat amplitude spectrum of bandwidth 20 kHz centred around the stretch mode secular frequency was generated using code written in Python. This ensured it would only cause heating, and not affect other aspects of gate performance, for example by reducing the coherence time. An AWG (Agilent 33522A) was used to produce this noise signal. The signal was capacitively coupled onto one of the DC endcap electrodes, bypassing the filter for that channel, and triggered during the gate. The DC voltage was applied in the usual way for that electrode through the filter. The amplitude of the signal was controlled to adjust the heating rate. The heating rates were measured using the method described in 4.3.3. The ion was sideband cooled to $\bar{n} \approx 0.15$ on the red sideband of the $|0\rangle \leftrightarrow |+1\rangle$ transition, and the ion temperature was measured using sideband thermometry on the $|0'\rangle \leftrightarrow |D\rangle$ sidebands. A variable delay time was introduced before ion temperature measurement, allowing the heating rate to be determined. The noise amplitude required to double the heating rate was found to be consistent with the heating rate dependence on the power spectrum discussed in section 2.2.3 of $\dot{\bar{n}} \propto S_E(\omega)$, where $S_E(\omega)$ is the power spectral density of the noise.

At each heating rate, the single tone gate was first optimised by scanning the symmetric detuning of the gate fields at 2τ, since features are sharper at twice the gate time making a frequency fit easier. Once the correct symmetric detuning had been determined, fidelity population and parity measurements were performed for both single and two tone gates. This symmetric detuning was optimised between fidelity measurements for different heating rates. In order to account for any unknown change in the phase of the Bell state produced with increased heating, the measured fidelity was multiplied by a factor $\cos \Delta\phi$

where $\Delta\phi = \phi - \phi_0$, ϕ is the fitted phase of the parity measurement and ϕ_0 is the fitted phase for the parity measurement at no induced heating.

The data was analysed by a maximum likelihood method, developed by Adam Lawrence [66, 62]. When we measure an outcome of an experiment, we observe three quantities, x_0, x_1, and x_2, which are the number of times we measure 0, 1 and 2 ions bright respectively. The total number of measurements is n, so that $x_0+x_1+x_2 = n$. Errors in the preparation and the detection of ions mean that these measurements may not correspond to the true probabilities of each state, given by p_0, p_1 and p_2. Before experiments, we measure a state detection histogram (as detailed in section 3.4.2), and this allows us to extract a linear map $p'_i = \sum_j P(i|j)p_j$, where p'_i is the probability of measuring outcome i, $P(i|j)$ is the probability of measuring outcome i given that the ion is actually in state j, and p_j is the true probability of the outcome j. For example, we find the probability of measuring one ion bright to be $p'_1(p_1, p_2) = P(1|2)p_2 + P(1|1)p_1 + P(1|0)(1 - p_1 - p_2)$, where we only need to use p_1 and p_2 since $p_0 + p_1 + p_2 = 1$. We then use this map to obtain the true probabilities by scaling the data using a log-likelihood function and maximising over p_1 and p_2 to find the most likely probabilities. The log-likelihood function is given by

$$f_B = \log\left(\frac{(n+1)(n+2)n!p'_1(p1,p2)^{x_1}p'_2(p_1,p_2)^{x_2}(1-p'_1(p1,p2)-p'_2(p_1.p_2)^{n-x_1-x_2}}{x_1!x_2!(n-x_1-x_2)!}\right). \tag{6.91}$$

For the parity measurement, we can consider two measurements instead of three: $x_{\text{even}} = x_0 + x_2$ and $x_{\text{odd}} = x_1$ so that $x_{\text{even}} + x_{\text{odd}} = n$. Our log-likelihood function then becomes

$$f_B = \sum_{i=1}^{N} \log\left(\frac{(n+1)n!p'_{\text{odd}}(p^i_{\text{odd}})^{x^i_{\text{odd}}}(1-p'_{\text{odd}}(p^i_{\text{odd}}))^{n-x^i_{\text{odd}}}}{x^i_{\text{odd}}!(n-x^i_{\text{odd}})!}\right) \tag{6.92}$$

where N is the number of data points. In order to fit the parity curve, we can use the expression for the parity $\Pi = x_{\text{even}} - x_{\text{odd}} = A_0 + A\cos(2\phi_p + \phi_0)$ from equation 6.32 to substitute p^i_{odd}, so that p'_{odd} is a function of the parity fit parameters A_0, A and ϕ_0. We can then maximise the likelihood function over the parity parameters. This allows us to obtain fits for the population and the parity, and thus find the overall fidelity.

The results of the experiment can be seen in figure 6.16. The fidelities have been normalised to the fidelity of the single tone gate at no induced heating to account for other errors. Solid lines show the result of a numerical simulation of the gate using the Master equation with the appropriate heating Lindblad operators. Good agreement is seen for the experimental data and the theoretical lines, showing a strong improvement

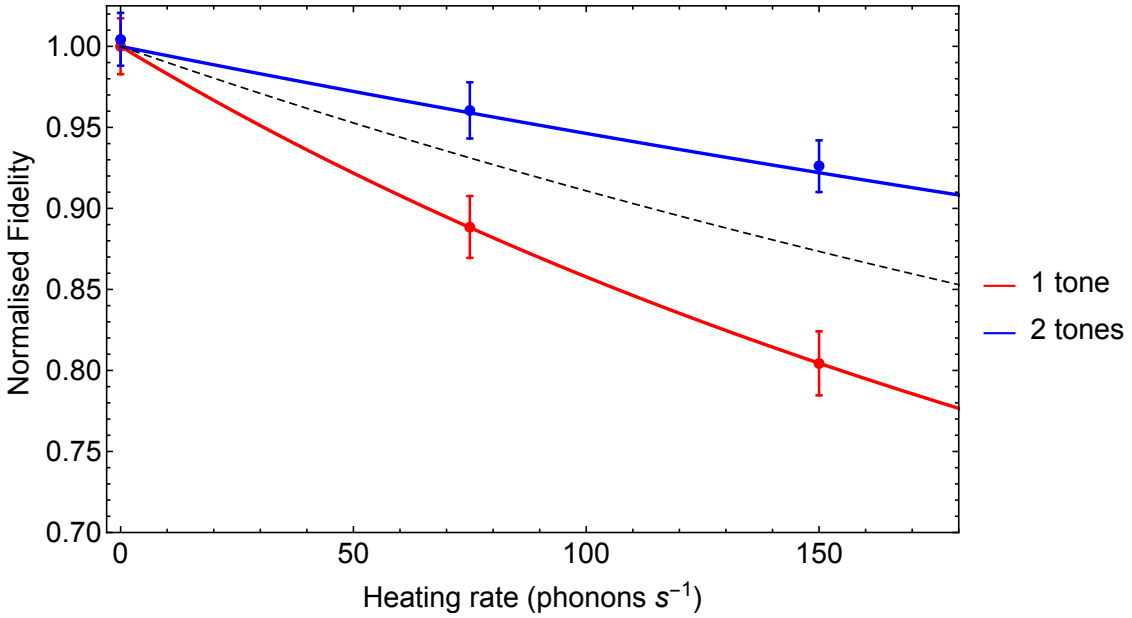

Figure 6.16: Gate fidelity for single and two tone gates with increasing heating rate (in phonons s^{-1}). The gate time τ and first order detuning δ were kept constant between each gate. Fidelities are normalised to the fidelity for the single tone gate at the lowest heating rate. The solid lines show the result of a numerical simulation, which shows good agreement with the experimental data. The dashed line is a numerical simulation for a faster single tone gate at the peak Rabi frequency of the two tone gate.

in fidelity for the two tone gate compared to the single tone gate. The dashed line shows the theoretical fidelity for a faster single tone gate, driven at the peak Rabi frequency of the two tone gate. An improvement in protection against heating is still seen for the two tone gate.

The fidelity of the single tone gate at no induced heating used as the normalisation factor is 0.94(2). At the time of this implementation, the lifetime and coherence time were measured to be approximately $T_1 \approx T_2 \approx 0.4\,\mathrm{s}$, and the heating rate with no induced heating was measured as approximately 1 phonon s^{-1}. This gives an error due to heating and depolarising of approximately 1%. The remaining error of around 5% is thought to be due to imperfect asymmetric detunings. This was largely uncompensated for to accelerate the data taking process, and since high fidelities were not the main aim of this demonstration. Although the two tone gate should provide some protection against asymmetric detunings, as described in section 6.5.4 , the additional complexity that arises from the time-varying AC Stark shift for two tone gates makes it more challenging to correctly set the parameters. For example, compression in the amplifiers may have reduced the instantaneous peak power from the expected value. Although this compression was partially compensated for by increasing the gate tone amplitudes, this may have resulted in an incorrect balance of gate tone amplitudes at δ and 2δ. Further optimisation should allow

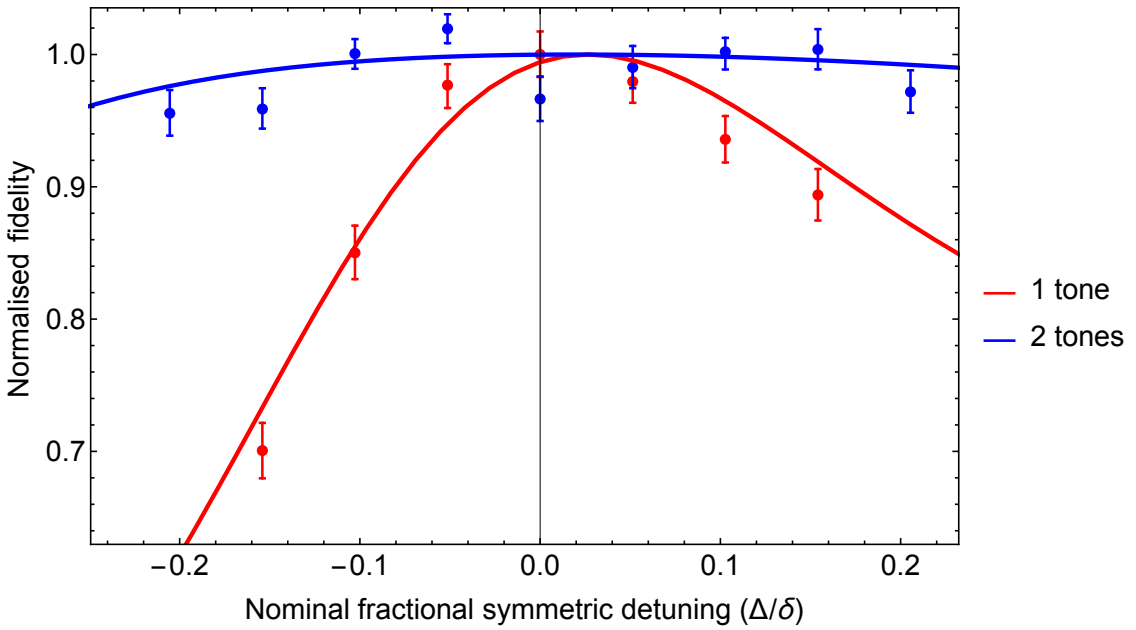

Figure 6.17: Gate fidelity for single and two tone gates with a symmetric detuning error. The solid lines are the result of a numerical simulation. To account for experimental parameter uncertainty, the symmetric detuning has been fitted to the data. The data has been normalised to the fidelity at 0 Hz nominal detuning.

for better compensation of these asymmetric detunings. Furthermore, an amplifying setup capable of producing higher power RF would reduce the effect of saturation on the gate fields. This could also allow for faster gates, which would reduce the absolute sensitivity of the gate error to an asymmetric detuning. The small contribution of heating to the overall error is the reason that no measurable increase in fidelity is seen for the two tone gate at no induced heating.

6.6.2 Symmetric detuning

Using the same gate parameters, the fidelity of two tone gates was measured up to a symmetric detuning mis-set of 60 Hz, which corresponds to 20% of the total gate detuning. Single tone gate fidelities were measured up to a symmetric detuning mis-set of 45 Hz for comparison. As in the previous section, the symmetric detuning was first optimised by scanning the symmetric detuning of the gate fields at 2τ. An offset was then added to the gate fields from this nominal zero detuning. Once the fidelities had been measured, the symmetric detuning offset of the data set was fitted using the single tone theory curve to account for uncertainty in the absolute symmetric detuning. This results from uncertainty in the initial setting of experimental parameters such as gate power, which can alter the frequency scan used to determine the nominal zero. Again, the solid lines are the result of a numerical simulation of the gate interaction, and data has been analysed using the

maximum likelihood method. Data has been normalised to the single tone fidelity at the nominal 0 Hz detuning, which was 0.96(2). This absolute fidelity agrees within error to the absolute fidelity given in the previous section, and the error is similarly expected to result from asymmetric detuning mis-sets which were not fully compensated for. As for the heating, a clear consistency is seen between the theoretical curves and the experimental data, demonstrating a significant improvement for the two tone case compared to the single tone.

6.6.3 'Hot' Gate

In these experiments, ions have been cooled to a near ground state occupation with a mean initial excitation of the motional mode of approximately $\bar{n} \approx 0.15$. Sideband cooling, however, is a time-consuming process compared to Doppler cooling. For comparison, in our experiment, sideband cooling takes 70 ms compared to only 0.7 ms for Doppler cooling. Usually, the sensitivity to parameters of the single tone gates mean that performing a gate at Doppler cooled temperatures results in very low fidelity. However, the elimination of the $\bar{n}$ dependence to first order of the symmetric detuning error for the MTMS two tone gate means that it becomes possible to perform a higher fidelity gate after only Doppler cooling.

The temperature of the ion after Doppler cooling was measured by driving one of the sidebands and fitting the resultant curve with the expected response, as outlined in section 3.5.5. This fit gives a value of $\bar{n} = 53(4)$. Gate parameters were optimised for a single tone gate after sideband cooling. The same gate was then implemented after only Doppler cooling, and the fidelity measured using a population and parity measurement. A single tone gate after only Doppler cooling resulted in a population measurement of $P(0'D) + P(D0') = 0.729(17)$. A parity measurement is shown in figure 6.18, with an amplitude fit of $A = 0.28(9)$. This gives a total fidelity of $F = 0.50(5)$. In comparison, the two tone gate population measurement of 1000 runs gave a probability $P(0'D)+P(D0') = 0.892(7)$. A parity measurement is shown in figure 6.18, which gives an amplitude fit of $A = 0.81(2)$. This gives a total fidelity of $F = 0.851(9)$, a significant improvement on the single tone gate. The infidelity is expected to be largely due to asymmetric detuning errors which remain sensitive to $\bar{n}$, as shown in figure 6.12. As before, further optimisation and higher power amplifiers to reduce saturation issues are expected to help increase this fidelity.

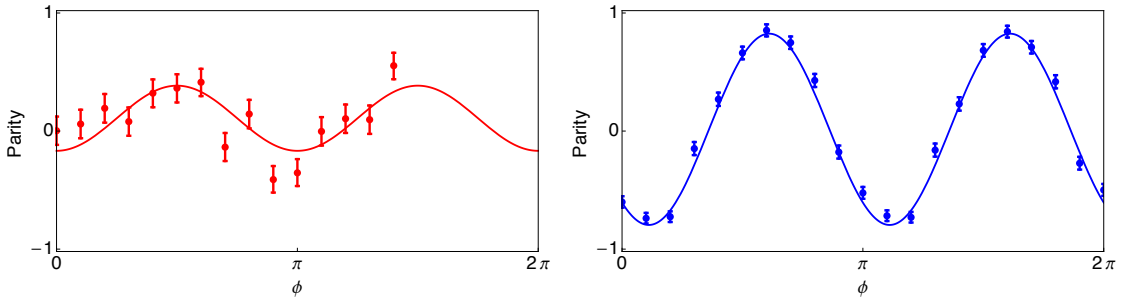

Figure 6.18: Parity curves shown for single (left) and two tone (right) gates where ions have been Doppler cooled to an initial motional mode of $\bar{n} = 53(4)$. A significant improvement can be seen for the two tone case due to its resilience to parameter mis-set, giving an amplitude fit of 0.81 compared to 0.28 for the single tone gate.

6.7 Conclusion

Multi-tone gates have been shown to provide significant protection against multiple error sources for a given gate time. This has been demonstrated experimentally for two tone gates. Three tone gates could provide further protection against heating, although improvement in protection against symmetric detuning is marginal, and there is a small detrimental effect on protection against asymmetric detuning. For our system, the time-varying AC Stark shift will become further complicated through the use of three tones, making it unlikely to yield further improvements. However, three or more tones may be useful in some implementations where protection against heating is critical.

After the work in this chapter was completed, the work of Shapira *et al.* came to our attention [92]. This work also uses multi-tone gates to perform resilient gates, and shows how they can be optimised for different experimental parameters. They optimise for protection against gate timing errors, which results in coefficients for the two tone gate of the form $c_1 = -c_2$, leading to cardioid shaped phase space trajectories. This robustness to gate timing error can be eliminated to $N-1$ leading orders in $\Delta\tau/\tau$ using N tones, where $\Delta\tau/\tau$ is the fractional timing error, giving an error of the form $(\Delta\tau/\tau)^{2N}$. The same gate coefficients were found to minimise error due to off-resonant coupling to the carrier transition. This set of gates was experimentally demonstrated using laser-driven gates on the ion $^{88}Sr^{+}$, including a gate demonstrated at a Doppler cooled ion temperature of $\bar{n} \approx 10$. Resilience to symmetric detuning errors is also discussed, as has been demonstrated here. Multi-tone gates are therefore a flexible tool which can be optimised for different sources of error to suit a particular system.

The protection demonstrated in this chapter comes at a cost in terms of resources,

with a two tone gate exhibiting a peak power three times higher than the single tone gate. However, even in the case where there is a limit in available power, MTMS gates will always provide protection against heating – as can be seen in figure 6.16, the heating infidelity is still lower when compared to a faster single tone gate driven at the peak power of the two tone gate. In this case, the faster single tone gate is performed at a gate power of $\sqrt{3}\Omega_0$, and the gate time is given by $\tau/\sqrt{3}$, where Ω_0 and τ are the parameters for the two tone gate. By approximating the heating infidelity from equation 6.77 as $\epsilon_{\text{heating}} = 4\dot{\bar{n}}_{\text{eff}}\tau$ for low errors, it can be seen that the two tone gate error is a factor of $1/\sqrt{3}$ smaller than the single tone error.

In many laser-based gate implementations, photon scattering is the dominant source of error [18, 19], which would become worse for the higher power gate fields required for the two tone gate at a given gate time. The average gate power is 5/3 times higher for the two tone gate, giving 5/3 times more photon scattering. In these cases, MTMS gates may not be suitable. However, infidelity due to heating is expected to get worse when performed on microfabricated traps with higher heating rates [18]. A careful balancing of error terms is therefore required to determine the suitability of MTMS gates for use in a specific system.

As well as protection against heating, multi-tone gates have also been shown to provide significant protection against errors due to symmetric detuning mis-sets. This will become a particularly useful feature in large scale quantum computing architectures, where it is likely that experimental environments may be noisier and less stable. Furthermore, this has opened up the possibility of performing gates at at higher initial values of the mean excitation of the motional state, such as can be achieved through only Doppler cooling. This symmetric detuning resilience also protects against error due to Kerr coupling, thus alleviating one of the main limitations in using the lower heating rate stretch mode for performing two qubit gates. The natural pulse shaping of two tone gates also provides some protection against off-resonant coupling, potentially allowing for faster gates to be driven if off-resonant coupling is a limiting factor. Further protection against off-resonant coupling can be achieved by optimising the coefficients for this error, as shown in the work by Shapira *et al.* [92]. This protection against multiple error sources makes MTMS gates a powerful tool for achieving high fidelity resilient two qubit gates in a large scale quantum computing architecture.

Chapter 7

Towards position-dependent quantum logic

7.1 Introduction

In this thesis, I have demonstrated the use of the dressed state qubit for performing high fidelity arbitrary single qubit gates with long-wavelength radiation, and a robust technique for performing two qubit gates particularly suitable for a large quantum computing architecture. These single and two qubit gate techniques have been demonstrated on one or two ions. However, one of the biggest challenges in the construction of a quantum computer is to integrate these quantum operations into a large scale architecture with high numbers of ions. A significant aspect of this challenge is the correlation between the number of physical qubits and the number of gate fields required, which could be either lasers or long-wavelength radiation. Weidt *et al.* [28] proposed a method to remove this correlation and replace the gate fields for each ion instead with global gate fields, by moving ions between different positions in a magnetic field gradient. A 'blueprint' to incorporate this idea into a modular design for a quantum computer was presented by Lekitsch *et al.* [38] This forms the framework for the research in our group, and in this chapter I present work towards demonstrating this key idea of position-dependent quantum logic with global gate fields. In the next section I summarise the proposals presented in these two papers, and in section 7.3 I describe how to implement a CNOT gate in our experimental system by moving ions in global radiation fields. I then demonstrate key experimental requirements for this demonstration: moving ions in a magnetic field gradient, preserving information stored in the qubit during ion movement, and optimising the phase of the two qubit gate in our system.

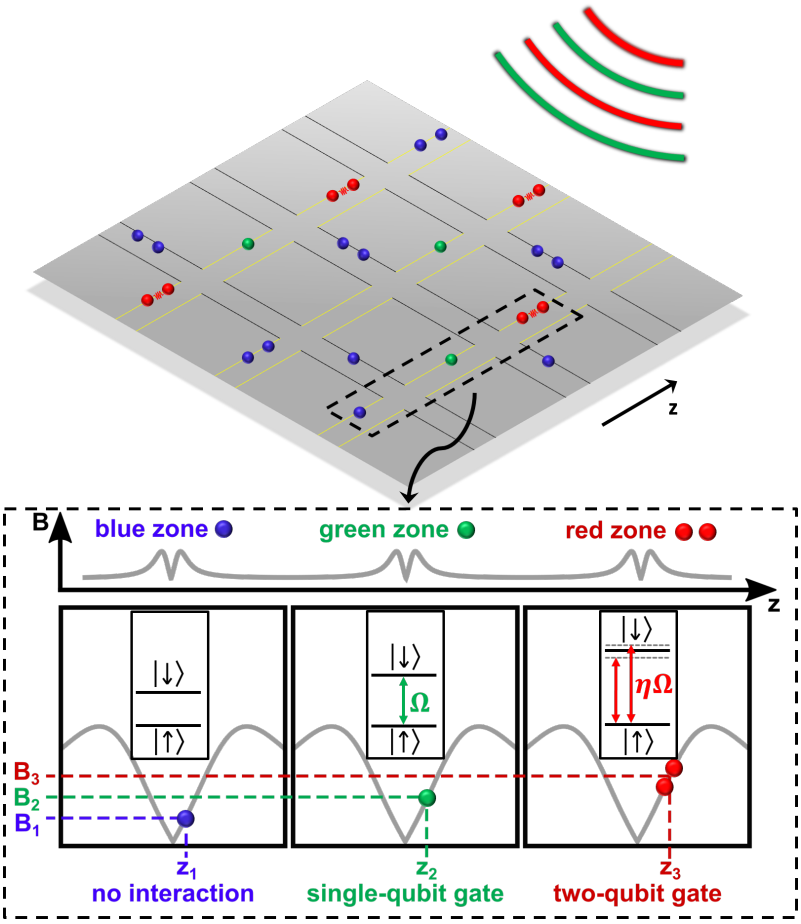

Figure 7.1: Schematic demonstrating the principle for using a small number of global radiation fields in order to implement quantum operations on many ions in parallel, therefore removing the correlation between the number of ions and the number of requires gate fields. Figure from [28].

7.2 Scalable architecture for quantum computing

A quantum computer capable of performing useful algorithms will require large numbers of ions. For example, in order to factorise a 2000 bit number using Shor's algorithm, and assuming gates with an error of 0.1%, it is estimated that a total of 220×10^6 physical qubits would be required because of the large overhead imposed by error correction [5]. Confining such large numbers of ions in a single potential for quantum operations is not possible, so most large scale architecture proposals use ion shuttling. Originally proposed by Kielpinski *et al.* [35], this method involves moving ions on microfabricated traps between zones. Different zones correspond to different operations, which include ion loading, quantum gates, and state readout. This means that only small numbers of ions need to be trapped in any single confining potential. However, there is still a limit to the number of ions that can be trapped and shuttled on a single microchip, so most proposals use a modular design. Individual modules are designed that can operate individually as a small quantum

processor, and then a method is used to connect multiple modules to scale to larger numbers of ions. In the proposal by Lekitsch *et al.*, each module for example would comprise 1296 X-junction surface ion traps fabricated on a single microchip, with two or more ions trapped in each X-junction.

Individual modules could for example be connected using photonic interconnects, to entangle a pair of ions held in two different modules, and then using this entanglement to teleport qubit states between modules [36, 37]. It is, however, challenging to obtain rates of high fidelity entangled pair generation that approach the speed at which gates can be performed, creating a bottleneck that could severely limit the computation capacity of such a device. Instead, Lekitsch *et al.* propose connecting modules by direct ion transport between physically adjacent modules. Precise alignment of the surface of the microfabricated ion traps is achieved by placing microchips on a precision machined steel frame, and using XYZ piezo actuators for fine alignment. This allows ions to be directly shuttled between modules, achieving a much faster rate of communication.

In many proposals the number of gate fields required, either lasers or microwaves, would be equal or comparable to the number of physical qubits. As well as the high number of gate field emitters this involves, a large problem is the alignment to individual ions. For example, laser access from the edge of microchips does not scale linearly with the number of ions that can be trapped on the surface of the microchip, making individual alignment and keeping cross talk to a minimum more challenging with increasing microchip size. In a proposal by Weidt *et al.*, however, this correlation between gate fields and number of ions is removed, and only a small number of gate fields are required. These gate fields are long-wavelength radiation fields which are broadcast globally to the architecture using a microwave horn and/ or RF emitters. Ions are shuttled between zones for different operations. In each zone, a static magnetic field is produced using current carrying-wires integrated into the chip structure. Local offset coils would also be included under chip in each gate zone to adjust the magnetic field and compensate for variations across the surface of the chip. By either adjusting the magnetic field offset using these coils, or moving the ion in the static magnetic field gradient by applying a voltage to an electrode, the qubit transition frequency of the ion, which is magnetic field dependent, can be controlled. In different zones, the qubit transition frequencies can therefore be tuned in order to interact with specific frequency fields in the global field that correspond to a specific gate. All other frequencies in the global field will have no effect. This principle is demonstrated in the schematic in figure 7.1, and is the key principle that I will work towards demonstrating in

this chapter. Lasers are still required for ion loading, cooling, preparation, and detection. However, the requirements for the control over the stability of these laser beams is lower, and the alignment of lasers is easier since, for example, a single laser beam can be used across multiple readout zones.

7.3 Demonstration of global addressing in a macroscopic ion trap

In this chapter, work towards demonstrating this principle of position-dependent quantum logic in the macroscopic trap used in this thesis is presented. Two ions are trapped in a magnetic field gradient, and moved between multiple positions to give different qubit transition frequencies. The global gate fields consist of a single qubit gate pulse and a two qubit gate pulse which are repeated alternately, as represented in figure 7.2. In this schematic, the single qubit gate pulses are in general $\pi/2$ pulses around an axis in the $x-y$ plane or identity pulses, and can be different for each ion. The two qubit gate pulse consists of a two qubit MS gate in one position, and identities in all other positions. Two qubit gates require high RF gate field powers, so simultaneous two qubit gate fields in more than one position would significantly reduce the available Rabi frequency for each gate in this experimental setup, making gates slower. This is not an issue for single qubit gates, which have much lower power requirements. Using these pulses, the ions will perform different quantum gates depending on their position.

In this demonstration, the controlled NOT (CNOT) gate was chosen for implementation as a simple example of performing sequences of gates by moving ions in a magnetic field gradient. The CNOT gate is of the form

$$U_{\mathrm{CNOT}} = \begin{pmatrix} 1 & 0 & 0 & 0 \\ 0 & 1 & 0 & 0 \\ 0 & 0 & 0 & 1 \\ 0 & 0 & 1 & 0 \end{pmatrix}. \tag{7.1}$$

The action of this gate is to swap the state of the 'target' qubit if the 'control' qubit is in the state $|1\rangle$. This gate cannot be performed directly in our system, but can be constructed from available single qubit and two qubit rotations.

Arbitrary single qubit rotations can be performed on the dressed state qubit, as has been demonstrated in chapter 5. From the unitary in equation 2.26, we can write a rotation

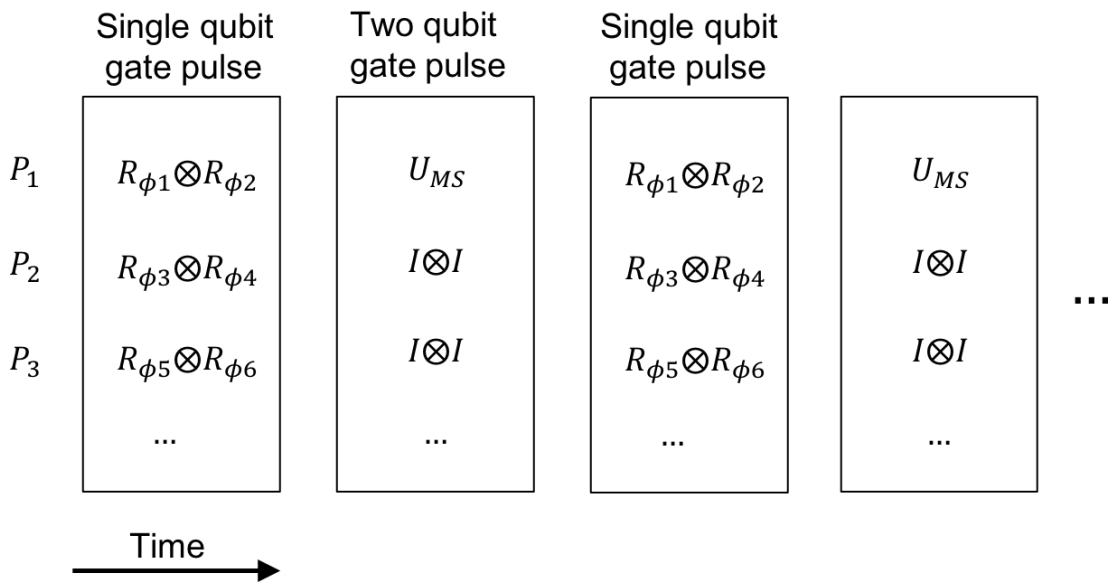

Figure 7.2: Schematic of the global gate fields used to demonstrate the principle of position-dependent quantum logic. The first pulse consists of multiple parallel single qubit gates performed at different RF frequencies corresponding to different positions, P_i. These are either $\pi/2$ pulses around an arbitrary axis or identity operators, and can be different for each ion. The second pulse consists of the fields required for a two qubit gate in one position, and identity pulses in all other positions. These pulses are repeated alternately in time.

of an angle θ around an axis in the $x-y$ plane at angle ϕ from the x axis as

$$R_\phi(\theta) = \begin{pmatrix} \cos\left(\frac{\theta}{2}\right) & -ie^{-i\phi}\sin\left(\frac{\theta}{2}\right) \\ -ie^{i\phi}\sin\left(\frac{\theta}{2}\right) & \cos\left(\frac{\theta}{2}\right) \end{pmatrix}. \tag{7.2}$$

All gates used in this chapter will be rotations of angle $\theta = \pi/2$. Rotations around the x and y axes can be performed by setting the phase to $\phi = 0$ and $\phi = \pi/2$ respectively. As in chapter 5, rotations around the z axis could be performed by adjusting the rotational basis for all subsequent gates.

The two qubit gate available in our system is the multi-tone Mølmer-Sørensen (MTMS) gate, as described and demonstrated in chapter 6. The MS gate interaction in an arbitrary basis ϕ can be described at the gate time by the unitary [93]

$$\begin{aligned} U_{\mathrm{MS}}(\phi) &= \exp\left\{\left(\frac{i\pi}{4}\sigma_1(\phi)\sigma_2(\phi)\right)\right\} \\ &= \frac{1}{\sqrt{2}}\begin{pmatrix} 1 & 0 & 0 & -ie^{-2i\phi} \\ 0 & 1 & -i & 0 \\ 0 & -i & 1 & 0 \\ -ie^{2i\phi} & 0 & 0 & 1 \end{pmatrix}. \end{aligned} \tag{7.3}$$

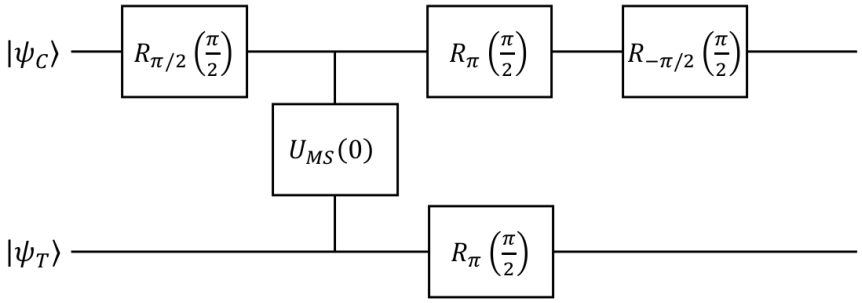

Figure 7.3: Circuit diagram showing the required operations to implement a CNOT gate using available gates in our system, where $R_\phi(\pi/2)$ represents a $\pi/2$ pulse around axis ϕ and $U_{MS}(0)$ represents a two qubit gate in the basis $\phi = 0$, or equivalently the x basis. The two input states $|\psi_C\rangle$ and $|\psi_T\rangle$ represent the control and target qubits respectively.

where, as for single qubit rotations, $\phi = 0$ corresponds to an MS gate in the x basis, and $\phi = \pi/2$ in the y basis. By adjusting the phase of the applied gate fields, it is possible to perform the gate in an arbitrary basis. We can then use this toolbox of single and two qubit gates to construct the CNOT gate, using the sequence of gates [94]

$$U_{\text{CNOT}} = \left(R_{-\frac{\pi}{2}}\left(\frac{\pi}{2}\right) \otimes I\right) \cdot \left(R_{\pi}\left(\frac{\pi}{2}\right) \otimes R_{\pi}\left(\frac{\pi}{2}\right)\right) \cdot U_{\text{MS}}(\phi = 0) \cdot \left(R_{\frac{\pi}{2}}\left(\frac{\pi}{2}\right) \otimes I\right) \quad (7.4)$$

where I represents the identity matrix, $R_\phi(\pi/2)$ is a $\pi/2$ pulse around axis ϕ as defined in equation 7.2, and $U_{MS}(\phi = 0)$ is the MS gate around axis $\phi = 0$ as defined in equation 7.3. This is represented as a circuit diagram in figure 7.3. In order to perform this sequence of gates using the technique described in the schematic in figure 7.2, the required single and two qubit gate pulses are shown in figure 7.4. A CNOT gate can then be performing by implementing one set of pulses with the ions in position one, followed by one set of pulses with ions in position two. In order to implement this experimentally, a method is required to move the ions in the magnetic field gradient, and to preserve the information stored in the dressed state qubit during this ion movement. This will be described in sections 7.4 and 7.5. A method is also required to fully characterise the phase of the two qubit gate in our system, in order to ensure that $U_{MS}(\phi = 0)$ is performed. This is described in section 7.6.

7.4 Moving the ions in a magnetic field gradient

While a full scale architecture will require sophisticated shuttling capabilities, this demonstration only requires two positions to be used so a simpler method for moving the ions

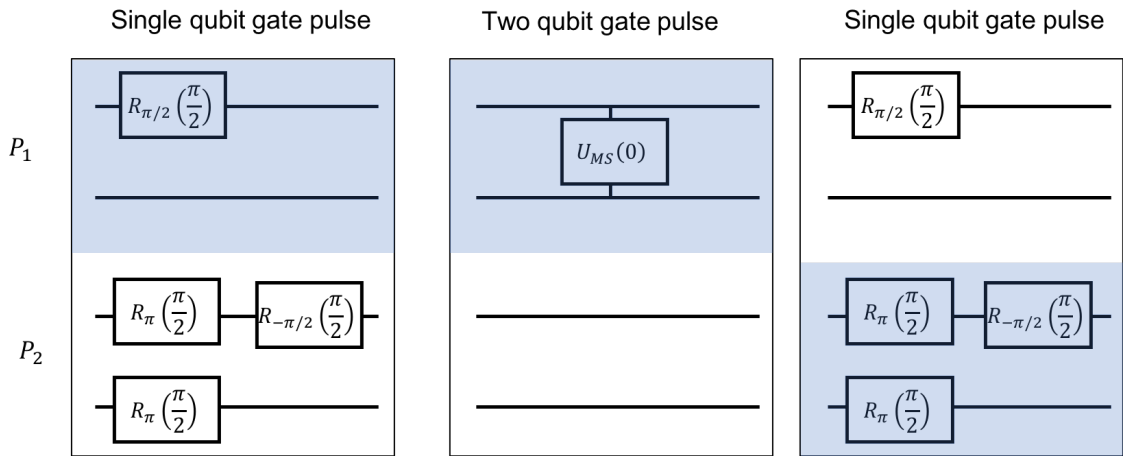

Figure 7.4: Schematic of the single and two qubit global gate pulses required for implementing a CNOT gate across two positions, P_1 and P_2. The gates performed depend on the ion position, and the blue area indicates the ion position required for each pulse to generate the CNOT gate sequence.

can be used. Ions are moved in the static magnetic field gradient by using a switch to alternate between two DC voltages (switch designed and built by Harry Godwin and Iain Hunter). This was composed of two solid state relay switches (Vishay V01462AABTR) controlled by TTL inputs. This switch was applied to an endcap electrode in order to move the ion axially. The electrical low-pass filter for that channel, described in section 3.1.2, was disconnected, since it was found to cause significant damping in switching time.

The effect of the voltage change between the two DC channels on the transition frequency of $|0\rangle \leftrightarrow |\pm 1\rangle$ was characterised, and the results are shown in figure 7.5. From this linear fit, a change in frequency per volt was extracted of 1.836(5) MHz/V, which was used to set the frequencies. From the static magnetic field gradient in the trap of 24.5(1) T/m, this can be calculated as a position change of 5.25(2) μm/V. The separation in frequency was chosen to minimise any effect of off-resonant coupling from the gate fields applied to an ion in one position on the ion in another position. In particular, the gate fields required for a two qubit gate must be taken into account, since at the secular frequency used in this experiment, they are separated from the carrier transition frequency, determined by the frequency of the transition $|0'\rangle \leftrightarrow |+1\rangle$, by nearly 0.5 MHz. A frequency separation of approximately 1 MHz was therefore chosen to be sufficient, corresponding to a voltage change of $\Delta V = 0.55$ V. A schematic of the resulting ion transition frequencies in the two positions is shown in figure 7.6.

The response of the ion to the switch was characterised by measuring the frequency of the $|0\rangle \leftrightarrow |+1\rangle$ transition of one of the ions at different delay times after switching DC voltages. The frequency of this transition is linearly dependent on magnetic field, and the

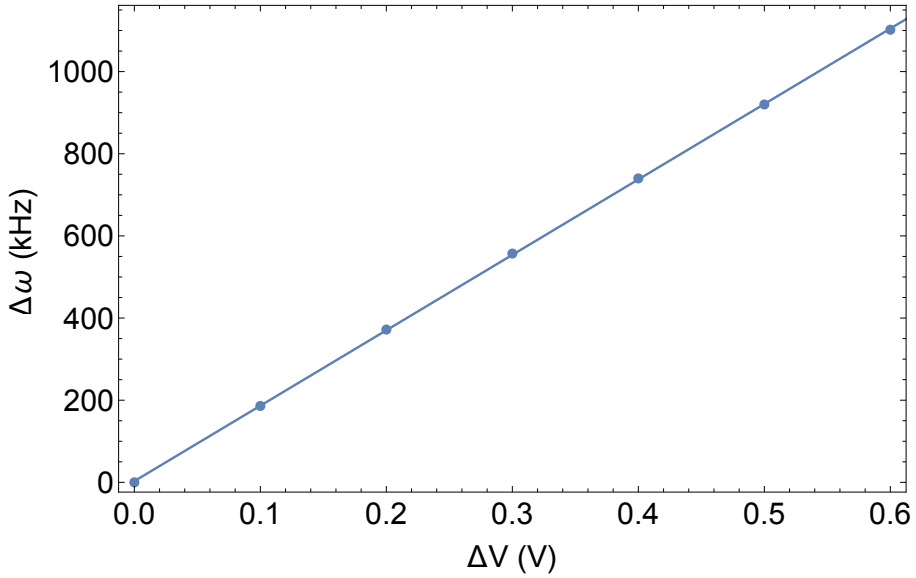

Figure 7.5: Calibration measurement of the $|0\rangle \leftrightarrow |+1\rangle$ transition frequency change resulting from a voltage change applied to one of the endcap electrodes. Error bars are smaller than the data points. The linear fit gives a change in frequency of 1.836(5) MHz/V.

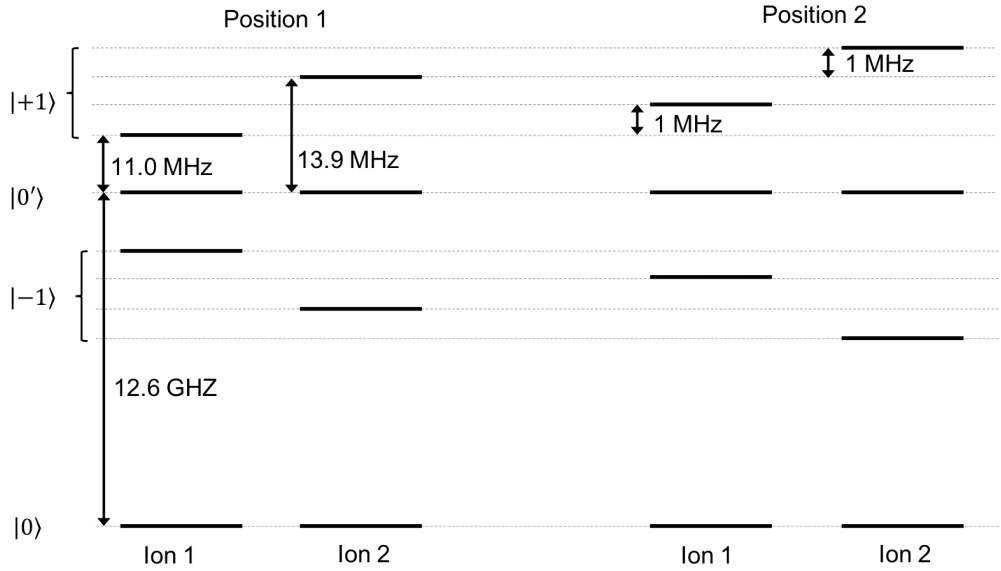

Figure 7.6: Schematic showing the two ion energy levels in two positions in the magnetic field gradient. Frequencies are chosen to minimise off-resonant coupling from non-resonant frequencies in the global gate fields.

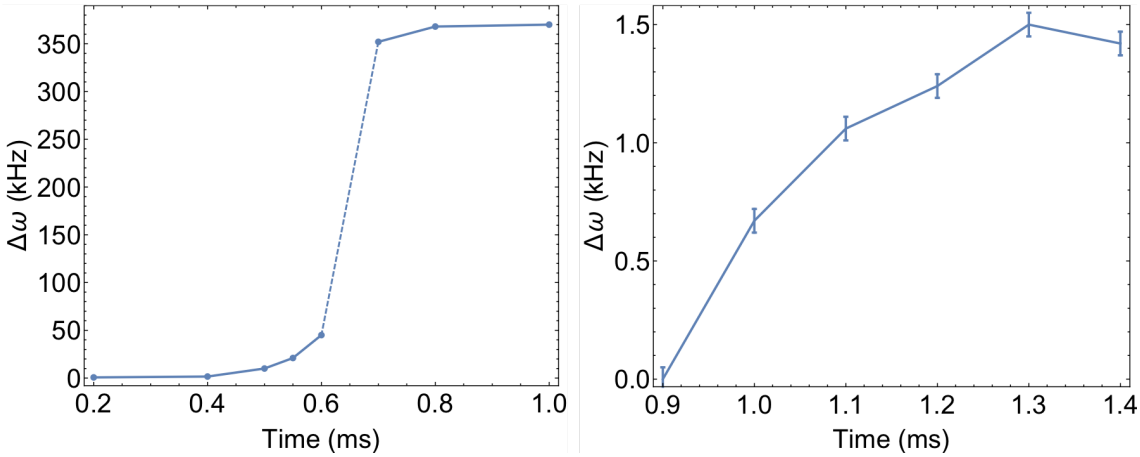

Figure 7.7: Graphs showing the frequency of the $|0\rangle \leftrightarrow |+1\rangle$ transition at different delay times after switching the voltage applied to an endcap electrode, therefore moving the ion axially. Frequency changes are calculated with respect to the first measured point in each graph. Left: Delay times from 0.2 ms to 1 ms. The dashed line shows the period during which most of the ion movement happens, and the movement is too fast to accurately measure the frequency. Errors are smaller than the data points at this scale. Right: Delay times of up to 1.4 ms, to ensure the ion is fully stationary before any operations are performed. This is a continuation of the graph on the left.

static magnetic field varies approximately linearly at the ion's position. This frequency measurement is therefore effectively a position measurement, tracking the movement of the ions through the gradient. The results of this experiment are shown in figure 7.7, where figure 7.7(a) is a measurement of the frequency over the entire switching time. On this scale, the error bars on the measured frequency are smaller than the data points. The dashed line between 0.6 ms and 0.8 ms represents the time period during which a proper frequency measurement could not be taken due to fast movement of the ion. This is therefore where most of the ion movement takes place, although the exact behaviour is unknown. Figure 7.7(b) shows a finer time scan at the end of switching. It must be ensured that the ion is stationary after switching before any coherent manipulation is performed, as any resultant change in frequency from the ion moving during quantum operations could affect the fidelity of both single and two qubit gates. A delay time of 1.4 ms was determined to be sufficient for the ion to be stationary within error.

An experiment was performed in order to measure any heating effect resulting from movement of the ions. The two ions were sideband cooled on the red stretch mode sideband of the $|0\rangle \leftrightarrow |+1\rangle$ transition of one of the ions, with frequency 460 kHz. The ion stretch mode temperature was measured as $\bar{n} \approx 0.4$ using sideband spectroscopy on the $|0'\rangle \leftrightarrow |D\rangle$ transition, as described in section 4.3, with a pulse time of 3 ms. To determine the effect of ion movement, the ions were sideband cooled and, before the temperature was measured,

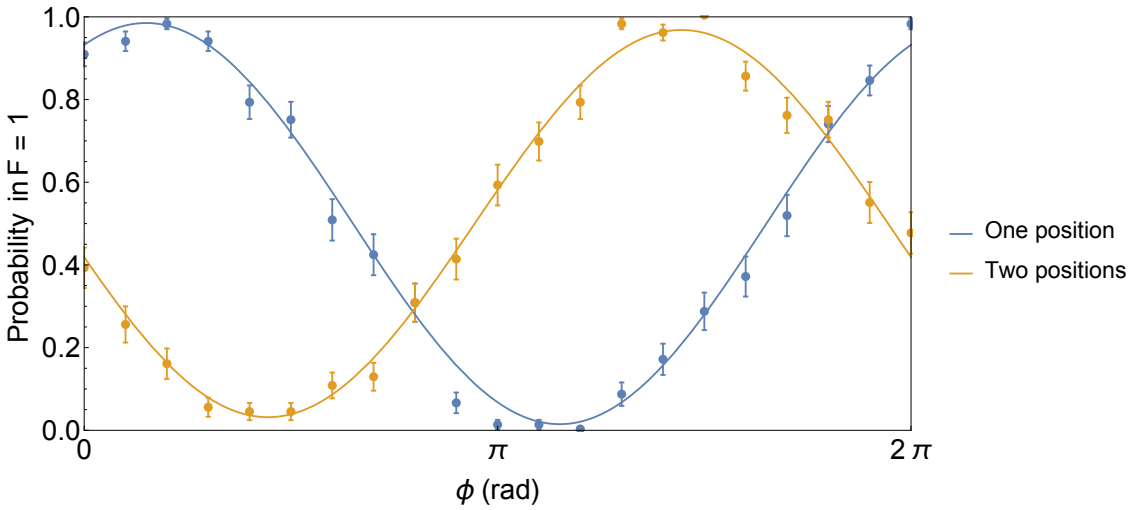

Figure 7.8: A Ramsey experiment performed on the clock qubit. Blue data points represent a Ramsey performed in one position, whereas orange show a Ramsey split across two positions, with shuttling between each $\pi/2$ pulse.

were shuttled between the two positions 25 times, giving a total of 50 ion movements of 1.4 ms. The experiment was also repeated where the ion remained stationary for the equivalent 70 ms delay before temperature measurement. In both cases, no increase in ion temperature was observed within error of 0.05 phonons. It can therefore be assumed that the heating rate is under 0.001 phonons per shuttle, and therefore this method of ion movement is sufficiently adiabatic to cause negligible stretch mode heating.

7.5 Mapping between dressed and clock qubits

Single and two qubit gates are performed in our system in the dressed state qubit. However, the dressed state qubit does not lend itself easily to preserving qubit information during ion movement, as the frequency of the dressing fields change as the ion moves through the magnetic field gradient. Instead, the dressed state qubit is mapped onto the clock qubit $\{|0\rangle, |0'\rangle\}$, which has only a second order dependence on magnetic field.

A test was implemented to ensure that the clock qubit could be moved between positions without decoherence by performing a Ramsey experiment across two positions. An ion was prepared in $|0\rangle$, and a $\pi/2$ pulse on the transition $|0\rangle \leftrightarrow |0'\rangle$ of time 450 μs with phase $\phi = 0$ was applied. The ion was then moved to position two, where a second $\pi/2$ pulse at the new transition frequency was applied with a varying phase. The second order Zeeman shifts for the two positions are $\Delta\omega_{z1} = 19.05$ kHz and $\Delta\omega_{z2} = 22.87$ kHz. The results of this experiment are shown in figure 7.8, where the results of a Ramsey experiment performed in a single position are shown as well as split across two positions. The

fit parameters for the Ramsey in one position give an amplitude of 0.97(1), and for two positions an amplitude of 0.94(2). These amplitudes agree within error, showing that a single movement causes no measurable decoherence on the clock qubit. A phase shift of $\Delta\phi = -0.92(2)$ can be seen, which results from the change in transition frequency across the two positions. The phase of the clock qubit in position two advances at a rate $\Delta(t)t$ relative to the phase in position one, where $\Delta(t)$ is the instantaneous detuning of the clock transition frequency from $\Delta\omega_{z1}$. This reaches a maximum in position two when $\Delta(t) = \Delta\omega_{z2} - \Delta\omega_{z1}$. The phase shift could therefore be calculated by integrating the expression $\Delta(t)t$ from time $t = 0$, which is the beginning of the initial $\pi/2$ pulse in position one, to the time that the second $\pi/2$ pulse is implemented in position two. However, the exact profile of $\Delta(t)$ is not known, since figure 7.7 is not a precise enough time profile. The phase shift is expected to be of order of multiple 2π's. An experimental measurement can be used instead of a calculation in order to calibrate gate phases.

Since single and two qubit gates are performed in the dressed state basis, a method is required to map the phase and populations of the dressed state qubit to the clock qubit. The method used previously in this thesis for preparing the state $|D\rangle$ is not suitable, since it only maps populations and phase information is lost, so a different technique is used [66]. I use a simple method as proof of principle, however our group has also developed high fidelity methods for this mapping [66]. To prepare the dressed state, the ion is first prepared in the state $|0\rangle$, and both dressing fields are turned on with Rabi frequency $\Omega_{\mu w}$. As in chapter 4, we can write the Hamiltonian for both dressing fields in the interaction picture with respect to the bare state energy levels Hamiltonian as

$$H'_{\mu w} = \frac{\hbar\Omega_{\mu w}}{2}(e^{-i\phi_+}\,|0\rangle\langle+1| + e^{-i\phi_-}\,|0\rangle\langle-1| + H.c.) \tag{7.5}$$

where we have assumed that there is no detuning on either dressing field. By applying dressing fields with phases $\phi_+ = 0, \phi_- = \pi$, this becomes

$$H'_{\mu w} = \frac{\hbar\Omega_{\mu w}}{2}(|0\rangle\langle+1| + |+1\rangle\langle 0| - |0\rangle\langle-1| - |-1\rangle\langle 0|). \tag{7.6}$$

We can then write the Hamiltonian as

$$H'_{\mu w} = \frac{\hbar\Omega_{\mu w}}{\sqrt{2}}(|0\rangle\langle D| + |D\rangle\langle 0|). \tag{7.7}$$

It can therefore be seen that under the influence of these fields, an ion will oscillate between states $|0\rangle$ and $|D\rangle$ at a frequency $\Omega_{\mu w}/\sqrt{2}$. A pulse of time $t = \sqrt{2}\pi/\Omega_{\mu w}$ on initial state

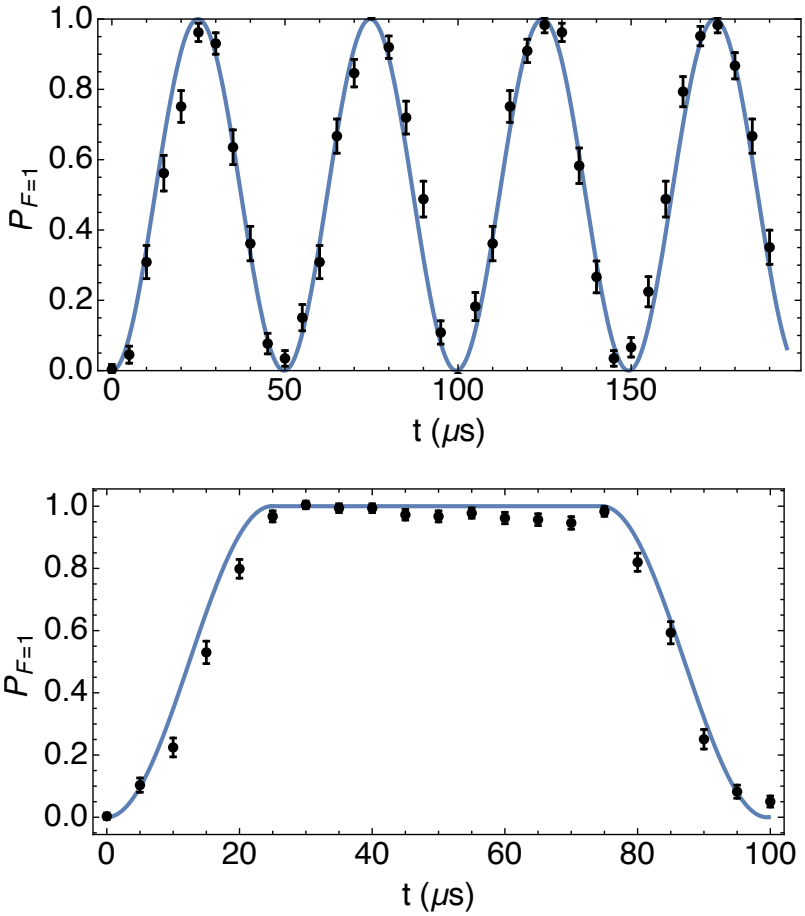

Figure 7.9: Demonstration of the method used for mapping between the clock qubit $\{|0'\rangle, |0\rangle\}$ and the dressed state qubit $\{|0'\rangle, |D\rangle\}$. Top: Rabi flop between the states $|0\rangle$ and $|D\rangle$ by constant application of the microwave dressing fields simultaneously on the transitions $|0\rangle \leftrightarrow |+1\rangle$ and $|0\rangle \leftrightarrow |-1\rangle$. Bottom: Demonstration of mapping from the state $|0\rangle$ into the state $|D\rangle$ using a π pulse on the two dressing fields, holding in that state for $50\,\mu$s, and mapping back to the state $|0\rangle$.

$|0\rangle$ will produce the state $|D\rangle$. In order to hold the ion in this dressed state to perform operations on the qubit $\{|0'\rangle, |D\rangle\}$, the phase of the applied dressing fields should be changed instantaneously to $\phi_+ = \phi_- = 0$, to give the Hamiltonian

$$H'_{\mu w} = \frac{\hbar\Omega_{\mu w}}{2}(|0\rangle\langle+1| + |+1\rangle\langle 0| + |0\rangle\langle -1| + |-1\rangle\langle 0|). \tag{7.8}$$

The state $|D\rangle$ is an eigenstate of this Hamiltonian. After coherent manipulation of the qubit is complete, an arbitrary state composed of $|0'\rangle$ and $|D\rangle$ will be formed. In order to map this back to the clock qubit, the phase of the dressing fields is returned to $\phi_+ = 0, \phi_- = \pi$ for a time $t = \sqrt{2}\pi/\Omega_{\mu w}$. Under the influence of the Hamiltonian in equation 7.7, the state $|0'\rangle$ will remain unaffected, and the population and phase in the state $|D\rangle$ will be transferred to the state $|0\rangle$. We therefore map the qubit $\{|0'\rangle, |D\rangle\}$ to the clock qubit $\{|0'\rangle, |0\rangle\}$.

This method for mapping has been demonstrated experimentally, shown in figure 7.9. First, a Rabi oscillation between the states $|0\rangle$ and $|D\rangle$ is shown by simply holding the microwave fields for increasing lengths of time. A fit of equation 2.32 gives a Rabi frequency of approximately 20.1 kHz, which corresponds to a mapping time of 25 μs. It was then demonstrated that the qubit could be held in the dressed state, by instantaneously swapping the phase of the dressing fields. A π pulse of time 25 μs was applied, after which the phase of the dressing field on the $|0\rangle \leftrightarrow |-1\rangle$ transition was changed by π. This was held for 50 μs, after which the phase was returned to the initial phase, and a final π pulse mapped the population back to $|0\rangle$.

Using this method for mapping between the dressed state qubit and the clock qubit, a Ramsey experiment was performed on the states $\{|0'\rangle, |D\rangle\}$ split across the two positions, which is shown in figure 7.10. The ion was prepared in the state $|0'\rangle$. The dressing fields were turned on with phase $\phi_+ = \phi_- = 0$, and an RF $\pi/2$ pulse of time 460 μs was performed on the $|0'\rangle \leftrightarrow |D\rangle$ transition with phase $\phi = 0$, to form a superposition of the two states. The phase of the dressing fields was then instantaneously changed to $\phi_+ = 0, \phi_- = \pi$ to map the qubit to the clock qubit. In this case, the mapping time was 21 μs. The ion was then moved to position two, and mapped back into the dressed state qubit using the same method. A second $\pi/2$ pulse was applied to the $|0'\rangle \leftrightarrow |D\rangle$ transition with a varying phase. The qubit was then mapped back to the clock qubit. A final clock pulse on the transition $|0\rangle \leftrightarrow |0'\rangle$ means that population in the state $|D\rangle$ is measured in the $F = 1$ bright state, and population in the state $|0'\rangle$ measured in the $F = 0$ dark state. This provides consistency with previous measurements of the dressed state qubit, but is

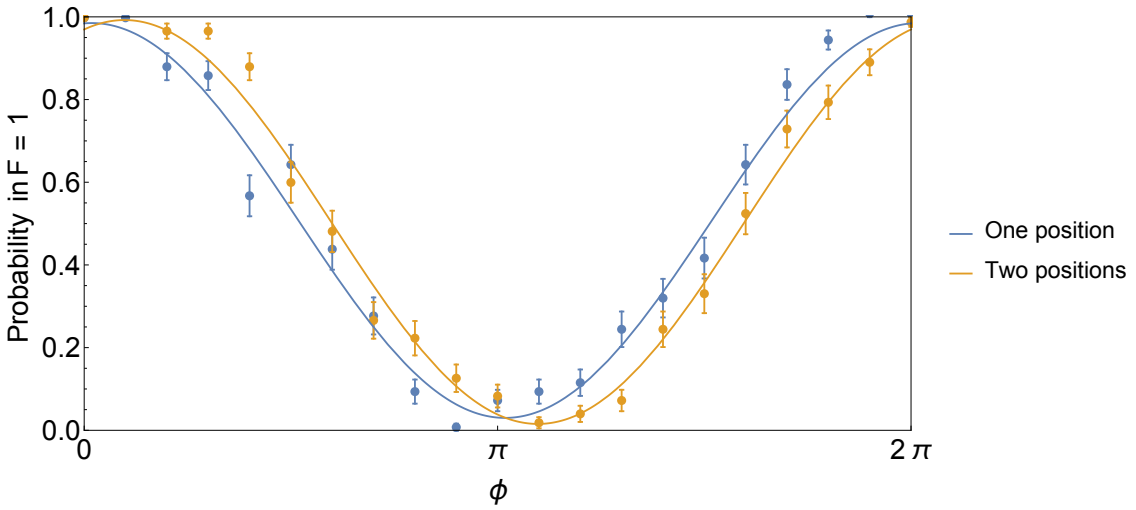

Figure 7.10: Ramsey fringes on the dressed state qubit in one position, and split across two positions by mapping into the clock qubit for ion movement between the two $\pi/2$ pulses.

not a necessary step for measurement. The resultant fringes are shown in figure 7.10. To compare with the Ramsey split across two positions, a Ramsey experiment in the qubit $\{|0'\rangle, |D\rangle\}$ is shown performed in one position. The fit gives an amplitude of 0.95(3) for the Ramsey in one position and 0.98(1) for the Ramsey split across two positions. There is therefore no loss in amplitude across two positions compared to the Ramsey fringe in one position, showing the suitability of this method for maintaining phase coherence between the dressed state qubit in two locations. A phase shift between the two results can be seen, which can again be calibrated for experimentally.

An alternative approach to this method for mapping between the dressed state qubit and the clock qubit is to use a rapid adiabatic passage method, which relies on adiabatically bringing detuned dressing fields into resonance [28, 66]. This method is experimentally simpler since it involves using only the dressing fields and the ion movement for mapping. The Hamiltonian for the dressing fields in the interaction picture with respect to the bare state energy levels is

$$H'_{\mu w} = \frac{\hbar\Omega_{\mu w}}{2}(e^{i\delta(t)t}\,|0\rangle\langle+1| + e^{-i\delta(t)t}\,|0\rangle\langle-1| + H.c.) \tag{7.9}$$

where $\delta(t)$ is a time-varying detuning. By defining the Hamiltonian $H_\delta = \hbar\delta(t)(|+1\rangle\langle+1| - |-1\rangle\langle-1|)$, we can move into an interaction picture with respect to the detuning of the

dressing fields, giving

$$\begin{aligned} H''_{\mu w} &= e^{iH_\delta t/\hbar}(H'_{\mu w} - H_\delta)e^{-iH_\delta t/\hbar} \\ &= \frac{\hbar\Omega_{\mu w}}{2}(|0\rangle\langle+1| + |+1\rangle\langle 0| + |0\rangle\langle -1| + |-1\rangle\langle 0|) - \hbar\delta(t)(|+1\rangle\langle+1| - |-1\rangle\langle -1|) \\ &= \frac{\hbar}{2}\begin{pmatrix} 2\delta(t) & \Omega_{\mu w} & 0 \\ \Omega_{\mu w} & 0 & \Omega_{\mu w} \\ 0 & -\Omega_{\mu w} & -2\delta(t) \end{pmatrix} \end{aligned} \tag{7.10}$$

where the states are ordered $\{|-1\rangle, |0\rangle, |+1\rangle\}$. If the ion starts in an eigenstate and the detuning $\delta(t)$ is varied slowly then the state of the qubit will adiabatically follow this. One of these eigenstates is the normalised state of the form

$$|\psi\rangle = (|+1\rangle + \frac{2\delta(t)}{\Omega_{\mu w}}|0\rangle - |-1\rangle). \tag{7.11}$$

It can therefore be seen that, for $\delta \gg \Omega_{\mu w}$, $|0\rangle$ is an eigenstate of this Hamiltonian. However, as $\delta(t) \to 0$, the eigenstate becomes the dressed state $|D\rangle = (|+1\rangle - |-1\rangle)\sqrt{2}$. This method of adiabatically varying the dressing field detuning has been demonstrated by changing the frequency of the dressing fields [66]. However, it could also be implemented by adiabatically moving the ion in the magnetic field gradient.

An experiment was performed to map the dressed state qubit between the two positions by moving the ion through the static field gradient. The ion was prepared in state $|0'\rangle$, and the four dressing fields corresponding to both position one and position two were turned on instantaneously. A $\pi/2$ pulse on the transition $|0'\rangle \leftrightarrow |D\rangle$ was implemented in position one, and the ion was then moved to position two. A second $\pi/2$ pulse with a varying phase was performed in position two on the transition $|0'\rangle \leftrightarrow |D\rangle$, and the resultant populations measured. If the movement of the ion corresponds to an adiabatic change of the transition frequencies $|0\rangle \leftrightarrow |\pm 1\rangle$, the dressed state qubit should be mapped from the state $|D\rangle$ in position one, to state $|0\rangle$ during movement, to state $|D\rangle$ in the second position. The results of this experiment are shown in figure 7.11. A clear Ramsey fringe is seen, showing that this simple method for mapping is working to some degree. However, the amplitude of the fringe is 0.6. In order to improve this, the timing characteristics of the switch should be more precisely characterised and controlled in order to ensure that the condition for adiabaticity, which is that the change in the detuning $\delta(t)$ is slow compared to the microwave Rabi frequency $\Omega_{\mu w}$, is fulfilled.

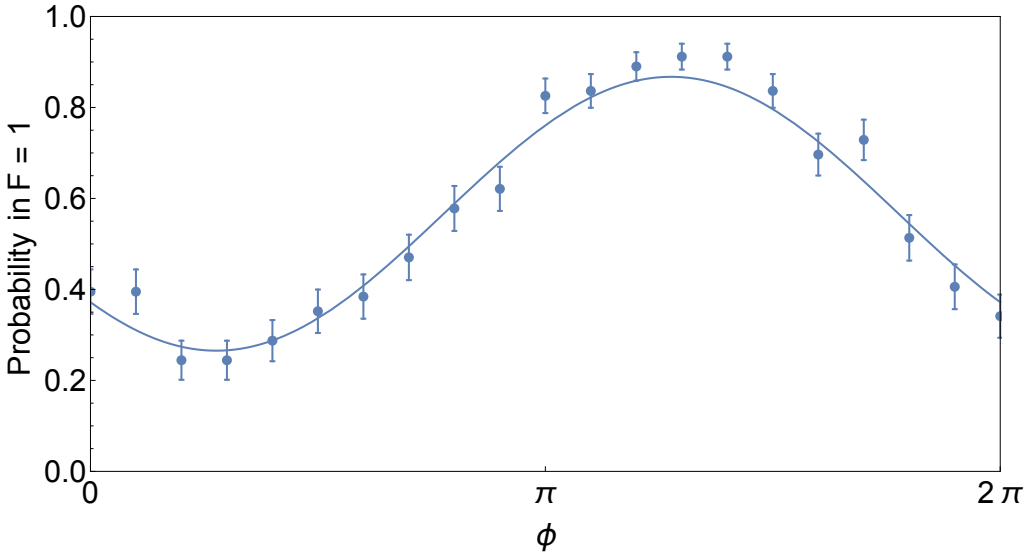

Figure 7.11: Ramsey pulse sequence on the transition $|0'\rangle \leftrightarrow |D\rangle$ split across two positions. The qubit is mapped by moving the ions through a magnetic field gradient so that the dressing fields are gradually swept away from or into resonance, depending whether the ion is being mapped out of or into the dressed state qubit. The low amplitude is due to the unoptimised timing behaviour of the switch, which does not result in an adiabatic transfer.

7.6 Characterising the phase of a two qubit gate

As discussed in section 7.3, a CNOT gate can be constructed from single and two qubit gates available in our system, using a sequence of gates defined in equation 7.4. The phase of the two qubit gate should be set as $U_{MS}(\phi = 0)$. In chapter 6, we do not fully characterise the MS gate performed, instead calculating the fidelity with which a state of form $|0'0'\rangle + e^{4i\chi}|DD\rangle$ is formed from the initial state $|0'0'\rangle$. We therefore need a method to fully understand the phases of the two qubit gate in our system.

A variable phase MS gate was defined in equation 7.3. However, in our implementation of the MS gate, the phase of the gate is more complex due to the differential AC Stark shifts on each ion. This effect is similar to the phase shift seen in the Ramsey split between two positions in the previous section, although in that case the phase shift resulted from the difference in transition frequencies between the two positions. In this case, it is the AC Stark shifts causing the phase to advance at a rate faster than the qubit frequency. The magnitude of these AC Stark shifts in relation to the gate time causes significant phase

shifts, and the resultant gate unitary matrix is

$$U_{\mathrm{MS}}(\phi_1,\phi_2) = \exp\left\{\left(\frac{i\pi}{4}\sigma_1(\phi_1)\sigma_2(\phi_2)\right)\right\} = \frac{1}{\sqrt{2}}\begin{pmatrix} 1 & 0 & 0 & -ie^{-i(\phi_1+\phi_2)} \\ 0 & 1 & -ie^{-i(\phi_1-\phi_2)} & 0 \\ 0 & -ie^{i(\phi_1-\phi_2)} & 1 & 0 \\ -ie^{i(\phi_1+\phi_2)} & 0 & 0 & 1 \end{pmatrix} \quad (7.12)$$

where ϕ_1 is the phase for ion 1 and ϕ_2 is for ion 2. The phase of the resultant parity curve on input state $|0'0'\rangle$ gives only partial information about the two qubit gate phases, since it depends on the sum of the phases, but does not give information on the difference.

In order to extract full phase information, we can instead use the CNOT gate sequence. We perform an experimental scan of the MTMS gate field phase embedded in the CNOT sequence applied to an initial state $|0'0'\rangle$ by adding the same phase shift to both sets of gate fields. This can be written as

$$U_{\mathrm{CNOT}} = (G(-\pi/2)\otimes I)\cdot(G(\pi)\otimes G(\pi))\cdot U_{\mathrm{MS}}(\phi_0+\phi, \phi_0+\Delta\phi+\phi)\cdot(G(\pi/2)\otimes I).\left|0'0'\right\rangle \quad (7.13)$$

where ϕ is the phase shift added to both the gate fields, and we have defined $\phi_1 = \phi_0$ and $\phi_2 = \phi_0 + \Delta\phi$. The resultant curves for different values of ϕ_0 and $\Delta\phi$ are shown in figure 7.12. It can be seen that different values of $\Delta\phi$ give distinct results when measuring the populations of $|0'0'\rangle$ and $|0'D\rangle + |D0'\rangle$ for this type of scan. The probability of the states $|0'D\rangle$ and $|D0'\rangle$ are plotted as a single probability due to the limits of detection using the PMT. Figure 7.12(a) at $\phi = 0$ shows the ideal case for implementing a CNOT. Similar scans could be performed on alternative input states.

A scan of this type is experimentally demonstrated in figure 7.13. This experiment is performed in one position. The phase of the single qubit gates are fixed to the values given in equation 7.13, and the phase of the applied gate fields begins at $\phi = 0$ and is stepped by $\pi/10$. The two qubit gate is a two tone Mølmer-Sørensen gate, as described in the previous chapter. Eight distinct gate fields are applied to the ions, with two per sideband. The gate was performed at a stretch mode secular frequency of 461 kHz, with a base Rabi frequency of $\Omega_0 = 36$ kHz giving a gate time of 3.4 ms. The gate was unoptimised and of fidelity 0.88(3). The resultant fit gives values of $\phi_0 = -0.36(2)$ and $\Delta\phi = 1.02(3)$, although the fit does not include the effect of the low fidelity. The effect of this on the phase scan is not known and may depend on the source of the error, so ideally the gate

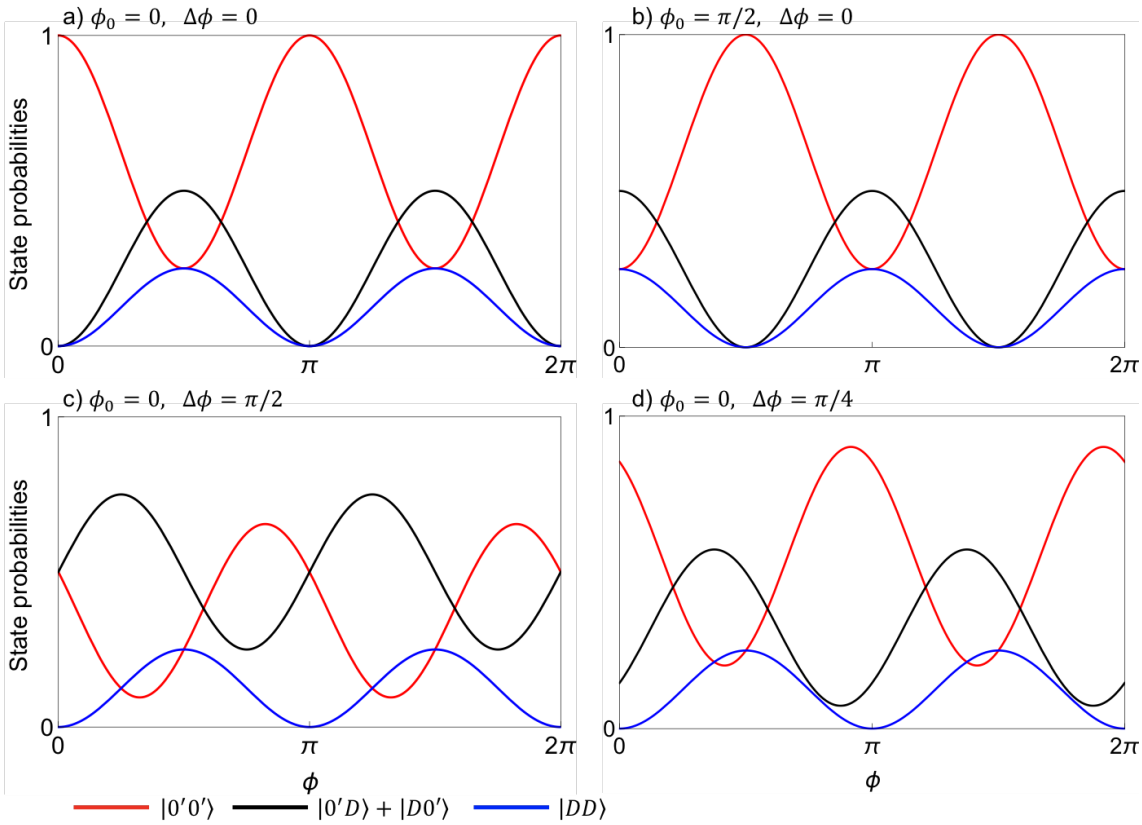

Figure 7.12: Theoretical curves showing a scan of the phase of the gate fields applied during the CNOT operation, shown for different values of ϕ_0 and $\Delta\phi$. This method can be used to extract phase information about a two qubit gate in an unknown basis, in order to correctly set the phases to $\phi_0 = \Delta\phi = 0$ for implementing a CNOT gate.

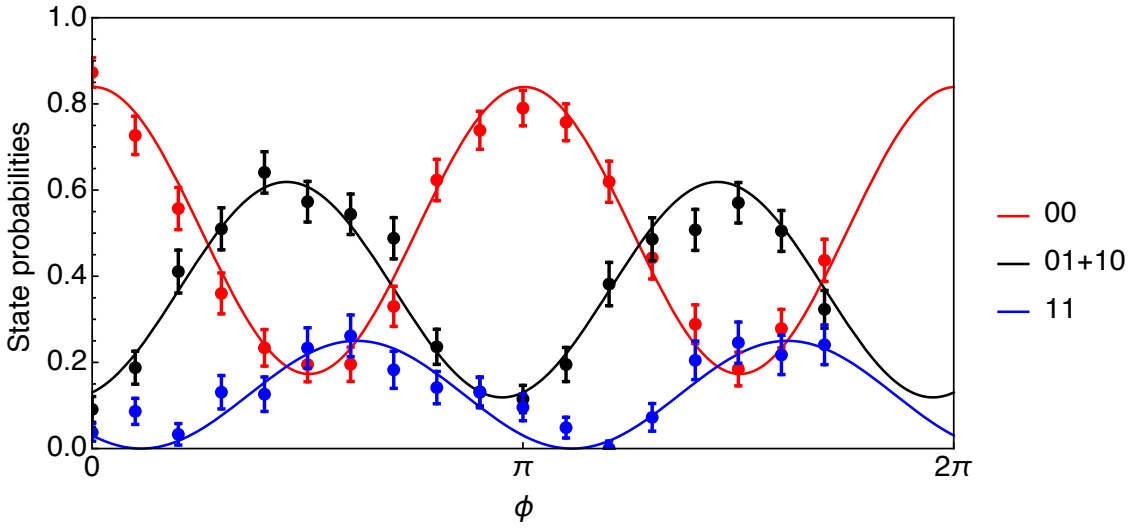

Figure 7.13: State probabilities for a scan of the gate fields applied to a two tone Mølmer-Sørensen gate embedded in the sequence of gates required for implementing a CNOT. A fit to the data gives $\phi_0 = -0.36(2)$ and $\Delta\phi = 1.02(3)$.

fidelity would be optimised to ensure that this effect is small. The measured phase offset and phase difference can then be used to adjust the phase of the gate fields to ensure that $\phi_0 = \Delta\phi = 0$, which is required for a CNOT gate.

Input state	$P(0'0')$	$P(0'D)$	$P(D0')$	$P(DD)$
$\|0'0'\rangle$	1	0	0	0
$\|0'D\rangle$	0	1	0	0
$\|D0'\rangle$	0	0	0	1
$\|DD\rangle$	0	0	1	0

Table 7.1: Theoretical result for a CNOT gate operating on the four classical input states.

Input state	$P(0'0')$	$P(0'D) + P(D0')$	$P(DD)$
$\|0'0'\rangle$	0.781(13)	0.150(12)	0.069(9)
$\|0'D\rangle$	0.180(17)	0.795(20)	0.025(14)
$\|D0'\rangle$	0.043(10)	0.038(18)	0.920(24)
$\|DD\rangle$	0.039(10)	0.958(16)	0.004(15)

Table 7.2: Preliminary data for a CNOT gate operating on the four classical input states.

After optimising the phase of the two qubit gate using this method, we can now perform a CNOT gate on a pair of ions. The CNOT was implemented on the four classical input states, and the preliminary results are shown in table 7.2. Since only detection on the PMT was available, it was not possible to distinguish between $P(0'D)$ and $P(D0')$. The theoretical results are shown in table 7.1 for comparison. The average of the probabilities of recording the correct result for a given input state is 0.86(1), which is a maximum limit to the fidelity since $P(0'D)$ and $P(D0')$ are not measured separately. This is assumed to be largely limited by the measured unoptimised two qubit gate fidelity of 0.88(3), and

single qubit gate infidelities are assumed to be negligible.

7.7 Conclusion

In this chapter, I have demonstrated the basic operations which when combined will demonstrate performing a CNOT gate using position-dependent quantum logic. I have shown a method to move ions in a static magnetic field gradient, and to preserve the quantum information stored in the qubit during movement. I have also demonstrated a method to characterise a two qubit MS gate of unknown phase, in order to optimise the phase of the gate for implementing a CNOT. Bringing these techniques together should allow for a CNOT gate to be performed across two positions, using the method outlined in section 7.3. The work presented here is a key step towards demonstrating the basic principle of position-dependent quantum logic.

Chapter 8

Conclusion

In this thesis, I have demonstrated key experiments towards a large scale quantum computing architecture based on trapped ion qubits. The average error on single qubit gates driven by long-wavelength radiation on the dressed state qubit has been characterised using the technique of randomised benchmarking. I have demonstrated a novel two qubit gate technique suitable for performing high fidelity two qubit gates in the presence of noise, which will become a particularly important property in a large scale architecture. I have also presented work towards demonstrating the principle of position-dependent quantum logic, an approach which would remove the correlation between the number of physical qubits and the number of gate fields required to construct a quantum computer.

8.1 Summary

Chapter 2 describes the background to using the ion $^{171}Yb^{+}$ as a qubit. I also show how use of long-wavelength radiation combined with a static magnetic field gradient generates a coupling between the spin and motional states of an ion which is analogous to the coupling generated using the momentum of optical photons. In chapter 3, the experimental setup used in this work is described, as well as initial experiments that underpin the later work in this thesis. I then go on in chapter 4 to discuss the use of dressed states to protect against magnetic field noise but retain sensitivity to magnetic fields in order to perform multi-qubit operations with long-wavelength radiation. These dressed states have a coherence time an order of magnitude longer than the coherence time of the bare states.

In chapter 5, I show the randomised benchmarking of single qubit gates using this dressed state qubit. This yields an error per computational gate of $9(3) \times 10^{-4}$. A discussion of sources of error suggests that the largest contributions to infidelity are a

systematic qubit transition frequency mis-set, and off-resonant coupling to transitions outside of the qubit subspace. The off-resonant coupling places a stringent limit on Rabi frequencies, and could be alleviated by increasing the second order Zeeman shift and the microwave dressing Rabi frequencies.

In chapter 6, a new type of robust two qubit gate is demonstrated: the Multi-Tone Mølmer-Sørensen gate. This technique provides a method to generate two qubit entanglement that is robust against multiple error sources. I discuss how these gates can simultaneously protect against infidelity due to heating and due to symmetric detuning errors caused by an incorrect secular frequency. I also show how these gates can alleviate restrictions placed on the use of the stretch mode for two qubit gates by Kerr coupling to the radial modes, and reduce the effect of off-resonant coupling to the carrier. An experimental demonstration shows the expected protection against heating and symmetric detuning errors by comparing two tone gates to a standard MS gate. This technique is demonstrated using long-wavelength radiation, but is also suitable for laser based quantum logic. These gates are expected to be particularly suitable for large scale architectures where experimental environments may be noisier or less stable, and in particular where error due to heating may become worse due to use of microfabricated ion traps with higher heating rates.

Finally, in chapter 7, I demonstrate techniques towards implementing position-dependent quantum logic, a key principle of a proposal for a scalable architecture by Weidt *et al.* [28]. In this proposal, ions are moved between positions on the surface of the chip and, by adjustment of local magnetic fields at each position, interact only with selected global radiation fields. I outline a method to use position-dependent quantum logic to implement a CNOT gate, and demonstrate important steps towards this goal. A technique for moving the ions in the experimental setup is demonstrated which causes negligible heating of the stretch mode. Mapping of the dressed state qubit to the clock qubit is also shown, in order to preserve quantum information during ion movement. I present a method to characterise the phase of an unknown two qubit gate, in order to optimise for a CNOT gate. This work provides the necessary tools to demonstrate the principle of position-dependent quantum logic.

8.2 Future work

The focus of future work in our group is to demonstrate key features of the architecture proposed by Lekitsch *et al.* This includes designing and testing X-junction microfabricated

ion traps suitable for use within a quantum computer module. Work is also ongoing into generating high magnetic field gradients using current-carrying wires, since high magnetic field gradients are necessary for increasing the effective Lamb-Dicke parameter and performing faster two qubit gates. A module prototype is being designed to test the ability to align microchips to high precision using piezo-actuators to allow direct shuttling of ions between chips.

The macroscopic ion trap used in this work has an important role in working towards the realisation of a large scale architecture as a test-bed for techniques required for coherent manipulation. Importantly, the work on position-dependent quantum logic can be continued to demonstrate a high fidelity CNOT gate across two positions. This experiment could be extended by adding further ion positions and gate fields, in order that different gates could be implemented depending on the sequence of ion position chosen. The technique could also be used to perform simple quantum circuits on higher numbers of qubits.

A large challenge facing the use of position-dependent quantum logic is the possibility of variations of Rabi frequency between different ion positions. Methods to protect against this for single qubit gates involve using composite pulses to reduce the sensitivity of gates to timing errors [66]. Methods to protect two qubit gates against incorrect Rabi frequencies should be investigated, as well as techniques for protection against other error sources such as asymmetric detuning. The possibility of combining MTMS gates with other robust gate techniques (for example [81] and [95]) may offer further protection. Different methods to perform faster high fidelity two qubit gates could also be investigated [96]. Alongside work on developing the required module architecture, the demonstration of robust and scalable coherent manipulation techniques provides a path forwards towards the construction of a quantum computer.

Bibliography

[1] R. P. Feynman. Simulating physics with computers. *Int. J. Theor. Phys.*, 21(467 – 488), 1982.

[2] D. Deutsch. Quantum theory, the Church–Turing principle and the universal quantum computer. *Proceedings of the Royal Society of London A: Mathematical, Physical and Engineering Sciences*, 400(1818):97–117, 1985.

[3] P. Shor. Polynomial-time algorithms for prime factorization and discrete logarithms on a quantum computer. *SIAM Journal on Computing*, 26(5):1484–1509, 1997.

[4] L. K. Grover. A fast quantum mechanical algorithm for database search. In *Proceedings of the Twenty-eighth Annual ACM Symposium on Theory of Computing*, STOC '96, pages 212–219, New York, NY, USA, 1996. ACM.

[5] A. G. Fowler, M. Mariantoni, J. M. Martinis, and A. N. Cleland. Surface codes: Towards practical large-scale quantum computation. *Phys. Rev. A*, 86:032324, 2012.

[6] D. P. DiVincenzo. The physical implementation of quantum computation. *Fortschritte der Physik*, 48(9-11):771–783, 2000.

[7] G. K. Brennen, C. M. Caves, P. S. Jessen, and I. H. Deutsch. Quantum logic gates in optical lattices. *Phys. Rev. Lett.*, 82:1060–1063, 1999.

[8] J. Clarke and F. K. Wilhelm. Superconducting quantum bits. *Nature*, 453:1031 E–1042, 2008.

[9] J. I. Cirac and P. Zoller. Quantum computations with cold trapped ions. *Phys. Rev. Lett.*, 74:4091–4094, 1995.

[10] Y. Wang, M. Um, J. Zhang, S. An, M. Lyu, J-N. Zhang, L-M. Duan, D. Yum, and K. Kim. Single-qubit quantum memory exceeding ten-minute coherence time. *Nature Photonics*, 11(10):646–650, 2017.

[11] F. Schmidt-Kaler, H. Häffner, M. Riebe, S. Gulde, G. P. T. Lancaster, T. Deuschle, C. Becher, C. F. Roos, J. Eschner, and R. Blatt. Realization of the Cirac–Zoller controlled-not quantum gate. *Nature*, 422:408 – 411, 2003.

[12] D. Leibfried, B. DeMarco, V. Meyer, D. Lucas, M. Barrett, J. Britton, W. M. Itano, B. Jelenkovic, C. Langer, T. Rosenband, and D. J. Wineland. Experimental demonstration of a robust, high-fidelity geometric two ion-qubit phase gate. *Nature*, 422:412–415, 2003.

[13] C. Monroe, D. M. Meekhof, B. E. King, S. R. Jefferts, W. M. Itano, D. J. Wineland, and P. Gould. Resolved-sideband Raman cooling of a bound atom to the 3D zero-point energy. *Phys. Rev. Lett.*, 75:4011–4014, Nov 1995.

[14] A. Sørensen and K. Mølmer. Entanglement and quantum computation with ions in thermal motion. *Phys. Rev. A*, 62:022311, 2000.

[15] A. Sørensen and K. Mølmer. Quantum computation with ions in thermal motion. *Phys. Rev. Lett.*, 82:1971–1974, 1999.

[16] G.J. Milburn, S. Schneider, and D.F.V. James. Ion trap quantum computing with warm ions. *Fortschritte der Physik*, 48:801–810, 2000.

[17] T. P. Harty, D. T. C. Allcock, C. J. Ballance, L. Guidoni, H. A. Janacek, N. M. Linke, D. N. Stacey, and D. M. Lucas. High-fidelity preparation, gates, memory, and readout of a trapped-ion quantum bit. *Phys. Rev. Lett.*, 113:220501, 2014.

[18] C. J. Ballance, T. P. Harty, N. M. Linke, M. A. Sepiol, and D. M. Lucas. High-fidelity quantum logic gates using trapped-ion hyperfine qubits. *Phys. Rev. Lett.*, 117:060504, 2016.

[19] J. P. Gaebler, T. R. Tan, Y. Lin, Y. Wan, R. Bowler, A. C. Keith, S. Glancy, K. Coakley, E. Knill, D. Leibfried, and D. J. Wineland. High-fidelity universal gate set for $^{9}Be^{+}$ ion qubits. *Phys. Rev. Lett.*, 117:060505, 2016.

[20] H. C. Nägerl, D. Leibfried, H. Rohde, G. Thalhammer, J. Eschner, F. Schmidt-Kaler, and R. Blatt. Laser addressing of individual ions in a linear ion trap. *Phys. Rev. A*, 60:145–148, 1999.

[21] T. Monz, P. Schindler, J. T. Barreiro, M. Chwalla, D. Nigg, W. A. Coish, M. Harlander, W. Hänsel, M. Hennrich, and R. Blatt. 14-qubit entanglement: Creation and coherence. *Phys. Rev. Lett.*, 106:130506, 2011.

[22] R. Ozeri, W. M. Itano, R. B. Blakestad, J. Britton, J. Chiaverini, J. D. Jost, C. Langer, D. Leibfried, R. Reichle, S. Seidelin, J. H. Wesenberg, and D. J. Wineland. Errors in trapped-ion quantum gates due to spontaneous photon scattering. *Phys. Rev. A*, 75:042329, 2007.

[23] F. Mintert and C. Wunderlich. Ion-trap quantum logic using long-wavelength radiation. *Phys. Rev. Lett.*, 87:257904, 2001.

[24] M. Johanning, A. Braun, N. Timoney, V. Elman, W. Neuhauser, and Chr. Wunderlich. Individual addressing of trapped ions and coupling of motional and spin states using RF radiation. *Phys. Rev. Lett.*, 102:073004, 2009.

[25] A. Khromova, Ch. Piltz, B. Scharfenberger, T. F. Gloger, M. Johanning, A. F. Varón, and Ch. Wunderlich. Designer spin pseudomolecule implemented with trapped ions in a magnetic gradient. *Phys. Rev. Lett.*, 108:220502, 2012.

[26] T. Ruster, C. T. Schmiegelow, H. Kaufmann, C. Warschburger, F. Schmidt-Kaler, and U. G. Poschinger. A long-lived Zeeman trapped-ion qubit. *Applied Physics B*, 122(10):254, 2016.

[27] N. Timoney, I. Baumgart, M. Johanning, A. F. Varón, M. B. Plenio, A. Retzker, and Ch. Wunderlich. Quantum gates and memory using microwave-dressed states. *Nature*, 476:185, 2011.

[28] S. Weidt, J. Randall, S. C. Webster, K. Lake, A. E. Webb, I. Cohen, T. Navickas, B. Lekitsch, A. Retzker, and W. K. Hensinger. Trapped-ion quantum logic with global radiation fields. *Phys. Rev. Lett.*, 117:220501, 2016.

[29] C. Ospelkaus, C. E. Langer, J. M. Amini, K. R. Brown, D. Leibfried, and D. J. Wineland. Trapped-ion quantum logic gates based on oscillating magnetic fields. *Phys. Rev. Lett.*, 101:090502, 2008.

[30] T. P. Harty, M. A. Sepiol, D. T. C. Allcock, C. J. Ballance, J. E. Tarlton, and D. M. Lucas. High-fidelity trapped-ion quantum logic using near-field microwaves. *Phys. Rev. Lett.*, 117:140501, 2016.

[31] T. P. Harty. *High-fidelity microwave-driven quantum logic in intermediate-field* $^{43}Ca^{+}$. PhD thesis, University of Oxford, 2013.

[32] L. Deslauriers, S. Olmschenk, D. Stick, W. K. Hensinger, J. Sterk, and C. Monroe. Scaling and suppression of anomalous heating in ion traps. *Phys. Rev. Lett.*, 97:103007, 2006.

[33] U. Warring, C. Ospelkaus, Y. Colombe, R. Jördens, D. Leibfried, and D. J. Wineland. Individual-ion addressing with microwave field gradients. *Phys. Rev. Lett.*, 110:173002, 2013.

[34] D. T. C. Allcock, T. P. Harty, C. J. Ballance, B. C. Keitch, N. M. Linke, D. N. Stacey, and D. M. Lucas. A microfabricated ion trap with integrated microwave circuitry. *Applied Physics Letters*, 102(4):044103, 2013.

[35] D. Kielpinski, C. Monroe, and D. J. Wineland. Architecture for a large-scale ion trap quantum computer. *Nature*, 417:709–711, 2002.

[36] C. Monroe, R. Raussendorf, A. Ruthven, K. R. Brown, P. Maunz, L.M. Duan, and J. Kim. Large-scale modular quantum-computer architecture with atomic memory and photonic interconnects. *Phys. Rev. A*, 89:022317, 2014.

[37] D. Hucul, I. V. Inlek, G. Vittorini, C. Crocker, S. Debnath, S. M. Clark, and C. Monroe. Modular entanglement of atomic qubits using photons and phonons. *Nature Physics*, 11:37 – 42, 2014.

[38] B. Lekitsch, S. Weidt, A. G. Fowler, K. Mølmer, S. J. Devitt, C. Wunderlich, and W. K. Hensinger. Blueprint for a microwave trapped ion quantum computer. *Science Advances*, 3(2), 2017.

[39] R. F. Wuerker, H. Shelton, and R. V. Langmuir. Electrodynamic containment of charged particles. *Journal of Applied Physics*, 30(3):342 – 349, 1959.

[40] D. F. Murgia. *Microchip ion traps with high magnetic field gradients for microwave quantum logic.* PhD thesis, Imperial College London, 2017.

[41] C. J. Foot. *Atomic physics.* Oxford University Press, 2004.

[42] D.F.V. James. Quantum dynamics of cold trapped ions with application to quantum computation. *Applied Physics B*, 66(2):181–190, 1998.

[43] Q. A. Turchette, Kielpinski, B. E. King, D. Leibfried, D. M. Meekhof, C. J. Myatt, M. A. Rowe, C. A. Sackett, C. S. Wood, W. M. Itano, C. Monroe, and D. J. Wineland.

Heating of trapped ions from the quantum ground state. *Phys. Rev. A*, 61:063418, 2000.

[44] S. Weidt, J. Randall, S. C. Webster, E. D. Standing, A. Rodriguez, A. E. Webb, B. Lekitsch, and W. K. Hensinger. Ground-state cooling of a trapped ion using long-wavelength radiation. *Phys. Rev. Lett.*, 115:013002, 2015.

[45] M. D. Hughes, B. Lekitsch, J. A. Broersma, and W. K. Hensinger. Microfabricated ion traps. *Contemporary Physics*, 52(6):505 –529, 2011.

[46] M. Brownnutt, M. Kumph, P. Rabl, and R. Blatt. Ion-trap measurements of electric-field noise near surfaces. *Rev. Mod. Phys.*, 87:1419–1482, 2015.

[47] C. D. Bruzewicz, J. M. Sage, and J. Chiaverini. Measurement of ion motional heating rates over a range of trap frequencies and temperatures. *Phys. Rev. A*, 91:041402, 2015.

[48] B. E. King, C. S. Wood, C. J. Myatt, Q. A. Turchette, D. Leibfried, W. M. Itano, C. Monroe, and D. J. Wineland. Cooling the collective motion of trapped ions to initialize a quantum register. *Phys. Rev. Lett.*, 81:1525–1528, 1998.

[49] A. H. Nizamani, J. J. McLoughlin, and W. K. Hensinger. Doppler-free Yb spectroscopy with the fluorescence spot technique. *Phys. Rev. A*, 82:043408, 2010.

[50] H. Metcalf and P. Van Der Straten. *Laser cooling and trapping.* Springer, 1999.

[51] S. Olmschenk, K. C. Younge, D. L. Moehring, D. N. Matsukevich, P. Maunz, and C. Monroe. Manipulation and detection of a trapped Yb^+ hyperfine qubit. *Phys. Rev. A*, 76:052314, 2007.

[52] G. Breit and I. I. Rabi. Measurement of nuclear spin. *Phys. Rev.*, 38:2082–2083, 1931.

[53] J. Randall. *High fidelity entanglement of trapped ions using long-wavelength radiation.* PhD thesis, Imperial College London, 2016.

[54] R. Sterling. *Ytterbium ion trapping and microfabrication of ion trap arrays.* PhD thesis, University of Sussex, 2011.

[55] S. Weidt. *Towards microwave based ion trap quantum technology.* PhD thesis, University of Sussex, 2013.

[56] J. Randall. Quantum logic in trapped ions using microwaves and dressed states. Master's thesis, Imperial College London, 2012.

[57] A. Nizamani. *Yb^+ ion trapping and optimum planar trap geometries for scalable quantum technology.* PhD thesis, University of Sussex, 2011.

[58] J. McLoughlin. *Development and implementation of an Yb^+ ion trap experiment towards coherent manipulation and entanglement.* PhD thesis, University of Sussex, 2011.

[59] T. Navickas. *Towards high-fidelity microwave driven multi-qubit gates on microfabricated surface ion traps.* PhD thesis, University of Sussex, 2017.

[60] J. Siverns. *Yb ion trap experimental set-up and two-dimensional ion trap surface array design towards analogue quantum simulations.* PhD thesis, University of Sussex, 2011.

[61] D. F. Murgia. A scalable approach to quantum logic operations. Master's thesis, Imperial College London, 2014.

[62] A. M. Lawrence. *Under preparation.* PhD thesis, Imperial College London, 2019.

[63] R. Noek, G. Vrijsen, D. Gaultney, E. Mount, T. Kim, P. Maunz, and J. Kim. High speed, high fidelity detection of an atomic hyperfine qubit. *Opt. Lett.*, 38(22):4735–4738, 2013.

[64] S. C. Webster, S. Weidt, K. Lake, J. J. McLoughlin, and W. K. Hensinger. Simple manipulation of a microwave dressed-state ion qubit. *Phys. Rev. Lett.*, 111:140501, 2013.

[65] J. Randall, S. Weidt, E. D. Standing, K. Lake, S. C. Webster, D. F. Murgia, T. Navickas, K. Roth, and W. K. Hensinger. Efficient preparation and detection of microwave dressed-state qubits and qutrits with trapped ions. *Phys. Rev. A*, 91:012322, 2015.

[66] J. Randall, A. M. Lawrence, S. C. Webster, S. Weidt, N. V. Vitanov, and W. K. Hensinger. Generation of high-fidelity quantum control methods for multilevel systems. *Phys. Rev. A*, 98:043414, 2018.

[67] Ch. Roos, Th. Zeiger, H. Rohde, H. C. Nägerl, J. Eschner, D. Leibfried, F. Schmidt-Kaler, and R. Blatt. Quantum state engineering on an optical transition and decoherence in a Paul trap. *Phys. Rev. Lett.*, 83:4713–4716, 1999.

[68] J. F. Poyatos, J. I. Cirac, and P. Zoller. Complete characterization of a quantum process: The two-bit quantum gate. *Phys. Rev. Lett.*, 78:390–393, 1997.

[69] M. Riebe, K. Kim, P. Schindler, T. Monz, P. O. Schmidt, T. K. Körber, W. Hänsel, H. Häffner, C. F. Roos, and R. Blatt. Process tomography of ion trap quantum gates. *Phys. Rev. Lett.*, 97:220407, 2006.

[70] E. Knill, D. Leibfried, R. Reichle, J. Britton, R. B. Blakestad, J. D. Jost, C. Langer, R. Ozeri, S. Seidelin, and D. J. Wineland. Randomized benchmarking of quantum gates. *Phys. Rev. A*, 77:012307, 2008.

[71] S. Olmschenk, R. Chicireanu, K. D. Nelson, and J. V. Porto. Randomized benchmarking of atomic qubits in an optical lattice. *New Journal of Physics*, 12(11):113007, 2010.

[72] K. R. Brown, A. C. Wilson, Y. Colombe, C. Ospelkaus, A. M. Meier, E. Knill, D. Leibfried, and D. J. Wineland. Single-qubit-gate error below 10^{-4} in a trapped ion. *Phys. Rev. A*, 84:030303, 2011.

[73] E. Magesan, J. M. Gambetta, B. R. Johnson, C. A. Ryan, J. M. Chow, S. T. Merkel, M. P. da Silva, G. A. Keefe, M. B. Rothwell, T. A. Ohki, M. B. Ketchen, and M. Steffen. Efficient measurement of quantum gate error by interleaved randomized benchmarking. *Phys. Rev. Lett.*, 109:080505, 2012.

[74] J. Kelly, R. Barends, B. Campbell, Y. Chen, Z. Chen, B. Chiaro, A. Dunsworth, A. G. Fowler, I.C. Hoi, E. Jeffrey, A. Megrant, J. Mutus, C. Neill, P. J. J. O'Malley, C. Quintana, P. Roushan, D. Sank, A. Vainsencher, J. Wenner, T. C. White, A. N. Cleland, and John M. Martinis. Optimal quantum control using randomized benchmarking. *Phys. Rev. Lett.*, 112:240504, 2014.

[75] J. Wallman, C. Granade, R. Harper, and S. T Flammia. Estimating the coherence of noise. *New Journal of Physics*, 17(11):113020, 2015.

[76] J. J. Wallman and J. Emerson. Noise tailoring for scalable quantum computation via randomized compiling. *Phys. Rev. A*, 94:052325, 2016.

[77] R. Blume-Kohout, J. K. Gamble, E. Nielsen, K. Rudinger, J. Mizrahi, K. Fortier, and P. Maunz. Demonstration of qubit operations below a rigorous fault tolerance threshold with gate set tomography. *Nature Communications*, 8:14485, 2017.

[78] V.S. Malinovsky and J.L. Krause. General theory of population transfer by adiabatic rapid passage with intense, chirped laser pulses. *The European Physical Journal D - Atomic, Molecular, Optical and Plasma Physics*, 14(2):147–155, 2001.

[79] A. Bermudez, X. Xu, R. Nigmatullin, J. O'Gorman, V. Negnevitsky, P. Schindler, T. Monz, U. G. Poschinger, C. Hempel, J. Home, F. Schmidt-Kaler, M. Biercuk, R. Blatt, S. Benjamin, and M. Müller. Assessing the progress of trapped-ion processors towards fault-tolerant quantum computation. *Phys. Rev. X*, 7:041061, 2017.

[80] I. Talukdar, D. J. Gorman, N. Daniilidis, P. Schindler, S. Ebadi, H. Kaufmann, T. Zhang, and H. Häffner. Implications of surface noise for the motional coherence of trapped ions. *Phys. Rev. A*, 93:043415, 2016.

[81] D. Hayes, S. M. Clark, S. Debnath, D. Hucul, I. V. Inlek, K. W. Lee, Q. Quraishi, and C. Monroe. Coherent error suppression in multiqubit entangling gates. *Phys. Rev. Lett.*, 109:020503, 2012.

[82] F. Haddadfarshi and F. Mintert. High fidelity quantum gates of trapped ions in the presence of motional heating. *New Journal of Physics*, 18(12):123007, 2016.

[83] S. Blanes, F. Casas, J. A. Oteo, and J. Ros. A pedagogical approach to the Magnus expansion. *European Journal of Physics*, 31(4):907, 2010.

[84] C. F. Roos. Ion trap quantum gates with amplitude-modulated laser beams. *New Journal of Physics*, 10(1):013002, 2008.

[85] C. J. Ballance. *High-fidelity quantum logic in Ca^+*. PhD thesis, University of Oxford, 2014.

[86] C. F. Roos, T. Monz, K. Kim, M. Riebe, H. Häffner, D. F. V. James, and R. Blatt. Nonlinear coupling of continuous variables at the single quantum level. *Phys. Rev. A*, 77:040302, 2008.

[87] X. R. Nie, C. F. Roos, and D.F.V. James. Theory of cross phase modulation for the vibrational modes of trapped ions. *Physics Letters A*, 373(4):422 – 425, 2009.

[88] G. Mikelsons, I. Cohen, A. Retzker, and M. B. Plenio. Universal set of gates for microwave dressed-state quantum computing. *New Journal of Physics*, 17(5):053032, 2015.

[89] K. G. Johnson, J. D. Wong-Campos, A. Restelli, K. A. Landsman, B. Neyenhuis, J. Mizrahi, and C. Monroe. Active stabilization of ion trap radiofrequency potentials. *Review of Scientific Instruments*, 87(5):053110, 2016.

[90] N. D. Guise, S. D. Fallek, H. Hayden, C-S. Pai, C. Volin, K. R. Brown, J. T. Merrill, A. W. Harter, J. M. Amini, L. M. Lust, K. Muldoon, D. Carlson, and J. Budach. In-vacuum active electronics for microfabricated ion traps. *Review of Scientific Instruments*, 85(6):063101, 2018/05/27 2014.

[91] S. Collingbourne. Entangling gates for quantum computation. Master's thesis, Imperial College London, 2017.

[92] Y. Shapira, R. Shaniv, T. Manovitz, N. Akerman, and R. Ozeri. Robust entanglement gates for trapped-ion qubits. *Phys. Rev. Lett.*, 121:180502, 2018.

[93] E. A. Martinez, T. Monz, D. Nigg, P. Schindler, and R. Blatt. Compiling quantum algorithms for architectures with multi-qubit gates. *New Journal of Physics*, 18(6):063029, 2016.

[94] D. Maslov. Basic circuit compilation techniques for an ion-trap quantum machine. *New Journal of Physics*, 19(2):023035, 2017.

[95] T. Manovitz, A. Rotem, R. Shaniv, I. Cohen, Y. Shapira, N. Akerman, A. Retzker, and R. Ozeri. Fast dynamical decoupling of the Mølmer-Sørensen entangling gate. *Phys. Rev. Lett.*, 119:220505, 2017.

[96] I. Cohen, S. Weidt, W. K. Hensinger, and A. Retzker. Multi-qubit gate with trapped ions for microwave and laser-based implementation. *New Journal of Physics*, 17(4):043008, 2015.